

# **Magnetism of unconventional nanoscaled materials: An X-ray circular dichroism and muon spin rotation study**

**Von der Fakultät Mathematik und Physik der Universität Stuttgart  
zur Erlangung der Würde eines  
Doktors der Naturwissenschaften (Dr. rer. nat.)  
genehmigte Abhandlung**

Vorgelegt von  
Thomas Hermann Tietze  
aus Horb am Neckar

**Hauptberichter: PD Dr. Eberhard Goering  
Mitberichter: Prof. Dr. Martin Dressel**

**Tag der mündlichen Prüfung: 15. Dezember 2014**

**Max-Planck-Institut für Intelligente Systeme Stuttgart  
2014**



## Contents

1.	Zusammenfassung der Arbeit .....	9
2.	Introduction.....	19
3.	Scientific Background .....	24
3.1.	Basics of Magnetism.....	24
3.1.1.	Interaction of Matter with an External Magnetic Field .....	24
3.1.2.	Magnetism of Single Atoms: Elementary magnetic moments .....	27
3.1.3.	Paramagnetism .....	29
3.1.4.	Ferromagnetism .....	30
3.1.5.	Superparamagnetism .....	35
3.2.	X-ray Magnetic Circular Dichroism (XMCD) .....	38
3.2.1.	X-ray Absorption.....	38
3.2.2.	Model Explanation for the X-ray Magnetic Circular Dichroism .....	40
3.2.3.	Sum Rules .....	45
3.3.	Magnetism of nano cluster systems .....	50
3.3.1.	From atomic to bulk properties .....	50
3.3.2.	Magnetic Anisotropy of Metal Nano Clusters.....	53
3.4.	Transition metal clusters on the graphene Moiré template.....	55
3.5.	Magnetism of doped and undoped ZnO systems .....	61
3.6.	Muon Spin Rotation ( $\mu$ SR).....	64
3.6.1.	Muon properties .....	64
3.6.2.	Muon beam production .....	65
3.6.3.	Muon interaction with matter .....	71
3.6.4.	Important $\mu$ SR Decay Functions .....	77
4.	Experimental Aspects.....	81
4.1.	Synchrotron Radiation .....	81
4.1.1.	Generation of synchrotron radiation .....	81
4.1.2.	WERA beamline at ANKA .....	85
4.1.3.	PM3 beamline at BESSY.....	86

---

4.2.	Low Energy Muons .....	87
4.2.1.	$\mu$ E4 beamline at the SpS .....	87
4.3.	7 Tesla fast switching XMCD setup .....	91
4.4.	XMCD data acquisition and evaluation .....	95
4.4.1.	XMCD measurement principles .....	95
4.4.2.	Fast continuous mode .....	96
4.4.3.	Offset correction of XMCD spectra measured with TEY .....	97
4.4.4.	Background references .....	100
4.4.5.	Background subtraction .....	106
5.	Magnetism of Ni-Nanoclusters on a Graphene Moiré Template .....	111
5.1.	In-Situ Sample Preparation .....	111
5.2.	Spherically shaped nanoclusters .....	115
5.2.1.	Pre-characterization: STM Properties .....	115
5.2.2.	XMCD Results .....	117
5.3.	Triangularly shaped nanoclusters .....	122
5.3.1.	Pre-characterization: STM Properties .....	122
5.3.2.	XMCD Results .....	124
5.4.	Comparison and Discussion .....	128
5.4.1.	Satellite Peaks in the Ni XAS spectrum .....	128
5.4.2.	Scaling of the main $L_3$ -peak: Estimating the number of holes $n_h$ .....	133
5.4.3.	Ni satellite features .....	138
5.4.4.	Ni cluster/graphene substrate interaction.....	143
5.4.5.	Ni magnetic moment analysis .....	153
5.4.6.	Magnetism at the Ni/graphene interface .....	166
5.4.7.	Magnetic Anisotropy .....	169
5.5.	Summary: Magnetism of Ni nanoclusters on graphene .....	178
6.	Magnetism in nanograined, undoped ZnO Systems .....	181
6.1.	Sample Preparation and Structural Properties .....	181
6.2.	Magnetic Properties .....	185



---

6.2.1.	SQUID Measurements .....	185
6.2.2.	XMCD Measurements .....	187
6.3.	$\mu$ SR Measurements .....	190
6.3.1.	ZnO <sub>1100K</sub> Sample.....	193
6.3.2.	ZnO <sub>700K</sub> Sample .....	197
6.4.	Discussion .....	201
6.4.1.	Formation of Muonium .....	201
6.4.2.	Magnetic Grain Boundary Area.....	202
6.5.	Summary: Magnetism in nanograined ZnO .....	206
7.	Thesis Summary .....	209
	Literature .....	215
	Danksagung.....	228
	Publikationsliste .....	231
	Selbständigkeitserklärung.....	233



## Abkürzungsverzeichnis

$\mu$ SR	Muon Spin Rotation/Relaxation
DOS	Density of States
ECD	Equivalent Circular Diameter
EDX	Energy Dispersive X-Ray Spectroscopy
FIB	Focused Ion Beam
FM	Ferromagnetic
FWHM	Full-Width-Half-Maximum
GKT	Gaussian-Kubo-Toyabe
LE- $\mu$ SR	Low Energy Muon Spin Rotation
LKT	Lorentz-Kubo-Toyabe
LT	Low Temperature
MAE	Magnetic Anisotropy Energy
MFV	Magnetic Volume Fraction
ML	Monolayer
$n_h$	Number of Holes
NI	Normal Incidence
NM	Nonmagnetic
PEY	Partial Electron Yield
PMA	Perpendicular Magnetic Anisotropy
PNR	Polarized Neutron Resonance
RT	Room Temperature
SC	Single Crystal
SOC	Spin Orbit Coupling
SPM	Superparamagnetic
SQUID	Superconducting Quantum Interference Device
STM	Scanning Tunneling Microscope
TEM	Transmission Electron Microscopy
TEY	Total Electron Yield
VKT	Voigtian-Kubo-Toyabe
VSM	Vibrating Sample Magnetometer
XAS	X-ray Absorption Spectroscopy
XMCD	X-ray Magnetic Circular Dichroism



# 1. Zusammenfassung der Arbeit

## Einleitung: Nickelnanocluster auf Graphen

Als Nanopartikel werden für gewöhnlich Teilchen in der Größenordnung eines milliardstel (!) Meters bezeichnet. In diesem Größenordnungsbereich unterscheiden sich die physikalischen Eigenschaften dieser Partikel zum Teil drastisch von ihrem makroskopischen Gegenstück, gleich aus welchem Material diese bestehen. Vor allem die magnetischen Eigenschaften ändern sich stark, da Magnetismus an sich ein kollektives Phänomen darstellt, Nanopartikel jedoch im Verhältnis zum Gesamtvolumen einen sehr großen Anteil von Oberflächenatomen mit offenen Bindungen besitzen. Daraus resultiert im Normalfall ein stark erhöhtes magnetisches Bahnmoment, welches in makroskopischen Materialien ausgelöscht ist. Das Bahnmoment wiederum ist sehr stark an das Nanopartikelgitter gekoppelt und lässt sich nur schwer durch ein äußeres Magnetfeld in eine andere als die bevorzugte Gitterrichtung bewegen. Die magnetische Anisotropie wird also durch ein erhöhtes Bahnmoment verstärkt und führt zu wichtigen potentiellen Anwendungen vor allem im Bereich magnetischer Datenspeicherung. Durch den konsequenten Einsatz von magnetischen Nanopartikeln mit geeigneter magnetischer Anisotropie können so sehr hohe Speicherdichten für Festplatten erreicht werden. Weitere interessante Möglichkeiten können sich aus der Wechselwirkung der Nanopartikel an der Grenzfläche zu einem Substrat ergeben. Zum Beispiel kann es an der Grenzfläche zwischen Nanopartikel und Substrat zu einem Ladungsaustausch kommen, der bei geeigneten magnetischen Eigenschaften der Nanopartikel spinpolarisiert erfolgen kann. Besitzt das Substratmaterial ebenfalls außergewöhnliche Eigenschaften, können die Vorteile beider Systeme beispielsweise in Spintronikbauteilen kombiniert werden.

Ein vielversprechendes System in dieser Hinsicht sind Übergangsmetallnanopartikel auf Graphen. Graphen ist eine monoatomare Schicht  $sp^2$ -hybridisierten Kohlenstoffes, in der sich die einzelnen Kohlenstoffatome honigwabenförmig anordnen. Aus dieser speziellen Anordnung folgen teilweise einzigartige Eigenschaften wie zum Beispiel eine lineare Dispersionsrelation, die zur Folge hat, dass sich Elektronen innerhalb der Graphenschicht mit sehr geringem elektrischem Widerstand fortbewegen können. Darüber hinaus ist Graphen ein Halbleiter ohne Bandlücke. Durch geeignete Substitution einzelner Kohlenstoffatome kann es in einen p- oder n-dotierten Halbleiter überführt werden. Aus diesen Eigenschaften

ergeben sich einige interessante, potentielle Anwendungen von Graphen, beispielsweise als transparente Leiterelektrode, lichtempfindlicher Transistor, Superkondensator oder auch als chemischer Sensor zur Detektion bestimmter Gase.

Wie bereits angedeutet, kann Graphen auch als Substrat für das gezielte Wachstum magnetischer Nanostrukturen benutzt werden. Abhängig von den Präparationsparametern, wie Deponierungstemperatur und nominelle Bedeckung, ist es möglich Nanocluster in verschiedenen Formen und Größen auf Graphen herzustellen.

Da sowohl magnetische Nanocluster als auch Graphen außergewöhnliche physikalische Eigenschaften besitzen, ist es naheliegend diese beiden Systeme zu vereinen. Jedoch müssen bei allen neu entdeckten Materialien beziehungsweise Systemen zuerst grundlegende Fragen beantwortet werden, um die Möglichkeit künftiger technisch relevanter Nutzung beurteilen zu können. Daher beschäftigt sich ein Teil dieser Promotion mit den elektronischen und magnetischen Eigenschaften von Nickelnanopartikeln auf Graphen. Die magnetischen Eigenschaften konnten mit Hilfe fortschrittlicher magnetischer Röntgenkontrastspektroskopie, dem sogenannten Röntgenzirkulardichroismus (engl. „X-ray Magnetic Circular Dichroism“, kurz XMCD) untersucht werden. XMCD ist elementspezifisch und ermöglicht es, das magnetische Spin- und Bahnmoment eines bestimmten Materials auf atomarer Skala zu bestimmen. Zusätzlich können aus den zugehörigen Röntgenabsorptionsspektren Rückschlüsse auf die elektronische Struktur und eine etwaige Wechselwirkung des untersuchten Materials mit seinem Substrat gezogen werden. Beispielsweise ist so möglich, die Anzahl der unbesetzten Nickel d-Zustände der Nanocluster auf Graphen in Abhängigkeit von deren Größen zu ermitteln.

### **Ergebnisse: Nickelnanopartikel auf einem Graphensubstrat**

Ziel dieses Teils der Arbeit war es, die elektronischen und magnetischen Eigenschaften von Nickelnanopartikel auf Graphen in Abhängigkeit ihrer Größe und ihrer Form zu untersuchen. Es wurden je eine Serie dreieckige (Grundfläche in der Größenordnung von etwa  $20 \times 20 \text{ nm}^2$ , 2 nm Höhe) und eine Serie elliptische (Größenordnung: Achsenlänge 3 nm, Höhe 1 nm) Nanopartikel mit variierender Größe unter Ultrahochvakuumbedingungen (UHV) *in-situ* präpariert und mit Hilfe von synchrotronbasierter XMCD Spektroskopie untersucht.

Überraschenderweise waren die gemessenen Werte für das magnetische Gesamtmoment bei allen Proben kleiner Werte als ursprünglich für Nanocluster erwartet. Für dreieckige Nanocluster und bei nomineller Bedeckung mit 0,2 Monolagen Nickel ist das magnetische Moment  $0,39 \mu_B$  pro Atom. Das magnetische Moment nimmt zu und nähert sich dann dem Wert einer makroskopischen Nickelprobe an, beispielsweise beträgt es  $0,67 \mu_B$  pro Atom bei einer nominellen Bedeckung mit 2 Monolagen Nickel.

Derselbe Verlauf zeigt sich für die elliptischen Nanopartikel. Das magnetische Moment nimmt mit zunehmender Clustergröße zu, beispielsweise von  $0,35 \mu_B$  pro Atom bei einer nominellen Bedeckung mit 0,15 Monolagen Nickel bis  $0,57 \mu_B$  pro Atom bei einer nominellen Bedeckung mit 1 Monolage Nickel. In beiden Fällen erfolgt die Zunahme des magnetischen Moments mit der nominellen Bedeckung stark nichtlinear. Es konnten keine großen Unterschiede des magnetischen Moments in Abhängigkeit von der Form der Nanopartikel festgestellt werden.

Ähnliche Ergebnisse eines abnehmenden magnetischen Moments mit geringerer nomineller Bedeckung wurden für Nanopartikel und dünne Filme von Nickel auf anderen Übergangsmetallen wie Kobalt und Kupfer gefunden. Diese wurden von den jeweiligen Autoren mit einer Hybridisierung des Nickels mit Kobalt oder Kupfer erklärt, was aufgrund der chemischen Ähnlichkeit der im Periodensystem benachbarten Elemente plausibel erscheint. Dass sich Nickel auf Graphen ähnlich verhält, ist dadurch jedoch nicht sofort ersichtlich, handelt es sich doch um zwei verschiedene Elementklassen (Metall auf Halbleiter ohne Bandlücke).

Analysen des nichtmagnetischen Röntgenabsorptionsspektrums (engl. „X-ray absorption spectroscopy“, kurz XAS) weisen tatsächlich Indizien einer starken Wechselwirkung zwischen den Nickelnanopartikeln und Graphen auf. Das integrierte XAS-Signal, welches proportional zur Anzahl der unbesetzten Zustände in der Nickel d-Schale ist, nimmt mit geringerer nomineller Nickelbedeckung stark ab. Dies bedeutet eine höhere Besetzung der d-Zustände, beispielsweise durch Ladungsausgleich zwischen den Nanoclustern und dem Graphensubstrat an deren Grenzfläche hin.

Im Allgemeinen wird innerhalb der XMCD-Gemeinschaft die Zustandsbesetzung von der anderen Seite her betrachtet, nämlich von der Anzahl der unbesetzten Zustände. Diese wird im Folgenden mit  $n_h$  (engl. „number of holes“ = Anzahl der Löcher) bezeichnet. Dieser Wert wird für die quantitative Bestimmung magnetischer Momente mit Hilfe der

sogenannten Summenregeln benötigt. Bei Untersuchungen von makroskopischen Proben wird dieser Wert für das jeweils untersuchte Material als konstant angenommen. Aus den gemessenen Absorptionsspektren wurde ersichtlich, dass diese Annahme im Falle der untersuchten Nickelcluster auf Graphen nicht mehr gerechtfertigt ist.

Daher wurde im Rahmen dieser Arbeit  $n_h$  für jede Probe durch Vergleich der jeweiligen Absorptionsspektren mit einer eigens präparierten, makroskopischen Nickelreferenzprobe, deren  $n_h$ -Wert bekannt ist, bestimmt. Die Zustandsdichte der Nickel d-Schale ändert sich stark,  $n_h$  nimmt mit zunehmender Partikelgröße zu und nähert sich dem makroskopischen Nickelwert von  $n_h = 1,45$ . Die Abhängigkeit der Anzahl der Löcher von der nominellen Bedeckung ist für beide Clusterformen, dreieckig und elliptisch, ähnlich und verläuft wie im Falle des magnetischen Momentes stark nichtlinear.

Anhand dieser Erkenntnis kann auch die starke Abnahme des magnetischen Momentes für kleine Nanopartikel erklärt werden. Durch die Wechselwirkung des Nickels mit dem Graphensubstrat und der daraus resultierenden erhöhten Besetzung der Nickel d-Zustände kommt es zu einer Depolarisation der spin-up und spin-down Zustände an der Fermikante, was dann die beobachtete starke Abnahme des magnetischen Moments zur Folge hat.

Prinzipiell können sich aus solch einer Wechselwirkung zahlreiche interessante Anwendungen ergeben, beispielsweise in Form von Spintronikbausteinen. Hierzu müsste man aber ebenfalls die elektronische Struktur des Graphens detailliert untersuchen. Entsprechende XAS- und XMCD-Messungen an der K-Kante des Kohlenstoffs wurden zwar durchgeführt, jedoch ist es aufgrund der Dämpfung des Absorptionssignals durch das darüber liegende Nickel und eines relativ großen Untergrundsignals nicht gelungen, das Graphensignal zu isolieren.

Eine weitere wichtige Eigenschaft im Hinblick auf die technische Anwendung der Cluster als magnetische Datenspeicher ist die magnetische Anisotropieenergie (engl. „Magnetic Anisotropy Energy“, kurz MAE). Zur Bestimmung der MAE wurden element-spezifische Magnetisierungskurven der Nickelnanopartikel winkelabhängig gemessen. Die leichte magnetische Achse der dreieckigen wie auch der elliptischen Nanopartikel liegt in der Dreiecks-/Ellipsoidebene. Um die Magnetisierung der Nanopartikel zu sättigen, mussten Magnetfelder von bis zu 4,5 T angelegt werden. Dies bedeutet, dass sich die Nanopartikel trotz Kühlung auf 10 K noch im superparamagnetischen Zustand befinden und die Blockingtemperatur daher darunter liegen muss.



Die magnetische Anisotropieenergie wurde für beide Partikelformen ermittelt. Sie nimmt in beiden Fällen überproportional mit der Partikelgröße zu. Dieses Verhalten ist für elliptische Partikel ausgeprägter als für dreieckige. Die Anisotropieenergie variiert in einem Bereich von  $29,5 \mu\text{eV}$  pro Atom für dreieckige Partikel bei nomineller Bedeckung mit 2 Monolagen Nickel bis  $16 \mu\text{eV}$  pro Atom für elliptische Partikel bei nomineller Bedeckung mit 0,1 Monolagen Nickel.

Modellhaft kann man die Anisotropieenergie in drei verschiedene Beiträge aufteilen: in Formanisotropie, einen größenunabhängigen „Volumenanteil“ und einen von der nominellen Bedeckung abhängigen Ober-/Grenzflächenanteil. Form- und Volumenanisotropie sind positiv und begünstigen daher eine leichte Magnetisierungsachse in der Probenebene. Der bedeckungsabhängige Oberflächenanteil ist negativ und könnte im Prinzip zu einer bevorzugten Magnetisierungsrichtung senkrecht zur Probenebene (sogenannte „Perpendicular Magnetic Anisotropy“, kurz PMA) führen, was bei modernen magnetischen Datenspeichern zu extrem hohen Speicherdichten führt.

Zusammenfassend wurde im Rahmen dieser Arbeit ein tieferes mikroskopisches Verständnis der elementaren elektronischen und magnetischen Eigenschaften von Nickelnanopartikeln auf Graphen und deren gegenseitiger Wechselwirkung ermöglicht. Daher stellt diese Arbeit einen wichtigen Beitrag zur Erforschung der Wechselwirkung zwischen Graphen und eventuellen metallischen Kontakten, wie sie beispielsweise in Spintronikbausteinen eingesetzt werden können, dar.

### **Einleitung: Magnetismus in nicht dotiertem ZnO**

Der zweite Teil dieser Arbeit beschäftigt sich mit dem indirekten Einfluss der Nanopartikelgröße auf die magnetischen Eigenschaften eines oxydischen Systems. Im konkreten Fall handelt es sich hierbei um das Auftreten von Ferromagnetismus in eigentlich unmagnetischem ZnO.

Ursprünglich wurde angenommen, dass ZnO bei geringer Dotierung mit Übergangsmetallatomen, wie zum Beispiel Kobalt, durch die ferromagnetische Kopplung der Dotieratome untereinander ferromagnetisch werden kann. Dieser Effekt wurde sogar für Raumtemperatur vorhergesagt. Dies ist in Anbetracht der Tatsache, dass bisher nur sehr wenige Materialien bekannt sind, die bei Raumtemperatur Ferromagnetismus zeigen, sehr außergewöhnlich und hat zu einer regen Forschungstätigkeit auf diesem Gebiet geführt.

Eine ferromagnetische Kopplung der Dotieratome konnte in früheren, auf XMCD Messungen basierten Arbeiten jedoch nicht bestätigt werden. Es verhält sich vielmehr so, dass sich die Übergangsmetallatome entweder paramagnetisch verhalten oder dass sie (ungewollt) zu größeren, magnetischen Clustern innerhalb des ZnO zusammenwachsen. Bald folgten jedoch Veröffentlichungen, die von ferromagnetischem ZnO berichteten, ohne dass dieses zuvor in irgendeiner Art und Weise dotiert wurden. Ein systematischer Abgleich der strukturellen und magnetischen Eigenschaften förderte das erstaunliche Ergebnis zu Tage, dass die Frage des Ursprungs von Ferromagnetismus in ZnO von der mikroskopischen Beschaffenheit der jeweiligen ZnO Proben abhängt. Für ferromagnetisches ZnO bedarf es einer nanokristallinen Probe mit genügend feiner Körnung der einzelnen ZnO Körner (engl. „grains“). Als möglicher Schlüsselparameter erwies sich das Verhältnis von Kornoberfläche zu Kornvolumen, die sogenannte spezifische Korngröße. Überschreitet diese einen gewissen Wert, der im Bereich von etwa  $5 \cdot 10^7 \text{ nm}^{-1}$  liegt, dann kann ZnO tatsächlich ohne Zugabe von Dotieratomen ferromagnetisch werden.

Im Gegensatz zu den oben angesprochenen magnetischen Nanopartikeln auf Graphen gibt es hier jedoch die Annahme, dass nicht die Partikel an sich, beispielsweise aufgrund ihrer reduzierten Geometrie, sondern der Bereich dazwischen, die Korngrenzen selbst ferromagnetisch werden. Dies wird zurzeit im Rahmen des sogenannten  $d^0$ -Magnetismus innerhalb der Wissenschaftsgemeinschaft äußerst kontrovers diskutiert. Eine Idee beispielsweise ist, dass sich aufgrund von Defekten und/oder Fehlstellen überschüssige Elektronen innerhalb der Korngrenzen häufen, diese sich um ein Fehlstellenzentrum sammeln und dort in einem gekoppelten, ferromagnetischen Triplettzustand vorliegen. Bei Überschreiten einer bestimmten Perkolationsschwelle, wenn der Anteil des Korngrenzen- am Gesamtvolumen groß genug ist, durchziehen diese die gesamte Probe und eine ferromagnetische Kopplung der einzelnen magnetischen Bereiche findet statt.

Problematisch ist vor allem der direkte Nachweis dieser These. Messmethoden wie SQUID (engl. „Superconducting Quantum Interference Device“, supraleitende Quanteninterferenzeinheit, kurz SQUID) oder Vibrationsmagnetometer (engl. „Vibrating Sample Magnetometer“, kurz VSM), die die Magnetisierung über das gesamte Probenvolumen hinweg integrieren, geben über die mikroskopische Ursache keine direkte Auskunft. Die zur Verfügung stehende XMCD Methode kann hier bestenfalls ausschließen, dass die mittels SQUID ermittelte Magnetisierung nicht doch durch magnetische Verunreinigungen der

Probe verursacht wird. Zum Nachweis eines magnetischen Effektes mittels XMCD bedarf es zudem eines definierten Überganges von einem Grund- in einen angeregten Zustand, der für das Fehlstellensystem jedoch nicht gegeben ist.

Um diesem Problem zu begegnen, wurde für diesen Teil der Arbeit die sogenannte „niederenergetische Myonenspinrotation/-relaxation“ (LE- $\mu^+$ SR) verwendet. Hierbei werden Antimyonen ( $\mu^+$ ) als magnetische Sonde in ZnO „eingepflanzt“. Ihr magnetisches Moment bewirkt, dass sie eine Präzessionsbewegung in einem eventuell präsenten, lokalen Magnetfeld vollführen und diese Präzessionsbewegung zu einer Änderung des Signals gegenüber dem des nichtmagnetischen Zustandes führt. Die positive Ladung des  $\mu^+$  führt außerdem dazu, dass  $\mu^+$  sich bevorzugt an die Stellen der Probe setzt, wo sie positive Ladungen des Kerns vermeiden können. Dies sind vornehmlich Korngrenzen und Fehlstellen. Somit eignet sich diese Methode besonders für den Nachweis eines eventuell auftretenden Korngrenzenmagnetismus.

### **Ergebnisse: Korngrenzenmagnetismus in undotiertem ZnO**

Um tiefere Einsicht in das Auftreten von Ferromagnetismus in ZnO zu erlangen, wurden drei verschiedene, nicht dotierte Proben mit unterschiedlichen Korngrößen untersucht. Zwei Proben wurden mittels hydrothermischer Spaltung einer metallorganischen Zinkbutanoatlösung auf Saphirsubstraten hergestellt. Die mittleren Korngrößen betrugen jeweils 31 nm (bei einer Filmdicke von 100 nm) und 65 nm (bei einer Filmdicke von 450 nm). Dies entspricht einer mittleren spezifischen Korngröße von  $5,32 \cdot 10^7 \text{ m}^{-1}$  beziehungsweise  $2,65 \cdot 10^7 \text{ m}^{-1}$ . Eine umfangreiche Analyse der Größe der einzelnen Körner mit Hilfe von Transmissionselektronenmikroskopie (TEM) ergab, dass in beiden Probensystemen eine signifikante Anzahl an Nanokristallen oberhalb der kritischen Korngröße von  $5 \cdot 10^7 \text{ m}^{-1}$  existieren. Als dritte Probe wurde ein ZnO Einkristall als nichtmagnetische Referenz vor allem für  $\mu$ SR-Messungen verwendet.

Die magnetischen Eigenschaften wurden zuerst mit Hilfe von SQUID-Messungen bestimmt. Hierbei zeigte sich die größte Magnetisierung bei der Probe mit der kleinsten mittleren Korngröße. Eine signifikante Magnetisierung wies auch die zweite nanostrukturierte ZnO Probe auf. Im Gegensatz hierzu konnte beim ZnO Einkristall keine bedeutende Magnetisierung nachgewiesen werden.

Mit Hilfe von XMCD Messungen an den nanostrukturierten Proben konnten etwaige Verunreinigungen mit magnetischen Fremdatomen wie Eisen, Kobalt oder Nickel ausgeschlossen werden. Auch die O-K Kante wies keinen messbaren XMCD-Effekt auf. Es konnten im Bereich der weichen Röntgenstrahlung (250 – 1200 eV) auch keine sonstigen Verunreinigungen mit Fremdatomen nachgewiesen werden.

Im Unterschied hierzu enthielten Untersuchungen der ZnO-Proben mittels  $\mu$ SR-Methode eindeutige magnetische Signaturen. Die Probe mit der feinsten Körnung und der größten SQUID-Magnetisierung zeigte dabei das stärkste  $\mu$ SR-Signal und den größten magnetischen Volumenanteil von 35 %. Insgesamt existieren zwei unterschiedliche Verteilungen dieser internen Magnetfelder.

Für die Probe mit der gröberen Nanostrukturierung konnte ein magnetischer Volumenanteil von 15 % bestimmt werden.

Bei der nichtmagnetischen Einkristallreferenzprobe hingegen konnte im Rahmen der Messgenauigkeit kein bedeutendes  $\mu$ SR Signal ermittelt werden.

Diese Resultate sind bemerkenswert, da für die Probe mit einem höheren Anteil an „kritischen“ Korngrenzen sowohl eine höhere Magnetisierung als auch ein größerer magnetischer Volumenanteil ermittelt wurde. Durch die Kombination integrierender (SQUID, Nachweis eines magnetischen Effekts), elementspezifischer (XMCD, Ausschluss von Verunreinigungen, magnetische Polarisierung an der Sauerstoff- und Zinkkante) und volumenselektiver ( $\mu$ SR, Ermittlung des magnetischen Probenvolumens) magnetischer Messmethoden ist es gelungen zu zeigen, dass es sich beim Phänomen des magnetischen, reinen Zinkoxids um einen realen, intrinsischen Effekt handelt.

Mit Hilfe eines semi-quantitativen Modells konnte gezeigt werden, dass es sich hierbei tatsächlich um ein Korngrenzenphänomen handelt. Der Anteil des Korngrenzen- am Probenvolumen ist ähnlich wie das magnetische Probenvolumen und die magnetischen Eigenschaften mit der Korngröße variieren.

Daher leistet diese Arbeit einen bedeutenden Beitrag zu einem Forschungsgebiet, auf dem in den letzten mehr als zehn Jahren mehrere tausend Veröffentlichungen erschienen sind und welches immer noch äußerst kontrovers diskutiert wird.

---

## Methodische Fortschritte

Ein weiterer Teilaspekt der Arbeit war die Schaffung der technischen Möglichkeiten, um *in-situ* Präparation und XMCD-Messungen der Nanopartikel überhaupt durchführen zu können. Hierfür wurde die bestehende XMCD-Messapparatur um einige Bestandteile erweitert. Es wurde eine speziell auf die Erfordernisse der Probenherstellung im UHV konzipierte Präparationseinheit entwickelt und zur Einsatzreife evaluiert. Diese Präparationseinheit wurde direkt in den bestehenden Messaufbau integriert und ermöglicht es, *in-situ* hergestellte Proben ohne Unterbrechen des Vakuums in die eigentliche Messkammer zu transferieren. Es ist nun möglich, Proben einerseits bis zu einer Temperatur von zirka 2.000 K auszuglühen, um beispielsweise Metalleinkristalle von Kohlenstoffverunreinigungen zu säubern. Außerdem verfügt die Präparationseinheit über eine Kühlvorrichtung, um Proben auf circa 200 K abzukühlen. Somit können Metalle auch bei niedrigen Probentemperaturen aufgedampft werden, was zu einer geringeren Mobilität der Metallatome auf dem Substrat und daher zu verändertem Wachstum führt.

Die zweite Erweiterung des bestehenden Aufbaus betrifft den Einbau eines neuen kryofreien, supraleitenden, schnell schaltenden Magnetsystems. Dieses neue Magnetsystem wurde von der Firma Cryogenic Ltd. (London, England) in enger Zusammenarbeit speziell für unsere Arbeitsgruppe gefertigt. Es ist nun möglich, Magnetfelder von bis zu 7 Tesla anzulegen, womit künftig auch superparamagnetische und hartmagnetische Materialien komplett gesättigt und somit mittels XMCD untersucht werden können. Das Magnetfeld kann mit einer maximalen Rate von 1,5 T/s (bei Feldern bis maximal 5 Tesla) verändert werden. Beim Umpolen des Maximalfeldes von 7 Tesla beträgt die maximale Ramprate noch 0,7 T/s, was einer Umpolzeit von +7 T nach -7 T von ungefähr 20 Sekunden entspricht. Zum Vergleich hatte das alte, ebenfalls von Cryogenic Ltd. stammende Magnetsystem ein Maximalfeld von 2 Tesla und eine maximale Ramprate von 0,6 T/s.

Erste XMCD Messungen an Nickel auf Graphen mit niedriger nomineller Bedeckung zeigten, dass die Rohdaten einen erheblichen Einfluss durch das Untergrundsignal des Einkristalls aufwiesen. Dadurch wurde es notwendig, den bisherigen Mess- sowie Auswertemodus entsprechend anzupassen. Für die Messung der XMCD-Spektren wurde der sogenannte „fast continuous“ Modus eingeführt, bei dem die Energie des Synchrotronstrahls kontinuierlich geändert und der Probenstrom ebenso kontinuierlich ausgelesen wird. Das für den XMCD Kontrast notwendige Umpolen des Magnetfeldes wurde nach Messung eines

einzelnen Spektrums durchgeführt. Ein für XMCD Messungen notwendiges Paar von XAS Spektren konnte somit innerhalb von 10 - 15 Minuten gemessen werden. Diese Zeitspanne betrug für den vorherigen Messmodus, bei dem die Energie schrittweise verändert und das Magnetfeld an jedem Energiepunkt umgepolt wurde, je nach Energiebereich ungefähr 120 Minuten. Daher konnte in kürzerer Zeit eine höhere Zahl von Spektren gemessen und so das Signal-Rauschverhältnis entscheidend verbessert werden.

Für eine möglichst genaue Bestimmung der unbesetzten Zustände und der magnetischen Momente wurde außerdem eine aufwändige, aber sehr effektive Bereinigung des Signals mittels geeigneter Modellierung des Untergrundes vorgenommen.

Mit Hilfe dieser technischen und methodischen Erweiterungen des bestehenden Systems war es bei geeigneter Untergrundmodellierung möglich, selbst geringste Bedeckungen von nominell 0,1 Monolagen Nickel auf Graphen zu untersuchen und dessen elektronischen und magnetischen Eigenschaften zu bestimmen.

## 2. Introduction

Nanoparticles consist of a countable number of atoms (up to several hundred or thousands) with a typical size of only one-billionth of a meter. On the nanometer scale, the physical properties of a certain materials usually differ strongly from its bulk values. Due to an elevated number of surface atoms, especially the magnetic properties of nano particles or clusters deviate strongly from its bulk counterparts. The total magnetic moment is usually enhanced, mainly caused by dangling bonds of the surface atoms; i.e. the orbital magnetic moment is no longer quenched as it is the case in bulk materials. The orbital magnetic moment is usually strongly linked to the crystal lattice. Thus, an increased orbital moment can result in an increased magnetic anisotropy which is of general importance in field of magnetic data storage technology. Very high data storage densities for hard disk drives can be achieved by a systematic use of embedded magnetic nanoclusters with suitable magnetic anisotropy. Another important aspect is the interaction of a metallic/magnetic nano cluster with its support or substrate. This interaction can for example result in charge transfer from the cluster to the substrate or vice versa. If the nano particles are magnetic with a certain spin polarization of their outer shell, this charge transfer may even be spin polarized which could be utilized in spintronic devices.

However, tuning the size of nanostructures can alter the magnetic properties also in an indirect way. Recently it was found that nanograining of oxide materials like ZnO can lead to ferromagnetism as well. Magnetism of these systems is not linked to nanocrystalline grains but to magnetic grain boundaries in-between. Tuning the grain size will alter the volume occupied by grain boundaries. If a certain percolation threshold is exceed, ferromagnetism will occur due to magnetic coupling through the grain boundary network within the sample. This topic has been intensively and controversially discussed in the past decade and is still a current scientific topic. A detailed understanding of grain boundary related ferromagnetism gives rise to the combination of semiconducting and ferromagnetic properties in a single device. As this form of magnetism can also be present in oxide materials other than ZnO (e.g.  $\text{TiO}_2$ ) a huge variety of new electronic devices, tailored to specific applications are possible.

---

## Ni clusters on a graphene Moiré template

A very promising candidate for possible applications in the field of high density magnetic data storage and spintronics are magnetic nanoparticles deposited on graphene. Graphene is a single layer of graphite with the carbon atoms aligned in a honey comb lattice. This special structure leads to some unique properties of the graphene mesh, like the existence of Dirac fermions or the half-integer quantum hall effect. A combination of the unique properties of both systems thus is congruous.

This is possible since graphene can also be used for template growth of magnetic Nickel nano clusters. Varying preparation conditions such as deposition rate and deposition temperature one can produce a variety of differently shaped and sized clusters on graphene.

However, before discussing future prospects and possible applications of nanoclusters on graphene one has to explore its elementary attributes. Thus one major part of this thesis is dedicated to investigations of size and shape dependent electronic and magnetic properties of Ni clusters on a graphene Moiré template.

The magnetic properties have been investigated using state-of-the-art X-ray magnetic circular dichroism (XMCD) techniques. Applying this element specific method, one is able to extract the magnetic spin and orbital moment of the Ni clusters. In addition, from the corresponding X-ray absorption (XAS) spectra, one can conclude the electronic properties of the Ni clusters. The XAS spectrum yields detailed information on the unoccupied density of the Ni d-states. Furthermore, it gives excellent information on whether oxidization and resulting change of the electronic properties occurred to the clusters.

The XAS and XMCD measurements were carried out using our own, self-designed XMCD setup. However, before this thesis was started it had been equipped only with a 2 Tesla magnet system and rudimental sample treatment tools. In order to allow the required *in-situ* sample preparation, a complete new flashing/sample preparation station had to be developed for this thesis. The preparation station allows heat treatment of up to 2000 K for graphene preparation and also gas cooling below 200 K for low temperature cluster growth. The preparation section is furthermore equipped with low energy electron diffraction (LEED) system, sputter gun, Ni evaporator and several gas inlets for sputter gas, oxygen treatment and graphene preparation via cracking gaseous carbon hydrates.

The second improvement to enable nanocluster studies was the installation of an all new cryo-free, superconducting, fast switching 7 Tesla magnet system from Cryogenic Ltd.,



London (UK). Fast switching means a maximum magnet ramp rate of 1.5 T/s (not minutes!) which can be maintained up to 5 Tesla. Reversing the maximum 7 Tesla field takes 20 seconds, at a reduced ramp rate of 0.7 T/s. With this new high performance magnet system, even (super) para- and hardmagnetic materials can be investigated.

### **Unconventional magnetism of “non-magnetic” ZnO**

The second major part of this thesis is dedicated to the investigation of the indirect influence of nano-scaling on the magnetic properties, namely the magnetism in magnetic, nanograined ZnO. Magnetism in ZnO was predicted theoretically at the beginning of this century, with transition metal doping as a crucial condition. The basic idea was that the transition metal ions couple ferromagnetically within the ZnO host material. Soon after this prediction several groups were able to produce ferromagnetic TM:ZnO, proofed by integrating methods like SQUID or VSM. Element specific methods like XMCD on the other hand found only paramagnetic behavior of the TM dopants or even worse could address ferromagnetism to an unwanted clustering of the TM ions.

A systematic investigation of the magnetic properties in dependence of the microscopic structure of ZnO revealed that even undoped ZnO can become ferromagnetic. A possible key parameter is the so-called specific grain boundary area  $s_{GBA}$  which is defined as grain surface to grain volume ratio. Above a certain threshold value, magnetism was found in most ZnO samples.

One attempt to explain the appearance of magnetism considers the formation of so-called “ferromagnetic foam” due to magnetic coupling of electrons located in the grain boundaries of nanocrystalline ZnO. The basic idea of this concept is the accumulation of defect and vacancy related excess electrons within the grain boundaries. Under certain conditions they may couple ferromagnetically and this magnetic state may percolate throughout the whole sample.

A direct proof of magnetic grain boundaries is rather difficult. Integrating techniques like SQUID or VSM can provide information about the magnetic response of the sample but they cannot locate its microscopic origin. Applying the XMCD technique in this case can only exclude magnetism due to magnetic impurities because defined transitions (like  $2p \rightarrow 3d$ ) in a core-shell system are required. Such a transition is not apparent for the grain boundary

related magnetism. Additionally, no significant XMCD effect was found on the remaining candidates, the Zn  $L_{2,3}$  and the O K-edge.

In order to gain further insight into possible grain boundary related magnetism in ZnO the so-called low energy muon spin rotation (LE- $\mu$ SR) was applied to different nanocrystalline ZnO sample systems. In LE- $\mu$ SR the antimuon ( $\mu^+$ ) is utilized as a magnetic probe. Owing to its magnetic moment the  $\mu^+$  senses very small magnetic moments and can thus provide detailed information on very small internal magnetic fields independent of its origin. From  $\mu$ SR one can in principle extract the magnetic volume fraction of a sample as well as the strength and the distribution of internal magnetic fields.

### General outline of this thesis

Within this thesis, the two aforementioned magnetic sample systems have been investigated mainly by the means of accelerator based techniques. In order to provide the reader maximum comfort this thesis has been outlined as follows:

- The first section is dedicated to a short review of the scientific background of the subjects treated within this thesis. It recalls fundamental basics of magnetism and gives a short review of the current status of magnetism of ZnO and magnetic nanoparticles. Also the experimental techniques XMCD and  $\mu$ SR are introduced and explained briefly as they are not every day's lab experiments.
- The second section covers the experimental aspects of this thesis. It contains a short description of synchrotron radiation and muon beam generation and also an introduction of the beamlines where the experiments for this thesis have been conducted. It also contains a brief introduction of our own XMCD setup, which has been upgraded with a unique 7 Tesla fast switching magnet system within the framework of this thesis. Furthermore it contains a detailed description of the newly introduced so-called fast scan mode and a detailed description of the XMCD data analysis.
- In the third section the results of the Ni clusters/graphene/Ir are presented. First of all the "raw" results are presented for spherical and triangular cluster systems followed by a detailed discussion of the electronic and magnetic properties that could be extracted from XAS/XMCD measurements.

- 
- In the fourth and last section the results of the magnetic ZnO system are presented. The sample production technique is introduced and the microstructural properties of the samples derived from TEM pictures are listed. The basic magnetic properties were probed by SQUID; XMCD measurements probed the samples for magnetic contaminations. Finally the  $\mu$ SR results are shown and discussed in terms of the proposed grain boundary related magnetism.

### 3. Scientific Background

This section gives a brief review of the scientific background of magnetism necessary for understanding the key issues of this work. However, this section is not exhaustive. It is rather a brief summary of basic knowledge provided by standard text books [1-7]. Detailed descriptions concerning the x-ray magnetic circular dichroism (XMCD) and its applications can be found in [7, 8]. More detailed information on the muon spin rotation ( $\mu$ SR) technique can be found in references [9-14].

#### 3.1. Basics of Magnetism

##### 3.1.1. Interaction of Matter with an External Magnetic Field

The magnetization  $\vec{M}$  of a certain material can be defined as the vector sum of all magnetic moments  $\vec{\mu}$  located within the material volume  $V$ :

$$\vec{M} = \frac{1}{V} \sum_V \vec{\mu} \quad (3.1)$$

For macroscopic samples<sup>1</sup>, one can use a continuous approximation and treat  $\vec{M}$  as a homogenous vector field.

If the material is exposed to an external magnetic field  $\vec{H}$  its internal magnetic moments  $\vec{\mu}$  will align with respect to the applied field and as a result will respond with a magnetization  $\vec{M}$  different from the case of no field applied. The relation between the applied field and the magnetization is given by the magnetic susceptibility  $\underline{\chi}$  which is usually a tensor:

$$\vec{M} = \underline{\chi} \cdot \vec{H} \quad (3.2)$$

The relation for the tensor elements is given by:

---

<sup>1</sup> If the length scale is large enough so that single atom contribution can no longer be distinguished.

$$\chi_{ij} = \frac{\partial M_i}{\partial H_j} \quad (3.3)$$

For the magnetic flux density  $\vec{B}$  in a certain material one obtains, using equation (3.2) [1]:

$$\vec{B} = \mu_0 \cdot (\vec{H} + \vec{M}) = \mu_0 \cdot (E_3 + \underline{\underline{\chi}}) \cdot \vec{H} = \mu_0 \cdot \underline{\underline{\mu_r}} \cdot \vec{H} \quad (3.4)$$

with the vacuum permeability  $\mu_0 = 4\pi \cdot 10^{-7} \text{ Vs / Am}$ ,  $E_3$  the 3-dim identity matrix, and  $\underline{\underline{\mu_r}} = (E_3 + \underline{\underline{\chi}})$  the relative permeability of the material. In vacuum there is no magnetization, thus  $\mu_r = 1$ , and equation simplifies to [1]:

$$\vec{B} = \mu_0 \cdot \vec{H} \quad (3.5)$$

One uses  $\underline{\underline{\mu_r}}$  to classify materials in different categories:

- $\mu_r < 1$  ( $\chi < 0$ ): Diamagnetism. The magnetization is directed opposite to the applied field. Diamagnetism can be empirically understood by Lenz's law. The external magnetic field alters the velocity and the orbit of electrons and thus their magnetic moment. This change will oppose the external field. Diamagnetism is present for all materials but usually covered by para- or ferromagnetism.
- $\mu_r > 1$  ( $\chi > 0$ ): Paramagnetism: In paramagnetic systems, the inherent magnetic moments  $\vec{\mu}$  do not interact. Due to thermal fluctuations moreover, they are arbitrarily aligned with respect to each other. In an applied magnetic field, the magnetic moments start to align in field direction as their potential energy will be minimized. The magnetization will be aligned in a way to amplify the external field.
- $\mu_r \gg 1$ : Ferromagnetism: Here, the magnetic moments are correlated and they exhibit magnetic ordering even without applied magnetic field.

Now consider an infinitely flat ferromagnetic sample with magnetization  $\vec{M}$  shown in figure 3.1.

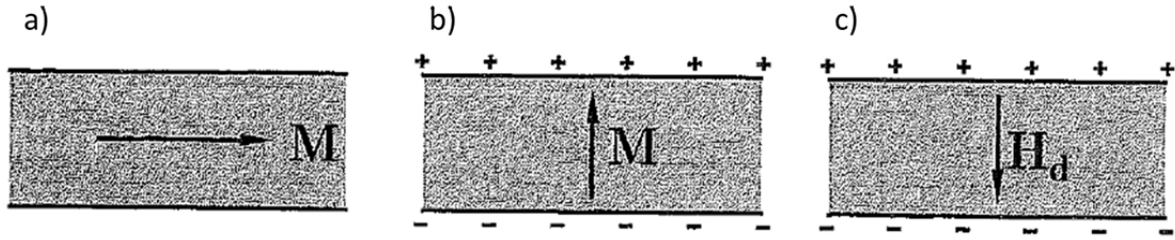


**Figure 3.1:** Cross-section of a sample flat plate ferromagnet in order to illustrate the demagnetizing field. a) For in-plane magnetization, no demagnetization field occurs. b) For out-of-plane magnetization, one finds a divergence of  $\vec{M}$ , resulting in c) the so-called demagnetization field  $\vec{H}_d$ . From [1].

Inside the sample one finds the magnetic flux density  $\vec{B}_i$  according to equation (3.4):  $\vec{B}_i = \mu_0 \cdot \vec{H}_i + \vec{M}$ . Following the Maxwell equation  $\nabla \cdot \vec{B} = 0$  (see [15]), one finds a divergence of  $\vec{M}$ :

$$\nabla \cdot \vec{H}_i = -\nabla \cdot \vec{M} \quad (3.6)$$

There is an equal and opposite divergence of  $\vec{H}_i$  in a way as if magnetic “monopoles” were left on the sample surface, as sketched in figure 3.1 b) and c), acting as a source of  $\vec{H}_i$ . As  $\vec{H}_i$  is opposite to  $\vec{M}$ , it is also called the demagnetization field  $\vec{H}_d$ . If  $\vec{M}$  lays in-plane, there will be no demagnetization field, as the plate is infinitely long.

Generalizing the demagnetization field to ferromagnetic materials of arbitrary geometry is quite complicated. For homogeneous, ellipsoidal shapes  $\vec{H}_d$  equals [1, 4]:

$$\vec{H}_d = -\underline{\underline{N}}\vec{M} \quad (3.7)$$

$\underline{\underline{N}}$  is the demagnetizing tensor:

$$\begin{pmatrix} N_x & 0 & 0 \\ 0 & N_y & 0 \\ 0 & 0 & N_z \end{pmatrix} \quad (3.8)$$

fulfilling the condition

$$\text{Tr } \underline{\underline{N}} = (N_x + N_y + N_z) = 1 \quad (3.9)$$

The demagnetizing factors for some special cases including sphere, cylinder, and the flat plate shown in figure 3.1 are listed in table 3.1.

**Table 3.1: Demagnetizing factors for special geometries, where they can be calculated explicitly.**

Shape	$N_x$	$N_y$	$N_z$
Sphere	1/3	1/3	1/3
Inf. long z-cylinder	1/2	1/2	0
Inf. long x-y plate	0	0	1

### 3.1.2. Magnetism of Single Atoms: Elementary magnetic moments

The elementary source of the magnetic moment of an atom is the spin and the orbital motion of its valence electrons<sup>2</sup>. Due to the Bohr model, electrons orbit the nucleus. In a classical sense, this orbiting displays a current loop and therefore it is related to a magnetic moment [3]:

$$\vec{m}_l = -\frac{\mu_B}{\hbar} \cdot \vec{l} \quad (3.10)$$

$\vec{m}_l$  is the orbital magnetic moment,  $\vec{l}$  is the orbital quantum number ( $|\vec{l}| = \hbar \cdot \sqrt{l(l+1)}$ ), and  $\mu_B$  is the Bohr magneton.  $\mu_B$  is the “elementary” magnetic moment and is defined as the magnetic moment of an electron with the orbital momentum  $\hbar$ , in numbers [3]:

$$\mu_B = \frac{e\hbar}{2m_e} = 9.247 \cdot 10^{-24} \text{ Am}^2 \quad (3.11)$$

Furthermore, the electron possesses a spin  $\vec{s}$  which is related to a spin magnetic moment [3]:

<sup>2</sup> The magnetic moment of the nucleus will be neglected here.

$$\vec{m}_s = -g_s \cdot \frac{\mu_B}{\hbar} \cdot \vec{S} \quad (3.12)$$

$g_s \approx 2$  is the Landé-factor,  $\vec{S}$  is the electron spin ( $|\vec{S}| = \hbar \cdot \sqrt{s(s+1)}$ ).

If an atom contains multiple electrons, the single spin and orbital moment add up to a total magnetic moment  $\vec{J}$ . This can be described in two different extreme ways, depending on the strength of the spin orbit coupling (SOC) in the system. The “real” system usually lies in between the two cases described in the following. For electrons of the light elements, as well as for the only weakly bound in heavier elements the Russel-Saunders or LS-coupling is dominant. Here, the single electron spins  $\vec{S}$  and orbital moments  $\vec{L}$  couple to a total spin  $\vec{S}$  and a total orbital moment  $\vec{L}$ :

$$\vec{L} = \sum_{i=1}^n \vec{L}_i \quad (3.13)$$

$$\vec{S} = \sum_{i=1}^n \vec{S}_i \quad (3.14)$$

The total spin and total orbital moment in turn couple to the total magnetic moment:

$$\vec{J} = \vec{L} + \vec{S} \quad (3.15)$$

For heavier elements and such with a strong SOC, i.e. for strongly bound electrons, the single spins and orbital moments sum up to a single electron total magnetic moment. For the total magnetic moment of the  $i$ -th electron one obtains:

$$\vec{J}_i = \vec{L}_i + \vec{S}_i \quad (3.16)$$

The single magnetic moments  $\vec{J}_i$  add to the total magnetic moment of the whole atom. One obtains the jj-coupling:

$$\vec{J} = \sum_{i=1}^n \vec{J}_i \quad (3.17)$$

In both cases, the absolute of the total magnetic moment is given by [3]:

$$\vec{m}_J = g_J \frac{\mu_B}{\hbar} \cdot \vec{J} \quad (3.18)$$

with  $|\vec{J}| = \hbar \cdot \sqrt{J(J+1)}$  and  $g_J$  the Landé factor [3]:



$$g_J = 1 + \frac{j(j+1) - l(l+1) - s(s+1)}{2j(j+1)} \quad (3.19)$$

In the case of LS-coupling one can estimate the ground state of atoms with multiple electrons according to Hund's rules. They state that electronic states are occupied in a way that:

- The total spin  $\vec{S}$  is maximized:  $|\vec{S}| = \max$ .
- The orbital moment along a preferred axis is maximized:  $|\vec{L}_z| = \max$ . If the outer shell is exactly half filled:  $|\vec{L}_z| = 0$
- The total magnetic moment is  $\vec{J} = |\vec{L} - \vec{S}|$  if the outer atom shell is less than half filled and  $\vec{J} = \vec{L} + \vec{S}$  if the outer atom shell is more than half filled.

### 3.1.3. Paramagnetism

In paramagnetic materials, the single atoms exhibit a net magnetic moment but their magnetic coupling is weak and will be destroyed by thermal oscillations. If an external field is applied, the magnetic moments start to align. The energy of a magnetic moment  $\vec{\mu}$  exposed to a magnetic field  $\vec{B}$  is  $E_{mag} = -\vec{\mu} \cdot \vec{B}$ . Thus the magnetic moments will align parallel to the applied magnetic field. The magnetization as a function of the applied magnetic field  $\vec{B}$  and the temperature  $T$  is given by [1]:

$$\frac{M}{M_s} = \underbrace{\frac{2J+1}{2J} \coth\left(\frac{2J+1}{2J}x\right) - \frac{1}{2J} \coth\left(\frac{x}{2J}\right)}_{B_J(x)} \quad (3.20)$$

where  $B_J(x)$  is the so-called Brillouin function. The saturation magnetization  $M_s$  and the parameter  $x$  are given by:

$$M_s = ng_J\mu_B J \quad (3.21)$$

$$x = g_J\mu_B \frac{JB}{k_B T} \quad (3.22)$$

$n$  is the number of magnetic moments per unit volume, and  $g_J$  the Landé factor as introduced in equation (3.19).

In the classical limit of large quantum number  $J \rightarrow \infty$ , the Brillouin function converges to the so-called Langevin function:

$$L(x) = \coth(x) - \frac{1}{x} \quad (3.23)$$

Brillouin functions for different  $J$  are plotted in figure 3.2.

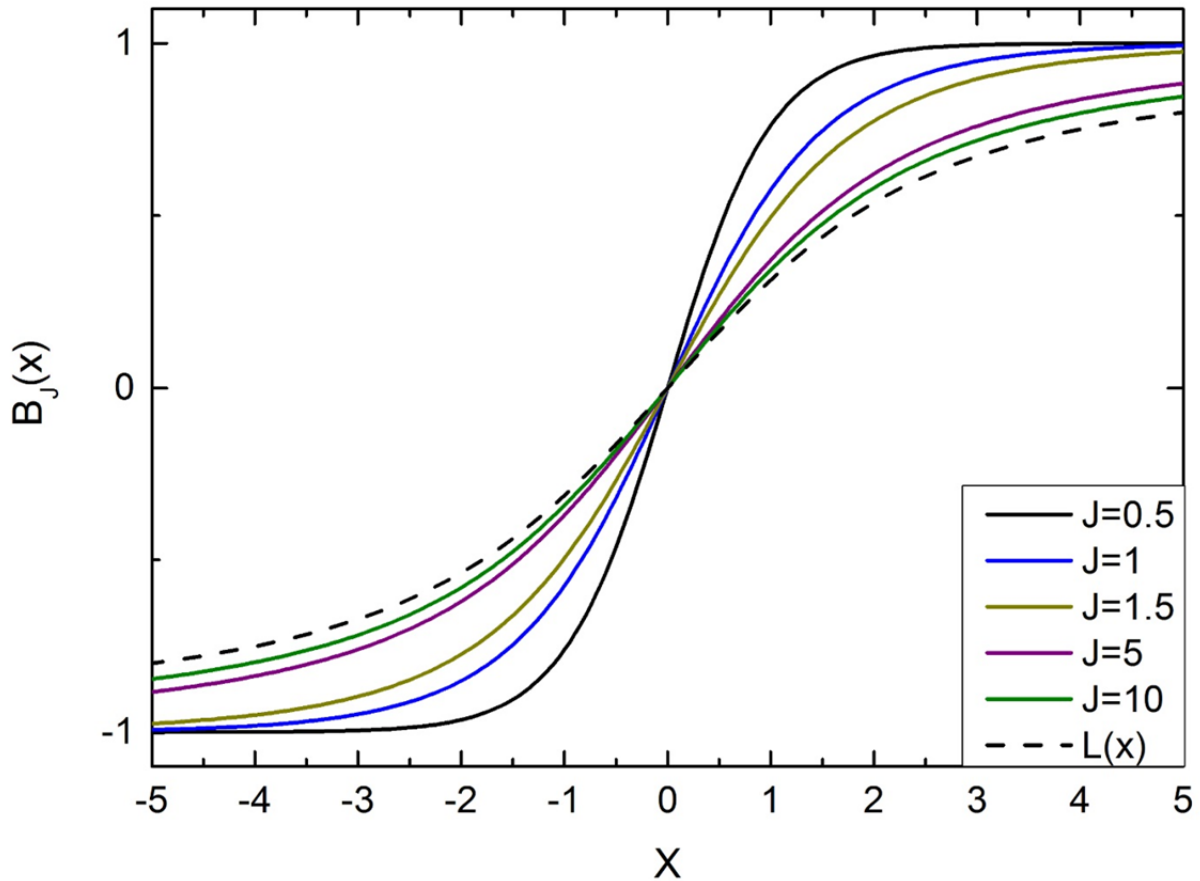


**Figure 3.2:** A paramagnets magnetization curve follows the Brillouin function which is plotted here for different values of  $J$ . The dashed line represents the Langevin function, the  $J \rightarrow \infty$  limit of the Brillouin function.

#### 3.1.4. Ferromagnetism

In addition to the previously mentioned dia- and paramagnetism, having its sources either in induced electron currents or elementary magnetic moments with missing long range order, bulk materials may also exhibit an intrinsic correlated long range ordering of their magnetic moments. The susceptibility  $\chi$  is then no longer a simple function of applied

field and ambient temperature but also of the history of the sample. The respective materials can be classified into three different basic magnetic systems, shown in figure 3.3:

- Ferromagnetism: All magnetic moments inside a magnetic domain are usually aligned along a preferred crystallographic direction, the easy axis.
- Anti-Ferromagnetism: Two or even more magnetic sub-lattices are present. Their respective magnetic moments have the same absolute magnetization but they are oriented anti-parallel with respect to each other, cancelling the total magnetization. The net magnetization vanishes.
- Ferrimagnetism: Almost the same case as anti-ferromagnetism, with different absolutes of the sub-lattice magnetic moments. Thus a significant net magnetization remains.

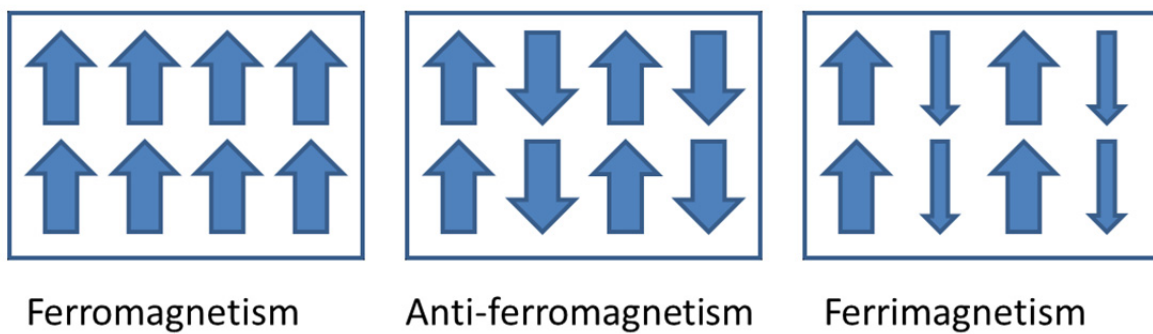


**Figure 3.3: Comparison of the three different systems of magnetically ordered materials: Ferro-, Anti-Ferro-, and Ferrimagnetism.**

A simple way to estimate magnetic interaction is the so-called mean field approximation. Here one assumes that alignment of a single magnetic moment occurs due to the “mean field” produced by all its neighbors. For reconsideration, a magnetic moment  $\vec{\mu}$  creates a magnetic field  $\vec{B}$  on a certain position  $\vec{r}$  which is given by the relation (after [16]):

$$\vec{B}(\vec{r}) = \frac{\mu_0}{4\pi} \left( \frac{3\vec{r} \cdot (\vec{\mu} \cdot \vec{r})}{r^5} - \frac{\vec{\mu}}{r^3} \right) \quad (3.24)$$

Assuming a magnetic dipole interaction of two neighboring atoms with magnetic moments<sup>3</sup>  $\vec{\mu}_1, \vec{\mu}_2$  and a distance  $\vec{r}$  one can now calculate the energy like  $E_{mag.} = -\vec{\mu} \cdot \vec{B}$ . Together with equation (3.24) one obtains:

$$E_{mag.} = \frac{\mu_0}{4\pi r^3} \left( \vec{\mu}_1 \cdot \vec{\mu}_2 - \frac{3}{r^2} (\vec{\mu}_1 \cdot \vec{r})(\vec{\mu}_2 \cdot \vec{r}) \right) \quad (3.25)$$

Usually the magnetic moment of a single atom is in the order of  $\mu \sim 1 \mu_B$ , and with an interatomic distance  $r \sim 0.1 \text{ nm}$  one obtains an energy gain of  $\sim 10^{-23} \text{ J}$  per parallel aligned pair of electron spins. One can now translate this energy gain into a temperature to see at which temperature the system transforms to the paramagnetic state. This transition temperature is called Curie temperature  $T_c$ . For the present case one obtains  $T_c \approx 1 \text{ K}$ .

On the other hand, typical high temperature ferromagnets like Iron, Cobalt, and Nickel exhibit a Curie temperature  $T_c$  of about 1033 K, 1395 K, and 627 K respectively [2]. Hence a simple dipole-dipole interaction between to neighboring electrons is too weak to establish a ferromagnetic order in bulk materials at ambient temperatures.

This problem can be solved by a quantum mechanical concept, the so-called exchange interaction. The exchange interaction is based on one hand the Pauli principle, on the other hand on the Coulomb repulsion.

One can assume a system of two electrons located at positions  $\vec{r}_1, \vec{r}_2$  and with initial single electron wave functions  $\Psi_a$  and  $\Psi_b$ . The total wave function then has to be antisymmetric and to behave properly under particle exchange. This can be achieved by an antisymmetric spatial wave function and a symmetric spin function  $\chi$ . Then for the total spin one obtains  $\vec{S} = 0$  (Singlet state). If the spatial wave function is symmetric, the spin wave function  $\chi$  has to be antisymmetric; the total spin will be  $\vec{S} = 1$  (Triplet state). The wave functions will be given by:

---

<sup>3</sup> Where, e.g. the magnetic moments can be derived according the rules introduced in section 3.1.2.

$$\Psi_s = \frac{1}{\sqrt{2}}(\Psi_a(\vec{r}_1)\Psi_b(\vec{r}_2) + \Psi_a(\vec{r}_2)\Psi_b(\vec{r}_1))\chi_s \quad (3.26)$$

$$\Psi_T = \frac{1}{\sqrt{2}}(\Psi_a(\vec{r}_1)\Psi_b(\vec{r}_2) - \Psi_a(\vec{r}_2)\Psi_b(\vec{r}_1))\chi_T \quad (3.27)$$

Resulting from the antisymmetric spatial wave function in equation (3.27), electrons in the triplet state will, in average, reduce the Coulomb repulsion. The electron-electron interaction is minimized in the triplet state, the parallel orientation of the electrons and a resulting non-vanishing spin<sup>4</sup> is preferred over the singlet state.

In many-body systems, calculating the electron configuration can become more difficult. In order to parallelize spins, electrons have to occupy also higher energy states. For ferromagnetic ordering, the energy saved from Coulomb interaction minimization must be larger than the energy needed to occupy higher energy states. The resulting spin orientation dependent energy can be described by an effective operator, the Heisenberg Hamiltonian:

$$\hat{H} = -\sum_{i,j} J_{ij} \cdot \hat{S}_i \cdot \hat{S}_j \quad (3.28)$$

$J_{ij}$  is the exchange constant between the  $i$ th and the  $j$ th spins<sup>5</sup>. In many-body systems one often can neglect a next-next-neighbor interaction and replaces  $J_{ij}$  by an isotropic exchange constant  $J$ . The sign of  $J$  is the determining factor for the relative spin orientation. If  $J > 0$  spins are parallel oriented and the system will be ferromagnetic. This is the case especially for the 3d-transition metals like Iron, Nickel and Cobalt. For  $J < 0$  anti-parallel spin orientation is energetically more favorable and the system will be ferri- or antiferromagnetic.

In many-body systems, the exchange interaction leads to spin split electron density of states. This results in an excess occupation of one of the two possible spin densities of states. Stoner derived a model that provides a criterion for ferromagnetic order within a material [17]. The so-called Stoner criterion is given by:

---

<sup>4</sup> Resulting in a net spin magnetic moment according to equation (3.12).

<sup>5</sup> In the two electron system,  $J$  is the difference of the energies of the triplet and the singlet state

$$J \cdot \rho(E_F) \geq 1 \quad (3.29)$$

Here,  $J$  is the exchange integral and  $\rho(E_F)$  is the electron density of states at the Fermi level. An example of the density of states for different transition metal magnets are shown in figure 3.4.

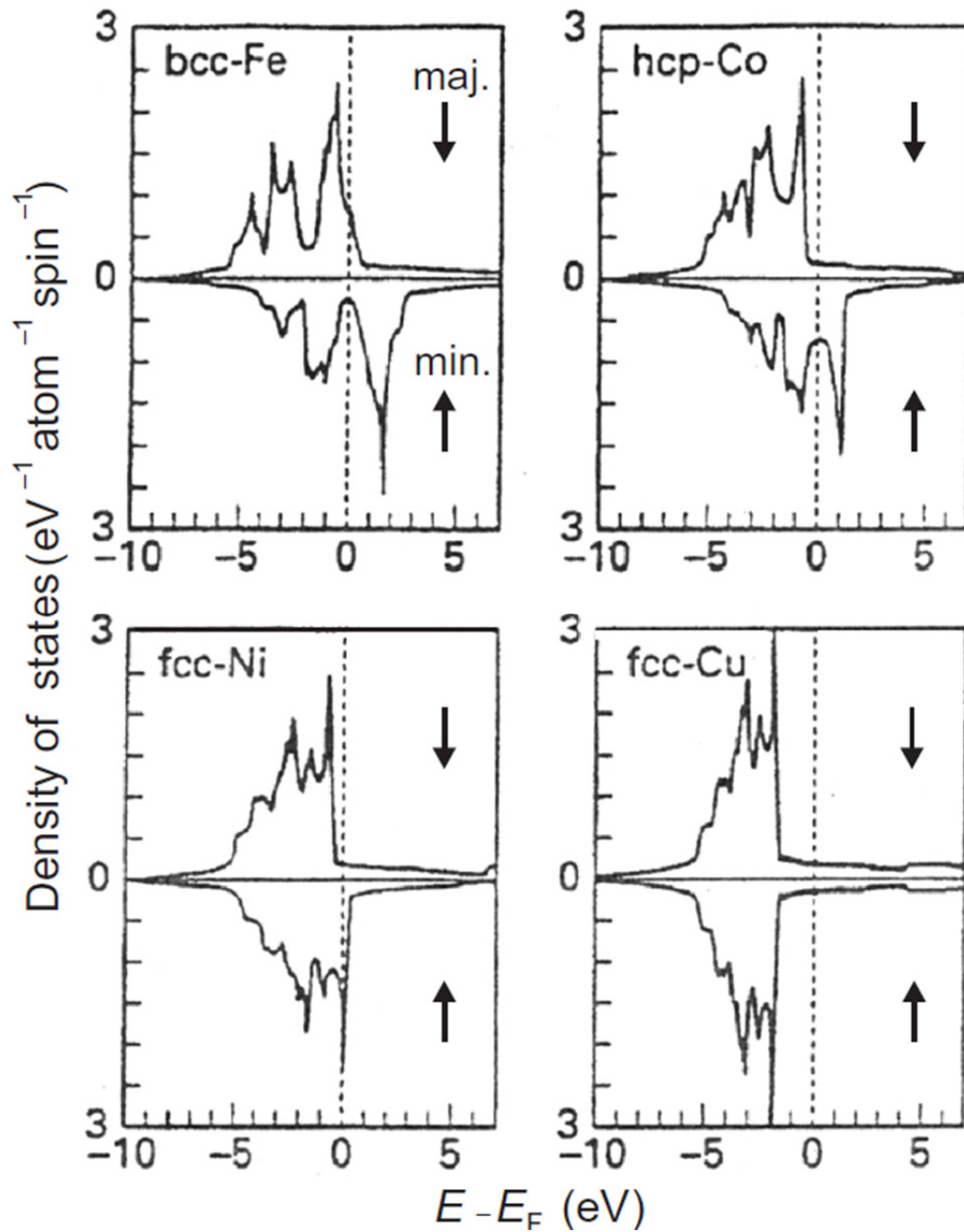


Figure 3.4: Density of states of transition metals Fe, Ni, Co, and Cu from [7]. Note the imbalance of the different spin directions directly at the Fermi level for Fe, Ni, Co (dashed line).

The magnetization can be evaluated from the imbalance of spin up and spin down electrons by integrating the respective spin polarized density of states:

$$m = \mu_B \cdot (n_{\uparrow} - n_{\downarrow}) = \mu_B \cdot \int_{-\infty}^{E_F} dE \cdot (n_{\uparrow}(E) - n_{\downarrow}(E)) \quad (3.30)$$

where  $n_{\uparrow}(E)$  denotes the majority and  $n_{\downarrow}(E)$  the minority spin density of states.

### 3.1.5. Superparamagnetism

Superparamagnetism is a special case of magnetic ordering that occurs in single domain ferromagnetic nanoclusters. The idea of superparamagnetism is related to paramagnetism in bulk materials and was first developed by Bean and Livingston [18]. In the superparamagnetic model, single domain (SD) particle is displayed as a single classical magnetic moment<sup>6</sup> with a net magnetization given by the number of containing atoms  $n_{At}$  and their atomic magnetic moment  $\vec{\mu}_{At}$ :  $\vec{\mu}_{SD} = n_{At} \cdot \vec{\mu}_{At}$ . The total magnetic moment  $\vec{\mu}_{SD}$  is usually aligned in a preferred magnetic easy axis as indicated on the left side of figure 3.5. The energy barrier that prevents  $\vec{\mu}_{SD}$  to align in an arbitrary direction is the uniaxial anisotropy energy, which is proportional to  $KV$ , the uniaxial anisotropy  $K$  and the particle volume  $V$ . The total magnetic energy of the SD is given by [19]:

$$E_B = KV \cdot \sin^2 \theta - \vec{\mu}_{SD} \cdot \vec{H} \quad (3.31)$$

---

<sup>6</sup> All atomic magnetic moments react coherently, below their  $T_c$ , they also can be coupled ferromagnetic.

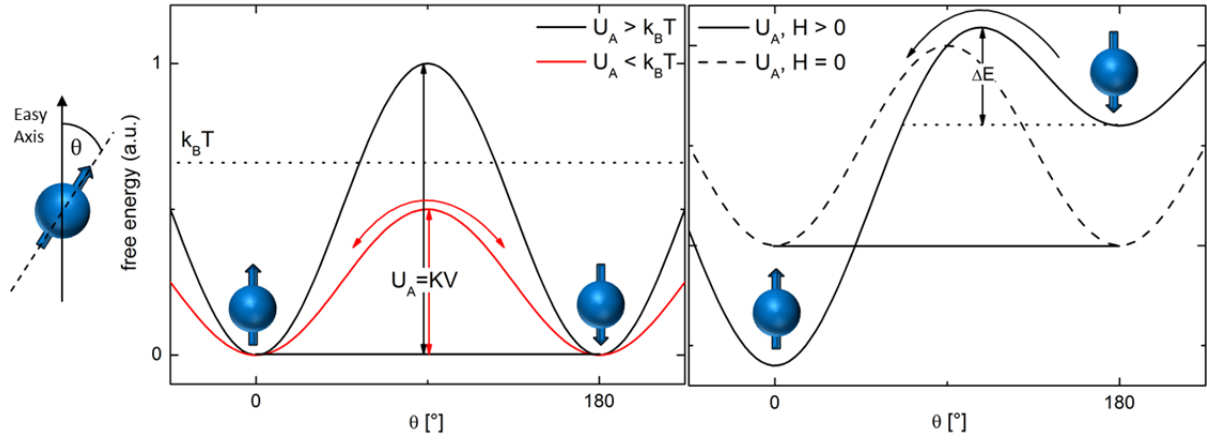


**Figure 3.5** Left: SD particle with net magnetization  $\vec{\mu}_{SD}$ . The direction of  $\vec{\mu}_{SD}$  is indicated by the blue arrow, the magnetic easy axis by the black one.  $\theta$  defines the angle between easy axis and  $\vec{\mu}_{SD}$ . Center: Potential barrier given by the uniaxial anisotropy  $KV$  for zero field. Right: Total magnetic energy of the SDP given by equation (3.31) with applied external field  $\vec{H}$ .

$\theta$  is the angle between  $\vec{\mu}_{SD}$  and the magnetic easy axis as defined in figure 3.5 a),  $KV$  the energy barrier that separates the two equilibrium positions of  $\vec{\mu}_{SD}$  (where the magnetization is turned  $180^\circ$ ) and  $\vec{H}$  is an applied external magnetic field. Without external magnetic field, one finds the energy of the system like shown in the center of figure 3.5. If the anisotropy energy  $U_A$  is smaller<sup>7</sup> than the thermal energy  $k_B T$ , red curve in the center of figure 3.5, the magnetization of the SDP will flip forth and back between  $\theta = 0^\circ$  and  $\theta = 180^\circ$  randomly. The mean or Néel relaxation time  $\tau_N$  between two flips is given by [19]

$$\tau_N = \tau_0 \exp\left(\frac{KV}{k_B T}\right) \quad (3.32)$$

$\tau_0$  is the inverse jump attempt frequency, and is typically of the order of  $\sim 10^{-9}$  s, [1]. If the system is cooled  $\tau_N$  increases and thus the fluctuations of the magnetization direction slow down. If  $\tau_N$  becomes much larger than the measuring time  $t_m$  of a certain measurement method, when  $U_A > k_B T$  as indicated by the black line in the center of figure 3.5, the magnetization direction will not flip anymore on the timescale of a single measurement.

<sup>7</sup> E.g. in smaller nanoparticles



Then  $t_m = \tau_N$  and the system then appears frozen or “blocked” as a static ordered magnetic system. The temperature where the system becomes blocked is called the blocking temperature  $T_B$ . From equation (3.32)  $T_B$  can be calculated, assuming a measurement time in the order of 100 s, as typical for XMCD spectroscopy:

$$T_B \approx \frac{KV}{25k_B} \quad (3.33)$$

Of particular interest is the interaction of superparamagnetic nanoparticles with applied magnetic fields. According to equation (3.31) the energy curve progression changes to the one shown in figure 3.5 c). A parallel alignment of magnetization direction with respect to the applied field, given by the  $\theta = 0^\circ$  position, becomes more favorable from an energy point of view than the anti-parallel ( $\theta = 180^\circ$ ) one.

If the temperature is above  $T_B$ ,  $KV \ll k_B T$  and the magnetization curve of a superparamagnetic ensemble is given by:

$$M = M_s \cdot \left( \coth\left(\frac{\mu_{SD}H}{k_B T}\right) - \frac{k_B T}{\mu_{SD}H} \right) = M_s \cdot L\left(\frac{\mu_{SD}H}{k_B T}\right) \quad (3.34)$$

where  $M_s$  is the saturation magnetization and  $L$  is the Langevin function already introduced in equation (3.23). This equation is also found for paramagnetic systems but here, the magnetic moment  $\mu_{SD}$  is much larger than the magnetic moments usually apparent in normal paramagnets. In summary, above the blocking temperature, superparamagnetic nanoparticles behave<sup>8</sup> just like a paramagnet with much larger magnetic moments and  $J \rightarrow \infty$ , as plotted in figure 3.2.

---

<sup>8</sup> Above the blocking temperature  $T_B$

### 3.2. X-ray Magnetic Circular Dichroism (XMCD)

#### 3.2.1. X-ray Absorption

When X-rays penetrate matter, they will be attenuated. Two different mechanisms are responsible for the attenuation: scattering and absorption. In the soft x-ray range, the photo-effect related absorption is dominating over the elastic Rayleigh and the inelastic Compton scattering [8].

The x-ray absorption can be determined in a classical “input-output” comparison experiment. One measures the x-ray beam intensity in front ( $I_0$ ) and behind ( $I(E, x)$ ) a sample with thickness  $x$ , the intensity in dependence of the thickness will be given by the so-called Lambert-Beer-law [3]:

$$I(E, x) = I_0 \cdot e^{-\mu_x(E) \cdot x} \quad (3.35)$$

$\mu_x(E)$  is the so-called absorption coefficient and is dependent on the X-ray energy  $E$  and the atomic number  $Z$ , thus the absorption coefficient is characteristic property for every material [3]:

$$\mu(E) \sim \frac{Z^4}{E^3} \quad (3.36)$$

If the incoming radiation energy  $\hbar\omega$  is sufficient in order to excite electrons from a lower energy level  $E_i$  into another (unoccupied) state  $E_f$ , the absorption coefficient is increasing strongly and its energy dependency becomes non-trivial, unless the condition

$$E_f - E_i = \hbar\omega \quad (3.37)$$

is matched.

The absorption coefficient can be derived in a quantum mechanical approach using first order time dependent perturbation theory. The result is given by Fermi's Golden Rule:

$$\mu_x(E) = \sum_{|f\rangle, |i\rangle} \left| \langle f | T(E) | i \rangle \right|^2 \cdot (1 - n(E_f)) \cdot \delta(E_f - E_i - \hbar\omega) \quad (3.38)$$

$\langle i |$  and  $\langle f |$  are the initial and final transition states, the term  $(1 - n(E_f))$  is a measure for the number of unoccupied final states,  $\delta(E_f - E_i - \hbar\omega)$  denotes the energy conservation. The

operator  $T(E)$  characterizes the interaction of the atom with the electrical field vector of the incoming electromagnetic wave  $e^{i\vec{k}\cdot\vec{r}}$  :

$$T(E) = e^{i\vec{k}\cdot\vec{r}} \cdot \hat{p}_e \cdot \hat{\varepsilon}_{0,\pm} \quad (3.39)$$

where  $\hat{p}_e$  is the electron momentum operator,  $\hat{\varepsilon}_{0,\pm}$  is the polarization of the electromagnetic field, which can be linear (0) or left/right circular ( $\pm$ ).

In the soft x-ray range, the wavelength  $\lambda$  is usually large with respect to the atomic diameter  $r$ . Thus it is justified to expand the electromagnetic wave and neglect terms with  $\vec{k}\cdot\vec{r}$  and their higher orders:

$$e^{i\vec{k}\cdot\vec{r}} \approx 1 + \underbrace{i\vec{k}\cdot\vec{r} + \dots}_{\sim 1} \Rightarrow |e^{i\vec{k}\cdot\vec{r}}| = 1 \quad (3.40)$$

This approximation is well-known as dipole approximation. Using the approximation from (3.40) in equation (3.38) and rewriting  $\hat{p}_e$  in terms of the length operator  $\hat{r}$  one obtains

$$\mu_{0,\pm}(E) = im_e \omega \cdot \sum_{|f\rangle, |i\rangle} \left| \langle f | \hat{\varepsilon}_{0,\pm} \cdot \hat{r} | i \rangle \right|^2 \cdot (1 - n(E_f)) \cdot \delta(E_f - E_i - \hbar\omega) \quad (3.41)$$

with the electron mass  $m_e$ , and  $\omega = \omega_f - \omega_i$  the transition frequency from the initial state  $i$  to the final state  $f$ .

An important result from the dipole approximation is that transitions fulfilling the condition given by equation (3.37) are not necessarily observed experimentally. In addition to energy conservation, orbital momentum conservation has to be considered, as well as the parity of the initial and final states, which have to be antisymmetric. The selection rules for the total angular momentum  $\vec{J} = \vec{L} + \vec{S}$ , orbital momentum  $\vec{L}$  and spin momentum  $\vec{S}$  and their respective projections  $m_{J,L,S}$  along the preferred axis are [3]:

$$\Delta J = 0, \pm 1 \quad (3.42)$$

$$\Delta S = 0 \quad (3.43)$$

$$\Delta L = \pm 1 \quad (3.44)$$

$$\Delta M_L = 0, \pm 1 \quad (3.45)$$

$$\Delta M_S = 0 \quad (3.46)$$

Transitions with  $\Delta L = 0(\pm 1)$  correspond to excitations using linearly (circularly) polarized light. Spin flipping is prohibited within dipole transitions, thus  $\Delta M_S = 0$ .

### 3.2.2. Model Explanation for the X-ray Magnetic Circular Dichroism

X-ray magnetic circular dichroism (XMCD) has been first measured on the Fe K-edge in 1987 by Prof. Gisela Schütz [20]. The origin of the XMCD effect is a difference in the absorption coefficients  $\mu_-(E)$  for left and  $\mu_+(E)$  right hand circular polarized light. The plus and minus sign indicates the  $\vec{k}$ -vector orientation with respect to the beam direction. A possible experimental setup for measuring the XMCD effect is sketched in figure 3.6. A sample with a certain magnetization  $\vec{M}$  is irradiated with left or right circular polarized light. Measuring the absorption coefficient at parallel (+, upper part of figure 3.6) and antiparallel (−, lower part of figure 3.6) orientation of the magnetization  $\vec{M}$  and the polarization  $\vec{P}$  and will result in the relation:

$$\Delta\mu = \mu_+ - \mu_- \sim \vec{P} \cdot \vec{M} = |\vec{P}| \cdot |\vec{M}| \cdot \cos(\vec{P}, \vec{M}) \quad (3.47)$$

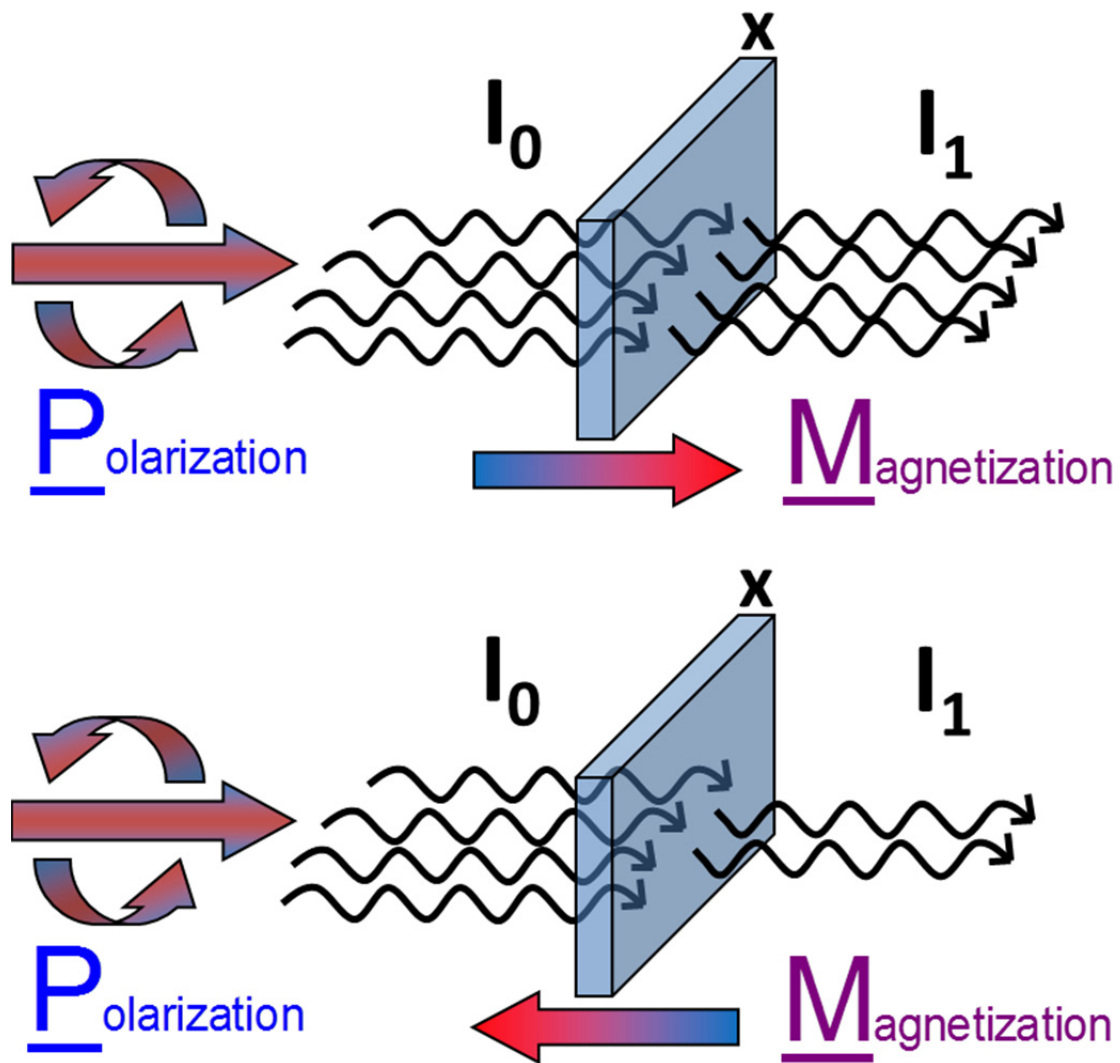


Figure 3.6: Basic principle of the XMCD effect. The absorption coefficient is different for parallel (a) and antiparallel (b) orientation of  $\vec{P}$  and  $\vec{M}$ . Adapted from [21].

The difference in the absorption coefficients  $\mu_+$  and  $\mu_-$  can be explained by a simplified two-step model. One considers subsequently the absorption of a circularly polarized photon (first step) and the placement of the respective photoelectron in higher energy levels (second step).

One can re-write Fermi's Golden Rule (equation (3.41)) in a simplified version just considering a photon with positive helicity<sup>9</sup> (+) exciting an electron with spin up ( $\uparrow$ ) or down ( $\downarrow$ ) from a lower energy level into unoccupied states:

$$\mu_+ \sim p_{+\uparrow}\rho_{\uparrow}(E) + p_{+\downarrow}\rho_{\downarrow}(E) \quad (3.48)$$

For negative helicity one can write:

$$\mu_- \sim p_{-\downarrow}\rho_{\downarrow}(E) + p_{-\uparrow}\rho_{\uparrow}(E) \quad (3.49)$$

Here,  $p_{ij}$  is the probability that an incoming photon with helicity ( $i$ ) induces a transition of an electron with spin ( $j$ ) into the respective unoccupied spin states  $\rho_j(E)$  in the valence band. As  $p_{+\uparrow} \neq p_{+\downarrow}$  (and  $p_{-\downarrow} \neq p_{-\uparrow}$ ) every incoming photon produces a spin polarized photo-electron which can only reach unoccupied valence band states of the same spin. If the helicity is reversed, the imbalance of spin polarized photo-electrons reverses; the absolute number of excited electrons remains the same. Thus, the transition probability depends only on the relative orientation of helicity and magnetization, which can be parallel ( $p_p = p_{+\uparrow}, p_{-\downarrow}$ ) or anti-parallel ( $p_p = p_{+\downarrow}, p_{-\uparrow}$ ). The difference of the absorption coefficients is then given by:

$$\Delta\mu = \mu_+ - \mu_- = \underbrace{(p_p - p_a)}_{\sim \vec{P}} \cdot \underbrace{(\rho_{\uparrow}(E) - \rho_{\downarrow}(E))}_{\sim \vec{M}} \quad (3.50)$$

This is in agreement with equation (3.47). The difference in the transition probability  $p_p - p_a$  depends on the polarization  $\vec{P}$ . The second term  $\rho_{\uparrow}(E) - \rho_{\downarrow}(E)$  gives the occupation imbalance of minority spin  $\uparrow$  and majority spin  $\downarrow$  states in the valence band, which is directly correlated to the magnetization  $\vec{M}$ .

One can observe for example the XMCD effect on the Ni  $L_{2,3}$ -edge, as displayed in figure 3.7.

---

<sup>9</sup> The helicity is defined as projection of the particle spin onto the direction of its momentum:  
 $h = \vec{S} \cdot \vec{p}$ .

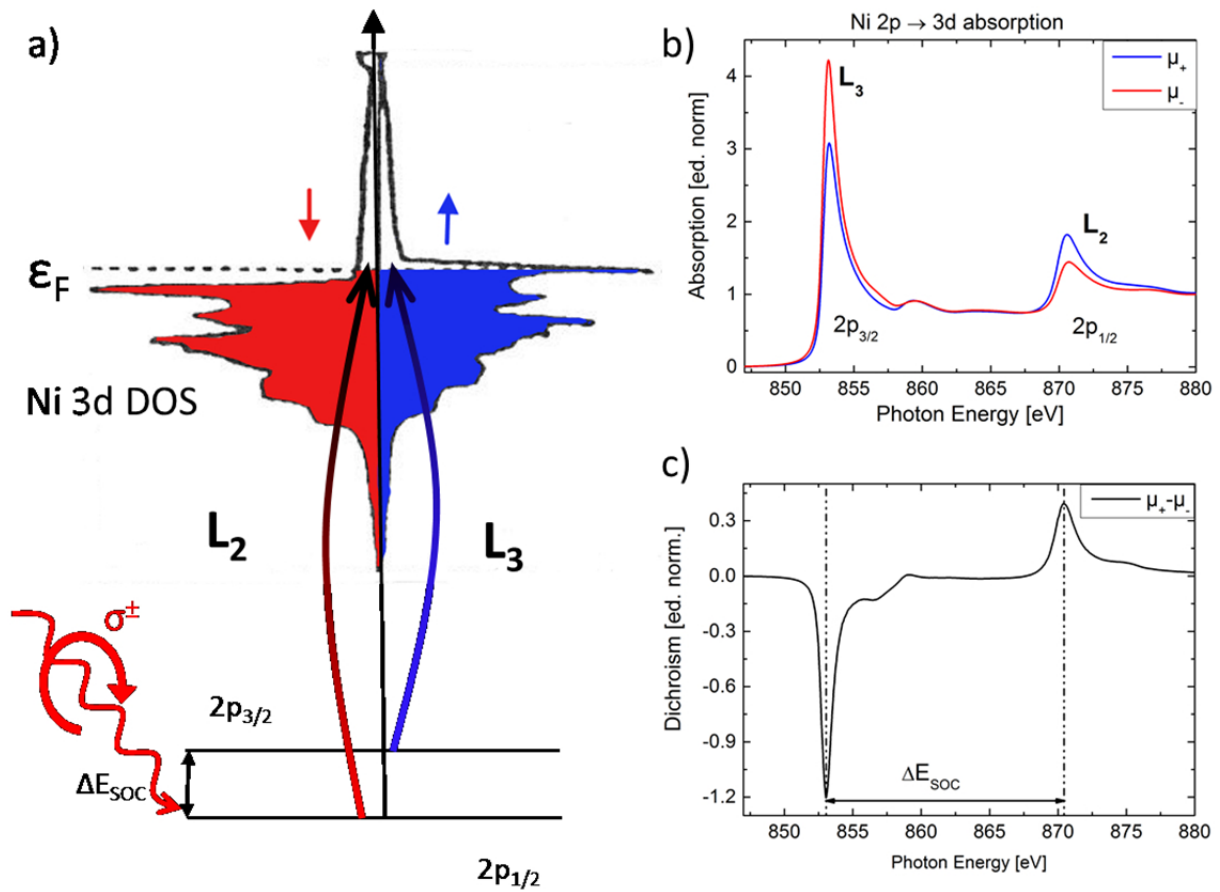


**Figure 3.7: XMCD effect on the Ni  $L_{2,3}$ -edge. A):** Excitation of spin polarized photo-electrons and their subsequent population of the unoccupied Ni density of states. **B)** X-ray absorption spectra with parallel and anti-parallel alignment of helicity and magnetization and **c)** the corresponding difference (XMCD) spectrum due to the imbalance in the spin density of states. Ni DOS on the left hand adapted from [22].

Due to the spin orbit coupling (SOC), the Ni 2p state is split into the  $2p_{1/2}$  and  $2p_{3/2}$  states. As a direct consequence of the SOC, one observes two lines in the x-ray absorption spectrum, the Ni  $L_3$  (transition from  $2p_{3/2}$  into the valence d-shell) and the Ni  $L_2$ -edge (transition from  $2p_{1/2}$ ). For example, calculating the respective transition probabilities for left circularly polarized light, preferentially electrons with spin  $\downarrow$  states are excited from the  $2p_{3/2}$  into the valence d-states. For transitions from the  $2p_{1/2}$  states preferably spin  $\uparrow$  electrons are excited. Excitation probabilities will be inverted if the calculation is performed for right circularly polarized light.

One can now “use” the spin polarized photo-electrons as a probe for the unoccupied density of the Ni valence d-states<sup>10</sup>, as indicated in figure 3.7 a). Electrons with spin  $\uparrow/\downarrow$  can be only excited into the respective  $\uparrow/\downarrow$  valence band. The total number of excited electrons depends on the number of unoccupied states in the respective d-spin band. In magnetic samples, the spin bands are split due to the exchange coupling meaning that the spin  $\uparrow$  and spin  $\downarrow$  bands are populated unequally and therefore the unoccupied number of states is different for each spin direction.

As an example, the experimental Ni  $L_{2,3}$ -edge X-ray absorption (XAS) and XMCD spectra of a bulk Ni sample is shown in figure 3.7 b) and c). Figure 3.7 b) shows two XAS spectra measured with parallel (blue line) and anti-parallel (red line) alignment of helicity and sample magnetization.  $\mu_+$  and  $\mu_-$  denote the absorption coefficient for parallel (+) and anti-parallel (-) alignment of helicity and magnetization.

For the absorption of right circularly polarized light mainly spin  $\downarrow$  electrons are excited. As most spin  $\downarrow$  states are populated, only a few electrons are excited into the d-states, therefore the corresponding absorption spectrum  $\mu_+$  (blue) is weak. The absorption of left circularly polarized light excites mainly  $\uparrow$  electrons which can find more unoccupied states in the d-shell, so the absorption spectrum  $\mu_-$  (red) is stronger. For the  $L_2$ -edge, the spin direction of the excited electrons is inverted, so are the respective absorption lines. Note that according to equation (3.12) the spin and magnetization direction are in antiparallel alignment with respect to each other. Therefore the sample magnetization  $\vec{M}$  is aligned parallel to the minority spins  $\downarrow$  and anti-parallel to the spin magnetic moment  $\vec{m}_s$ . The difference spectrum  $\mu_+ - \mu_-$  yields the XMCD spectrum, as shown in figure 3.7 c). The height of this line is a measure for the imbalance in the occupation of the respective spin states and is thus a direct measure for the magnetization of the sample. The results remain equivalent if the magnetization is switched instead of the helicity [23].

At the end it shall be annexed that it is a tacit procedure within the XMCD community to plot the dichroic spectra of the 3d transition metals Fe, Co, Ni in the way that the  $L_3$  edge dichroism is negative [7]. Usually only the relative orientation (parallel or anti-parallel) of magnetization and helicity is regarded.

---

<sup>10</sup> As the SOC energy is larger than the exchange interaction energy, spin flip shall be neglected here.



### 3.2.3. Sum Rules

The so-called sum rules are a powerful tool to extract quantitative values out of XMCD spectroscopy measurements. Using sum rules, one can extract important valence band properties from the polarization (magnetization) dependent absorption measurements: from the difference spectra one can obtain the spin magnetic moment  $\mu_s$ , and the orbital magnetic moment  $\mu_l$  on a  $\mu_B$  per atom basis. From the averaged absorption spectra, one can furthermore estimate the so-called “number of holes”  $n_h$ , which equates the number of unoccupied density of states.

As already indicated in the previous subsection, XAS measurements probe the unoccupied density of states, the number of holes  $n_h$ , as indicated in figure 3.8 a) and b). One can show that  $n_h$  can be estimated from the XAS spectrum and obtains the so-called charge sum rule [7]:

$$\langle I \rangle = \langle I_{L_3} + I_{L_2} \rangle = C \cdot n_h \quad (3.51)$$

$I_{L_{2,3}}$  is the averaged resonant XAS intensity on the respective absorption edge,  $C$  is a proportionality factor containing the radial matrix element of the respective core valence transition. For the 3d transition metals the number of holes and therefore the absorption or “white” line intensity decreases from Fe, Co, Ni to Cu as shown in figure 3.8 c).

Knowledge of the  $n_h$  value is crucial in order to determine the spin and orbital magnetic moment from the “magnetic” sum rules. Even one has measured  $\langle I_{L_3} + I_{L_2} \rangle$  with XAS, the factor  $C$  still remains unknown. It can be derived theoretically from Fermi’s Golden Rule by calculating the radial transition matrix part in equation (3.41). However, usually  $n_h$  is determined via band structure calculations. Therefore, one integrates over all states above the Fermi level:  $n_h = \int_{E_F}^{\infty} \rho(E) dE$ . This approach does only a good job for a few systems like Fe, but not for more complicated compounds like the oxide ferromagnets.

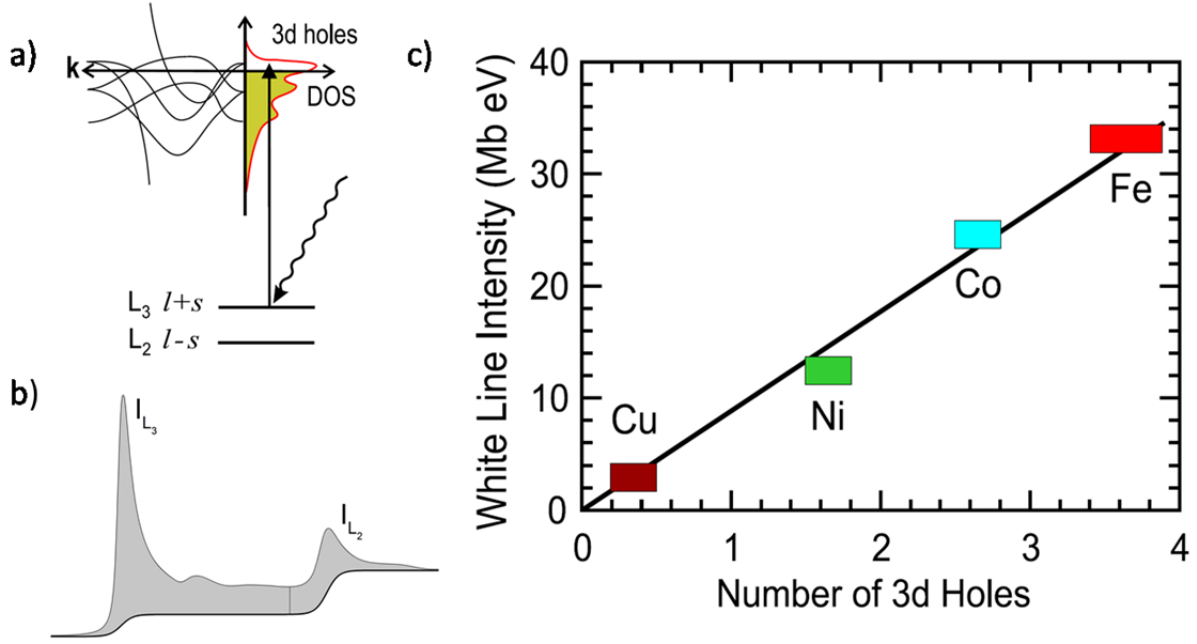


**Figure 3.8: Principle of obtaining the number of holes from integrating the XAS spectrum.** a) XAS probes the valence band for empty states. b) Number of empty states is proportional to the area of the XAS spectrum. c): Relationship of  $n_h$  and the intensity of the XAS (white line) signal.  $n_h$  is decreasing with increasing position in the periodic table, approaching the completely filled  $3d^{10}$  configuration. From [7].

The spin and orbital magnetic moments can be obtained from the sum rules derived by Cara et. al [24, 25]. They are available in a general form for both the orbital magnetic moment  $\langle L_z \rangle$ :

$$\frac{\int_{j_+ + j_-} (\mu_+(E) - \mu_-(E)) dE}{\int_{j_+ + j_-} (\mu_+(E) + \mu_-(E) + \mu_0(E)) dE} = \frac{1}{2} \frac{l \cdot (l+1) + 2 - c \cdot (c+1)}{l \cdot (l+1) \cdot (4l+2-n)} \langle L_z \rangle \quad (3.52)$$

For the spin magnetic moment  $\langle S_z \rangle$  in combination with the magnetic dipole term  $\langle T_z \rangle$ :

$$\frac{\int_{j_+} (\mu_+(E) - \mu_-(E)) dE - \left(\frac{c+1}{c}\right) \cdot \int_{j_-} (\mu_+(E) - \mu_-(E)) dE}{\int_{j_+ + j_-} (\mu_+(E) + \mu_-(E) + \mu_0(E)) dE} = \quad (3.53)$$

$$\frac{l \cdot (l+1) - 2 - c \cdot (c+1)}{3c \cdot (4l+2-n)} \langle S_z \rangle + \frac{l \cdot (l+1) \cdot [l \cdot (l+1) + 2c \cdot (c+1) + 4] - 3(c-1)^2 \cdot (c+2)^2}{6lc \cdot (l+1) \cdot (4l+2-n)} \langle T_z \rangle$$

$c$  and  $l$  are the orbital quantum numbers of the initial and the final state,  $n$  is the number of occupied final states.  $\mu_+(E) - \mu_-(E)$  is the difference of the absorption coefficients measured at different helicity/magnetization,  $\mu_+(E) + \mu_-(E) + \mu_0(E)$  is the orientation-averaged intensity and contains the nonmagnetic absorption  $\mu_0$ . Usually, one assumes that the average of the circularly polarized absorption<sup>11</sup> is a good approximation for the nonmagnetic absorption:  $\mu_0 \sim (\mu_+ + \mu_-) / 2$ .  $j_+$  and  $j_-$  label the different absorption lines in the spectrum, e.g. the  $L_3$  and the  $L_2$ -edge in the Ni XAS spectrum shown in figure 3.7. The notation is  $j_{\pm} = c \pm 1/2$ .

$\langle T_z \rangle$  is the magnetic dipole term. It is related to the quadrupole moment of the spin density distribution. In systems with cubic symmetry  $\langle T_z \rangle$  usually is negligible [26, 27]. For systems with a high magneto crystalline anisotropy however, the magnetic dipole term can contribute significantly to equation (3.53). In this case, one has to eliminate the  $\langle T_z \rangle$  term using a set of angle dependent measurements.

For this thesis, the relevant transition is the  $2p \rightarrow 3d$  transition at the transition metal  $L_{2,3}$  edges. Placing the proper values into equations (3.52) and (3.53), one obtains (see [28]):

$$m_l = -\frac{4 \int_{L_2+L_3} (\mu_+(E) - \mu_-(E)) dE}{3 \int_{L_2+L_3} (\mu_+(E) + \mu_-(E)) dE} \cdot n_h \cdot \mu_B = -\frac{2}{3} \frac{A+B}{\langle L_2 + L_3 \rangle} \cdot n_h \cdot \mu_B \quad (3.54)$$

for the orbital magnetic moment  $m_l$  (in  $\mu_B$  per atom) and

<sup>11</sup> Only the resonant part of the spectrum has to be considered. The non-resonant part has to be removed as indicated on the left hand part of Figure 3.8.

$$m_s = - \frac{6 \cdot \int_{L_3} (\mu_+(E) - \mu_-(E)) dE - 4 \cdot \int_{L_2+L_3} (\mu_+(E) - \mu_-(E)) dE}{\int_{L_2+L_3} (\mu_+(E) + \mu_-(E)) dE} \cdot n_h \cdot \mu_B = -2 \cdot \frac{A - 2 \cdot B}{\langle I_{L_2} + I_{L_3} \rangle} \cdot n_h \cdot \mu_B \quad (3.55)$$

for the spin magnetic moment  $m_s$  (also in  $\mu_B$  per atom).  $A$  (blue),  $B$  (red) and  $\langle I_{L_2} + I_{L_3} \rangle$  (green) correspond to the highlighted areas in figure 3.9.

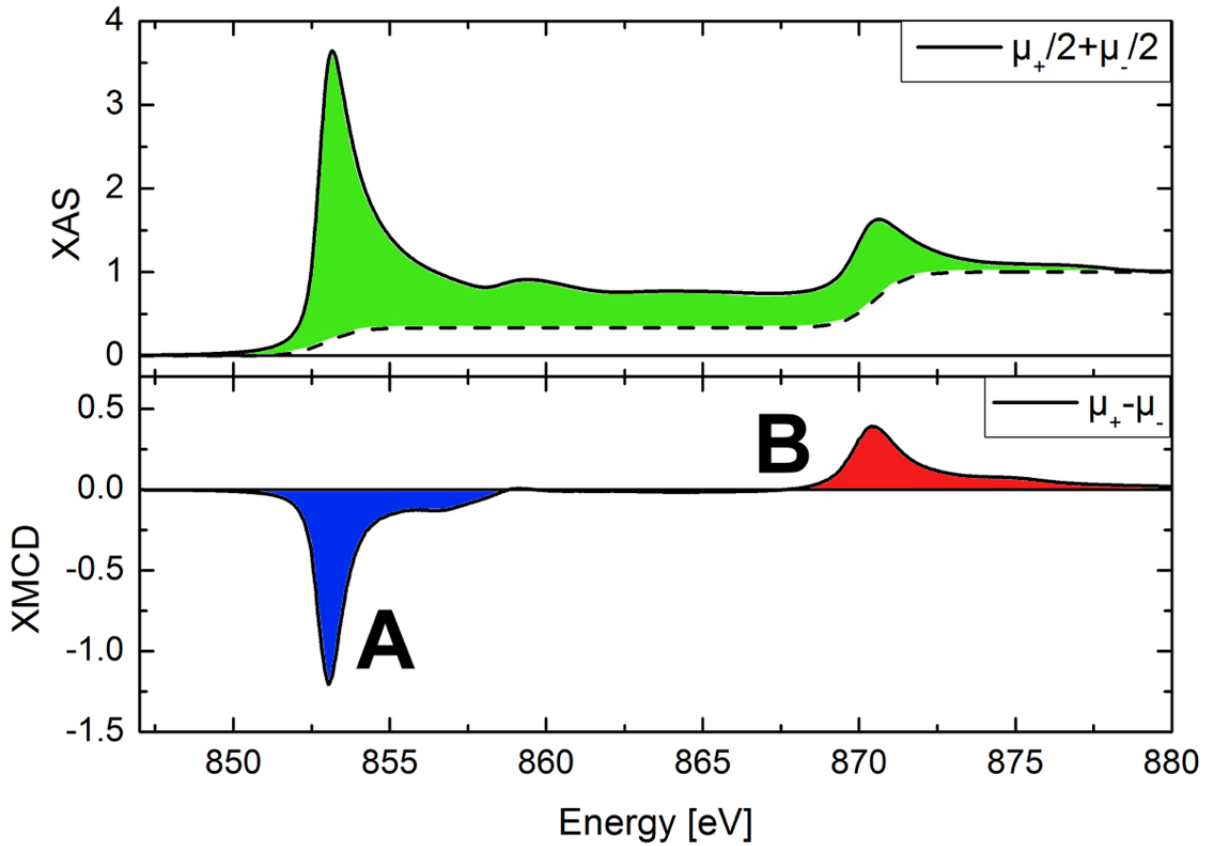


**Figure 3.9:**  $L_{2,3}$ -edge XAS (top) and XMCD (bottom) spectrum of bulk Ni. The areas necessary for sum rule calculations are highlighted green, blue and red.

Applying sum rules in order to obtain element specific spin and orbital magnetic moments is quite simple, at least for the metallic transition metal spectra. One only needs to integrate the respective resonant areas of the XMCD and the XAS spectrum.

Besides the problem of knowing  $n_h$  properly, two smaller problems remain applying the sum rules (3.54) and (3.55): Especially for the light transition metals<sup>12</sup> where the SOC is small, the  $L_3$ - and the  $L_2$ -edge contribution to the spectrum overlap. Therefore, one has to

<sup>12</sup> Especially for Vanadium and Chrome

set the separation between the  $L_2$ - and the  $L_3$ -edge carefully for estimating  $m_s$ . Another problem is the quantum mechanical mixing of the  $j_{3/2}$  and  $j_{1/2}$  states, where the  $L_3$ - and the  $L_2$ -edge cannot be distinguished properly anymore. These effects affect the sum rule value for  $m_s$  because (3.55) contains a term where integration has to be performed over the  $L_3$  edge only. Estimating sum rules for  $m_l$  on the other hand is not affected by these effects because integration is performed over the complete  $L_{2,3}$  edge.

Both problems can be solved. The overlapping problem can be overcome by the so-called momentum analysis [29]. Here, the XMCD signal is considered as a combination of different so-called ground state moments, e.g. pure spin moment, pure orbital moment. For the intermixing problem, a correction mechanism can be derived [30]. For the heavier transition metals like Fe, Co, Ni, due to their large SOC<sup>13</sup>, the intermixing problem is negligible.

In principle, sum rules can also be applied for the  $1s \rightarrow 2p$  transition, e.g. to determine a possible induced magnetic moment ([31]) on the C K-edge of the graphene Moiré template. Unfortunately, the sum rule (3.55) for the spin magnetic moment becomes indefinite for  $c = 0$ . Thus only the orbital magnetic moment can be determined:

$$m_l = -\frac{2 \int_K (\mu_+(E) - \mu_-(E)) dE}{3 \int_K (\mu_+(E) + \mu_-(E)) dE} \cdot n_h \cdot \mu_B \quad (3.56)$$

---

<sup>13</sup>  $\sim 17.5$  eV for Ni, see e.g. Figure 3.7

### 3.3. Magnetism of nano cluster systems

#### 3.3.1. From atomic to bulk properties

Nano clusters (NCs) are defined as agglomeration of 3 to >1000 atoms [4]. The cluster size plays a key role in the electronic and the magnetic properties.

One can use a simple picture in order to deduce the development of magnetism from atomic to bulk properties. This is sketched in figure 3.10 using the example of Fe. The electron configuration of Fe is  $4s^2 3d^6$  and the d-states are occupied according to Hund's rules (see section 3.1.2), so the single Fe atom has a net magnetic moment, see figure 3.10. When several Fe atoms form a cluster, their discrete atomic energy levels will overlap and form an energy band. However, the d-band remains narrow as the bandwidth is proportional to the coordination number, which is reduced due to the elevated number of surface atoms in cluster systems, [32]. The corresponding density of states for "surface" d-states is shown in figure 3.10 b). The bandwidth is indeed narrowed compared to the bulk material. The d-levels can be considered as being strongly localized to the atomic site, one can approximate the electron filling again with Hund's rules. The majority band is filled with 5 electrons, the minority band with two electrons<sup>14</sup>, resulting in a spin imbalance of  $\Delta n = n_{\uparrow} - n_{\downarrow} = 3$ . For bulk Fe, an imbalance of  $\Delta n = 2.15$  is reported [33]. This simple approach can also be applied to the other technically relevant transition metals as Ni and Co. One finds  $\Delta n = 1$  for cluster/surface Ni compared to  $\Delta n = 0.55$  for bulk ( $\Delta n = 2$  compared to  $\Delta n = 1.58$  for Co), [34, 35]. According to the Stoner criterion (see section 3.1.4), the spin imbalance at the Fermi level is the decisive factor for ferromagnetic ordering. As the spin imbalance is larger for less coordinated atoms in cluster or surface systems, one would expect increased magnetic moments for systems of lower dimensions compared to bulk values.

---

<sup>14</sup> Due to spd-hybridization, one s-electron is transferred from the 4s into the d-states.

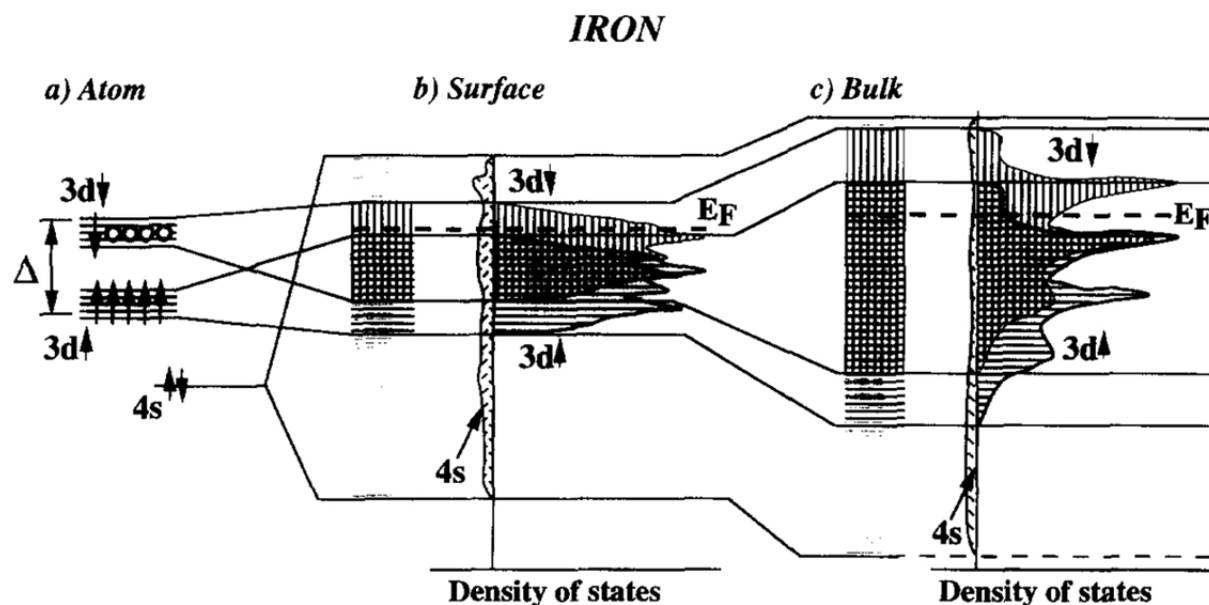


Figure 3.10: Transition from atomic to bulk properties demonstrated on the example of Fe. For clusters, where the number of atoms on the surface is increased with respect to the total number, the 3d valence band is narrowed which results in different magnetic properties. Reprinted from [36] with permission from Elsevier.

One approach to measure the magnetic properties of metal nanoclusters is to measure a cluster beam created out of the gaseous phase with a Stern-Gerlach setup [36-39]. Due to their net magnetic moment, the clusters are deflected in an inhomogeneous magnetic field. One finds a strong enhancement of magnetic moments for small clusters with progressive convergence towards the bulk value with increasing cluster size, as shown in figure 3.11. The magnetic moment in Fe clusters is found to be  $3 \mu_B$ , compared to the bulk value of  $2.2 \mu_B$ , which is a relative enhancement of more than 35 %. For Co and Ni, the cluster values yield  $2.4 \mu_B$  and  $1.05 \mu_B$  respectively compared to a bulk value of  $1.75 \mu_B$  and  $0.62 \mu_B$ .

Although the Stern-Gerlach method is unable to resolve the spin and orbital contribution to the total magnetic moment, these experiments show nicely the transition of cluster towards bulk values as sketched in the previous section.

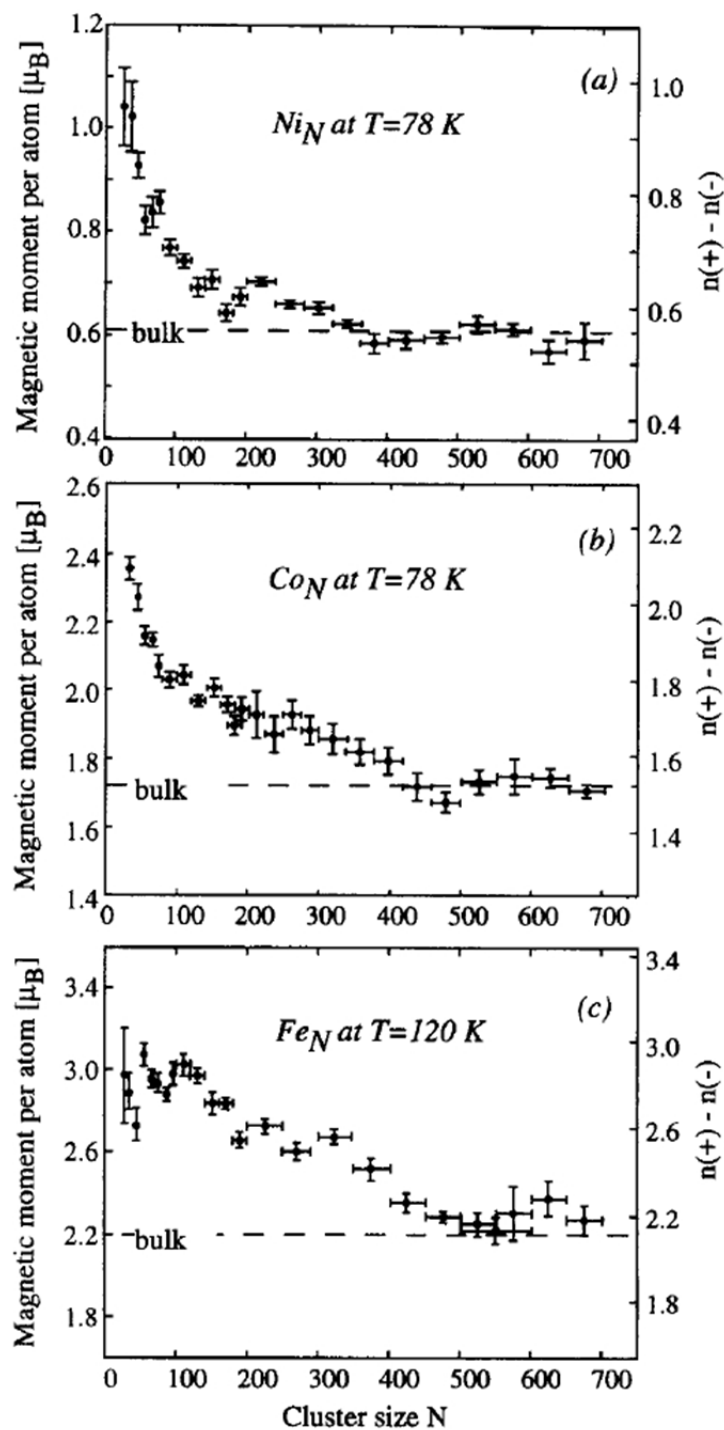


Figure 3.11: Size dependency of the magnetic moment (per atom) of Fe, Co, and Ni nanocluster. Magnetic moments were obtained from a molecular beam via the Stern-Gerlach effect. With increasing cluster size, the magnetic moment converges progressively towards the bulk value (dashed line). Reprinted from [36] with permission from Elsevier.



### 3.3.2. Magnetic Anisotropy of Metal Nano Clusters

Another interesting feature of reduced size cluster system is the development of large magnetic anisotropy with decreasing size. The reason is an enhanced orbital magnetic moment, which is due to a lack of orbital quenching [40] and different crystal geometry in systems with reduced symmetry. Although the pure spin moment is isotropic, due to spin orbit coupling it is linked to the orbital moment and thus to the atomic structure, causing the magnetic anisotropy [41, 42]. Due to the magnetic anisotropy, magnetic moments tend to align along a preferred spatial direction. This is the driving mechanism behind many important technological implications such as magnetic data storage devices.

As larger orbital magnetic moments mean larger magnetic anisotropy, it is important to understand how  $m_j$  evolves with the cluster size. Several works have been performed on this subject, mainly by XMCD on in-situ prepared metal clusters. For very small Co clusters, consisting of 40 and less atoms, on a Pt (111) single crystal surface the orbital magnetic moment is drastically enlarged,  $m_l = 1.1 \mu_B$  compared to the bulk value of  $m_l = 0.15 \mu_B$  [43]. The size dependent XMCD spectra are summarized in figure 3.12. There is a clear decrease in the XMCD signal with increasing cluster size. Additionally, the orbital magnetic moment declines exponentially and so does the magnetic anisotropy.

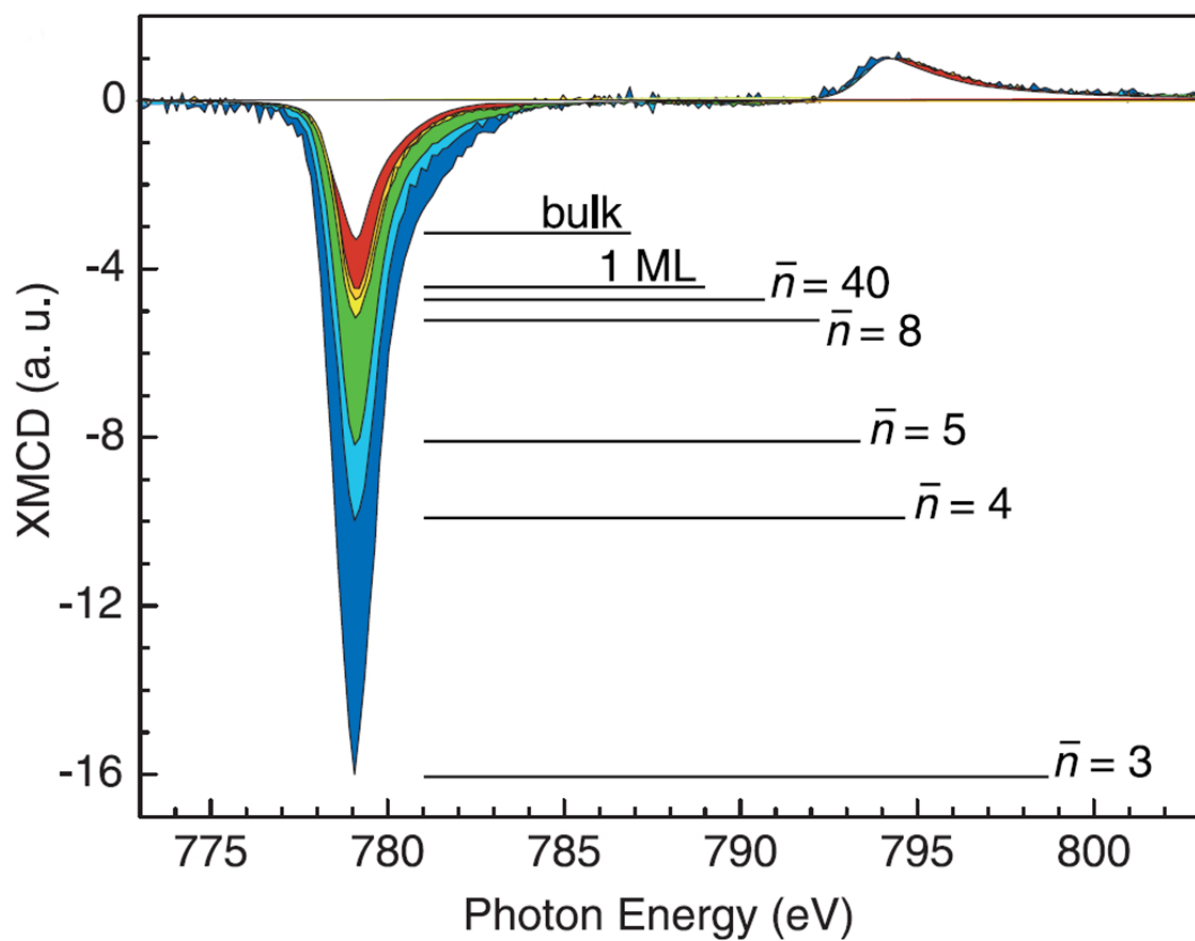
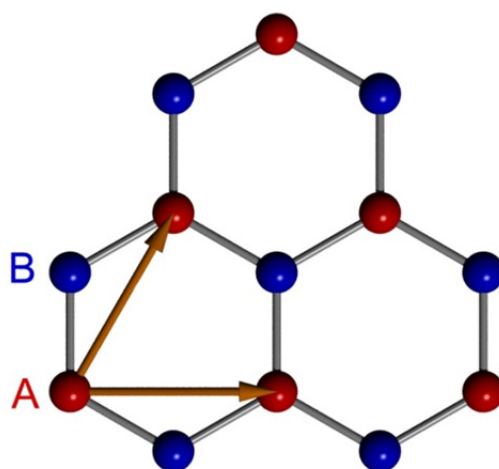


Figure 3.12: L<sub>2</sub>-edge intensity normalized XMCD effect of small Co clusters on Pt (111) in dependence of the number of containing atoms. From [43]. Reprinted with permission from AAAS.

### 3.4. Transition metal clusters on the graphene Moiré template

Graphene is a two-dimensional (2D) layer of carbon atoms as it naturally occurs in graphite. It generated great impact on the scientific community after the first experimental investigations of the electronic properties of exfoliated single layer graphite sheets, [44]. It revealed some unique properties such as the existence of practically massless Dirac fermions and the half integer quantum hall effect [45, 46]. From these properties, a large number of exciting possible applications arise, like graphene based electronic devices, the use as conducting electrodes, ultra-capacitor, photosensitive transistor or chemical sensors [47-50].



**Figure 3.13 a): Real space lattice of graphene with the graphene unit cell consisting of two carbon atoms (A and B) (see also e.g. [51]). The lattice can be expanded with the lattice vectors  $\vec{a}_1$  and  $\vec{a}_2$ . b) Continuous graphene honeycomb lattice.**

The real space lattice of graphene is shown in figure 3.13 a). Six  $sp^2$ -hybridized carbon atoms form a hexagon with a carbon-carbon bonding length of  $a_0 = 0.142 \text{ nm}$  ( see e.g. [48]). The graphene unit cell is established by two carbon atoms, marked red (A) and blue (B) in figure 3.13 a). The graphene mesh shown in figure 3.13 b) can be expanded by a linear combination of the basis vectors  $\vec{a}_1$  and  $\vec{a}_2$ . The lattice parameter is  $a_0 = 0.245 \text{ nm}$  (e.g. [52]).

Besides mechanical exfoliation and segregation from carbon rich materials like SiC, graphene sheets can also be produced by carbon hydrate cracking on the hot metal surfaces like Ir (111), Rh (111), Ru (0001), Ni (111), or Cu (111) (see e.g. [52-59] and the detailed sample preparation description for the samples investigated within this thesis in section 5.1). Table 3.2 lists the lattice constants of common noble metal graphene supports.

**Table 3.2: Lattice constants of common noble metal graphene supports in comparison with the graphene lattice constant [59].**

Support	Lattice constant [nm]	Lattice Mismatch [nm]
(Graphene)	0.245	0
Ir (111)	0.272	0.027
Rh (111)	0.269	0.024
Ru(0001)	0.271	0.026
Ni (111)	0.249	0.003
Pt (111)	0.277	0.032

As a consequence of this small lattice mismatch, graphene forms a Moiré superstructure atop of these noble metal supports. This superstructure can be identified for example with LEED. A comparison of LEED pictures of a thoroughly cleaned Ir (111) single crystal and the graphene/Ir (111) system after a successful preparation attempt is shown in figure 3.14.

The graphene Moiré pattern reflects in LEED as small sharp satellites around the substrate Ir (111) spots. It is clearly visible in figure 3.14 b).

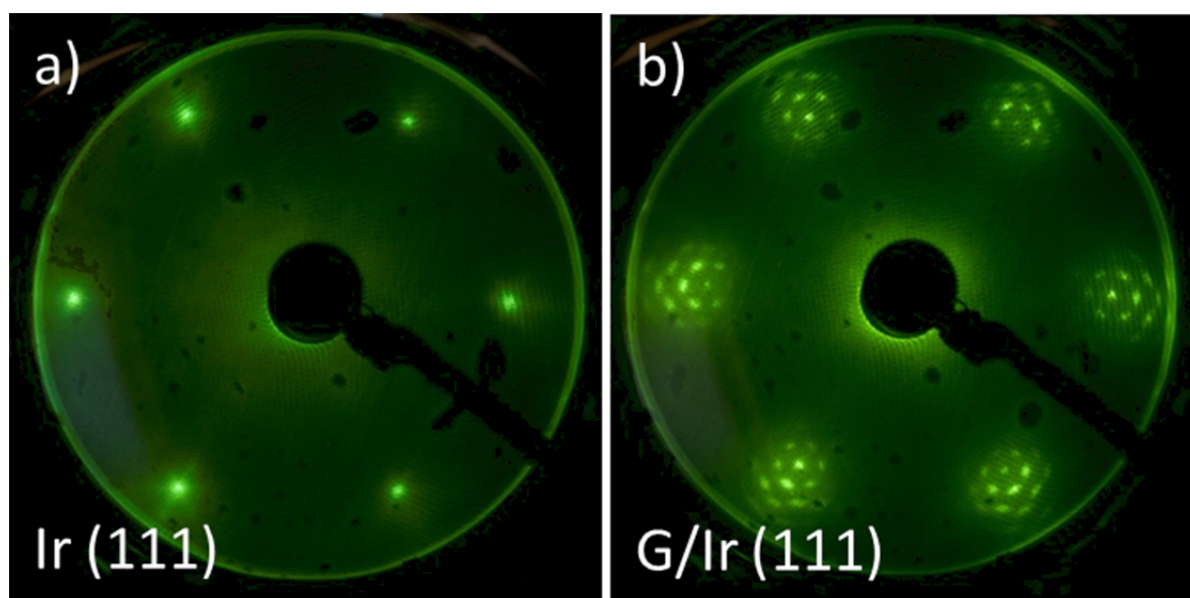


**Figure 3.14: a) LEED picture of bare Ir (111) single crystal compared to b) LEED picture of the same Ir (111) single crystal with graphene atop. Electron energy was set to 75 eV.**

A more advanced technique to study details of graphene on metal substrates is scanning tunnel microscopy (STM). An STM picture of graphene on the Ir (111) substrate is shown in figure 3.15 a). The Moiré super lattice is marked by a black rhombus and the lattice constant is 2.52 nm (see also [52]). Taking the lattice constants given in table 3.2, a single super lattice cell contains 10.3 graphene and 9.2 underlying Ir unit cells. Due to the very high in-plane stiffness of graphene, it buckles slightly on any kind of metal support (except for Ni (111) due to the much smaller lattice mismatch). The carbon atoms occupy different sites of the Ir lattice which is also visible in the STM topograph. Bright areas correspond to carbon atoms occupying hollow fcc/hcp sites of the Ir (111) lattice, darker areas correspond to one carbon atom sitting atop an Ir atom.

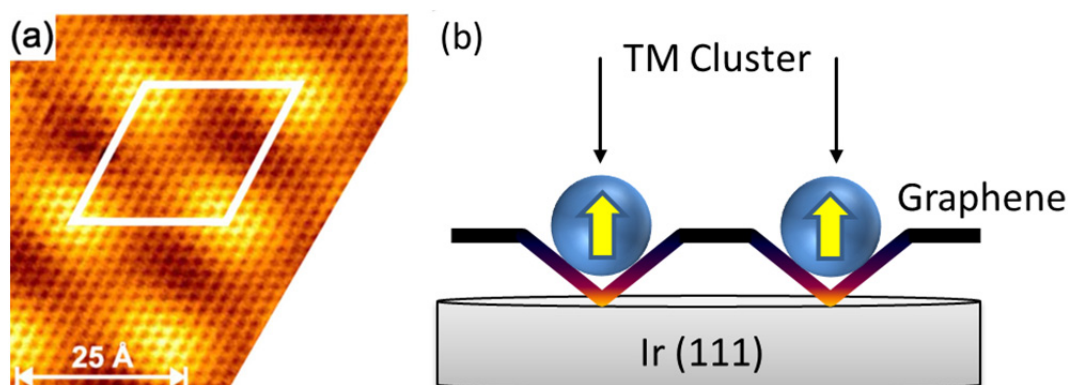


**Figure 3.15: a) STM topograph of graphene on Ir (111) with highlighted Moiré supercell (white rhombus). Reprinted with permission from [60]. Copyright (2006) by the American Physical Society. b) Buckled bonding of graphene to Ir (111) (or other noble metal substrates) as possible template for growth of a defined nanopattern of magnetic TM clusters.**

The buckled bonding of graphene to the Ir (111) substrate can be utilized as a template for the growth of TM clusters as sketched in figure 3.15 b). The graphene mesh forms a “landscape” of mounds and swales on Ir (111). Cluster growth can be obtained by e.g. e-beam evaporation of TM. The TM atoms agglomerate within the mounds of graphene and form larger clusters. This template growth of well-defined patterns of metal clusters such as Fe, Co, Ni, Pt, or Ir has indeed been observed (see e.g. [60-64]). Using magnetic nanoclusters, the TM/graphene/Ir (111) system is a promising candidate for next generation high density data storage devices.

A detailed investigation of Ni clusters on a graphene Moiré template (grown on Rh (111)) has been performed by Sicot et. al. [63]. They report two different growth modes resulting in two different types of nanoclusters. One key parameter is the deposition temperature. If Ni is deposited at RT, the Ni atoms exhibit a high mobility on the graphene substrate. They finally start growing clusters at certain agglomeration sites and form larger, triangularly shaped nanoclusters, as shown in figure 3.16 a). The dimensions of the clusters are typically around  $20 \times 20 \times 2 \text{ nm}^3$  (see inset). They are aligned along the main symmetry lines (white lines in figure 3.16 b) and c)) of the graphene substrate, sometimes with slight rotations ( $4^\circ$  with respect to the symmetry line for the cluster in figure 3.16 b).

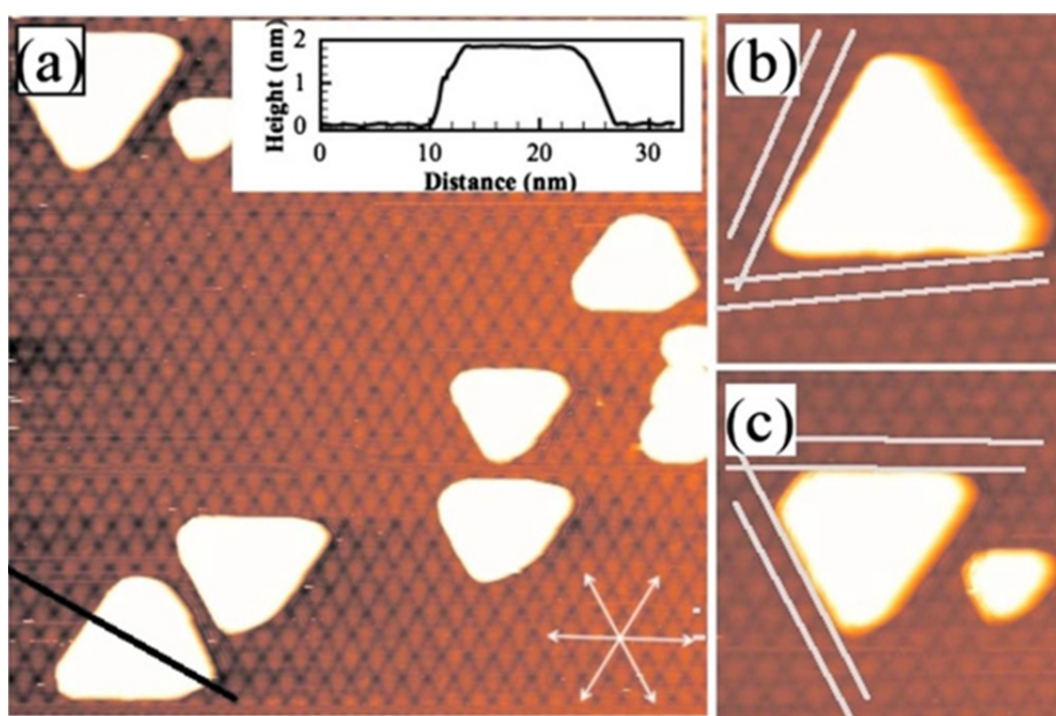


**Figure 3.16 a):** STM topograph of triangular Ni nanoclusters, obtained by RT deposition of nominally 0.90 ML Ni/graphene/Rh( $85 \times 85 \text{ nm}^2$ ). Inset shows the height profile of a selected nanocluster along the black line in the lower left part. b) and c): Slightly rotated and non-rotated alignment of nanoclusters with respect to the main symmetry lines of graphene (white). Reprinted with permission from [63]. Copyright 2010, AIP Publishing LLC.

Ni deposition at a temperature below 200 K reduces the mobility of the Ni atoms and they tend to agglomerate close by their landing site. As a result one obtains spherically shaped nanoclusters instead. Figure 3.17 a) shows an STM figure of 0.25 ML Ni on



graphene/Rh(111). The spherical clusters align mainly along the regular Moiré grid of the graphene substrate as shown in figure 3.17 b). From the cluster diameter in figure 3.17 c) distribution one estimates a mean diameter of approximately 3 nm. If one increases the nominal Ni deposition one obtains a much denser distribution of the clusters, shown in figure 3.17 d). However, higher increasing the deposition also results in a slightly broader diameter distribution (see figure 3.17 e)) and an increased mean cluster diameter. It increases to 3.5 nm. Further details on the nucleation and growth of Ni on graphene/Rh (111) can be found in [63].

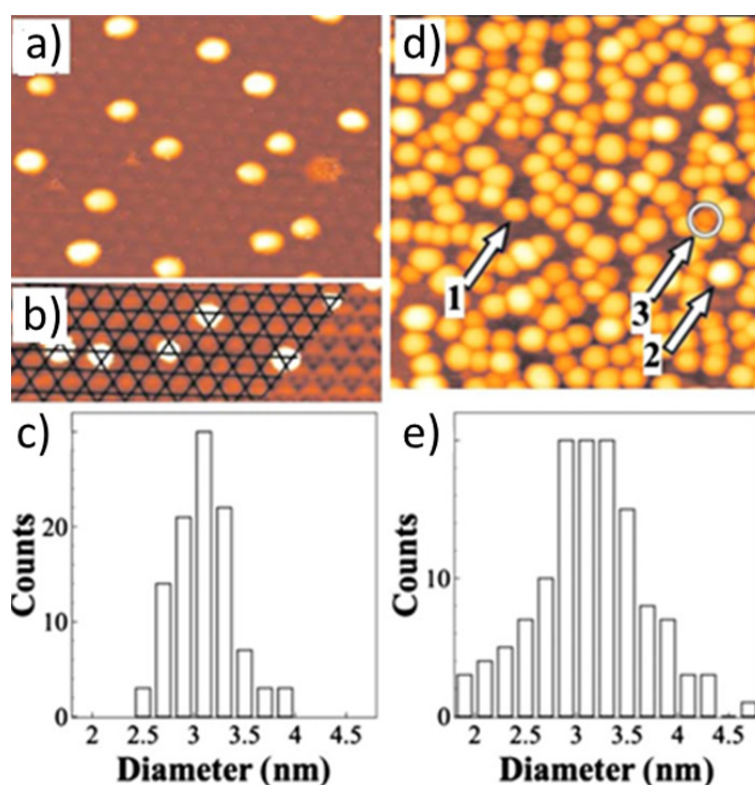


**Figure 3.17** a): Nominal deposition of 0.25 ML Ni at 150 K results in growth of spherical clusters. b) Location of the spherical clusters on the Moiré grid (black lines). c) Cluster size distribution for 0.25 ML Ni. d) Nominal deposition of 1.5 ML Ni at 150 K results in a higher density of clusters on the graphene mesh. e) Size distribution of spherical clusters for higher nominal deposition. Reprinted with permission from [63]. Copyright 2010, AIP Publishing LLC.

A general problem for applications based on TM nano clusters is the high sensitivity of the clusters to ambient conditions. TM clusters oxidize rapidly when exposed to air due to its small surface-to-volume fraction. A possible way to protect nanoclusters is to use

intercalation of TM clusters under the graphene substrate [65]. The basic principle of intercalation is to anneal the TM/graphene/Rh (111) system to 700-900 K. The TM then diffuses underneath the graphene mesh through e.g. lattice defects and forms monoatomic nano islands. Figure 3.18 shows a Ni nano island protected by graphene. Intercalation was performed by annealing Ni deposited on graphene and to 670 K. Further details on intercalation of TM underneath graphene can be found in [66].

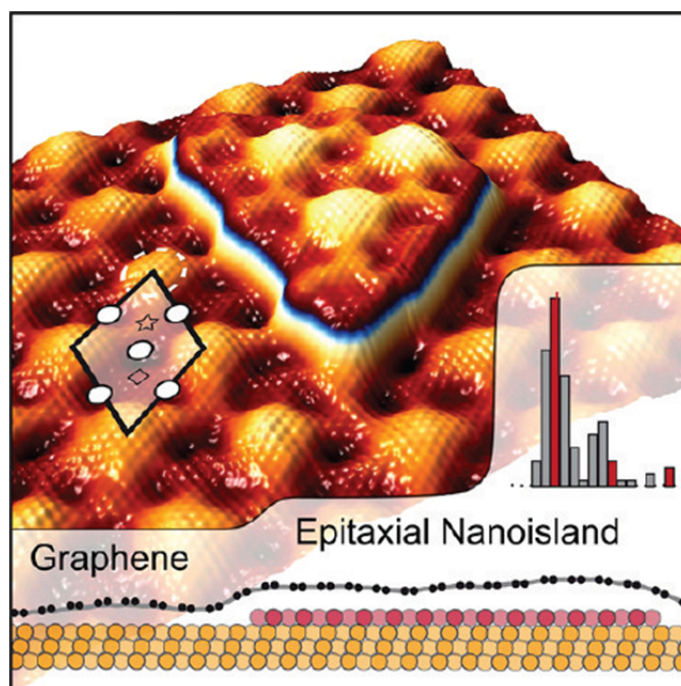


**Figure 3.18: Oxidation protection of a Ni nanoisland through intercalation under graphene/Rh (111). Reprinted with permission from [66]. Copyright 2012 American Chemical society.**

To summarize, using the TM/graphene/Rh (Ir) systems allows studying both, the shape and size dependent properties of TM nanostructures. Furthermore, intercalation is an effective tool to prevent the nano clusters from oxidation which is very important for possible applications, whether in the field of data storage or spintronics.



### 3.5. Magnetism of doped and undoped ZnO systems

More than ten years ago, Dietl. et.al. predicted that semiconductors like ZnO can become ferromagnetic even at RT by doping with a small amount (less than 10 %) of transition metal ions like Mn or Co [67]. Soon thereafter, first groups indeed were able to prepare ferromagnetic transition metal doped samples [68, 69]. The main idea was that the transition metal ions couple ferromagnetic within the host material without changing its semiconducting behavior, which makes these dilute magnetic semiconductor systems a promising candidate for an application in future spintronic devices [70]. However, the main problem is that integrating measurement methods like SQUID and VSM always showed ferromagnetic hysteresis loops. Element specific methods like on the other hand XMCD couldn't address the ferromagnetism to any of the containing elements [71-73]. In particular, the transition metal was only found to be paramagnetic, and there was no detectable magnetic signal from all other elements.

By detailed literature investigation of published TEM micrographs of doped and undoped nanograined ZnO samples, we found a relation between the grain size and the magnetism of the respective sample [74-78]. The key parameter is the so-called specific grain boundary area  $s_{GB}$ , defined as the grain area to volume ratio [74]:

$$s_{GB} = \frac{A_{GB}}{V_{GB}} = \frac{1.65 \cdot a}{D} \quad (3.57)$$

where  $D$  is the mean grain size and  $a$  is the aspect ratio, depending on the grain shape<sup>15</sup>. They found that ferromagnetism occurs even in undoped ZnO if the grain size is small enough, or if the specific grain boundary area  $s_{GB}$  exceeds a certain threshold value  $s_{th}$ .

Figure 3.19 a)-d) shows the result of this detailed literature investigation for the most common ZnO systems: Fe:ZnO, Co:ZnO, Mn:ZnO, and undoped ZnO. Here, the preparation temperature is plotted over  $s_{GB}$ . Samples found to only para- and diamagnetic are marked as open symbols, ferromagnetic samples are marked with filled symbols.

---

<sup>15</sup>  $a < 1$  for elongated grains,  $a > 1$  for flattened grains.

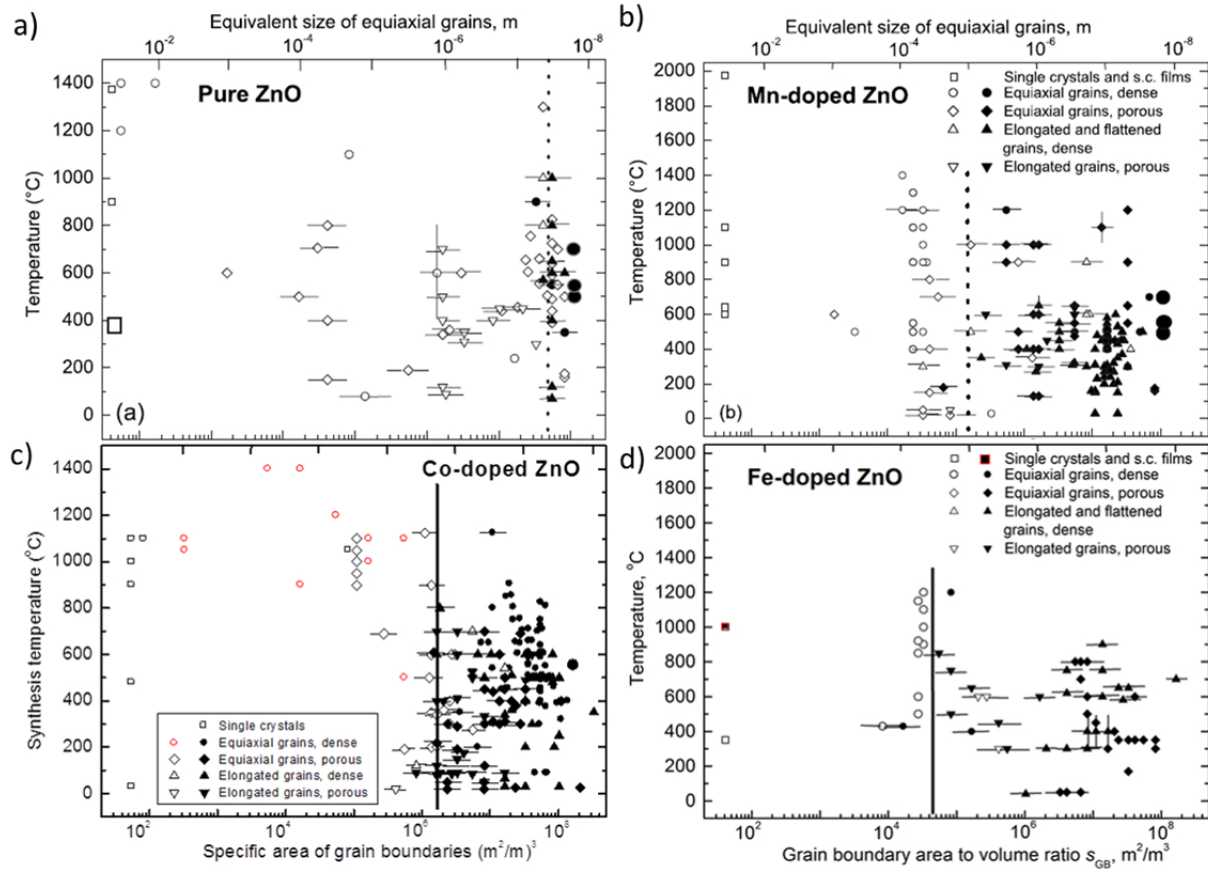


**Figure 3.19: Magnetic behavior of a) undoped ZnO, [74], b) Mn:ZnO [74], c) Co:ZnO (with permission from [76]), d) Fe:ZnO [77]. Open dots display samples showing dia- or paramagnetic, filled black dots indicate ferromagnetic samples. The threshold value for the  $s_{GB}$  area,  $s_{th}$  is marked in every figure by a vertical line. a), b) reprinted with permission from [74]. Copyright (2008) by the American Physical Society.**

Interestingly, in every investigated sample system, a clear threshold line between non-magnetic and ferromagnetic behavior is found. The threshold  $s_{GB}$  is  $5 \cdot 10^5 m^2/m^3$  for Fe:ZnO, corresponding to a mean grain size of about 40  $\mu m$ . For Co:ZnO and Mn:ZnO, one finds  $s_{th}(Co) = 1.5 \cdot 10^6 m^2/m^3$ ,  $s_{th}(Mn) = 2 \cdot 10^5 m^2/m^3$ , corresponding to a grain size of 1  $\mu m$  and 10  $\mu m$ . Additionally, magnetism was also found in completely undoped ZnO samples, confirming XMCD results that FM order at RT in ZnO is not related to a FM coupling of the TM dopants. The threshold value however was much higher,  $s_{th}(undoped) = 5 \cdot 10^7 m^2/m^3$ , which corresponds to a grain size of 35 nm. A summary of values is given in table 3.3.

**Table 3.3: Comparison of the threshold specific grain boundary area  $s_{th}$  (from figure 3.19) and the corresponding maximum grain size for TM doped and undoped ZnO.**

Dopant	$s_{th}$ [ $m^2/m^3$ ]	Mean Grain Size [nm]
Fe	$5 \cdot 10^5$	40
Co	$1.5 \cdot 10^6$	1
Mn	$2 \cdot 10^5$	10
Undoped	$5 \cdot 10^7$	0.035

A possible explanation of these finding is the formation of the so-called ferromagnetic grain-boundary foam which is located between the crystalline nanograins. This grain-boundary was identified as amorphous ZnO phase separating the crystalline ZnO grains from each other and to be a sufficient feature for ferromagnetism [79]. The amorphous interlayer is a host to imperfections and vacancies which are sources of excess electrons (holes) – similar to dopants. Furthermore, it exhibits an increased solubility of transition metals compared to the crystalline ZnO which explains the much smaller threshold value  $s_{th}$  for the doped FM ZnO [80-82].

### 3.6. Muon Spin Rotation ( $\mu$ SR)

In Muon Spin Rotation, Muon Spin Relaxation or Muon Spin Resonance ( $\mu$ SR) positively charged muons ( $\mu^+$ , actually anti-muons) are implanted into matter. Due to the unique properties of the  $\mu^+$  (especially its magnetic moment of  $3.18 \mu_B$ ) they are used as a sensitive magnetic microprobe to detect an intrinsic local magnetic field. These local magnetic fields cause a gyromagnetic rotation of the  $\mu^+$ -spin, hence the name Muon Spin rotation ( $\mu$ SR).

#### 3.6.1. Muon properties

Muons were first observed in 1936 by Anderson and Neddermeyer as a “hard component<sup>16</sup>” of the cosmic radiation [83]. It turned out that the muon ( $\mu^-$ ) is an elementary particle with similar properties as the electron, but with a 207 times higher mass and a lifetime of only 2.2  $\mu$ s. The  $\mu^-$  and its anti-particle, the anti-muon ( $\mu^+$ ) decay via the weak interaction into an electron/positron and respective electron/muon neutrinos<sup>17</sup>:

$$\begin{aligned}\mu^+ &\rightarrow e^+ + \nu_e + \bar{\nu}_\mu \\ \mu^- &\rightarrow e^- + \bar{\nu}_e + \nu_\mu\end{aligned}\tag{3.58}$$

The muon decay violates parity and the momenta of the resulting electrons/positrons are mainly directed along the initial muon spin direction. For the  $\mu$ SR technique, usually the  $\mu^+$  is being used. Due to its positive charge, it avoids core regions and mainly sits into interstitials and vacancies. Because of its magnetic moments it can detect local magnetic fields within this vicinity.  $\mu^-$  are usually not used for  $\mu$ SR as they strongly interact with the electron cloud, thus in the following the discussion shall be limited to the  $\mu^+$ . The exact numbers for the muon properties are given in table 3.4.

---

<sup>16</sup> Particle with a large range in condensed matter

<sup>17</sup> Because of its similarity to the electron, the muon decay could also occur involving a photon:

$\mu^\pm \rightarrow e^\pm + \gamma$ , but this transition is forbidden by the Lepton flavor conservation.

Table 3.4: Summary of the basic muon properties (see e.g. [10]).

	$\mu^-, \mu^+$
Mass :	$\sim 207 m_e = 0.1056 \text{ GeV}/c^2$
Charge:	- 1, + 1
Spin:	$\frac{1}{2}$
Lifetime:	$2.2 \mu\text{s}$
Magnetic moment:	$3.18 \mu_p = 4.836 \cdot 10^{-3} \mu_B$
Gyromagnetic Ratio:	$2\pi \cdot 135.54 \text{ MHz/T}$

### 3.6.2. Muon beam production

Muons occur in high numbers in the cosmic radiation. However, in order to perform  $\mu$ SR, it is necessary to have a defined muon beam with a defined initial muon spin direction. Therefore, in  $\mu$ SR facilities one produces muons via the production and the decay of pions. The common way to produce pions is to hit a Carbon or a Beryllium target with high energy protons.

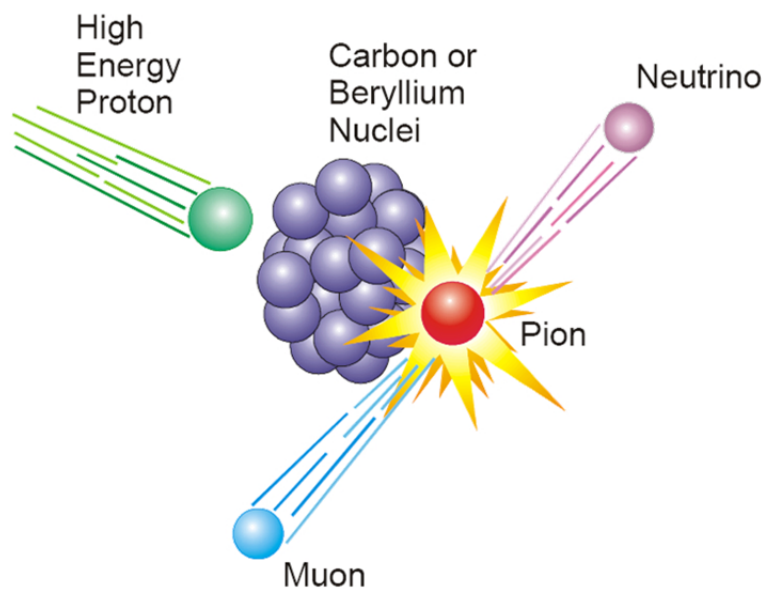


Figure 3.20: Scheme of Pion production, the preliminary stage of Muon production. A high energy proton hits a carbon or beryllium nucleus and pions are produced according to equation (3.59) (From [14]).

The pion is then produced in different ways out of the initial proton and the targets neutrons/protons:



The lifetime of a pion is  $\sim 38$  ps before it mainly decays into an antimuon/muon and the corresponding neutrino/antineutrino<sup>18</sup>:

$$\begin{aligned}
 \pi^+ &\rightarrow \mu^+ + \nu_\mu \\
 \pi^- &\rightarrow \mu^- + \bar{\nu}_\mu
 \end{aligned}
 \tag{3.60}$$

We now have a closer look at the upper equation in equation (3.60), the decay involving the  $\mu^+$ . The initial  $\pi^+$  spin is  $S_\pi = 0$ , as well as the momentum  $p_\pi$ , and both are conserved during the process. Thus, the spin of the  $\mu^+$  ( $S_\mu$ ) and the  $\nu_\mu$  ( $S_\nu$ ) have to be opposite, as well as their respective momenta ( $p_\mu$  and  $p_\nu$ ). As nearly massless particle, the  $\nu_\mu$  is completely left-handed with helicity<sup>19</sup>  $h_\nu = -1$ , meaning  $S_\nu$  points in the opposite direction of  $p_\nu$ . Due to spin and momentum conservation, this automatically impacts  $S_\mu$ , which now also has to point in the opposite direction of  $p_\mu$ . Due to this parity violation, the spin polarization of  $\mu^+$  obtained from pion decay is 100 %, with  $S_\mu$  pointing opposite to the direction of the initial  $\mu^+$  momentum.

---

<sup>18</sup> The energetically more favorable decay  $\pi^- \rightarrow e^- + \bar{\nu}_e$  is strongly suppressed due to helicity reasons.

<sup>19</sup> Helicity in particle physics is defined as component of the spin of a particle, pointing along its momentum,  $h = \vec{S} \cdot \hat{p}$  with  $\hat{p} = \vec{p}/|\vec{p}|$ .

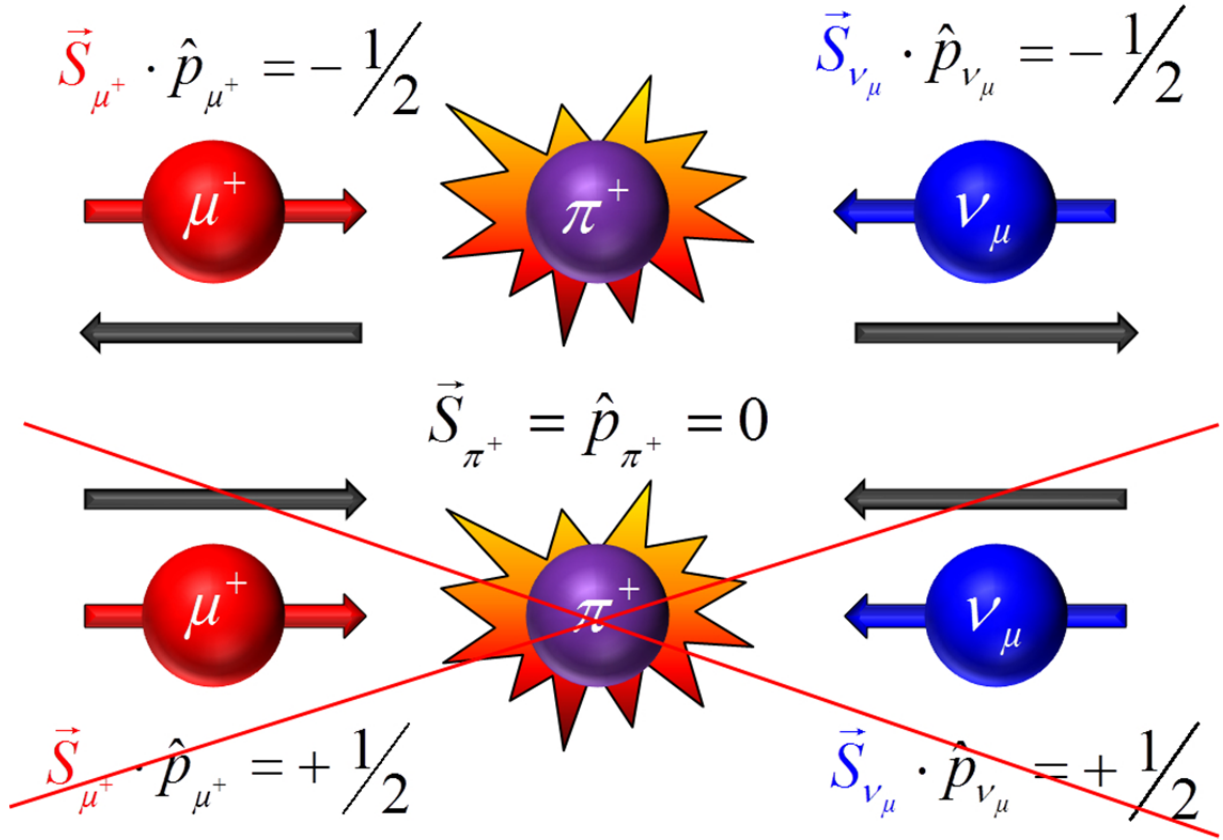


Figure 3.21: Scheme of the major channel of the  $\pi^+$  decay. As nearly massless fermion, the  $\nu_\mu$  exhibits  $h = -1/2$ , with its spin aligned anti-parallel to its momentum, as sketched in the upper part. Inverting space coordinates (applying parity operator to the system) is sketched in the lower part. In principle, the  $\mu^+$  could also align its spin parallel to its momentum, but this case is completely suppressed, because the helicity of the  $\nu_\mu$ . The lower case is practically not observed, so that via  $\pi^+$  decay, one can generate a 100% spin polarized  $\mu^+$  beam, where  $S_\mu$  is always aligned antiparallel to the direction of movement of the  $\mu^+$ .

This example of the  $\pi^+$  decay shows that decays via the weak interaction come along with the creation of neutrinos and thus parity is violated. A swift glance at equation (3.58) shows that in the  $\mu^+$ -decay a similar mechanism is involved. In this case, it is the positron ( $e^+$ ) momentum that is linked to the initial spin direction of the  $\mu^+$ , as shown in figure 3.22.

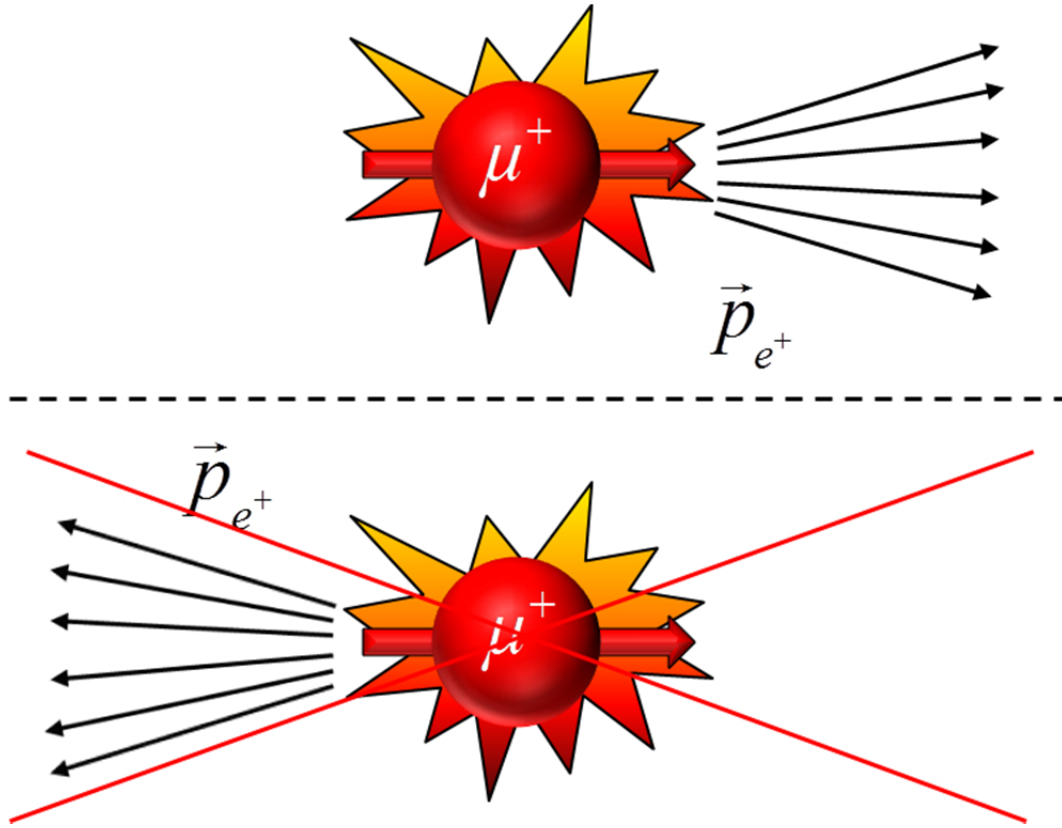


Figure 3.22: Parity violation in the  $\mu^+$  decay leads preferentially to a parallel alignment of the  $e^+$  momentum with respect to the  $\mu^+$  spin direction. In other words, the  $e^+$  is always emitted along the  $\mu^+$  spin direction. For clarity, the respective muons involved are not shown here.

The angular distribution of the  $e^+$  emission probability is given by:

$$W(\theta) = 1 + a_0 \cdot \cos(\theta) \quad (3.61)$$

Here,  $\theta$  is the angle between the positron trajectory and the  $\mu^+$ -spin, and  $a_0$  is an asymmetry parameter, depending on the  $\mu^+$  beam polarization and the positron energy. Theoretically one finds  $a_0 = 1/3$ , in experiments values of  $a_0 \sim 0.25$  are obtained. The probability function (3.61) is shown in figure 3.23. The emission of the  $e^+$  is asymmetric and occurs preferably along the  $\mu^+$  spin direction.



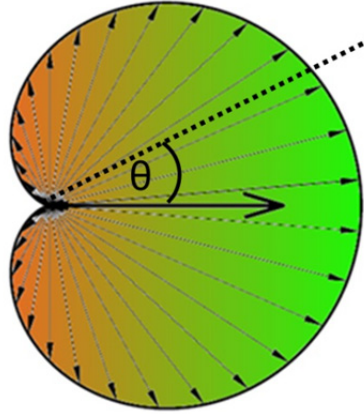


**Figure 3.23: Angular distributions of the emitted  $e^+$  with respect to the initial  $\mu^+$  spin direction.  $e^+$  are preferably emitted along the initial  $\mu^+$  spin direction. Adapted from [10].**

One should note that the positron emission is asymmetric and linked to the  $\mu^+$  spin orientation which is exploited in  $\mu$ SR experiments. A typical  $\mu$ SR experiment consists of an initial trigger (“muon time 0”) detector, a magnet in order to apply an external magnetic field, and a positron detector. In low energy  $\mu$ SR (LE- $\mu$ SR), additionally an Argon moderator is used to slow down muons to approximately thermal velocity. The sample is set to a variable positive high voltage in order to be able to implant muons in different shallow sample depths, ranging from 5-200 nm. This is favorable especially for thin film systems as investigated in this thesis. Two of several possible geometries for LE- $\mu$ SR experiments were used and thus shall be discussed: transverse-field (TF) and longitudinal/zero-field (ZF) geometry. The methods are sketched in figure 3.24:

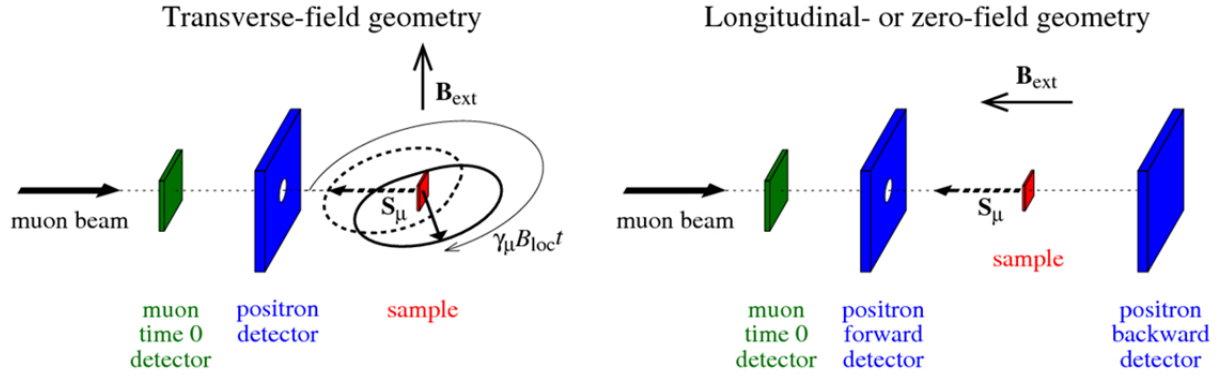


**Figure 3.24 a): Transverse-field (TF) geometry  $\mu$ SR setup.** An external field  $\vec{B}_{ext}$  is applied transversal to the muon spin direction, leading to a  $\mu^+$  precession depending on  $\vec{B}_{ext}$  and the samples internal magnetic field  $\vec{B}_{loc}$ . **b): Longitudinal or zero-field (ZF) geometry  $\mu$ SR setup.**  $\vec{B}_{ext}$  is applied along  $\vec{S}_\mu$ , giving no torque to the muon. Thus, the detected signal is only dependent on components of  $\vec{B}_{loc}$  perpendicular to  $\vec{S}_\mu$ . The experiment can also be performed without applied magnetic field (“zero-field”), if the internal field  $\vec{B}_{loc}$  is very small. From [13].

One now detects the  $e^+$  signals from the forward and backward detectors over the time. The number of counts that are detected at the forward ( $N_F$ ) and backward ( $N_B$ ) detector is given by:

$$N_{F,B}(t) = N_0 \exp\left(-\frac{t}{\tau_\mu}\right) \cdot [1 \pm a_0 P_{x,z}(t)] \quad (3.62)$$

,where  $N_0$  is the incoming muon beam intensity,  $a_0$  the parameter from equation (3.61),  $\tau_\mu$  is the muon lifetime and  $P_{x,z}(t)$  is the so-called polarization function, which is defined as the average over the muon ensemble of the muon normalized magnetic moment. In order to remove the muon lifetime influence in equation (3.62), one can calculate the asymmetry  $A_z(t)$  which is defined as:

$$A_z(t) = \frac{N_F(t) - N_B(t)}{N_F(t) + N_B(t)} \quad (3.63)$$

A comparison between the raw data signal  $N_{F,B}(t)$  and the corresponding asymmetry function  $A_z(t)$  for a typical  $\mu$ SR experiment in ZF geometry is shown in figure 3.25

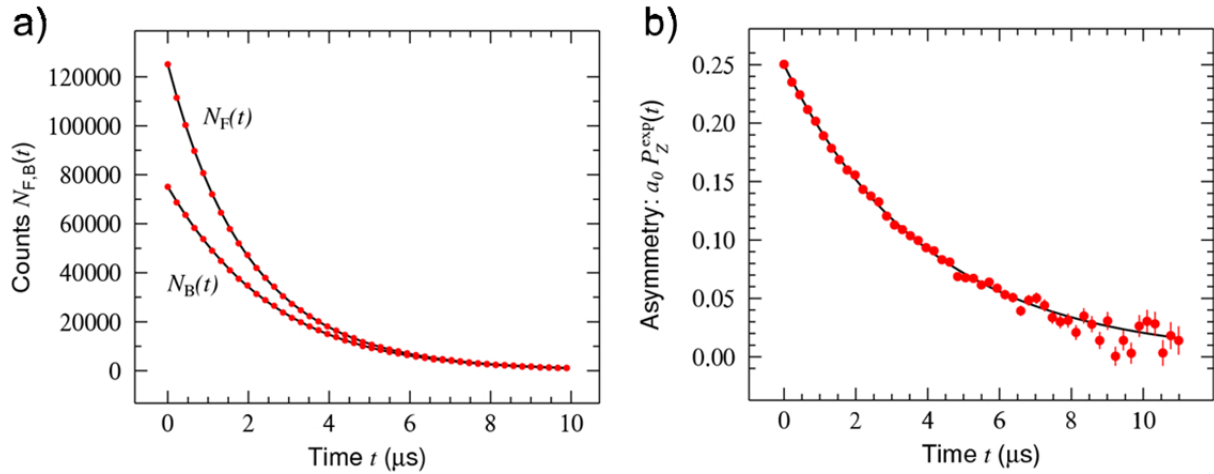


**Figure 3.25 a):** Positron forward and backward detector signal. In addition to the actual  $\mu$ SR signal, the influence of the muon lifetime is still apparent. **b):** Asymmetry function after removing lifetime influence according to equation (3.63). The lifetime influence to the signal vanishes. The remaining decay is caused by the depolarization of the  $\mu^+$  spin due to their interaction with magnetic fields within the investigated sample. From [13].

The asymmetry  $A_z(t)$  is strongly influenced by the interaction of the  $\mu^+$  with magnetic fields within its vicinity, usually local magnetic fields within the investigated sample. For example, in a non-magnetic sample, the  $\mu^+$  will maintain their initial spin direction.  $A_z(t)$  remains constant within the observation time. For a sample with 100 % ferromagnetic volume fraction,  $\mu^+$  will strongly interact with the local magnetic fields and thus quickly and completely depolarize. In general, by measuring the decay  $A_z(t)$  one can conclude to the strength and the distribution of magnetic fields within the investigated sample. This will be discussed in the following section.

### 3.6.3. Muon interaction with matter

If a muon is implanted into a sample it will interact with local magnetic field  $\vec{B}_{loc}$  present. The muon spin  $\vec{S}_{\mu^+}$  will carry out a Larmor precession around the magnetic field direction as indicated in figure 3.26.

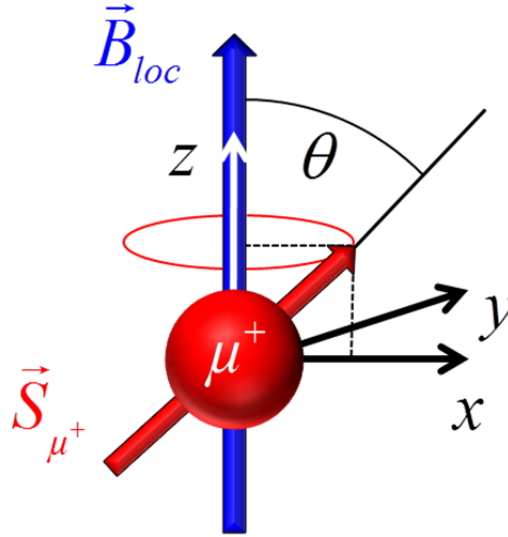


**Figure 3.26: Precession of the muon spin  $\vec{S}_{\mu^+}$  around a local magnetic field.  $\vec{B}_{loc}$  defines the z-axis,  $\theta$  is defined as the angle between  $\vec{S}_{\mu^+}$  and  $\vec{B}_{loc}$ .**

One can describe the muon spin precession also mathematically. The time derivative of an angular momentum is given by the sum of all torques. In this case, the time dependent torque is given by  $\vec{B}_{loc}(t)$  and the muon magnetic moment  $\vec{m}_{\mu}(t)$ :

$$\frac{d\hbar\vec{S}_{\mu}}{dt} = \vec{m}_{\mu}(t) \times \vec{B}_{loc}(t) \quad (3.64)$$

Using the relation

$$\vec{m}_{\mu}(t) = \gamma_{\mu} \vec{S}_{\mu} \hbar \quad (3.65)$$

where  $\gamma_{\mu}$  is the gyromagnetic ratio given in table 3.4, one obtains the well-known Larmor equation:

$$\frac{d\vec{S}_{\mu}(t)}{dt} = \gamma_{\mu} \vec{S}_{\mu}(t) \times \vec{B}_{loc}(t) \quad (3.66)$$

A possible solution is given by:

$$\vec{S}_\mu(t) = \begin{pmatrix} S_\mu^\perp(0)\cos(\omega_\mu t) \\ -S_\mu^\perp(0)\sin(\omega_\mu t) \\ S_\mu^\parallel(0) \end{pmatrix} \quad (3.67)$$

Here, the Larmor frequency  $\omega_\mu$  is defined as:

$$\omega_\mu = \gamma_\mu B_{loc} \quad (3.68)$$

$S_\mu^\parallel(0)$  and  $S_\mu^\perp(0)$  are the projections of the initial  $\vec{S}_{\mu^+}$  at  $t=0$  onto the z-axis ( $S_\mu^\parallel$ ) and the x-y plane ( $S_\mu^\perp$ ) as they are defined in figure 3.26. One has to note that, typical for spin 1/2 systems, the precession frequency depends only on the strength of  $\vec{B}_{loc}$  but not on the angle  $\theta$  between  $\vec{B}_{loc}$  and  $\vec{S}_{\mu^+}$ .

If  $\vec{B}_{loc}(t)$  is constant<sup>20</sup>, one can neglect the time evolution of  $\vec{B}_{loc}$  in equation (3.66) and continue with an approach of static fields:

$$\vec{B}_{loc}(t) = \vec{B}_{loc} \quad (3.69)$$

Of major interest is now the time evolution of  $\vec{S}_{\mu^+}(t)$  in a given  $\vec{B}_{loc}$ , as it is directly related to the positron detector signal. Therefore one calculates the projection of  $\vec{S}_{\mu^+}(t)$  along  $\vec{S}_{\mu^+}(0)$ .

$$\vec{S}_{\mu^+}(t) \cdot \vec{S}_{\mu^+}(0) = \begin{pmatrix} S_\mu^\perp(0)\cos(\omega_\mu t) \\ -S_\mu^\perp(0)\sin(\omega_\mu t) \\ S_\mu^\parallel(0) \end{pmatrix} \cdot \begin{pmatrix} S_\mu^\perp \\ 0 \\ S_\mu^\parallel \end{pmatrix} \quad (3.70)$$

Subsequent normalization leads to the so-called “polarization” already mentioned in section 3.6.2:

---

<sup>20</sup> This is the case if  $\vec{B}_{loc}$  is not changing significantly on a timescale of the muon lifetime  $\tau_\mu$ .

$$P(t) = \frac{\vec{S}_\mu^\alpha(t)}{S_\mu} = [\cos^2(\theta) + \sin^2(\theta)\cos(\omega_\mu t)] = \frac{B_z^2}{B^2} + \frac{B_x^2 + B_y^2}{B^2} \cos(\omega_\mu t) \quad (3.71)$$

One now can calculate the polarization under certain given conditions. For example one can assume, that all muons are submitted to the same local magnetic field  $|\vec{B}_{loc}| = |\vec{B}_0|$ , like in the ordered phase of a single crystal ferromagnet.

For TF geometry,  $S_\mu \perp B_0$  ( $\theta = 90^\circ$ ), using equation (3.71) yields:

$$P_x(t) = \cos(\omega_\mu t) \quad (3.72)$$

One obtains an oscillating polarization function. According to equation (3.68), the oscillation frequency gives direct information on the strength of  $\vec{B}_{loc}$  that caused the depolarization.

For ZF geometry with  $S_\mu \parallel B_0$  ( $\theta = 0^\circ$ ), one obtains:

$$P_z(t) = 1 \quad (3.73)$$

As for this case  $\vec{S}_{\mu^+}$  and  $\vec{B}_{loc}$  are parallel, there is no torque resulting in a precession of  $\vec{S}_{\mu^+}$ . Therefore, the polarization function remains constant. The corresponding polarization functions are shown in figure 3.27:

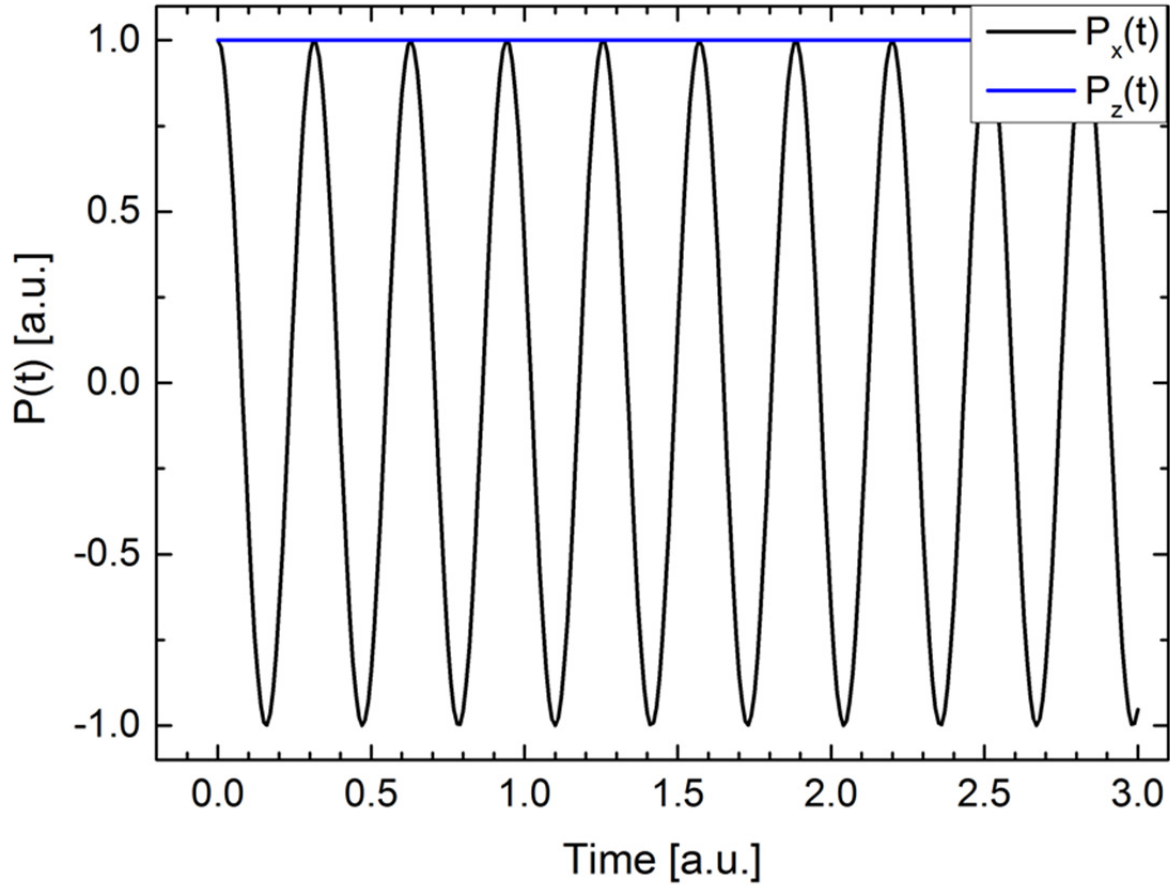


**Figure 3.27:** Oscillating TF (black,  $P_x(t)$  according to equation (3.72)) and constant ZF (blue,  $P_z(t)$  according to equation (3.73)) polarization functions found for muons exposed to the same local magnetic field  $\vec{B}_{loc}$ .

However, a more realistic scenario is an arbitrarily distribution of  $\vec{B}_{loc}$  ( $|\vec{B}_{loc}| = |\vec{B}_0|$  still valid) in space, like in a ferromagnet with ferromagnetic domains or a ferro- or anti-ferromagnetic polycrystalline sample. The field distribution for this case is given by:

$$D_V(\vec{B}_{loc}) \sim \delta(\vec{B}_{loc} - \vec{B}_0) \quad (3.74)$$

In this case the polarization function has to be calculated by integrating over all possible orientations of  $\vec{B}_{loc}$ :

$$P(t) = \frac{\int [\cos^2(\theta) + \sin^2(\theta) \cos(\omega_\mu t)] \cdot d(\cos \theta) \cdot d\varphi}{\int d(\cos \theta) \cdot d\varphi} \quad (3.75)$$

where  $\varphi$  is the azimuth angle. Performing integration of equation (3.75) yields the polarization function:

$$P(t) = \frac{1}{3} + \frac{2}{3} \cos(\gamma_\mu B_{loc} t) \quad (3.76)$$

In principle, the result is a superposition of equations (3.72) and (3.73). One finds a time-independent and an oscillating part in the polarization function. The time-independent part is related to the fact, that in average  $1/3$  of the muons have their spin aligned parallel to  $\vec{B}_{loc}$  and therefore they are not contributing to the oscillating part of the polarization function. The remaining  $2/3$  experience a torque from  $\vec{B}_{loc}$  and oscillate with the Larmor frequency  $\omega_\mu$ . The polarization function  $P(t)$  for muons submitted to a local magnetic field of  $\vec{B}_{loc} = 1000 \text{ G}$  is shown in figure 3.28.

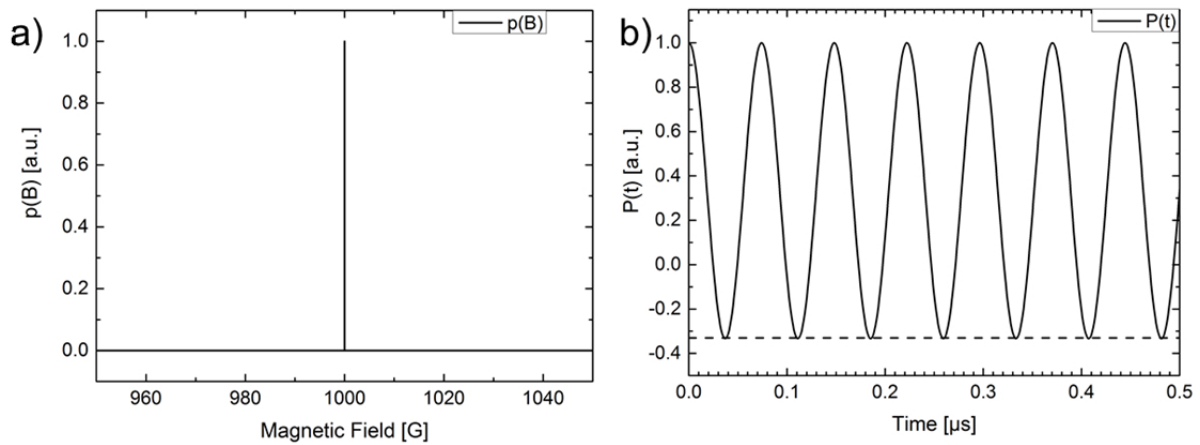


**Figure 3.28 a): A magnetic field of  $|B_{loc}| = 1000 \text{ G}$  causes a muon precession, resulting in b) the polarization function  $P(t)$ , given by equation (3.76).**

In general, if a certain distribution of local magnetic fields  $D_V(\vec{B}_{loc})$  is given, one can calculate  $P(t)$  analytical or numerical by solving the equation:



$$P(t) = \int [\cos^2(\theta) + \sin^2(\theta) \cos(\omega_\mu t)] \cdot D_V(\vec{B}_{loc}) \cdot d^3\vec{B}_{loc} \quad (3.77)$$

However, experimentally one measures  $P(t)$  and  $D_V(\vec{B}_{loc})$  can be found by e.g. a Fourier transformation of the polarization function. In the case of more a more complicated  $D_V(\vec{B}_{loc})$ , e.g. a combination of different magnetically ordered areas within the sample, it is necessary to use a fitting tool like MUSRFit from provided by the Swiss Muon Source (S $\mu$ S, see [84, 85] for details). It provides a broad set of fitting functions with different possible field distributions  $D_V(\vec{B}_{loc})$ . Examples of essential polarization functions will introduced in the following subsection.

#### 3.6.4. Important $\mu$ SR Decay Functions

The case of a completely homogeneous internal magnetic field with uniform magnitude over the whole sample as shown in figure 3.28 is usually not found in real sample systems. Especially in the case of magnetic ZnO, one expects a variety of magnetically inequivalent muon sites. Each site will then contribute to the total signal according to equation (3.76), but with different oscillation frequencies due to the inhomogeneous distribution of  $\vec{B}_{loc}$ . This situation is sketched in figure 3.29, where several curves of equation (3.76) for different (arbitrary)  $\vec{B}_{loc}$  are plotted together. On a short time scale at the beginning, the respective curves show the same behavior (falling to from 1 to a minimum) but they dephase very quickly with respect to each other. From the minimum value the respective single polarization functions recover and result in an average value of  $1/3$ , the fraction of muons that don't precess (see previous subsection).

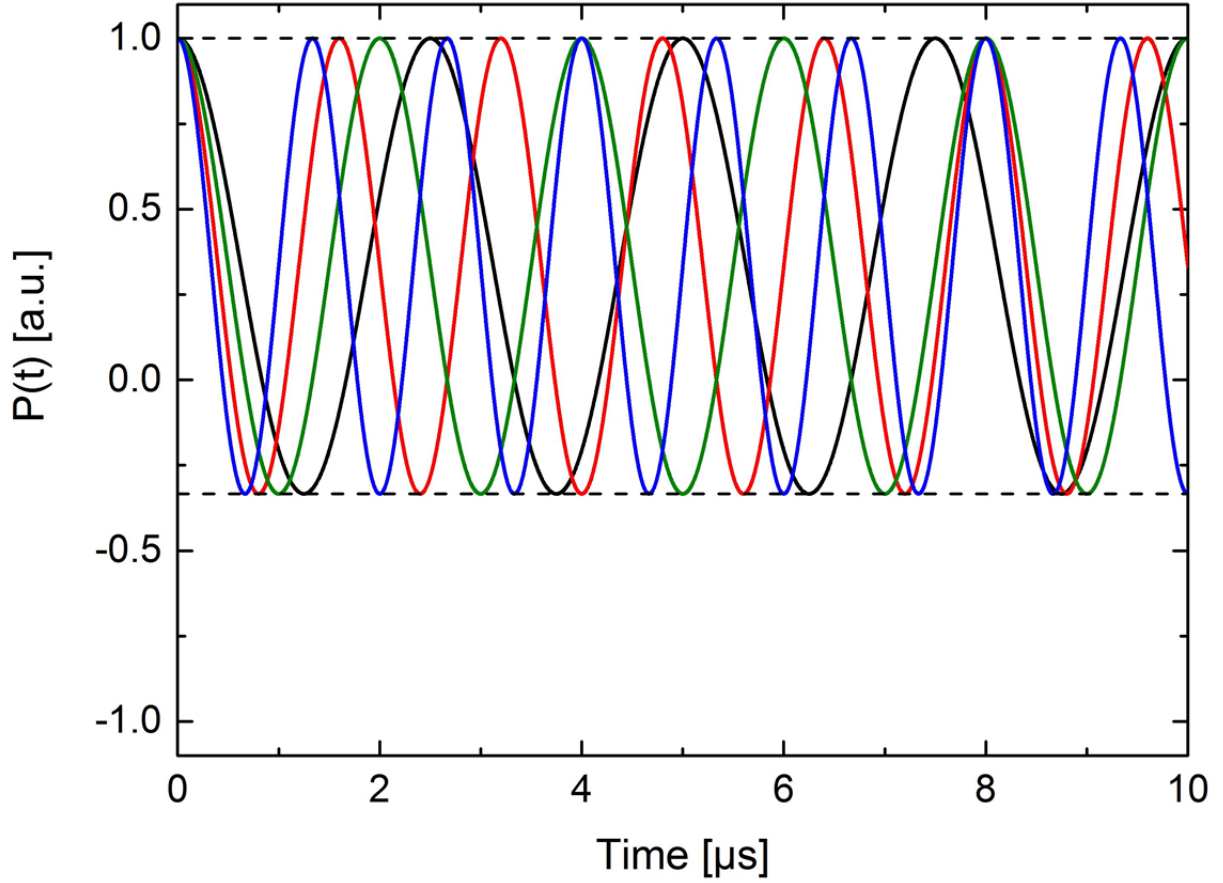


**Figure 3.29: Polarization functions according to (3.76) for different  $\vec{B}_{loc}$  as present in magnetically inhomogeneous samples.**

The actual measurement signal is then a superposition of the single muon site contributions, as indicated by the integration performed in equation (3.77). For example, the local magnetic field could follow a Gaussian distribution  $D_G(\vec{B}_{loc})$  of width  $\sigma \approx |\vec{B}_{loc}| \cdot \gamma_\mu$  (see [10, 86]):

$$D_G(\vec{B}_{loc}) = \frac{\gamma_\mu}{\sqrt{2\pi} \cdot \sigma} \cdot \exp\left(-\frac{(\gamma_\mu \vec{B}_{loc})^2}{2\sigma^2}\right) \quad (3.78)$$

Such a Gaussian distribution might be obtained from densely packed, randomly oriented magnetic moments. Inserting (3.78) into (3.77) and performing the integral yields the so-called Gaussian-Kubo-Toyabe (GKT) decay function (see [87] and [10, 13, 86]).

$$P_{GKT}(t) = \frac{1}{3} + \frac{2}{3} \cdot (1 - \sigma^2 t^2) \cdot \exp\left(-\frac{\sigma^2 t^2}{2}\right) \quad (3.79)$$

A Gaussian field distribution and the corresponding GKT polarization function are shown in figure 3.30 a) and b).

If the magnetic moments are more dispersed, the local field distribution is better described by a Lorentz curve  $D_L(\vec{B}_{loc})$ :

$$D_L(\vec{B}_{loc}) = \frac{\gamma_\mu}{\pi} \cdot \frac{a}{(a^2 + \gamma_\mu^2 \vec{B}_{loc}^2)} \quad (3.80)$$

where  $a$  is the half-width-half-maximum (HWHM) of the distribution function. Performing the integration in (3.77) with the Lorentzian field distribution given by (3.80), one obtains the Lorentz-Kubo-Toyabe (LKT) decay function [13, 86, 88]:

$$P_{LKT}(t) = \frac{1}{3} + \frac{2}{3} \cdot (1 - at) \cdot \exp(-at) \quad (3.81)$$

An example for a Lorentzian field distribution and the resulting LKT polarization function are shown in figure 3.30 c) and d).

The border between a dense (GKT decay) and disperse (LKT decay) distribution of local magnetic fields is not a sharp line. The distinction between both cases is rather arbitrary and a generalized form of the Kubo-Toyabe polarization function may be applied (see [86, 89]):

$$P(t) = \frac{1}{3} + \frac{2}{3} (1 - (\Delta t)^\alpha) \cdot \exp\left(-\frac{(\Delta t)^\alpha}{\alpha}\right) \quad (3.82)$$

where  $1 \leq \alpha \leq 2$ , resulting in the LKT function for  $\alpha = 1$  and in the GKT function for  $\alpha = 2$ .

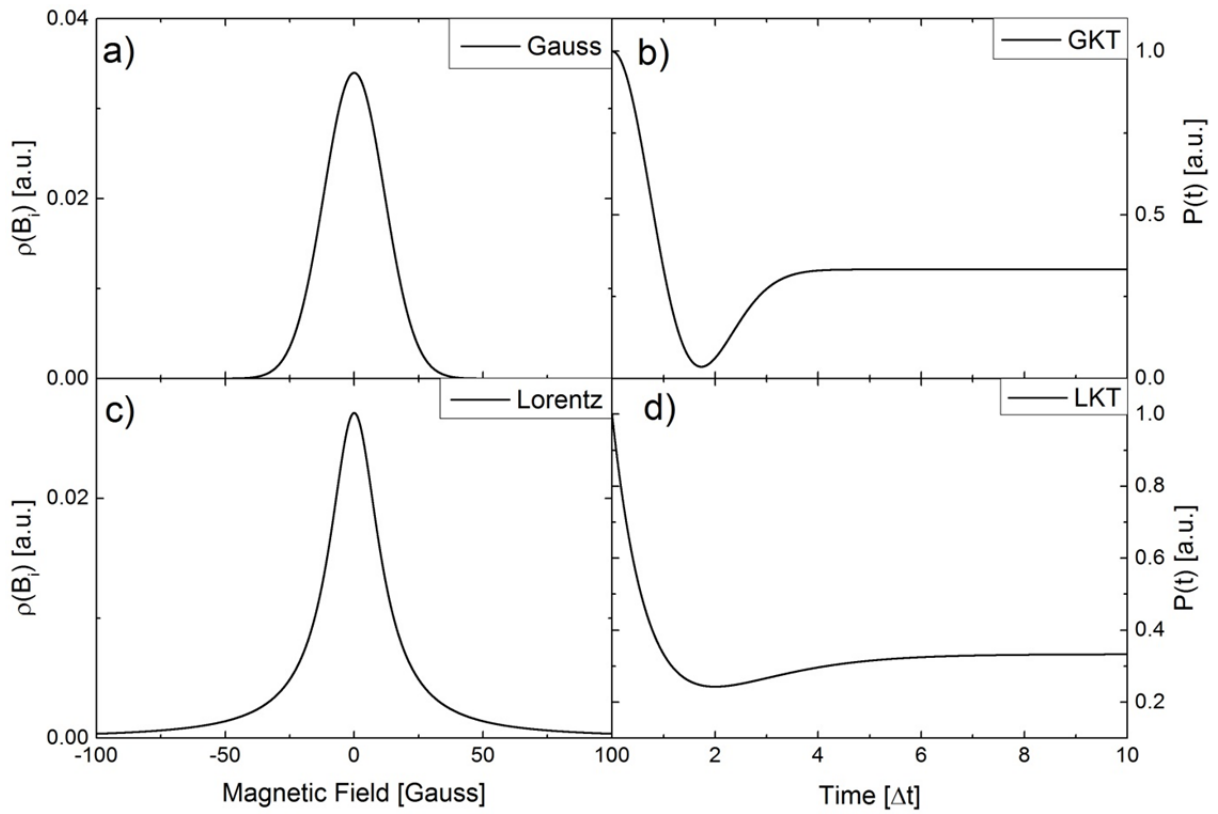


**Figure 3.30** a) Gaussian distribution of local magnetic fields around  $B=0$  with FWHM  $\sigma \approx \gamma_\mu \cdot |\vec{B}_{loc}|$ . b) The so-called Gaussian-Kubo-Toyabe (GKT) polarization functions  $P(t)$  is obtained if muons are sensing a field distribution like shown in a). c) Lorentzian distribution of local magnetic fields around  $B=0$  results in the polarization function d): The Lorentz-Kubo-Toyabe (LKT) function.

## 4. Experimental Aspects

### 4.1. Synchrotron Radiation

In order to measure XMCD on the transition metal  $L_{2,3}$ -edges, soft x-rays with an energy between 200 eV and 1200 eV are required. It is necessary that the energy of the x-ray light is tunable and exhibits a high degree of circular polarization. These requirements are only met by modern synchrotrons.

#### 4.1.1. Generation of synchrotron radiation

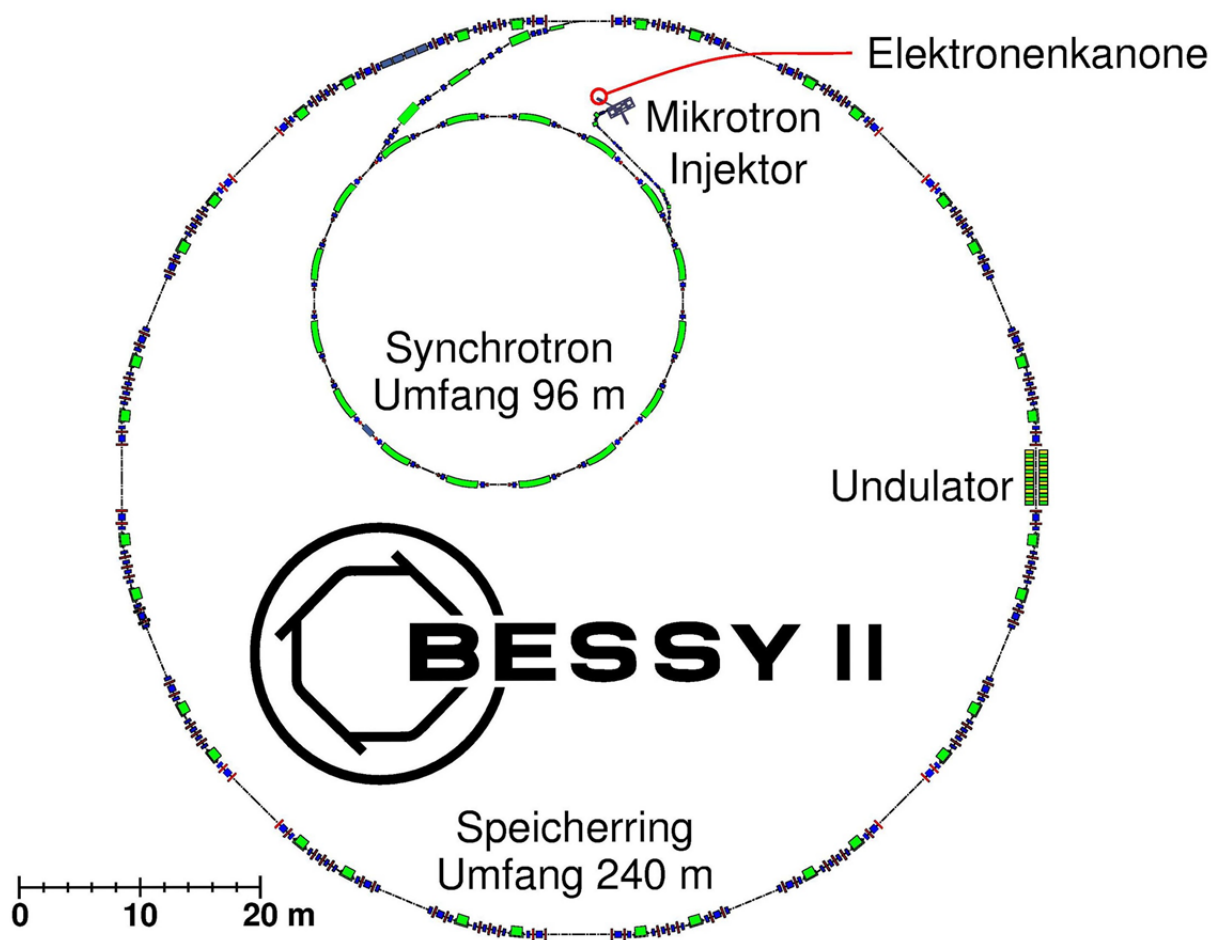


**Figure 4.1: Schematic layout of the BESSY II synchrotron in Berlin, from [90].**

A synchrotron is a circular particle accelerator in combination with a storage ring. The schematic layout is shown in figure 4.1. A hot cathode produces electrons which are accelerated by the microtron to almost the speed of light and then injected into the synchrotron. Here the electrons are again accelerated to their terminal energy, usually in the GeV range. From the synchrotron, the electrons are injected into the storage ring. At certain

positions, undulators, wigglers and bending magnets are installed. Bending magnets are necessary to keep the electrons on a circular orbit in the storage ring, whereas undulators/wigglers are installed on the straight sections in between.

As an accelerated electron emits radiation<sup>21</sup>, the bending magnet/undulator locations are the spots where synchrotron radiation is produced. If an electron moves with almost the speed of light, nearly all radiation is emitted along the trajectory of movement – tangential to its orbit in the storage ring.

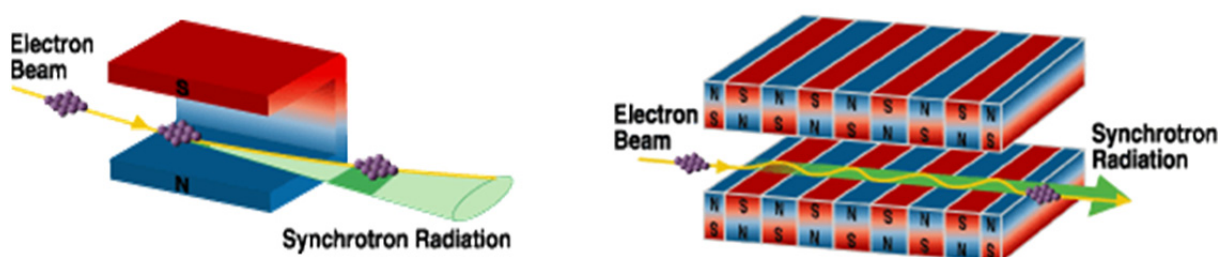


**Figure 4.2: Bending magnet (left), used to keep the electrons on a circular orbit in the storage ring, and a planar undulator (right), from [91].**

The bending magnet, shown on the left side of figure 4.2, is a dipole magnet, “bending” the electron orbit a few degrees to the center of the storage ring. This lateral acceleration leads to the production of synchrotron radiation. A typical bending magnet, e.g. of the WERA beamline, has a magnetic field of 1.5 T. Synchrotron radiation emitted at bending magnets covers a spectral range of approximately 100-1200 eV, giving access to the transition metal  $L_{2,3}$  or the oxygen K-edges for example. However, their primary task is to keep the electrons on a closed loop in the storage ring, restricting the bending magnet properties. Furthermore, their access to the hard x-ray energy range is limited, and in comparison to wigglers and undulators, radiation of a bending magnet is less brilliant.

Wigglers and undulators are, in contrary to the bending magnet, magnetic devices which were especially designed to produce synchrotron radiation with much higher brightness and to extend the energy range in comparison to bending magnets. Wigglers/undulators consist of a periodic array of magnets to deflect electrons in alternate directions. As an example, a planar undulator is shown on the right side of figure 4.2.

<sup>21</sup> An orbital movement doesn’t change the absolute but the direction of the velocity vector.

The difference between the wiggler and the undulator is given by its emitted radiation. The magnets used for wigglers are stronger than bending magnets, leading to a larger deflection of electrons from their original orbit. Thus the energy of the emitted radiation is higher for wigglers than for bending magnets. The intensity is proportional to the number of wiggler periods  $N$ :  $I \propto N$ . The spectrum of the wiggler radiation covers a broad energy range up to the hard x-ray energy range.

In undulators, the deflection of the electrons is intentionally kept narrow, so that the emitted radiation can interfere in a constructive way. The radiation emitted at every back and forth movements at the each single magnet superimpose and interfere. The radiation intensity is then proportional to the square of the undulator periods:  $I \propto N^2$ . The emitted radiation spectrum is concentrated on certain photon energies. To tune the photon energies, the undulator magnets have to be rearranged. For more detailed information on synchrotron radiation, especially the respective spectral distribution of each device, see for example [92].

The synchrotron radiation obtained from bending magnets or insertion devices is still polychromatic. In order to extract circularly polarized soft x-rays, the synchrotron beam has to pass a number of optical elements, the so-called beamline. As an example, the schematic setup of the WERA beamline at the ANKA synchrotron is given in figure 4.3. The most important components are polarization aperture in order to set the polarization, and the monochromator grating to tune the beam energy.

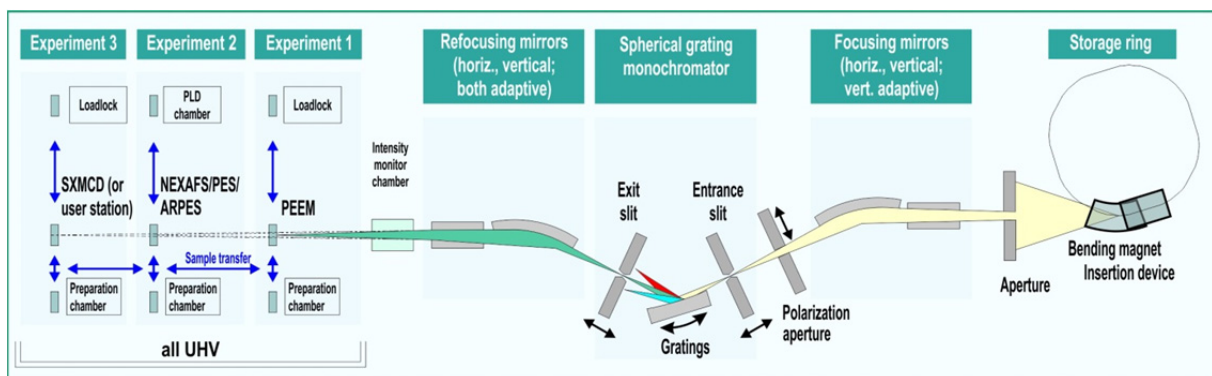


**Figure 4.3: Schematic layout of the WERA beamline at ANKA [93, 94].**

Synchrotron radiation is linearly polarized within the electron orbit/storage ring plane, with an increasing degree of circular polarization above and below, as sketched on the left side of figure 4.4. The degree of circular polarization increases with the distance from the

orbit plane. Left or right circularly polarized light can be obtained by moving the aperture above or below the orbit plane. However, the incoming beam intensity decreases quickly along the beam spot profile, as shown on the right of figure 4.4. Thus, one has to compromise between the desired high degree of circular polarization to maximize the XMCD effect, and sufficient incoming beam intensity  $I/I_0$  for reasonable signal to noise ratio of the drain current. The degree of circular polarization achieved in experiments is usually 85-95%.

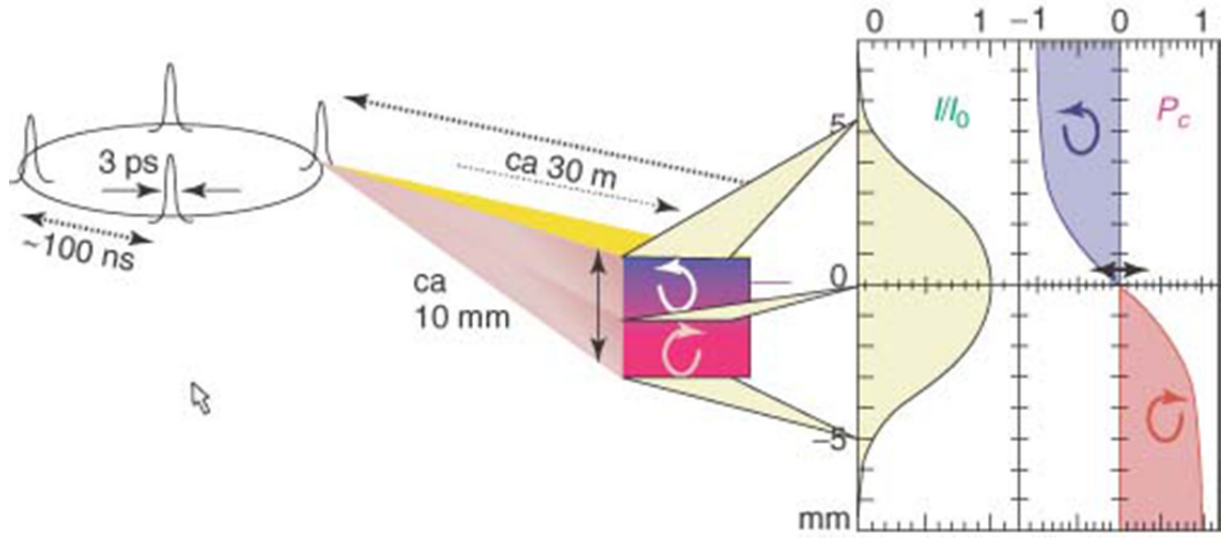


**Figure 4.4: Synchrotron radiation polarization characteristics of a bending magnet beamline [8]. Circularly polarized light is emitted above and below the electron orbit in the storage ring.**

In order to extract monochromatic soft x-rays from the synchrotron radiation, a diffraction grating is used (“gratings” in figure 4.3). The grating disperses the incoming white light according to the grating equation [3]:

$$m\lambda = g \cdot (\sin\theta_i + \sin\theta_m) \quad (4.1)$$

where  $m$  is the diffraction order,  $g$  the lattice constant of the grating,  $\theta_i$  and  $\theta_m$  are the incident and the observation angle respectively. By varying the grating position with respect to the exit slit, the beam energy can be set to a well-defined value. A detailed description of optical devices for synchrotrons and especially soft x-ray beamlines can be found in [92].

For this thesis, experiments were performed at two different beamlines at two different synchrotrons: the WERA beamline at the ANKA synchrotron in Karlsruhe and the



PM3 beamline at the BESSY II synchrotron in Berlin. Therefore, both beamlines shall be introduced briefly in the following subsections.

#### 4.1.2. WERA beamline at ANKA

The WERA<sup>22</sup> beamline is especially designed for soft x-ray experiments in the energy range of 100 to 1500 eV. The beamline is equipped with different experimental setups (see also figure 4.3):

1. A photoemission electron microscope (PEEM) with a lateral resolution of < 100 nm
2. An electron energy analyzer in order to perform photoemission (PES), angle resolved photoemission (ARPES), and resonant photoemission (resPES). The energy resolution is < 2 meV
3. A main chamber with total (TEY), partial electron yield (PEY), and total fluorescence yield (TFY) detection in order to perform near edge x-ray absorption (NEXAFS)
4. An XMCD end station equipped with a 7 T fast switching magnet system. This end station is provided by our group, Magnetic X-Ray Spectroscopy, from the Schütz department at the Max-Planck-Institute for Intelligent systems. The system is described in more details in section 4.3.

The layout of the WERA beamline is shown in figure 4.3. The synchrotron radiation is produced by a bending magnet<sup>23</sup>. The polarization (circular/linear) can be selected by a polarization aperture. The degree of polarization is typically 80-85 % without significant beam intensity loss. A spherical grating monochromator (SGM) with three different gratings is used to obtain monochromatic synchrotron light in the respective energy range. The typical energy resolution is  $\Delta E / E \sim 2 \cdot 10^{-4}$ , with a maximum  $\Delta E / E < 10^{-4}$  verified at the Nitrogen 1s edge ( $\sim 400$  eV). Entrance and exit slit are moveable in order to optimize the energy resolution for the required x-ray energy. Finally, via bendable plane elliptical refocusing mirrors the beam focus can be set to the different sequential experimental

---

<sup>22</sup> WERA is an abbreviation for „Weichröntgenanalytikanlage“, soft x-ray analytics facility.

<sup>23</sup> An undulator as alternative source is available, as soon as the required transfer optics is installed.

stations. Beamline and experimental stations are kept under ultra-high vacuum (UHV) conditions with a typical base pressure of  $10^{-10}$  mbar.

#### 4.1.3. PM3 beamline at BESSY

Like WERA, the PM3 beamline at BESSY is also designed for measurements in the soft x-ray range. The layout of the beamline is shown in figure 4.5. PM3 is also bending magnet beamline but a planar grating monochromator (PGM) is installed instead. The beam energy can be selected from 20-1900 eV with a maximum energy resolution  $\Delta E/E = 3 \cdot 10^{-3}$  at 64 eV. The polarization can be set by the toroidal mirror M1 with a degree of circular polarization of  $\sim 93\%$ . The PM3 beamline does not provide a fixed end station, so that experiments at BESSY II have been performed with the same XMCD chamber used at the WERA (ANKA) beamline.

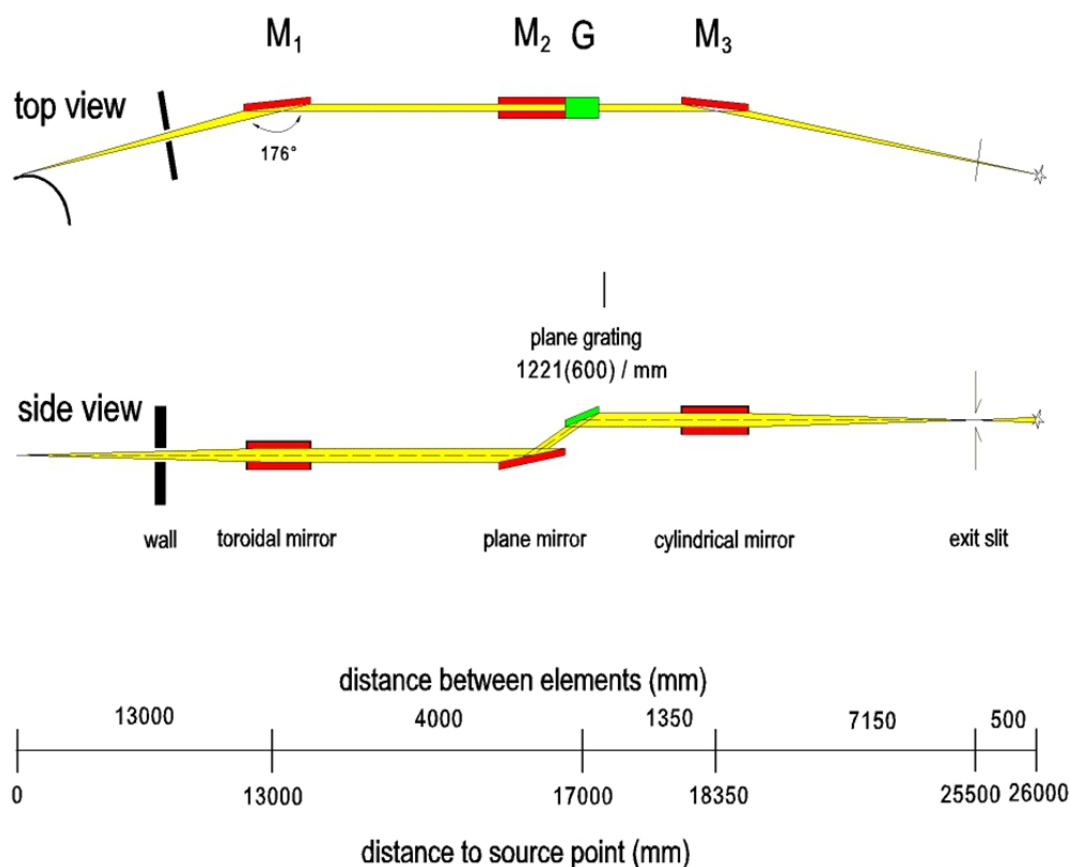


Figure 4.5: Layout of the PM3 beamline at the BESSY II synchrotron [95].

---

## 4.2. Low Energy Muons

### 4.2.1. $\mu$ E4 beamline at the S $\mu$ S

A basic description of the production of muons is already given in section 3.6.2. All muon related experiments have been performed at the Swiss Muon Source (S $\mu$ S) at the Paul-Scherer-Institute (PSI) in Villigen, Switzerland. A short introduction into the facility and the low energy muon beamline  $\mu$ E4 is given.

In order to produce muons a high energy proton beam is required. The required protons are gained from a source of hydrogen atoms. In a first step, the protons are pre-accelerated in a Cockroft-Walton-accelerator and then injected into a smaller ring cyclotron. There, protons are accelerated to energy of 72 MeV, corresponding to 37 % speed of light and injected into the main ring cyclotron, shown in figure 4.6. In the main cyclotron, the protons are accelerated again, this time to energy of 590 MeV ( $\sim 80\%$  speed of light). The resulting proton beam current is 2200  $\mu$ A, according to [96] this sets a world record for machines of this type. A part of the proton beam<sup>24</sup> is then directed to a carbon target where pions are produced. Finally, the corresponding muons are directed by a set of magnets to the respective experimental stations.

---

<sup>24</sup> The proton accelerator also supplies the neutron source SINQ, where protons hit a lead target and the subsequent decay of the excited lead core produces neutrons.

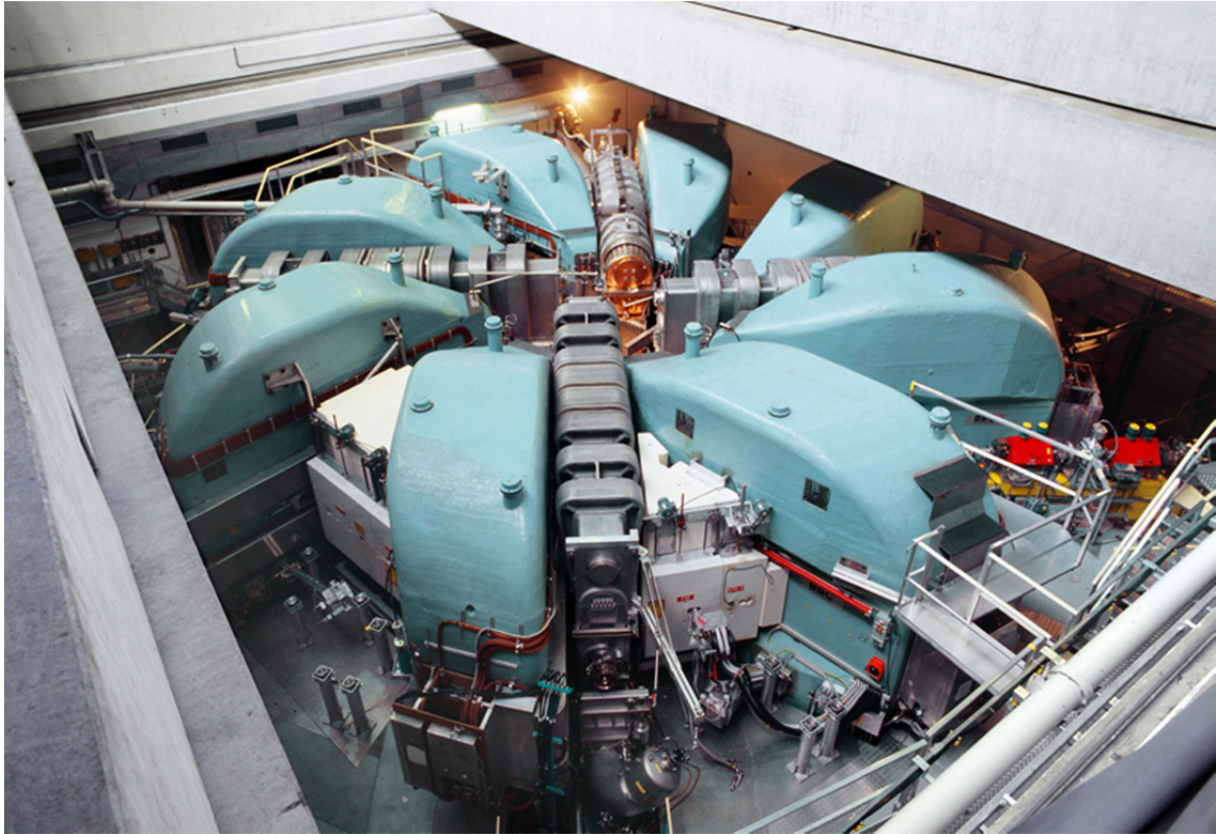


**Figure 4.6:** The main ring cyclotron at the Paul-Scherer-Institute. The ring cyclotron is equipped with eight magnets (cyan) and four cavities in order to accelerate the protons to 590 MeV, corresponding to 80 % of the speed of light. The total circumference of the cyclotron is 47 m [96].

The  $\text{SpS}$  also provides low energy muons especially for the study of thin film and layered samples. The implantation depth can be varied in order to probe depth dependent effects. This technique is unique among the muon facilities worldwide.

The  $\mu\text{SR}$ -experiments for this thesis have been performed at the  $\mu\text{E4}$  low energy muon (LEMU) beamline. The layout of the beamline is shown in figure 4.7.

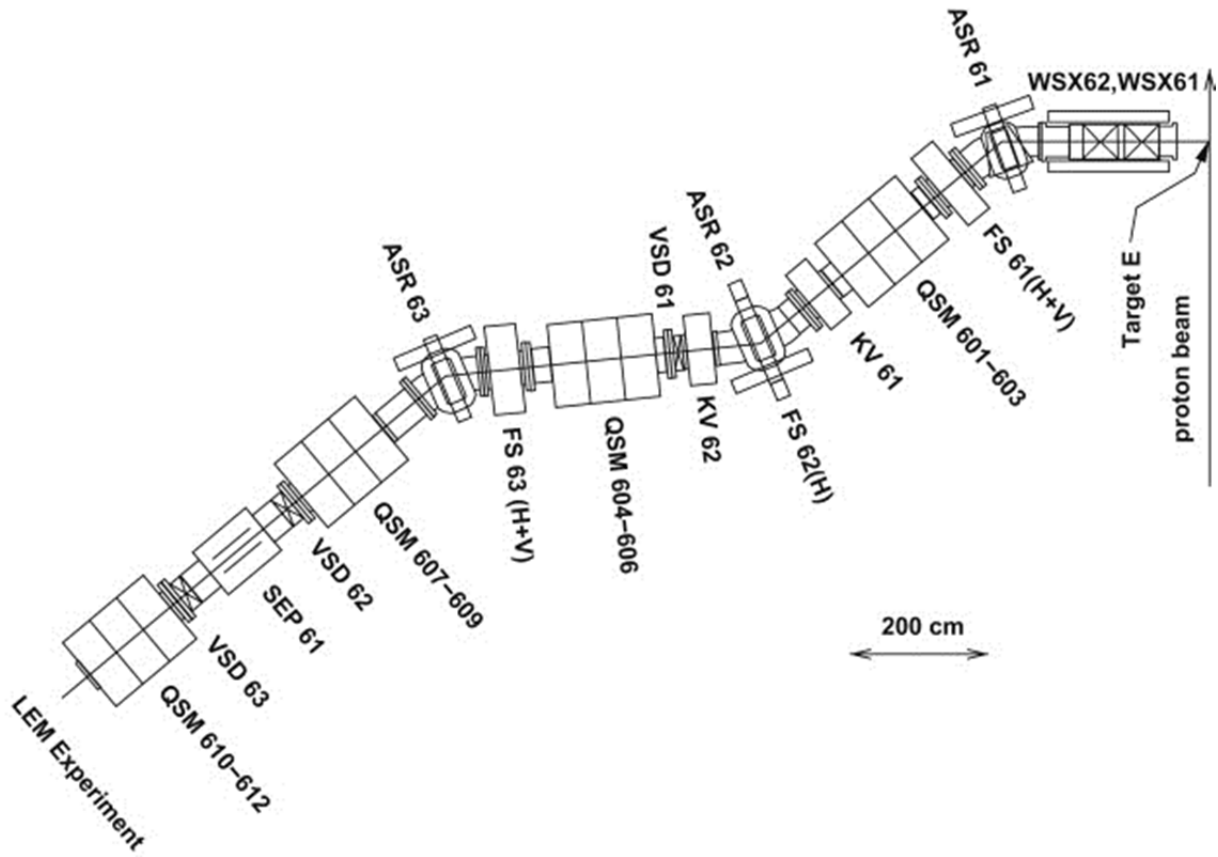


**Figure 4.7:** Layout of the  $\mu$ E4 low energy muon beamline at the SpS. A set of solenoids, bending, and quadrupole magnets is necessary to provide a high flux of low energy muons. Reprinted with permission from [97] with permission from Elsevier.

WSX61, 62 are two identically constructed normal conducting solenoids. The solenoids are operated on magnetic field of 0.34 T and  $\sim 0.17$  T respectively in order to provide maximum acceptance of the beamline. ASR 61-63 and QSM 601-612 are conventional dipole and quadrupole magnets; they direct the beam to the experimental chamber and can be used to deflect the beam in vertical direction if necessary. SEP 61 is a static  $\vec{E} \times \vec{B}$  filter, separating  $e^+$  contaminations from the  $\mu^+$  beam. Behind SEP 61, the beam contamination  $e^+/\mu^+$  is lower than 1%, [97].

Depending on the solenoid conditions, the primary  $\mu^+$  beam has energy of  $\sim 4$  MeV. In order to slow the muons down to low energy of several keV, they are passed through a moderator. The schematic setup of the moderator used at the  $\mu$ E4 beamline is shown in figure 4.8.

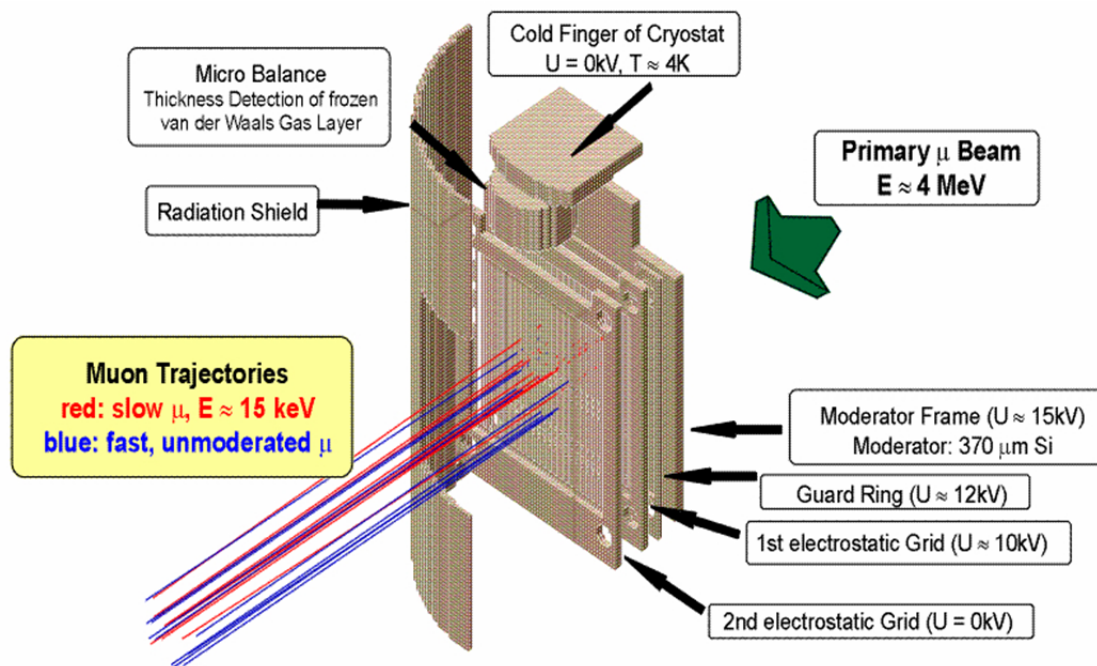


**Figure 4.8: Moderation of muons in the  $\mu\text{E4}$  beamline, [98].**

The moderator itself consists of a few hundred nm thick frozen van-der-Waals bond Argon gas layer deposited on a cold  $370\text{ }\mu\text{m}$  thin Silicon substrate. The incoming beam passes the substrate where the muons are degraded by ionization process. The resulting energy range is a few hundred eV. In the solid gas layer, the muons are further decelerated, mainly by charge-exchange processes. Below a certain energy ( $\sim 50\text{ eV}$ ), inelastic energy loss in the gas layer is strongly suppressed and no other energy loss process is present. Thus, once the muons reached certain energy, they can pass the gas layer with no further energy loss. Owing to the small thickness of the gas layer, the moderation probability is of the order of  $10^{-5}$  and  $10^{-4}$ . The main fraction of muons leave the moderator unmoderated with energy of  $500\text{ keV}$ . The slow muons are extracted from the moderator via the guard ring and the electrostatic grids shown in figure 4.8. They are finally accelerated to  $20\text{ keV}$ .

In the next step, the slow muons have to be separated from the fast ones. This is done by a  $90^\circ$  deflection of the slow muons on an electrostatic mirror. Muons with energy higher than some tens of keV are hardly affected by the electric field of the mirror and just pass through. After the low energy muons are separated, they are focused on the sample position by “Einzel-lenses”. The sample holder system can be set on high voltage, so that in principle the muons can be accelerated to any desired muon energy between 0 and  $30\text{ keV}$ .

### 4.3. 7 Tesla fast switching XMCD setup

All XMCD spectra presented in this thesis have been measured with our own self-designed UHV XMCD chamber. As an important technical part of this thesis a previous XMCD setup, originally equipped with a 2 T magnet system, has been upgraded with a unique superconducting and fast switching 7 T magnet system. Furthermore, for the in-situ preparation of graphene and Ni cluster deposition a sample preparation unit equipped with a flashing station for SC cleaning and a cooling stage for cluster deposition at low temperature has been developed and implemented into the XMCD setup.

The chamber consists of four different sections and the centerpiece, a newly developed and now commercially available “cryogen-free<sup>25</sup>” fast switching 7 Tesla magnet system from Cryogenic Ltd. (London, UK), installed and first used within the framework of this thesis. A sketch of the setup is shown in figure 4.9. The setup consists of four different main system sections:

1.  $I_0$  section, cyan colored on the left hand side from point of view. This section comes along with a gold mesh in order to probe the incoming beam intensity and a mirror prism for sample/beam adjustment purposes. For experiments at BESSY this option was indispensable, whereas for measurements at ANKA a beamline side  $I_0$  gold mesh was used instead, with the  $I_0$ -section gold mesh removed. The base pressure of this section is usually  $3 \cdot 10^{-10}$  mbar.
2. Fast load lock section, yellow colored on the front right from point of view. This section provides an UHV sample transfer system with a sample magazine with six slots. Samples can easily and quickly be transferred from and to the manipulator and preparation section. A complete transfer including removal of the old sample, mount, and adjustment of the new sample needs no longer then 30-45 minutes. All steps can be performed without breaking the vacuum of the main manipulator section. Changing the complete set of samples in the sample magazine requires about six hours until the UHV conditions required for sample transfer (usually below  $5 \cdot 10^{-9}$  mbar) have recovered. The sample

---

<sup>25</sup> Meaning no liquid gas like LHe is necessary to cool the magnet coil to superconducting state. This is a major advantage because it saves costs for the liquid gas and time it takes to refill a cryostat.

magazine stage of the load lock section is also equipped with a new non-evaporable getter pump (NEG). The NEG contains a framework of Zr-V-Fe, where most active gases are adsorbed to. It works without an external power source (except for the process to refresh the active surface), so the magazine stage can now be used to transport sensitive samples under UHV conditions over long distances, e.g. from external laboratories to the synchrotron or vice versa.

3. Main manipulator section, colored dark red in the mid right. Here the sample is mounted for measurements. The manipulator contains a cryostat for liquid N<sub>2</sub> and liquid He cooling, as well as a sample heater. The temperature can therefore be set continuous to any temperature between 10 and 350 K. The manipulator is equipped with three different measurement modes: total electron yield (TEY), total fluorescence yield (TFY), and a transmission photo diode. The sample can be rotated both azimuthal (0 to 360°) and polar (0 to 90° in principle). For experiments the polar angle is set to a maximum of 75° in because the effective sample area<sup>26</sup> becomes too small and sample adjustment becomes extremely difficult. The base pressure of the main manipulator section is usually  $3 \cdot 10^{-10}$  mbar.
4. Preparation section, colored dark blue in the rear right (shown without preparation manipulator and LEED). In this section, the Ni nano cluster on a graphene Moiré have been prepared *in-situ* and subsequently transferred to the main manipulator section. The preparation section is equipped with a new high power electron bombardment heating as well as a separate cold gas cooling stage. With the heating stage, samples can be flash annealed to temperatures up to 1700 K, the cooling stage can reach temperatures of ~ 190 K. Furthermore, a sputter gun for cleaning sample surfaces with Ar<sup>+</sup> ion bombardment and LEED in order to check sample surface quality is available. The base pressure in this section can reach  $< 1 \cdot 10^{-10}$  mbar.

---

<sup>26</sup> Projection of the sample are to the incoming beam direction.



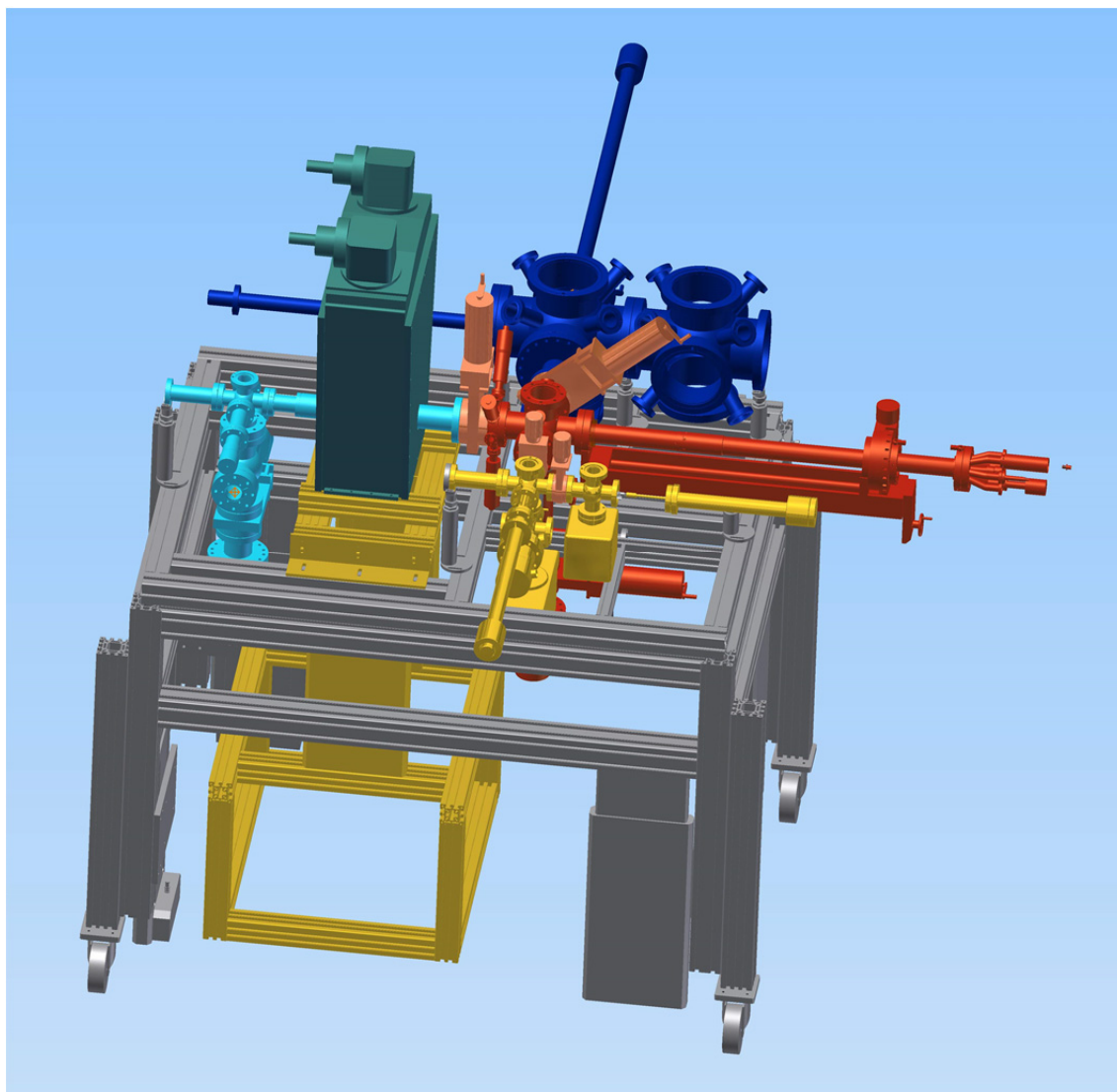


**Figure 4.9: 7 Tesla fast switching XMCD setup, designed, developed and constructed at the Schütz department, Max-Planck-Institute for Intelligent Systems.**

The centerpiece of the XMCD setup however is the new superconducting fast switching 7 Tesla magnet. It comes along with some outstanding properties. Driven by a power supply from Controlled Power Inc. (Troy, Michigan, USA) the maximum ramp rate is 1.5 T/s (!) which can be maintained to fields up to 5 T. Thus, reversing 5 T takes only 7 s. For a reversal of the maximum field of 7 T, the maximum ramp rate is 0.7 T/s, a complete reversal then takes 20 s. The magnet system is cooled to the superconducting state by two cryocoolers from Sumitomo Heavy Industries (Tokyo, Japan). The cooling mechanism is driven by compressing and expanding 6.0 He gas in a closed cycle system instead of a liquid He bath cryostat cooling system as common in other superconducting magnet systems. The omission of liquid He refill is a third big advantage of our XMCD setup as the liquid He refill is

time consuming (usually to be performed once a day, with no measurements during the refilling procedure) and quite expensive (3-4 €/L, makes up to 500 € for one standard 120 L Dewar).

In summary the new 7 Tesla fast switching magnet systems provides three main advantages over the previous 2 T magnet systems:

1. High magnetic fields of up to 7 T. Sample systems that couldn't be fully magnetically characterized with the previous system, like superparamagnetic nanoparticles or rare earth permanent magnets and other hard magnetic systems are now accessible for soft x-ray XMCD spectroscopy.
2. Fast ramp rates of up to 1.5 T/s. The magnetization reversal necessary for XMCD measurements can thus be performed quickly. This improves the quality of the measured spectra as effects occurring on a long term time scale like drift of the synchrotron beam or slight fluctuations of the sample temperature during the field switching are negligible.
3. Cryo free cooling of the superconducting 7 T magnet. It saves both time for the refill and costs for the use of liquid He.

## 4.4. XMCD data acquisition and evaluation

### 4.4.1. XMCD measurement principles

The basic principle of an XMCD measurement was already illustrated in chapter 3.2. As the XMCD effect only depends on the relative orientation of the polarization of the incoming synchrotron beam and the magnetization, the measurement procedure is optimized to the technical situation at the synchrotron. Instead of switching the helicity, one usually reverses the magnetization of the sample in order to obtain the absorption spectra with parallel and antiparallel alignment of polarization and magnetization. The main advantage of this procedure is to avoid the slight energy shift that can occur when switching helicity on the PM3 and the WERA beamline (see chapter 4.1). A slight energy shift of two absorption spectra will lead to a so-called “first derivate” structure in their difference spectrum, which sometimes can be misinterpreted as XMCD effect (especially in systems with multiplett structures). Another reason is of course the availability of the 7 T magnet system (see chapter 4.3), that allows a fast reversal of the sample magnetization, quicker than switching the helicity.

There are two ways to measure one complete dataset for an XMCD spectrum with flipping the sample magnetization. In previous works of our group, XMCD was measured by flipping the magnetic field at each energy data point [73, 99-102]. This method reduced noise caused by beam drift effects strongly. However, the disadvantage of this method is the time needed to take one spectrum, even applying a fast switching magnet system. Depending on the sample quality, it can take 2-3 hours. Compared to the spectrum quality this time consumption was acceptable for sample systems that did not require *in-situ* treatment. However, for this thesis a time consuming *in-situ* sample preparation procedure had to be performed, so the measurement mode was changed to the so-called “fast continuous mode”. Instead of flipping the magnetic field at each energy data point, the magnetization was reversed after each complete XAS spectrum. The energy was altered uniformly with a rate of 0.2 eV/s (in the following referred to as “(monochromator) speed”) while simultaneously reading out the TEY and  $I_0$  current.

#### 4.4.2. Fast continuous mode

An important issue for data acquisition was to find an appropriate compromise between the maximum speed possible and the loss of resolution of fine structured absorption spectra. For measuring TEY and  $I_0$  currents, commercial Keithley 6517A multimeters with a time constant of about 1 second were used. Above a certain monochromator speed, only discharge of input capacitance is measured and spectral structure can't be resolved anymore.

Therefore, the monochromator speed was optimized with NiO (for measurements at ANKA) and CoO (for measurements at BESSY) reference systems, measuring the respective transition metal  $L_3$  absorption edge.

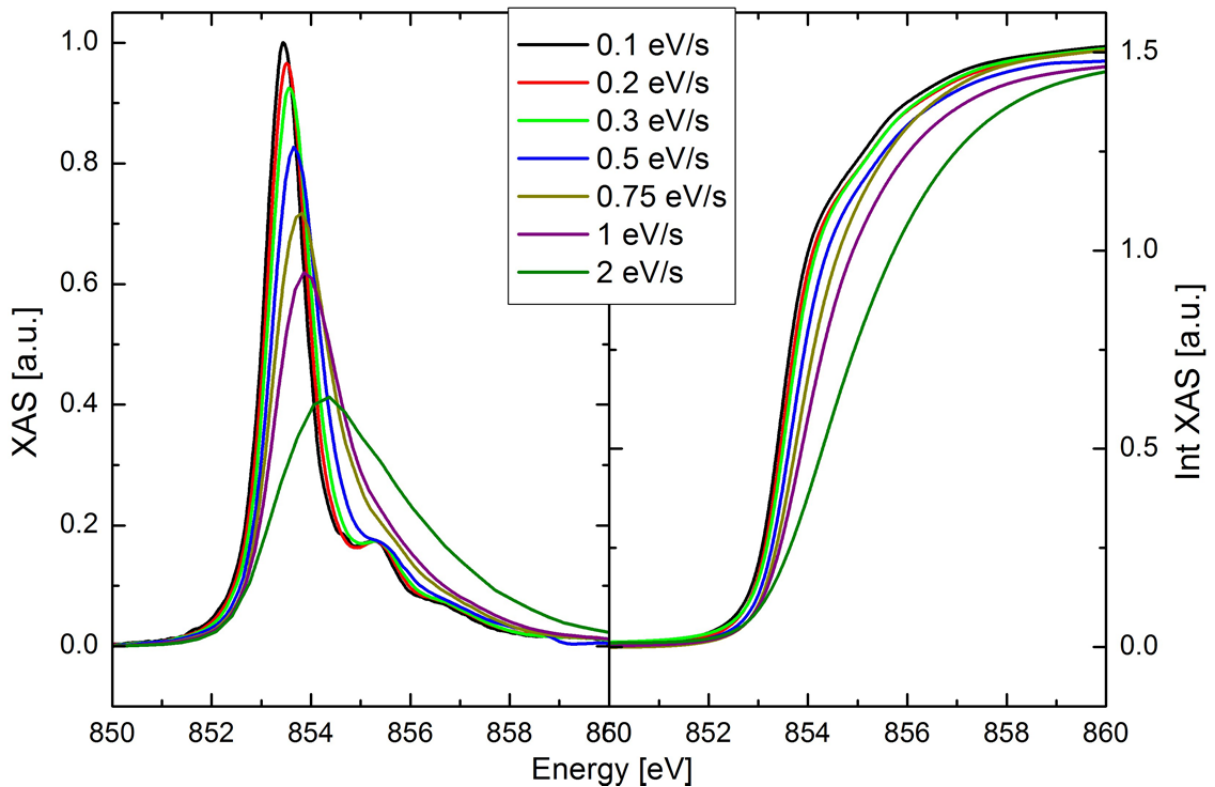


**Figure 4.10: Peak normalized XAS spectra, and their respective integrals, on the Ni  $L_3$ -edge, taken of a NiO single crystal at different monochromator speeds.**

The calibration for the WERA beamline was performed measuring the Ni  $L_3$ -edge of a NiO single crystal at different monochromator speeds varying from 0.1 eV/s to 2 eV/s. The result is shown in the left of figure 4.10. With increasing monochromator speed, the  $L_3$  peak position is shifted slightly to a higher energy and the FWHM is increasing, while the

maximum peak intensity is decreasing, see also table 4.1. A probe for the spectrum quality is the NiO satellite feature next to the Ni  $L_3$ -edge, at the energy of  $\sim 855$  eV. While the satellite is clearly resolved at 0.1 eV/s and 0.2 eV/s, it already starts smearing out at 0.3 eV/s and disappears at 0.75 eV/s and above due to the fast increase of the FWHM.

Another important key figure is the integrated intensity because it is used to determine the magnetic spin and orbital moment, as described in chapter 3.2. The XAS integral value over the Ni  $L_3$ -edge peak in dependence of the monochromator speed is shown on the right side of figure 4.10. It is constant for monochromator speed between 0.1 eV/s and 0.3 eV/s, though the tail is slightly different due to the change in the FWHM (see also table 4.1). For higher monochromator speed, the integrated XAS value drops slightly within the peak energy range.

**Table 4.1: Comparison of energy shift  $\Delta E$ , peak maximum decrease  $\Delta I$ , FWHM, and  $L_3$ -edge XAS integral for different monochromator speeds.**

Monochromator speed [eV/s]	$\Delta E$ [eV]	$\Delta I$ [a.u.]	FWHM [eV]	Integrated XAS [a.u.]
0.1	0	0	1.26	1.511
0.2	0.08	3.5 %	1.24	1.505
0.3	0.13	7.4 %	1.31	1.508
0.5	0.25	17 %	1.49	1.4
0.75	0.36	28.5 %	1.94	1.477
1	0.46	38.4 %	2.05	1.464
2	0.92	58 %	3.92	1.451

#### 4.4.3. Offset correction of XMCD spectra measured with TEY

A major problem that occurs when acquiring XMCD spectra in the TEY mode is the so-called “offset”. In particular, offset is reflected as a constant shift of the XMCD on the y-axis. Usually, the XMCD effect disappears in the off-edge regions and is 0.

The origin of an offset signal is usually a different trajectory of electrons in magnetic fields pointing in  $+\vec{B}$  or  $-\vec{B}$  direction, as the Lorentz force inverts its sign for opposite fields. The photoelectrons move on a spiral orbit and some of them may be refracted back to the

sample surface, reducing the TEY current. The electron orbit is not necessarily the same for opposite applied magnetic field, thus the TEY signal becomes not only energy but also field dependent.

As for the results in thesis mainly a field of 7 T was applied, almost all XMCD spectra exhibited offset. A comparison of an XMCD spectrum with offset and offset corrected is shown in figure 4.11. The aboriginal XMCD signal is slightly shifted downwards on the y-axis.

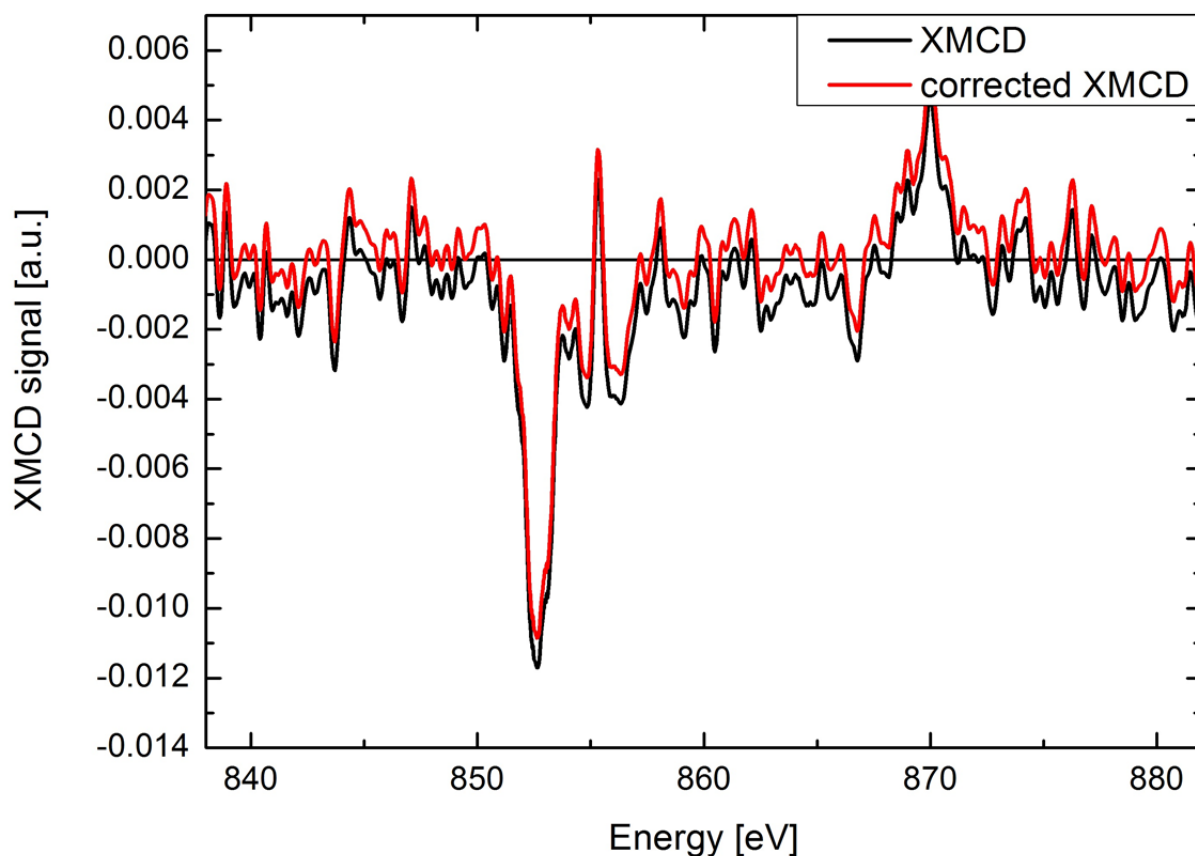


**Figure 4.11: Comparison of an XMCD spectrum with offset and after offset correction.**

Offset correction is crucial for XMCD data analysis. In order to apply sum rules it is necessary to integrate the corresponding XAS and XMCD signals. If the XMCD spectrum is slightly shifted on the y-axis this will result in an additional slope in the integrated XMCD signal. A comparison of the integrals of the XMCD spectra in figure 4.11 is shown in figure 4.12. Whereas the integral of the corrected signal (black line) is constant aside the Ni  $L_{2,3}$ -edge, the non-corrected signal (red line) is sloping in addition to the primary signal.

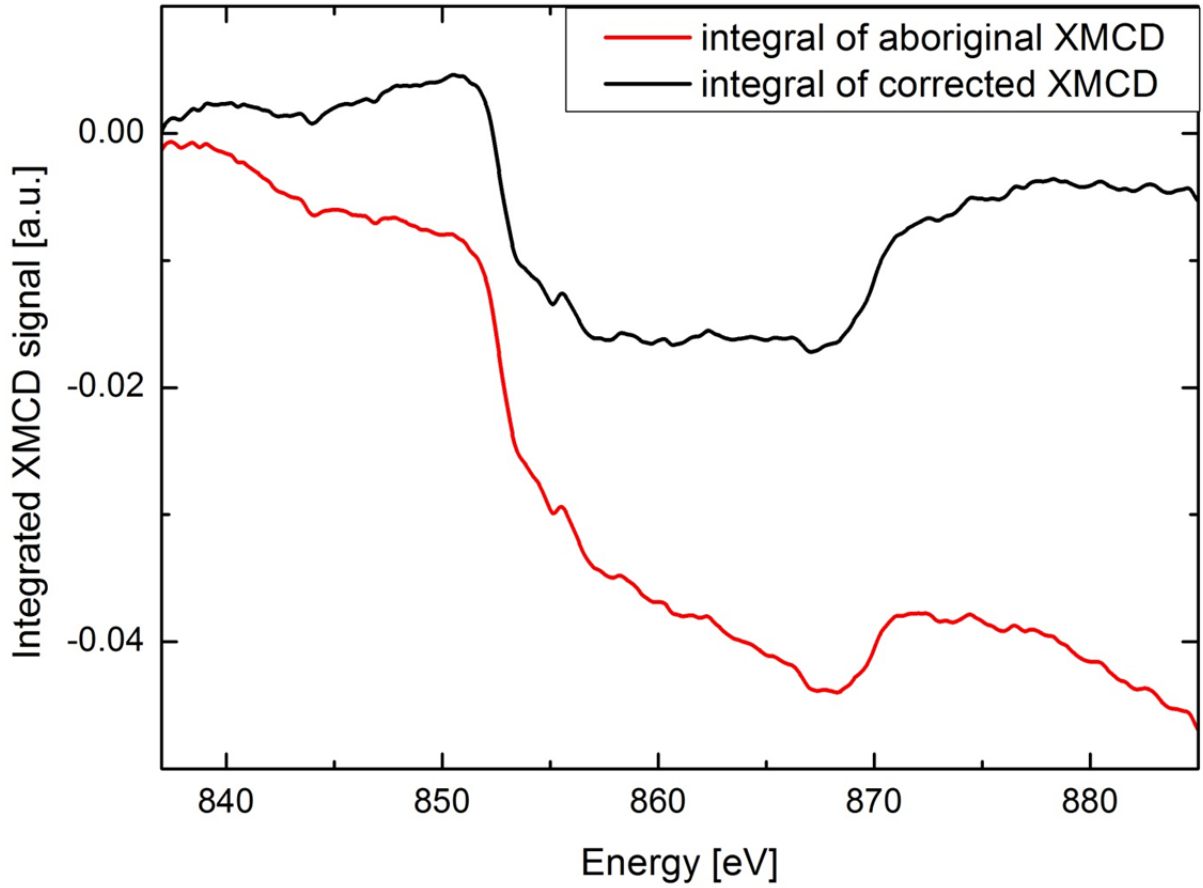


**Figure 4.12: Comparison of the integrals of offset corrected (black) and non-corrected (red) XMCD signal.**

The offset correction cannot be performed by just subtracting the shift in y-direction. This will lead to a falsified XMCD signal and hence to falsified values for the magnetic moments if sum rules are applied, as can be seen on the discussion in [103]. A proper correction of the XMCD signal has to be performed in the following way.

The measured XMCD signal is usually given by (see also section 3.2):

$$I_{XMCD}(E, \vec{B}) = I_{\uparrow\uparrow}(E) \cdot k_{\uparrow\uparrow}(\vec{B}) - I_{\uparrow\downarrow}(E) \cdot k_{\uparrow\downarrow}(\vec{B}) \quad (4.2)$$

$I_{\uparrow\uparrow}(E)$  and  $I_{\uparrow\downarrow}(E)$  is the respective,  $I_0$ -normalized TEY current for parallel and antiparallel alignment of magnetization and polarization.  $k_{\uparrow\uparrow}(\vec{B})$  and  $k_{\uparrow\downarrow}(\vec{B})$  are constants depending on the applied magnetic field. They display the proportionality of the TEY signal and the absorption signal. On the other hand, the sole absorption spectrum is given by:

$$I_{XAS}(E) = \frac{I_{\uparrow\uparrow}(E) + I_{\uparrow\downarrow}(E)}{2} \quad (4.3)$$

If one additionally defines the “true” XMCD signal as

$$XMCD = I_{\uparrow\uparrow}(E) - I_{\uparrow\downarrow}(E) \quad (4.4)$$

Using equations (4.3) and (4.4), one can isolate  $I_{\uparrow\uparrow}(E)$  and  $I_{\uparrow\downarrow}(E)$ :

$$I_{\uparrow\uparrow}(E) = I_{XAS}(E) + \frac{XMCD}{2} \quad (4.5)$$

$$I_{\uparrow\downarrow}(E) = I_{XAS}(E) - \frac{XMCD}{2} \quad (4.6)$$

Substituting  $I_{\uparrow\uparrow}(E)$  and  $I_{\uparrow\downarrow}(E)$  in equation (4.2) by the expressions (4.5) and (4.6) yields:

$$I_{XMCD}(E, \vec{B}) = I_{XAS}(E) \cdot (k_{\uparrow\uparrow}(\vec{B}) - k_{\uparrow\downarrow}(\vec{B})) + XMCD \cdot \left( \frac{k_{\uparrow\uparrow}(\vec{B}) + k_{\uparrow\downarrow}(\vec{B})}{2} \right) \quad (4.7)$$

If the field dependent parameters  $k_{\uparrow\uparrow}(\vec{B})$  and  $k_{\uparrow\downarrow}(\vec{B})$  are equal, there will be no offset observed in the measured XMCD signal. If they are different, a fraction of the absorption signal  $I_{XAS}(E)$  will be added to the measured XMCD signal, as can be seen from the first term in equation (4.7). Thus, a correction of the XMCD signal has to be like:

$$XMCD = I_{XMCD} + c \cdot I_{XAS} \quad (4.8)$$

Where  $XMCD$  again means the true XMCD signal as defined in equation (4.4). The parameter  $c$  is chosen in a way that the XMCD signal disappears off-edge:  $XMCD = 0$ . The corresponding absorption signal  $I_{XAS}$  must be  $I_0$ -normalized only. If the signal is very noisy as in figure 4.11, the accuracy of the correction can also be controlled via the integrated XMCD signal. As indicated in figure 4.12, the pre-edge region integral value must be zero, in the post-edge region; it has to converge towards a constant value.

#### 4.4.4. Background references

A major problem in the XMCD data evaluation of a sub-monolayer coverage of transition on noble metal surfaces is the background signal as a consequence of noble metal



absorption lines and their EXAFS features, see references [43, 104-121] where XAS and XMCD spectra of transition metal nano clusters are given on different supports/substrates.

For the Ni/Gr/Ir system, there are the  $N_1$  to  $N_5$  absorption lines of the Ir (111) within the energy range of interest for this thesis (300 - 1200 eV). An  $I_0$ -normalized large scale overview scan of 0.1 ML nominally deposited Ni on Gr/Ir (111) is shown in figure 4.13 and gives an idea about the tininess of the signals to be measured. The Ni  $L_{2,3}$ -edge region is dominated by a Gaussian like background feature, unfortunately peaking right between the Ni  $L_3$  and the  $L_2$ -edge. The relative “peak” jump (ratio between the pre- and on-edge value) of this background feature is only about 1.05. For the Ni  $L_{2,3}$  edge, zoomed and highlighted red in the inset of figure 4.13, the peak jump ratio is even smaller, only 1.03. For comparison, for XAS/XMCD measurements in a 5 % Co doped ZnO DMS system, the peak jump factor from an  $I_0$  normalized spectrum is  $\sim 1.7$  (see [122], and also [71, 73]).

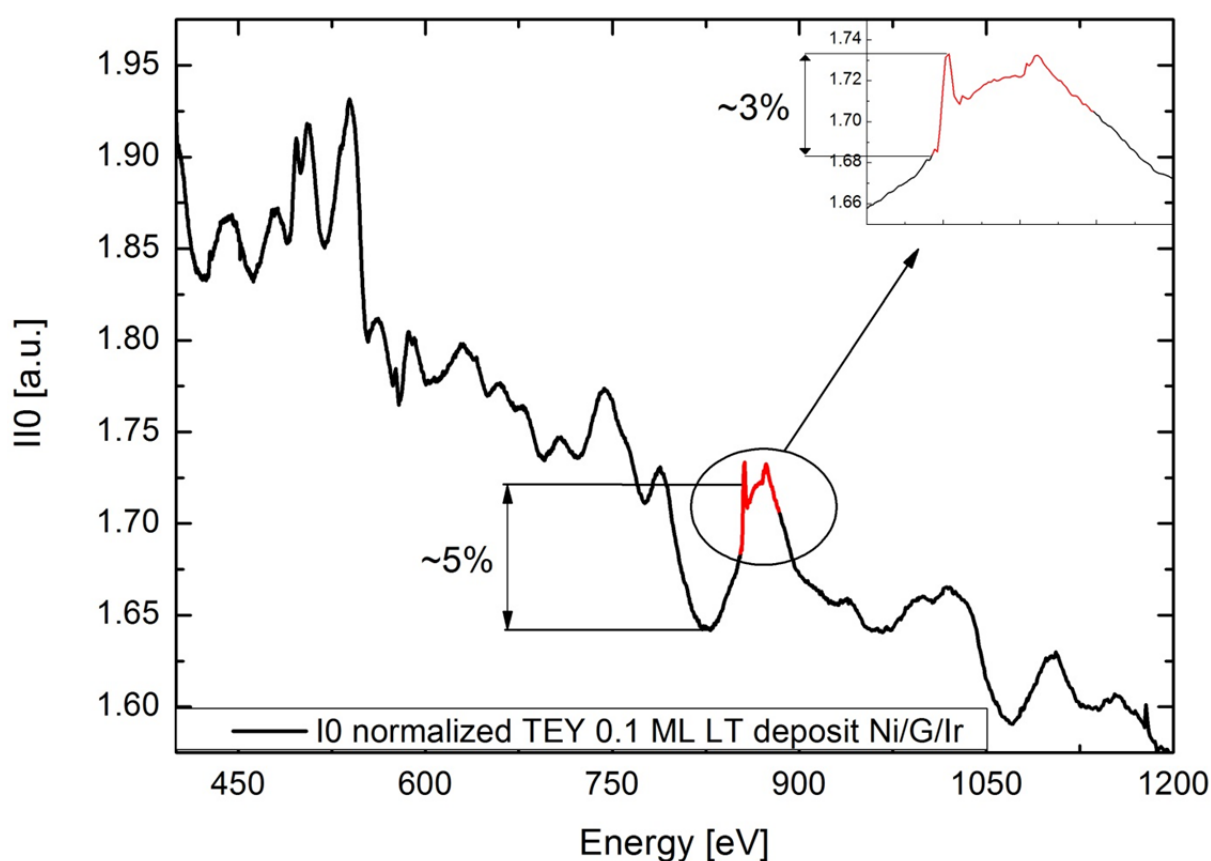


**Figure 4.13:** Overview scan of 0.1 ML nominally deposited Ni/G/Ir (111), measured at  $\sim 10$  K without applied magnetic field. The inset shows a zoom into the Ni  $L_{2,3}$  edge region of interest.

In order to apply sum rules, the XAS spectrum has to be free of any kind of background [28], otherwise the denominator in formula x.x will be overrated and the values for spin and orbital momentum will be underestimated. The background feature superimposing the Ni  $L_{2,3}$  edge displays a major problem for proper data analysis. In order to deal with the background properly, reference spectra were taken from either the thoroughly cleaned Ir(111) or the Gr/Ir(111) system. In both cases, there is no significant difference in the background shape as the TEY signal is not damped significantly by graphene layer atop.

The background reference spectra were measured under the same experimental conditions as the XMCD spectra, except for the applied magnetic field, which was set to  $B = 0T$ . Reference spectra were taken at each beam time at a temperature of  $\sim 10$  K, for both positive and negative helicity and in normal incidence and  $65^\circ$  with respect to the incoming beam intensity.

An overview of the  $I_0$ -normalized reference spectra used for background subtraction is shown in figure 4.14. For the reasons of simplicity and clarity, the references have been additionally normalized to the background minimum at  $\sim 830$  eV and only spectra measured with positive helicity and under normal incidence geometry are shown.

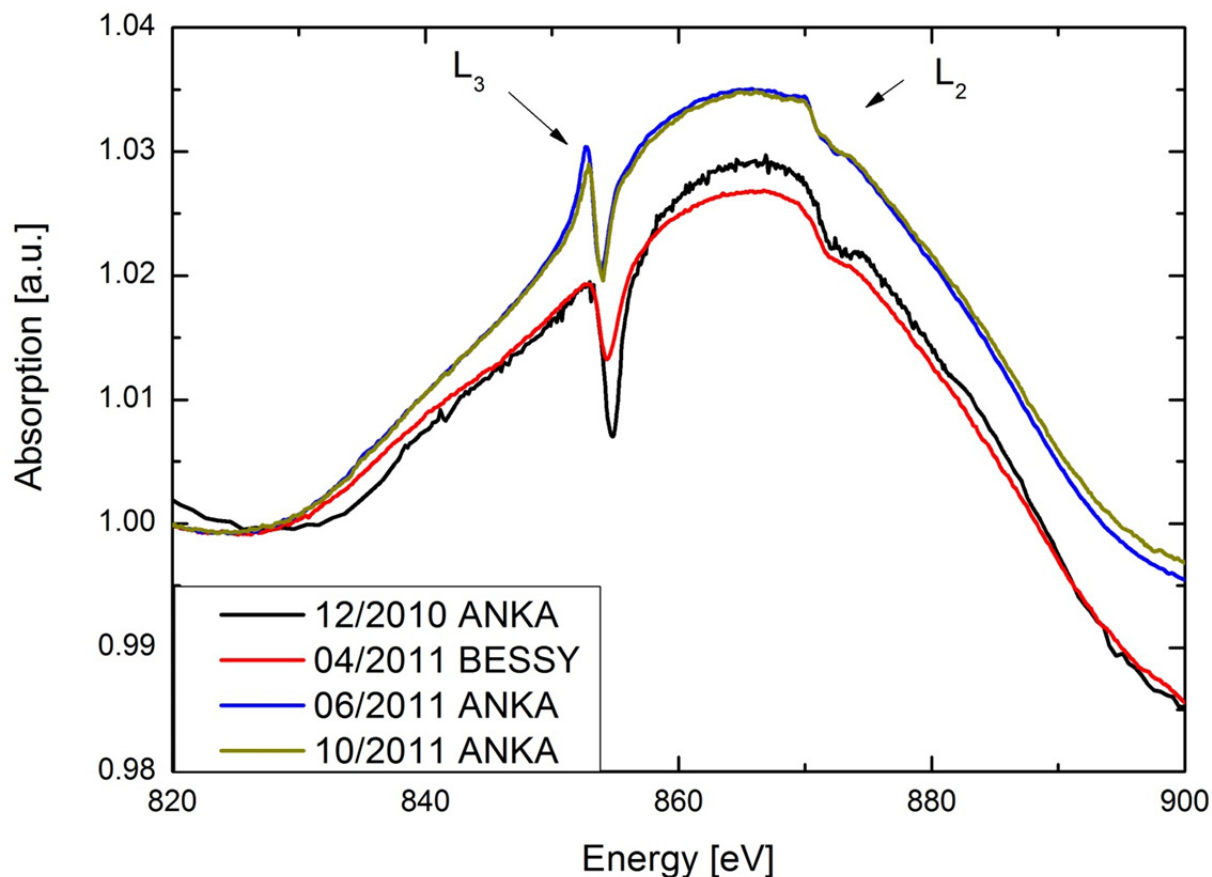


**Figure 4.14:** Comparison of reference spectra used for background subtraction measured at the respective beam times. It has to be noted that the 12/2010 reference spectrum is measured in a different, step-by-step mode with a larger energy step width.

The curve progressions of the respective spectra are similar but not exactly the same. At 853 eV and 875 eV, the Ni  $L_{2,3}$ -edge energies, a dipping structure appears in all reference spectra. This dipping structures are most likely related to slight Ni containment of the beamline optics, especially in the focusing mirrors [123, 124], and the  $I_0$  gold mesh. Main indicator to this assumption is the characteristic of the  $I_0$ -gold mesh signal in the energy region of the Ni  $L_{2,3}$ -edge. Figure 4.15 shows the raw TEY signal from Ir (111) (upper part, labeled as “ $I_1$ ”), the simultaneous measured  $I_0$ -signal (center part), and the ratio between both (labeled as  $I_1/I_0$ , lower part), taken from the reference measurement labeled as 10/2011 ANKA in figure 4.14. One can see a dipping structure in both the TEY and the  $I_0$ -signal at around 854 eV and 873 eV. As the signal of the  $I_0$ -gold mesh is proportional to the incoming beam intensity, a dipping feature in this signal means a loss of beam intensity. The loss in intensity is also visible in the  $I_1$ -signal. Normalizing  $I_1$  to  $I_0$ , the dip should actually disappear. This is not the case here. The dip remains, although its structure is different now. A possible

reason is a slight contamination of the  $I_0$  mesh with Ni, which leads to a slightly altered, enhanced  $I_0$  current at the Ni  $L_{2,3}$  edges and the  $I_0$  current is no longer linear proportional to the beam intensity in this energy region.

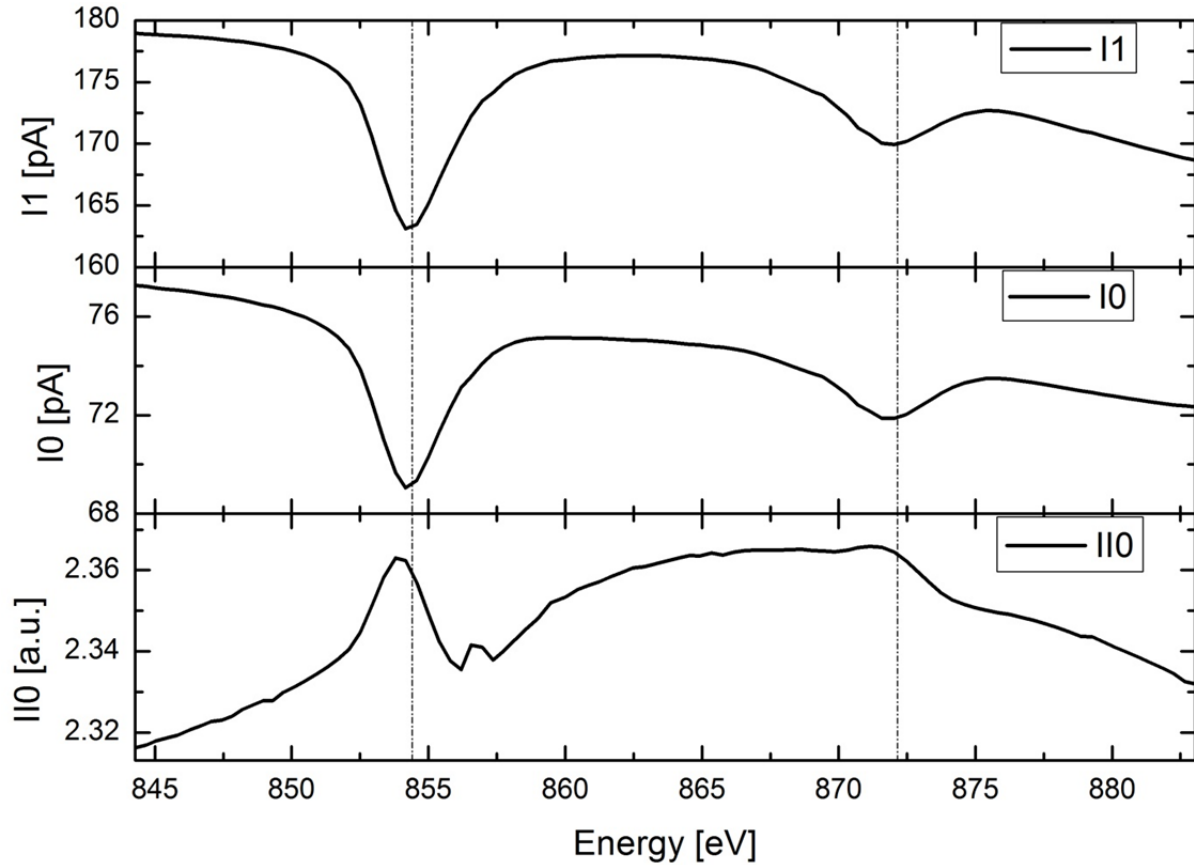


**Figure 4.15: Raw electron yield signal  $I_1$ , electron yield signal from the  $I_0$  grating and the resulting  $I_1/I_0$  normalized spectrum of bare Ir(111) on the energy range of the Ni  $L_{2,3}$ -edge.**

Other possible sources would be a “true” spectral feature of the Ir (111) and residual Ni contamination of Ir (111). However, this is very unlikely as the feature also appears in the  $I_0$  normalized signal from a GaAs photodiode installed in our XMCD setup. Fig. XX shows an overview scan of the GaAs directly exposed to the soft x-ray beam of the WERA beamline. It shows the same shape on the Ni  $L_{2,3}$ -edge region as the measurement of the Ir (111) background signal shown in figure 4.14.

As the measured Ni signals are very small, even this small feature can affect the final result significantly. Thus, one has to eliminate this non-spectral feature from both the reference signals and the measured spectra. The  $I_0$ /beamline related energy loss on the Ni  $L_{2,3}$  edge energy range is convoluted to the measured background signal, as shown in figure 4.16:

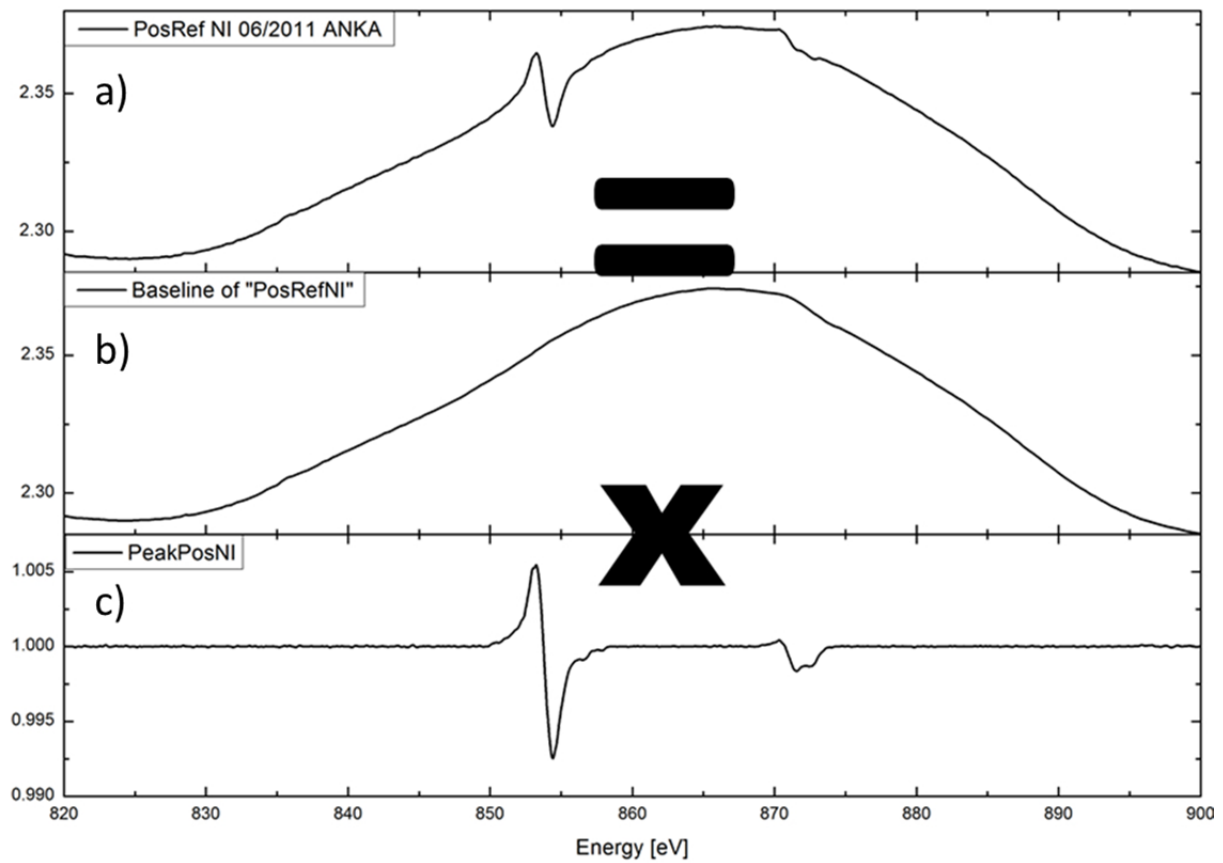


**Figure 4.16: Convolution of the measured TEY signal of a sample Ir (111) reference spectrum (a) of two different contributions: the true Ir (111) spectrum (b) and a peak like, non-spectral feature convoluted to the measurements due to a slight Ni contamination of the  $I_0$  gold mesh/beamline optics (c).**

The  $I_0$ /beamline influence was eliminated by interpolating the spectral shape of the Ir(111) background on the Ni  $L_{2,3}$  edge energy range. The result is shown in figure 4.16 (b) and shall be labeled as “baseline”. The  $I_0$ /beamline influence was then extracted by dividing the measured signal by the baseline. The result is shown in figure 4.16 (c) and shall be labeled as “peakline”. By means of normalizing the measured Ni spectra not only by  $I_0$  but also to the peakline, the  $I_0$ /beamline influence can be eliminated. Reference base- and peaklines have been extracted for all measured background references that were used within this thesis.

Unless otherwise mentioned, all presented spectra were additionally normalized to the respective peaklines.

#### 4.4.5. Background subtraction

After eliminating the annoying  $I_0$ /beamline influence from reference spectra, the obtained baselines can be used in order to remove the Ir (111) background from the actual Ni L<sub>2,3</sub>-edge spectra. A sample spectrum of 0.1 ML nominally deposited Ni/G/Ir (111) is shown in figure 4.17. Black and red lines display the TEY signal obtained with parallel and antiparallel alignment of magnetic field and helicity, the blue line displays the background signal.

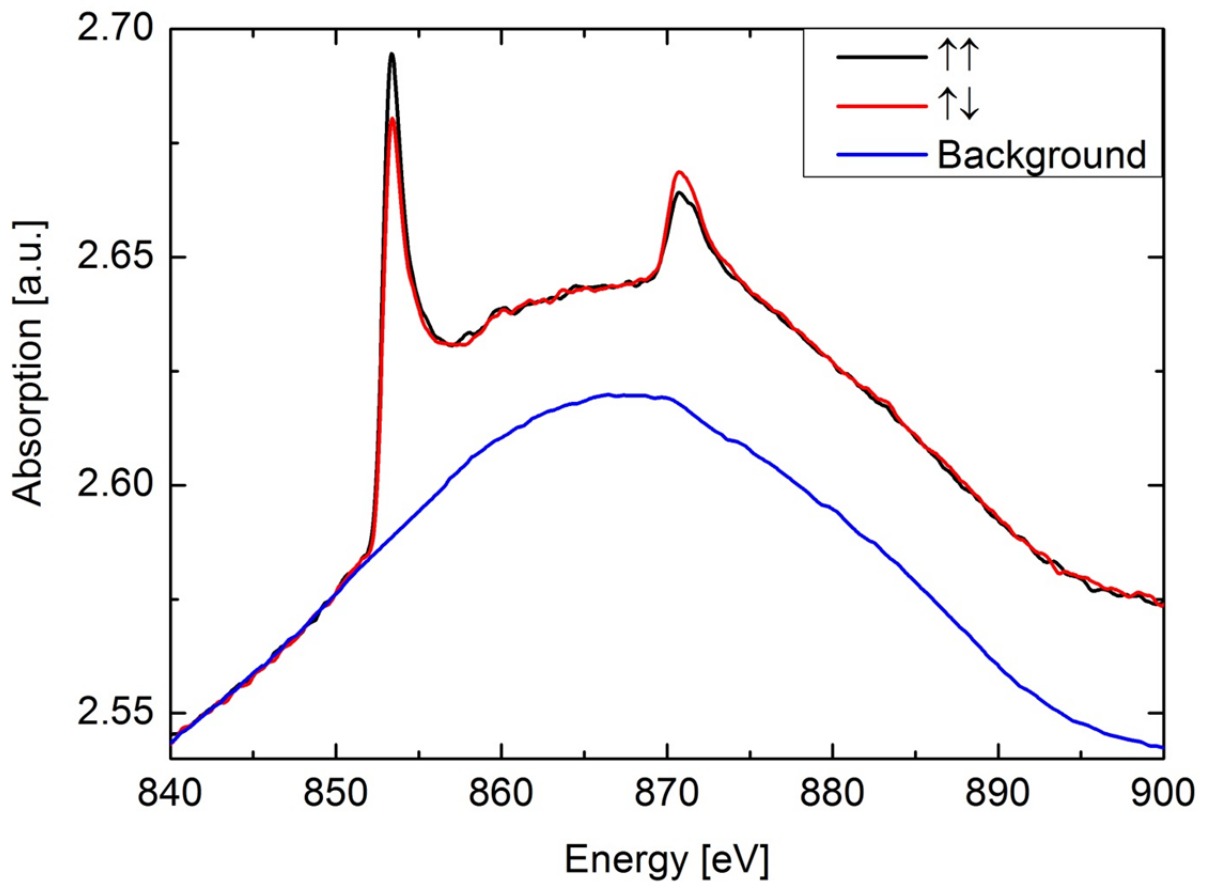


**Figure 4.17:** Measured TEY (black, red lines) and fitted background function (blue line). The blue function can be used to subtract the background.

The measured TEY signal can be described as a combination of different signals contributing to the complete TEY signal, as given in equation (4.9):

$$I_{TEY}(E) = \underbrace{I_{NiL_{2,3}}(E)}_{\text{Actual Signal}} + \underbrace{A_0 \cdot I_{Ir}(E - de)}_{\text{Signal Background}} + \underbrace{a + b \cdot (E - de)}_{\text{Linear Background}} + \underbrace{A_1 \cdot I_{Step}(E - de)}_{\text{Continuum Background}} \quad (4.9)$$

$I_{TEY}(E)$  is the energy dependent,  $I_0$ -normalized TEY signal,  $I_{NiL_{2,3}}(E)$  is the actual signal of interest, the electron yield fraction caused by the Ni  $L_{2,3}$ -edge, a linear background that is always apparent in raw TEY x-ray absorption spectra,  $A_1 \cdot I_{Step}(E - de)$  a step-like function to consider the continuum background (see section 3.2.3), and  $A_0 \cdot I_{Ir}(E)$  is the weighted Ir (111) background signal like the baseline shown in figure 4.16 (b). The variable  $de$  is necessary to correct small energy shifts between the measured signal and the background reference caused by beam or synchrotron orbit drifts. Using equation (4.9) the background signal can be estimated by fitting the background function to the pre- and post-edge area of the spectrum. The parameters obtained by fitting can then be used to obtain the edge-normalized Ni  $L_{2,3}$ -edge spectrum by separating subtracting the background from the measured  $I_{TEY}(E)$ . The result for the sample measurement in figure 4.17 is shown in figure 4.18. As common for XAS spectroscopy, the pre-edge region is set to zero and the post edge region is normalized to one.

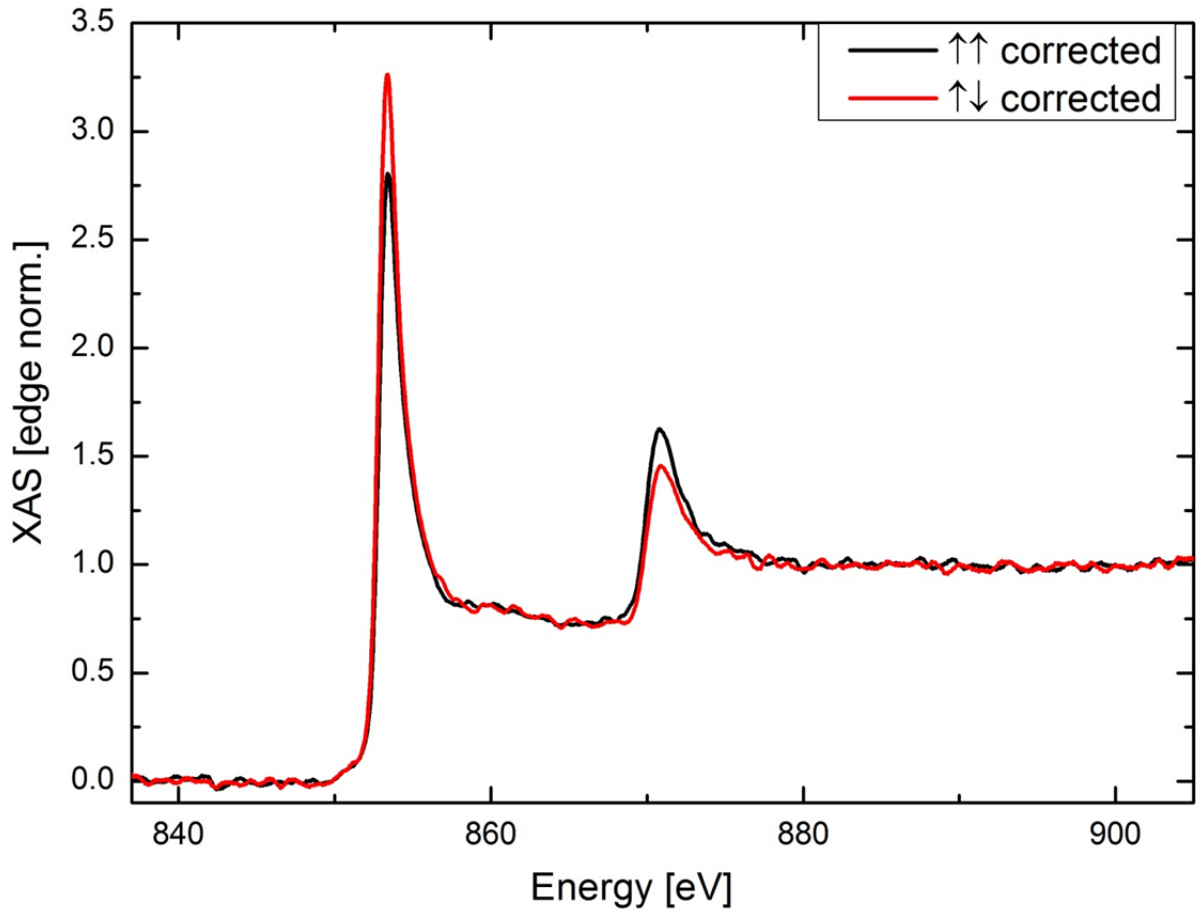


**Figure 4.18:** Resulting edge normalized XAS spectrum of the Ni  $L_{2,3}$  edge of 0.1 ML nominally deposited Ni/G/Ir (111) after proper background correction.

In principal, several combinations of the parameters in equation (4.9) are suitable for background subtraction. Sometimes, for reasons of statistics, a series of multiple spectra has to be measured. If one now subtracts a slightly different background for two different samples, this may result in an over- or underestimation of the absorption lines. This is problematic, especially if one wants to extract the magnetic anisotropy from XMCD measurements where slight angle dependent changes in the spectrum have to be observed. To prevent this, one can perform the so-called “fit normalization”. In this procedure, one picks an edge normalized spectrum, called “norm spectrum”. Assuming that differences in the respective  $I_0$ -normalized spectra stem from slightly deviating signal background, one then tries to reproduce the “fit spectra” by actually adding background to the norm spectrum. The equation for this procedure is given by:



$$I_{Fit}(x) = a + b \cdot (x - de) + A_0 \cdot I_{lr}(x - de') + A_1 \cdot I_{Norm}(x - de) \quad (4.10)$$

The first term considers the linear background caused by the C K- and the Ni K-edge. The second term considers the reference background and the third term provides the factor relevant for the final post-edge normalization. The parameters  $de$  and  $de'$  take slight energy drifts of the fitted spectrum with respect to the norm spectrum and the background reference into account. The respective background subtracted Ni spectra are then obtained by using the respective fit parameters obtained from equation (4.10).

To summarize, by fit normalizing one tries to avoid differences in the normalized absorption spectra that arise from a subtraction of different background only. The comparison of similar spectra is largely improved. However, due to the large number of fitting parameters and the small signal on a large background (see figure 4.13), a systematical error cannot be excluded completely.



## 5. Magnetism of Ni-Nanoclusters on a Graphene Moiré Template

As demonstrated in section 3.4, the graphene Moiré pattern can serve as a template for the growth of TM nanoclusters. The combination of the unique properties of graphene with magnetic nanoparticles could lead to a fully new class of technological devices. However, a detailed study of the fundamental electronic and magnetic properties of the nanocluster/graphene system is required in order to evaluate their potential for its technical utilization in e.g. nano patterned high density data storage or spin tronic devices.

Thus, this section is dedicated to the size and shape dependent analysis of the electronic and magnetic properties of Ni clusters on a graphene Moiré template.

### 5.1. In-Situ Sample Preparation

Usually, TM clusters oxidize quickly under ambient conditions. In order to prevent oxidation of the nanoclusters all investigated samples have been prepared in-situ in the preparation section of our own XMCD setup (see section 4.3) where the base pressure was maintained at  $\sim 2 \cdot 10^{-10}$  mbar. The sample preparation was performed in three major steps:

1. Thorough cleaning of Rh (111)/Ir (111) surface by repeated cycles of  $\text{Ar}^+$  sputtering (removing adsorbates), oxygen annealing ( $T \sim 1000$  K,  $p_{\text{O}_2} \sim 5 \cdot 10^{-8}$  mbar, removing residual carbon contaminations due to carbon monoxide formation) and flash annealing ( $\sim 1500$  K, reconstructing the single crystal surface).
2. Graphene preparation by carbon hydrate (e.g.  $\text{C}_3\text{H}_6$ ,  $p_{\text{CH}} \sim 10^{-8}$  mbar) cracking on the hot metal surface. Subsequently, LEED check is performed to test the graphene quality.
3. Quartz microbalance controlled deposition of Ni with e-Beam evaporator at the required substrate surface temperature.

The basic principles of graphene preparation have been described already in section 3.4. For this thesis, the graphene template was grown on an Ir (111) single crystal (SC), produced by using either temperature programmed growth (TPG), chemical vapor deposition (CVD), or a combination of both, TPG followed by CVD, in order to obtain good quality graphene films. The working principle of both methods is

sketched in figure 5.1, a detailed description of graphene preparation on noble metal supports (especially on Ir (111) surfaces) is given for example in [52, 57, 63, 66, 125].

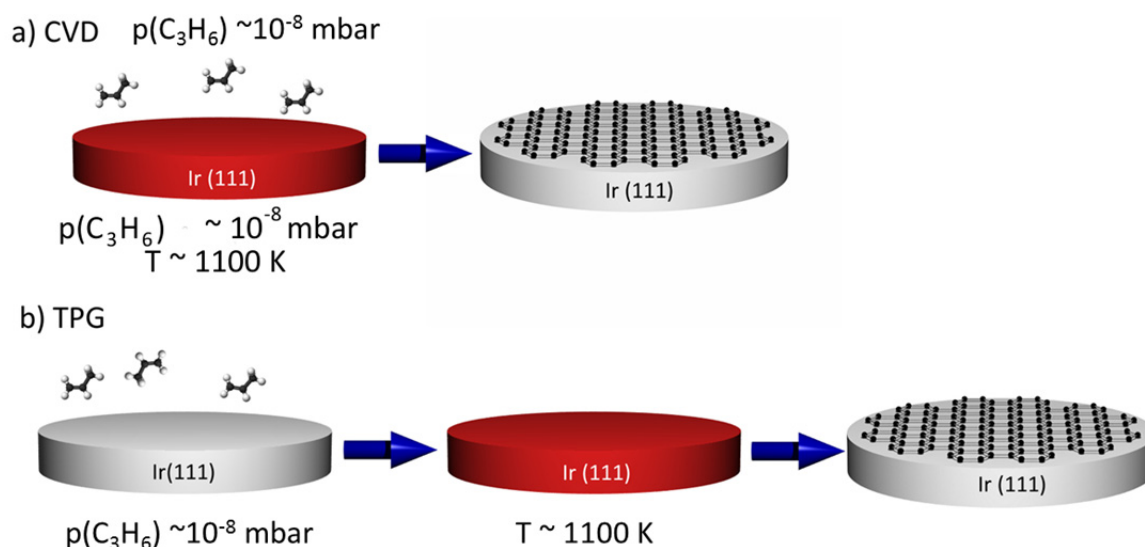


**Figure 5.1: Working principle of the two different methods that were used for this thesis to prepare graphene on Ir (111). a) Chemical vapor deposition (CVD), where carbon hydrates (propene or propylene) are cracked on the hot substrate surface. b) Temperature controlled growth (TPG), where the carbon hydrates are adsorbed to the substrate surface and cracked by subsequent annealing. In both cases the remaining carbon atoms form a graphene mesh on the Ir (111) substrate surface.**

In case of CVD growth (see figure 5.1 a)), a hydrocarbon gas, commonly propene ( $\text{C}_3\text{H}_6$ ) or ethylene ( $\text{C}_2\text{H}_4$ ) is catalytically decomposed on a hot metal surface. The carbon atoms nucleate on the noble metal surface until a complete monolayer of graphene is formed. This process is self-limiting as no carbon hydrate cracking occurs on the graphene layer. Especially no graphene multilayers will be obtained with this method. In particular, the Ir (111) SC is heated to  $\sim 1100 \text{ K}$ , then the preparation chamber is set under a propene pressure of  $\sim 10^{-8} \text{ mbar}$  for 10 minutes.

The second way to prepare graphene is TPG. Here, the carbon hydrate (ethylene or propene) is pre-adsorbed to saturation to the noble metal surface at RT. Subsequent, the sample is annealed to temperature above  $1000 \text{ K}$ , where the C-H bonds of the carbonhydrates will be cracked, the hydrogen will desorb and the remaining adsorbed carbon atoms can form the graphene layer.

A third possible way is to combine both preparation methods, TPG with subsequent CVD. First of all, propene is pre-adsorbed to the noble metal surface. Subsequent annealing leads to the formation of graphene nanodots. These nanodots operate as seeds for the graphene layer which is grown in the following CVD step as described above.

The quality of the grown graphene monolayer has to be checked after the preparation procedure. This can be done by either STM or LEED. Owing to the disadvantageous conditions during synchrotron beamtimes (limited space, oscillations from turbo molecular pumps and cooling devices of the magnet system) graphene quality checks via STM were abandoned for this thesis. Thus, the success of the graphene preparation for synchrotron measurements was checked by LEED, as described more detailed in the following. As an example, an *in-situ* prepared graphene layer that served as template for Ni cluster deposition was chosen.

Prior to the graphene preparation, LEED pictures of the thoroughly cleaned Ir (111) SC surface were taken in order to exclude formation of e.g. unwanted carbon super structures (see [126, 127]). LEED pictures of the thoroughly cleaned Ir (111) SC surface are shown in figure 5.2 a) and b). The electron energy has been set to 75 eV in figure 5.2 a) and 45 eV in figure 5.2 b). Additionally the sample surface was tilted 45° with respect to the LEED electron beam direction in figure 5.2 b). In figure 5.2 a) one can clearly recognize the six fold spots of the Ir (111) SC layers with three brighter and three darker spots. Figure 5.2 b) shows a magnification of one of the six fold spots. This geometry allows a better judgment of the graphene quality in the upcoming process.

Subsequently graphene was prepared atop the clean Ir (111) surface by a combination of TPG and CVD. For the TPG process the Ir (111) surface was exposed to propene ( $\text{C}_3\text{H}_6$ , partial pressure  $p_{\text{Propene}} = 1 \cdot 10^{-7}$  mbar) for 90 s. After the base pressure recovered to  $5 \cdot 10^{-10}$  mbar the Ir (111) SC was annealed to 1200 K for 25 s. The complete TPG procedure was repeated twice in order to create a sufficient amount of graphene seeds. The subsequent CVD procedure was performed in three steps. Starting with pre-annealing the Ir (111) SC to 1400 K for 120 s, continuing with propene cracking at a partial pressure of  $p_{\text{Propene}} = 1 \cdot 10^{-7}$  mbar, and closing with 120 s of post-annealing at the same temperature.

After cooling down the SC, LEED was performed. The result is shown in figure 5.2 c) and d). Like for the bare Ir (111) SC, LEED pictures have been taken again at energies of 75 eV and 45 eV (tilted) in order to check for a successful graphene preparation attempt.

Owing to the lattice mismatch between the graphene and the Ir (111) surface, the typical Moiré pattern surrounding the primary Ir (111) spots can be observed. Here, almost three orders of the Moiré pattern are visible, indicating a very good graphene quality [128, 129].

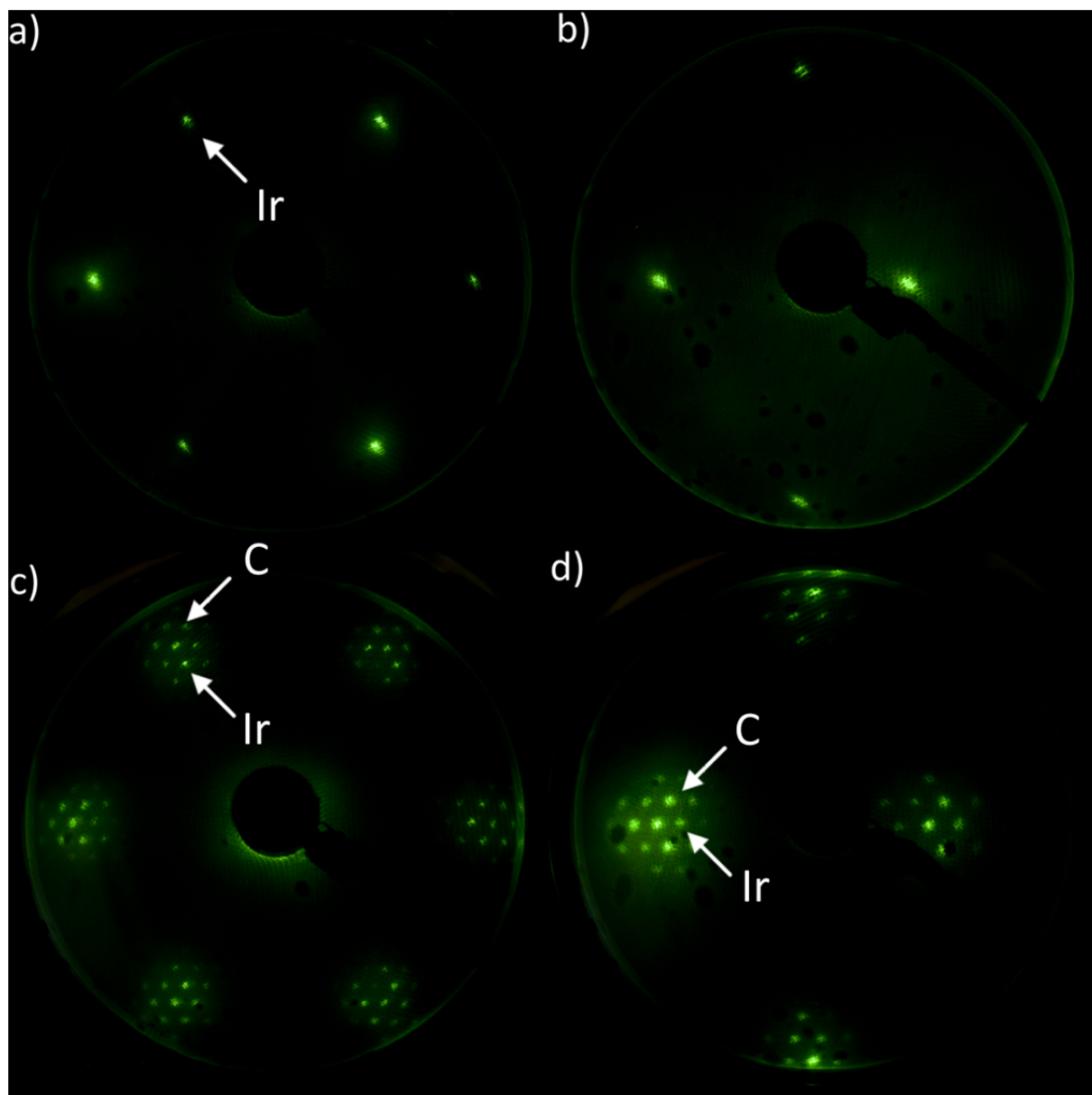


**Figure 5.2:** LEED picture of the thoroughly cleaned Ir(111) surface (a, b). After the successful preparation of graphene, the typical Moiré pattern arises around the initial Ir (111) SC spots (c, d). In b) and d) the angle between the sample surface and the LEED electron beam was tilted in order to magnify one Gr/Ir spot.

---

## 5.2. Spherically shaped nanoclusters

### 5.2.1. Pre-characterization: STM Properties

Owing to the lack of the possibility to perform *in-situ* STM measurements, the structural properties of Ni/graphene has been performed prior to the synchrotron experiments. The temperature and deposition dependent growth properties of Ni/graphene/Ir(111) and Ni/graphene/Rh(111) have been studied intensively by Philipp Leicht and Muriel Sicot from the group of Mikhail Fonin in their laboratory at the University of Konstanz (see references [63, 66] for details).

As mentioned in section 3.4, spherically shaped Ni clusters on a graphene Moiré template can be obtained by depositing Ni at low sample surface temperature, which is usually below 200 K. The average cluster size can be varied changing the nominal Ni deposition. Higher nominal deposition results in cluster with larger average diameter.

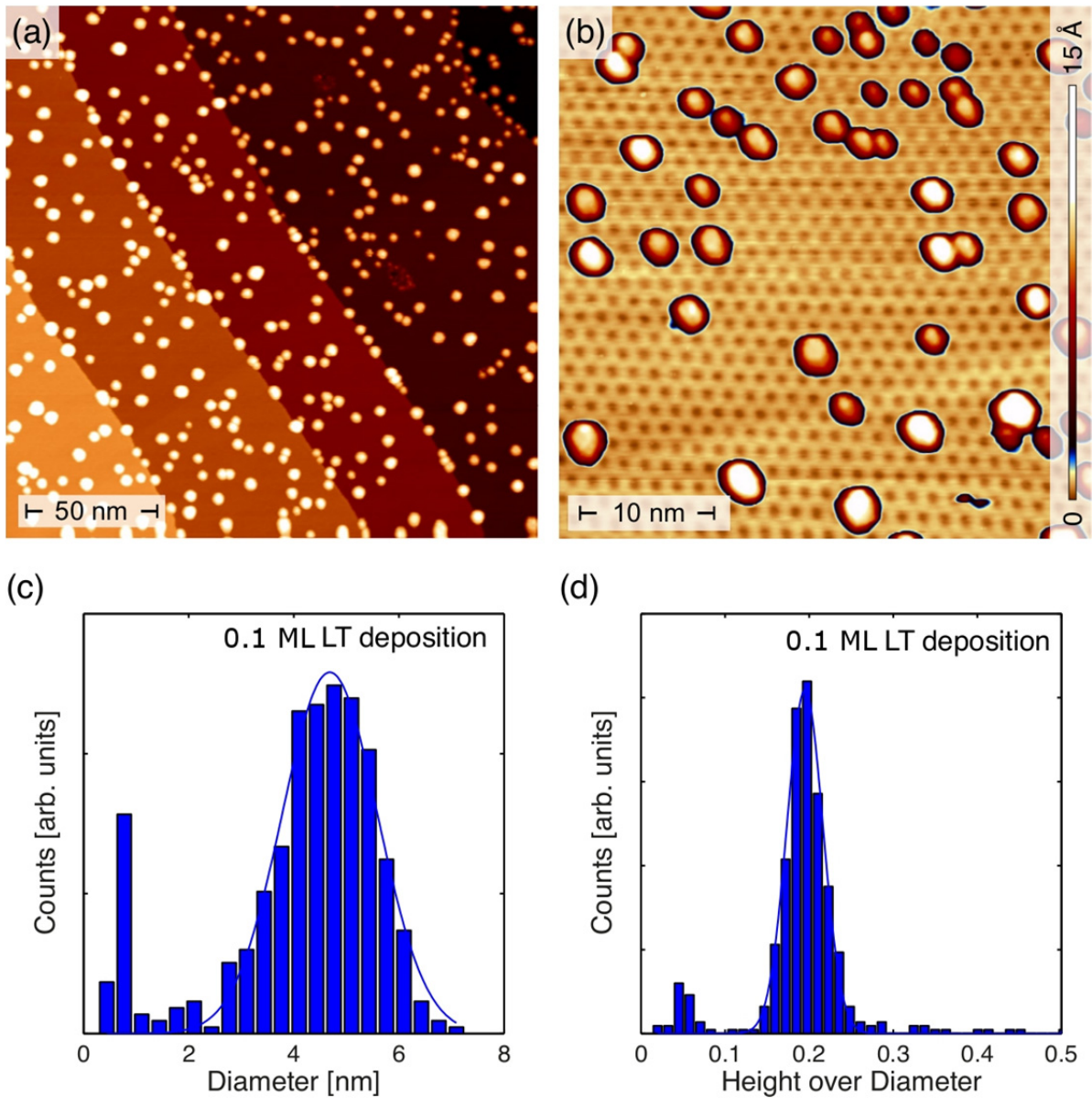


**Figure 5.3: STM characterization of spherical nanoclusters obtained from deposition of nominal 0.1 ML Ni on graphene at a substrate temperature of  $\sim 180$  K. a) Large scale overview. The clusters have spherical shape and are homogeneously distributed over the complete graphene layer. b) Zoom in shows that the clusters mainly remain separated but already starting to agglomerate c) Diameter distribution and d) Vertical aspect ratio (height over diameter). STM topographs and statistics were provided by Philipp Leicht, Universität Konstanz [130].**

Figure 5.3 a) shows a large scale STM picture of nominally 0.1 ML Ni/Gr/Ir (111) deposited at a substrate temperature of  $\sim 180$  K. Spherically shaped nanoclusters (bright spots) on the Gr/Ir (111) substrate are obtained. The clusters are homogeneously distributed



over the graphene area, with a slight tendency to align along the single crystal steps (border line between areas with different color).

In figure 5.3 b) a magnified STM topography of the same sample is shown. The honeycomb structure of graphene is clearly visible, covering the complete image section. The alignment of clusters is not correlated to the underlying graphene substrate. The majority of clusters is isolated and is separated far enough from each other to avoid any magnetic interaction. Only some smaller clusters tend to aggregate. Analyzing multiple STM topographs, one can compile a statistic for the diameter<sup>27</sup> and the vertical aspect ratio distribution<sup>28</sup>. The cluster diameter distribution is displayed in figure 5.3 c). The clusters are Gaussian distributed, with a small, sharp side peak of clusters with diameter of less than 1 nm. The average cluster diameter is  $d_{\text{Ave}} = 4.7 \pm 1$  nm. Another interesting number is the height over diameter or vertical aspect ratio. It provides information about the regularity of clusters and is plotted in figure 5.3 d). The average vertical aspect ratio is  $r = 0.2$ , which implies an average height of  $1 \pm 0.1$  nm. The distribution is very narrow, indicating similar spherical and oblate shape for all clusters, independent from their actual size.

Within this thesis, spherically shaped Ni clusters were produced with four different nominal coverages, given in multiples of equivalent monolayer deposition: 0.1 ML, 0.17 ML, 0.2 ML and 0.35 ML. The range of nominal depositions was chosen quite narrow for two reasons. First of all, below 0.1 ML nominal coverage the detection limit of Ni absorption signal on the single crystal background is reached (see section 4.4.5). Secondly, above 0.4 ML the nanoclusters start to agglomerate quickly and are no longer to be considered as interaction free, isolated particles (see reference [63] for more details).

### 5.2.2. XMCD Results

Immediately after preparation, the respective samples were transferred to the main chamber of the XMCD setup without breaking vacuum conditions. All XMCD measurements<sup>29</sup>, unless otherwise mentioned, have been performed using the XMCD setup

---

<sup>27</sup> Precisely the Heywood or equivalent circular diameter, defined as diameter of a circle having the same area than the respective shape.

<sup>28</sup> Defined as the ratio of height to diameter

<sup>29</sup> Including measurements of the triangular shaped clusters presented in section 5.3.

described in section 4.3. XMCD spectra were measured in total electron yield (TEY) mode, using the fast continuous measurement mode described in section 4.4.2. The samples were cooled down to 10 K and a magnetic field of  $\pm 7$  Tesla was applied to ensure to measure all samples at magnetic saturation. For standard XMCD measurements, samples were aligned in normal incidence (NI) geometry, where the sample surface normal and the k-vector of the incoming x-ray beam are in parallel alignment.

Magnetization curves were obtained by subtracting the XAS signal in the pre-edge region (847 eV) from the Ni  $L_3$ -peak value (853 eV) and subsequently normalizing to the pre-edge value. The magnetic anisotropy was probed by measuring magnetization curves not only in NI geometry, but also at an angle of  $65^\circ$  with respect to the incoming beam direction (in the later solely called “ $65^\circ$  geometry”) to probe the in-plane magnetic component as well.

All XMCD related experiments were performed at the WERA beamline of the ANKA synchrotron in Karlsruhe, and the PM3 beamline of the BESSY II synchrotron in Berlin. For more details on the respective beamlines, see sections 4.1.2 and 4.1.3.

Raw data was post-processed to eliminate the single crystal substrate background as described in section 4.4.5. Owing to the low sub-monolayer deposition and the resulting small XAS and XMCD signals on a huge background, a set of up to 10 spectra was taken at both, positive and negative helicity, and averaged after post-processing. For sum rule application, a step-like background function has been subtracted from the respective XAS spectra, following the notation introduced by Chen et. al., see [28]. The intensity ratio of the  $L_3$  to the  $L_2$ -edge was assumed to be 2:1. Since the nominal coverages of the samples investigated here are in the (sub-)monolayer range, saturation and self-absorption effects were disregarded [131].

Additionally, a bulk Nickel sample was prepared *in-situ* in order to double check the cluster spectra with a reference system. Therefore,  $\sim 60$  ML of Ni have been grown on the thoroughly pre-cleaned, bare Ir (111) SC at RT. The XMCD spectra for the bulk Ni reference were measured under equal experimental conditions as the Ni cluster spectra. This sample will be referred to as the “bulk Ni reference” in the following sections.

A comparison of XAS and XMCD spectra of spherical Ni clusters on graphene at the Ni  $L_{2,3}$ -edge in dependence of the respective nominal Ni deposition is shown in figure 5.4. Additionally, the bulk Ni reference XAS and XMCD spectra were added to this plots.

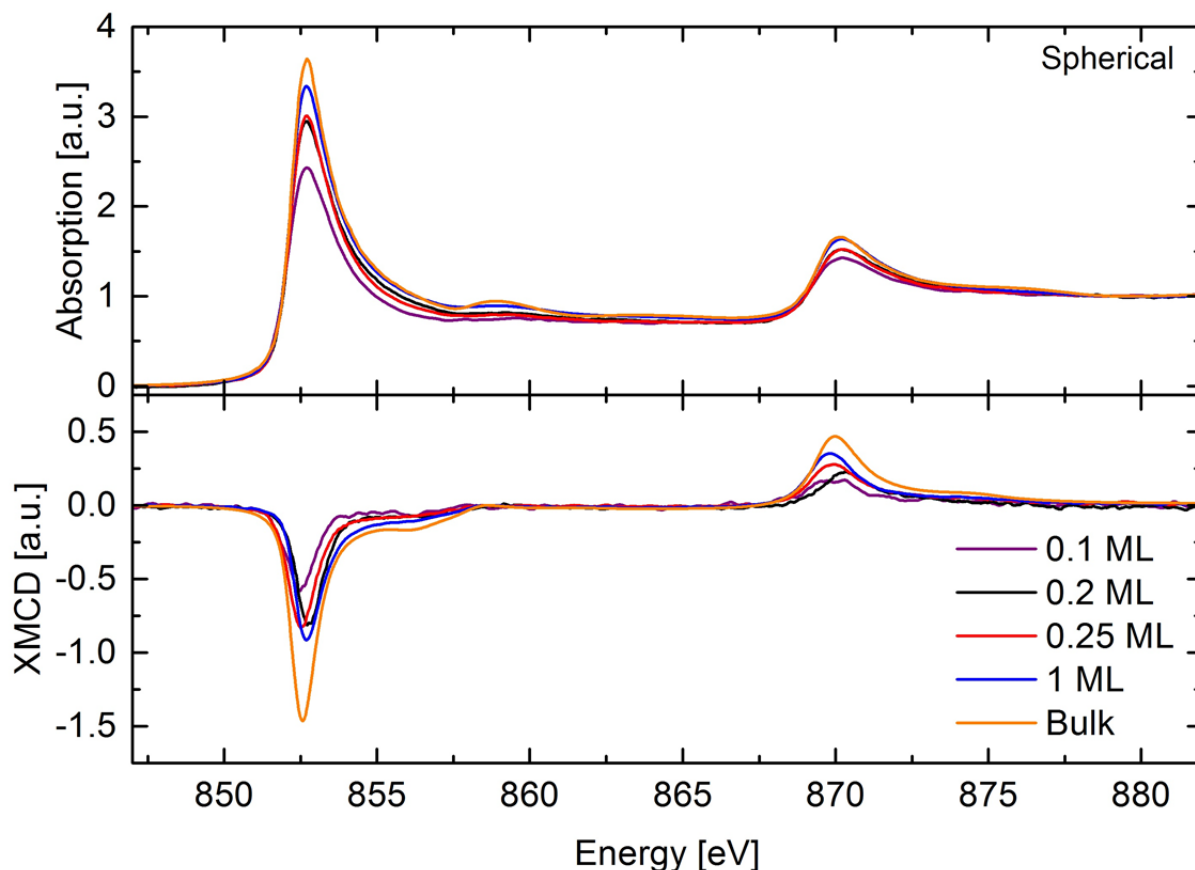


**Figure 5.4:** XAS and XMCD spectra, measured at 10 K and 7 T in NI geometry, for LT deposited, spherically shaped nanoclusters, in dependence of the nominal deposition. Both XAS and XMCD signal scale with cluster size, approaching bulk properties when the nominal deposition is increased.

Comparing the Ni nanocluster spectra to the bulk reference, one finds some distinct features being different or gone missing. At the first glance, XAS as well as the corresponding XMCD spectra obtained for different nominal depositions deviate in the maximum intensity. The XAS white line as well as the XMCD intensity increase with increasing nominal deposition. This indicates a different electronic structure for Ni clusters compared to the bulk material. As the total XAS intensity is proportional to the unoccupied states in the 3d valence shell (see section 3.2.3), a possible explanation is a change of the number of unoccupied states in the Ni 3d shell with increasing cluster size. A variation of the XAS and XMCD peak intensities due to measurements in an unsaturated state can be excluded from the magnetic hysteresis loops (see figure 5.5). Due to the change in the respective XAS intensities, it is not justified to assume a constant value for the number of holes  $n_h$  in sum

rule equations (3.54) and (3.55). Therefore, spin, orbital, and total magnetic moments are listed normalized to the number of holes  $n_h$  in table 5.1.

**Table 5.1:  $n_h$  normalized spin, orbital, their respective ratio, and total magnetic moments obtained by applying magnetic sum rules to the XMCD spectra shown in figure 5.4.**

Nominal Deposition [ML]	$m_s [\mu_B/n_h]$	$m_l [\mu_B/n_h]$	$m_{total} [\mu_B/n_h]$	$m_l/m_s [\%]$
0.1	0.32	0.045	0.365	14.1
0.2	0.33	0.07	0.40	22.7
0.25	0.4	0.04	0.44	10
1	0.38	0.04	0.42	10.5
Bulk Ni Ref.	0.47	0.06	0.53	12.8

Most remarkably, the magnetic moment normalized to  $n_h$  decreases with decreasing cluster size. This observation is completely opposite to the expected increase of the magnetic moment with increasing cluster size, which is usually observed for magnetic nanoclusters (see section 3.3.1 and e.g. references [36, 37]). For the bulk Ni reference, the  $n_h$  normalized spin moment is  $m_s = 0.47 \mu_B/n_h$ . The spin magnetic moment of 0.1 ML nominal deposited Ni nanocluster is  $m_s = 0.32 \mu_B/n_h$ , which is only around 2/3 of the bulk reference value. The spin magnetic moment increases with nominal deposition and for 1 ML nominal deposition  $m_s = 0.38 \mu_B/n_h$  is obtained, which is nearly 80 % of the bulk reference value.

The orbital magnetic moment scatters around  $m_l = 0.05 \mu_B/n_h$ , which is 85 % of the bulk reference value. This value is constant within the large possible error when determining the orbital magnetic moment from XMCD sum rules.

Congruously with constant  $m_l/n_h$  and increasing  $m_s/n_h$  values, the orbital to spin moment ratio  $m_l/m_s$  is enhanced for the lower nominal deposition and follows the expected progressive convergence towards the bulk value when increasing the cluster size. For the smallest nominal cluster deposition of 0.1 ML, the ratio of orbital to spin magnetic moment is 14.1 %, for 0.2 ML it is estimated to be 22.7 %, and it reached 10 % at 0.25 ML.

Magnetization curves for the spherical nanoclusters obtained from XMCD are shown in figure 5.5. The curves are normalized to the saturation magnetization. The large saturation field which is 3.5 T for measurements in NI and 1 T for measurements in 65° geometry

indicates superparamagnetic behavior of the Ni nanoclusters. Even at the lowest possible measuring temperature of 10 K, the system did not change into the blocked state. The magnetic easy axis lays in-plane. Further features obtained from magnetization curves such as magnetic anisotropy energy will be discussed in more detail in section 5.4.7.

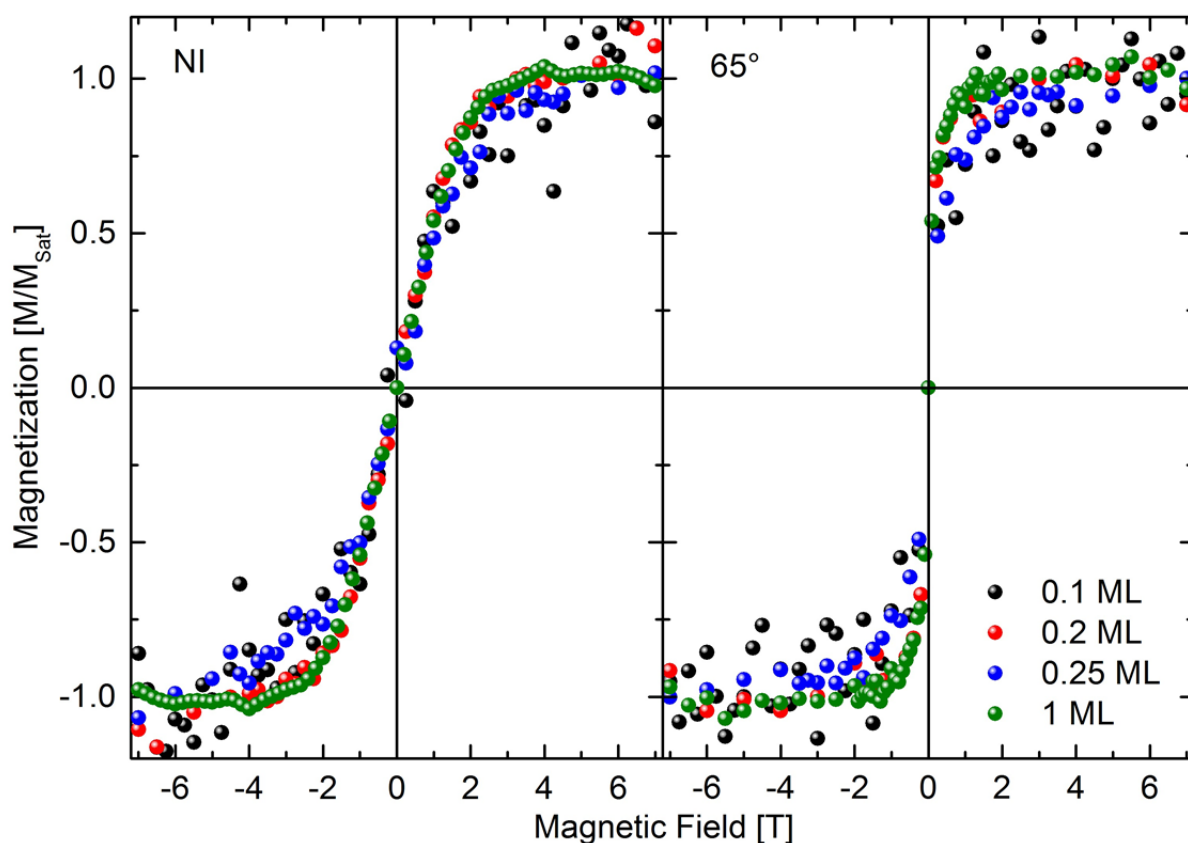


**Figure 5.5:** Magnetization curves of spherical Ni nanoclusters on the graphene/Ir(111) system in dependence of the nominal deposition, in NI (left) and 65° (right) geometry. Curves were normalized to saturation magnetization.

### 5.3. Triangularly shaped nanoclusters

#### 5.3.1. Pre-characterization: STM Properties

The triangular shaped Ni nanoclusters are obtained by RT deposition of the Ni atoms on Gr/Ir (111) substrate. The average cluster size was varied by altering the nominal Ni deposition. Triangular shaped Ni nanoclusters were deposited with nominal coverages of 0.1 ML, 0.15 ML, 0.2 ML, 0.25 ML, 1 ML, and 2 ML. In contrary to spherical nanocluster preparation, the range of nominal coverage was extended above a single Ni ML. For spherical clusters, the actual triangle thickness is several MLs and a complete wetting of the substrate surface requires even higher nominal coverage [63].

Similar to spherical nanocluster, the sample preparation was tested and optimized prior to the synchrotron based experiments. A detailed STM characterization has been performed on triangularly shaped nanoclusters obtained by deposition of nominal 0.25 ML Ni on Gr/Ir (111) substrate while the substrate is kept at RT. The resulting STM topographs as well as the statistical distribution of the nanocluster diameter and the vertical aspect ratio distribution are shown in figure 5.6. a)-d).

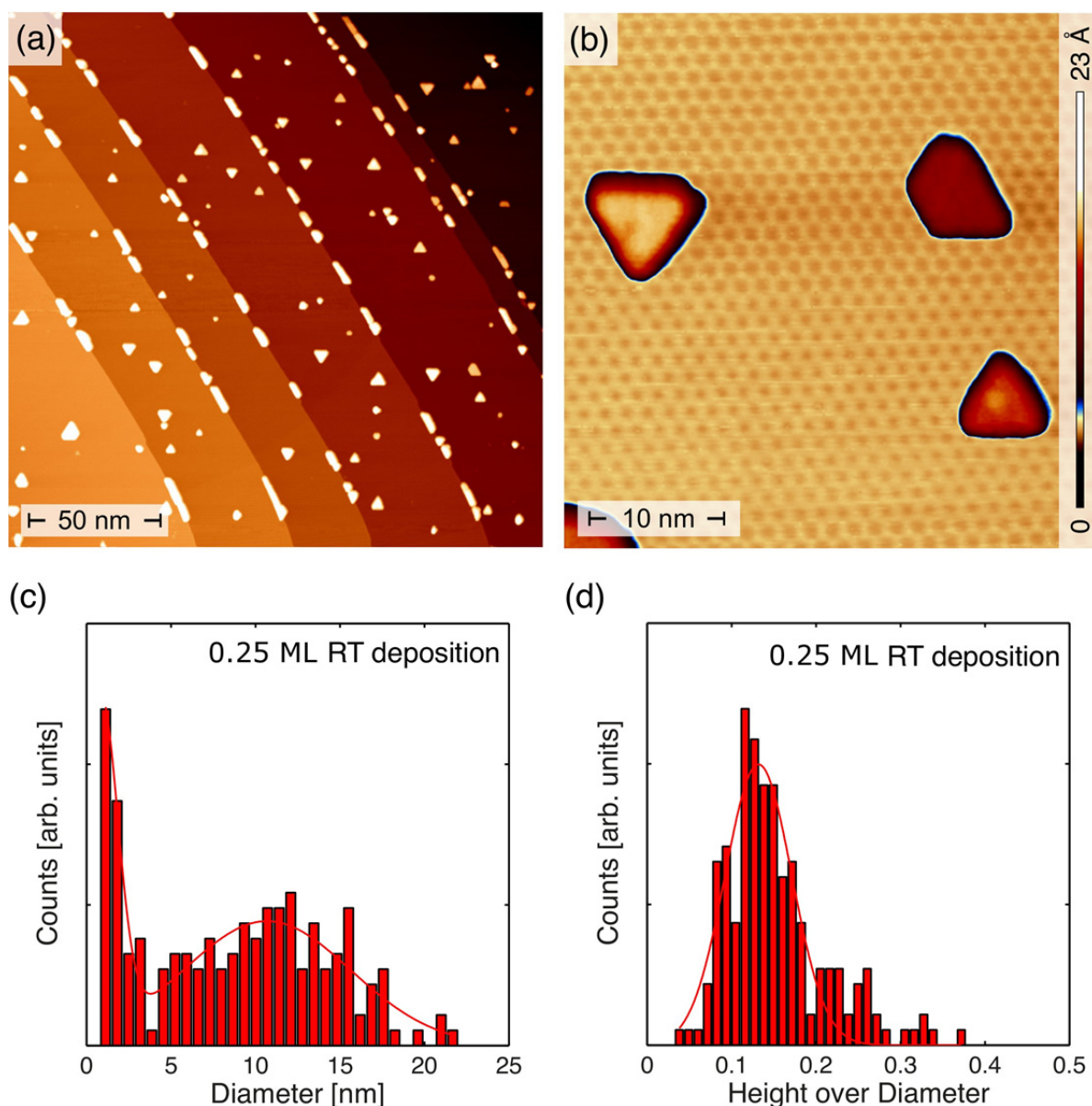


**Figure 5.6: STM characterization of triangular nanoclusters obtained by deposition of nominal 0.25 ML Ni on graphene while the substrate is kept at RT. a): Large scale overview. The clusters are preferentially aligned along the Ir (111) single crystal steps. b): Zoom in reveals that the nanoclusters are still separated from each other and indeed of triangular shape. c): Diameter distribution and d) vertical aspect ratio distribution. STM topographs and statistical analysis were provided by Philipp Leicht, University of Konstanz [130].**

Figure 5.6 a) shows large scale STM topography of triangular shaped nanoclusters on Gr/Ir (111). The clusters are preferably aligned along the Ir (111) single crystal steps. Only a few nanoclusters are found on the SC plateaus, but without any obvious patterning. At a first glance it seems as if the nanoclusters already agglomerated, but a magnification of a cluster rich region shown in figure 5.6 b) reveals that the single triangular islands are still separated

from each other. Furthermore one recognizes that the triangle edges are well aligned along the graphene Moiré pattern.

The diameter distribution was estimated using an equivalent circular diameter (ECD, Heywood diameter) approach. From the cluster area  $A$  the “cluster diameter” can be estimated by the relation:

$$D = \sqrt{\frac{4 \cdot A}{\pi}} \quad (5.1)$$

The result is shown in figure 5.6 c). In contrary to the spherical case, the size distribution of the triangular clusters is much broader. The average cluster diameter is  $10.7 \pm 4.9$  nm. The corresponding vertical aspect ratio is shown in figure 5.6 d). Compared to the diameter distribution, the distribution of the vertical aspect ratio is rather narrow with an average value of  $0.13 \pm 0.04$ . This value corresponds to an average nanocluster height of approximately  $1.4 \pm 0.4$  nm.

### 5.3.2. XMCD Results

The XAS and corresponding XMCD spectra at the Ni  $L_{2,3}$ -edge of the triangularly shaped nanoclusters and the bulk Ni reference are shown in figure 5.7. The findings are similar to the results found for spherical nanoclusters. The intensity of both the XAS and XMCD spectra scales with the nominal deposition, starting with a reduced intensity and converging towards the bulk reference spectra while increasing the nominal deposition. Like for the spherical nanoclusters, it is not justified to assume a constant value for  $nh$  when applying sum rules to the spectra in figure 5.7.



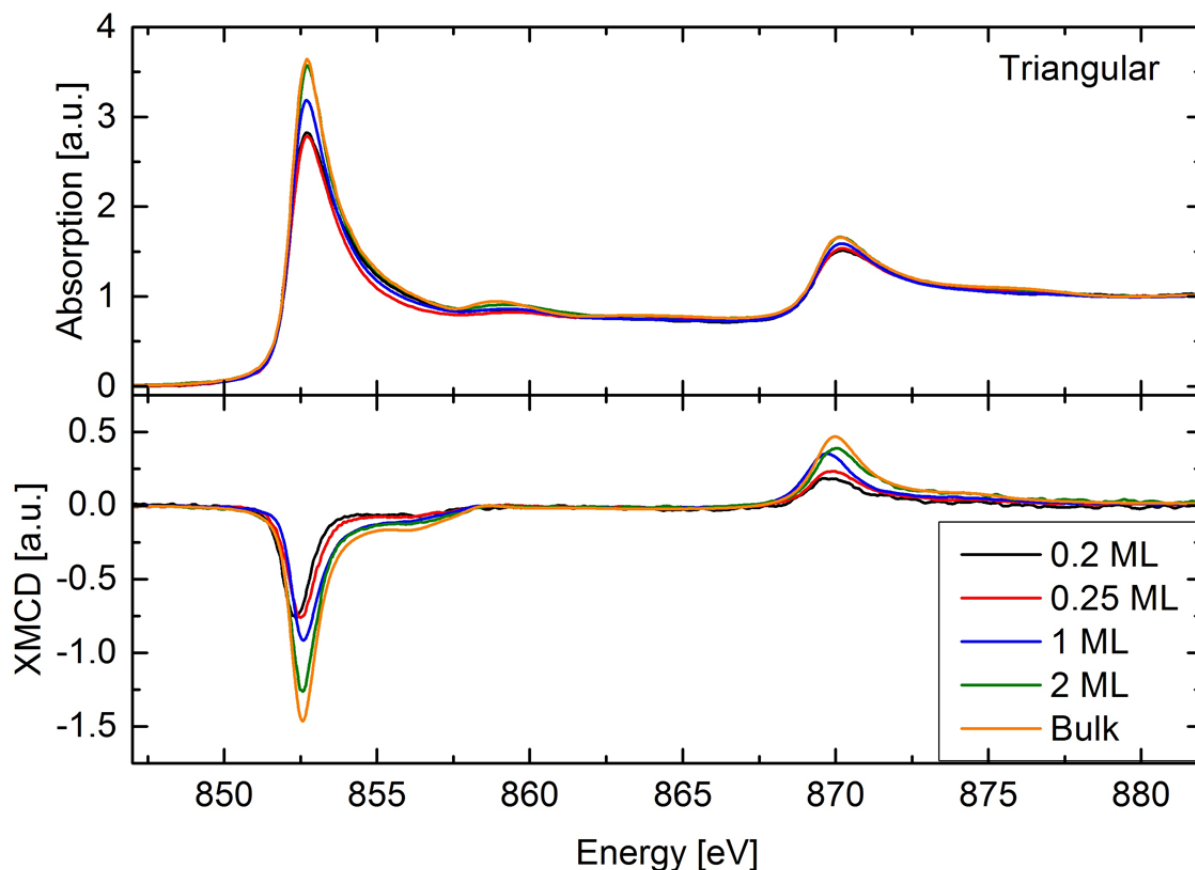


**Figure 5.7: XAS and XMCD spectra at the Ni  $L_{2,3}$ -edge for triangularly shaped nanoclusters in dependence of the nominal Ni deposition. Spectra were measured in NI geometry, at 10 K and an applied magnetic field of 7 Tesla.**

From magnetic sum rules magnetic moments were calculated, normalized to  $n_h$ . The results are listed in table 5.2. Like for spherical nanoclusters, the spin magnetic moment converges logarithmically towards the bulk value with increasing nominal deposition. For 0.1 ML nominal deposition one finds  $m_s = 0.15 \mu_B/n_h$ , which is approximately 32 % of the value obtained for the bulk reference. Bulk properties are nearly reached when the nominal deposition is 2 ML. The  $m_l/m_s$  ratio is enhanced only for the lower nominal depositions, 20 %, 30 %, and 21 % for 0.1 ML, 0.2 ML, and 0.25 ML respectively. Increasing the nominal deposition the ratio practically remains constant around 11-12 % which is similar to the result for bulk reference. Similar to the results for spherical nanoclusters, the enhancement of the orbital to spin moment ratio is owed to the decrease of the spin magnetic moment, not to a significant increase of the orbital magnetic moment. Furthermore, the reduction of the magnetic moment is not related to saturation effects, e.g. measuring XMCD when the sample magnetization is not completely saturated.

**Table 5.2: Spin, orbital, and total magnetic moment, normalized to number of holes  $n_h$  in the Ni 3d valence band for triangularly shaped Ni nanoclusters of different size.**

Nominal Deposition [ML]	$m_s [\mu_B/n_h]$	$m_l [\mu_B/n_h]$	$m_{\text{total}} [\mu_B/n_h]$	$m_l/m_s [\%]$
0.1	0.15	0.03	0.18	20.0
0.15	0.2	0.06	0.26	30.0
0.2	0.28	0.06	0.34	21.4
0.25	0.39	0.046	0.44	11.8
1	0.37	0.044	0.41	11.9
2	0.46	0.05	0.51	10.9
Bulk Ni Ref.	0.47	0.06	0.53	12.8

The corresponding size dependent XMCD magnetization curves are shown in figure 5.8. The magnetization curves indicate superparamagnetic behavior of the triangular nanoclusters and an in-plane magnetic easy axis. The saturation magnetization is 2 T for NI and 0.75 T for 65° geometry. Further features obtained from magnetization curves such as magnetic anisotropy energy will be discussed in more detail in section 5.4.7.

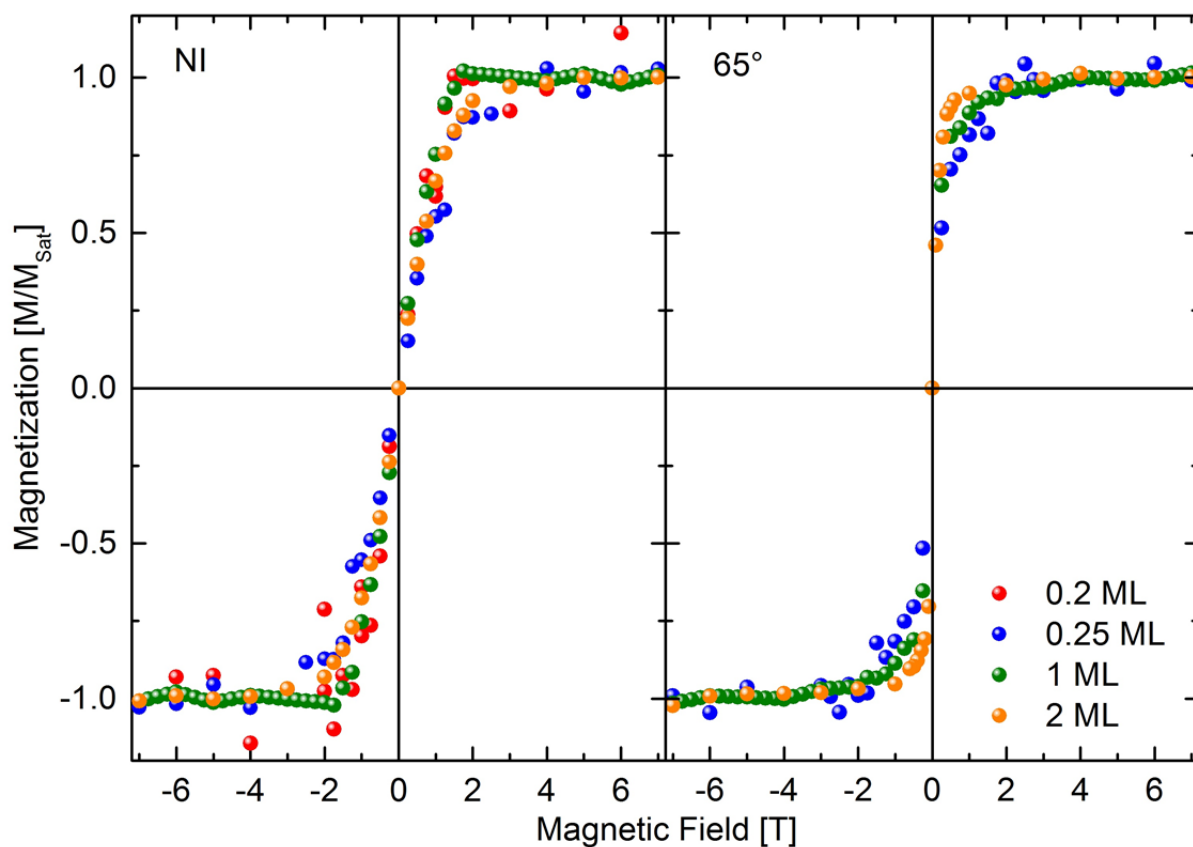


Figure 5.8: Saturation normalized XMCD magnetization curves of triangular Ni nanoclusters on graphene/Ir (111) in dependence of the nominal Ni deposition in NI (left) and 65° (right) geometry.

## 5.4. Comparison and Discussion

### 5.4.1. Satellite Peaks in the Ni XAS spectrum

A remarkable feature of the bulk Ni XAS spectrum, in contrary to its Fe or Co TM counterparts, is the occurrence of satellite structures located 3 eV and 6 eV above the main  $L_3$  absorption line (see e.g. [132, 133]). These satellite peaks were subject to intensive theoretical and experimental investigations. Jo and Sawatzky [134] as well as van der Laan and Thole [135] explained the satellite structure in terms of a “configuration interaction” (CI) picture. In this CI picture, a single Ni atom is picked out of the bulk sample and treated separately from other Ni atoms, which serve as a “charge reservoir”. The number of valence d-electrons in this isolated atom fluctuates due to hybridization with the charge reservoir. Then the ground state  $|g\rangle$  of the isolated Ni atom is represented by a superposition of three possible different electronic configurations (for more details, see the discussion in [134]):

$$|g\rangle = a|3d^{10}\rangle + b|3d^9v\rangle + c|3d^8v^2\rangle \quad (5.2)$$

where the coefficient  $a_i^2$  represent the relative fraction of the respective electronic state and  $v$  denotes orbitals of the reservoir. Depending on the respective publication, the values for a-c are in the order of  $a = 15\text{-}20\%$ ,  $b = 60\text{-}70\%$ , and  $c = 15\text{-}20\%$  (calculated by Jo and Swatzky) and  $a = 18\%$ ,  $b = 49\%$ , and  $c = 33\%$  (calculated by van der Laan and Thole).

From these ground states, several possible final states  $|f\rangle$  can be reached:

$$|f\rangle = a'|2p^5 3d^{10}v\rangle + b'|2p^5 3d^9v^2\rangle \quad (5.3)$$

Note that for the  $|3d^{10}\rangle$  ground state no final state exists after photo electron excitation, thus it cannot contribute to the absorption spectrum.

This shall be discussed in more detail on the basis of figure 5.10. Here the size dependence of the Ni  $L_{2,3}$ -edge XAS and XMCD spectra are shown. The major spectral features in the vicinity of the  $L_3$ -edge are labeled with letters A-D.

Feature A labels the main  $L_3$  peak which arises from a transition from the  $3d^9$  ground to the  $3d^{10}$  final state (see also [134]):

$$A: \langle 3d^9 | T | 2p^5 3d^{10} \rangle \quad (5.4)$$

The features B and C denote the Ni satellite peaks at 3 eV and 6 eV respectively. They stem either from a mixing of  $2p^5 3d^9$  and  $2p^5 3d^{10}$  configurations in the final states or from a significant admixture of  $3d^8$  ground states. In the first case, B and C are feedback peaks from the main  $L_3$  edge in the XAS/XMCD spectrum. For the latter, transitions from  $3d^8$  to  $3d^9$  states additionally contribute to B and C:

$$B, C: \langle 3d^8 | T | 2p^5 3d^9 \rangle \quad (5.5)$$

For feature B one finds a pair of spin up holes in the  $3d^8$  ground state which results in triplet state of the 2p 3d holes, as shown on the left side of figure 5.9. Thus, this feature is XMCD active and lays 3 eV above the main  $L_3$ -peak. This satellite is difficult to identify in the averaged XAS spectrum but is clearly visible in the corresponding XMCD signal.

For feature C the final state of the 2p-3d holes is of singlet type as shown on the right side of figure 5.9. This satellite lies about 6 eV above the main  $L_3$ -peak and is clearly visible in the XAS spectrum. It is furthermore XMCD inactive, so that the dichroic signal at the 6 eV satellite position falls back to zero.

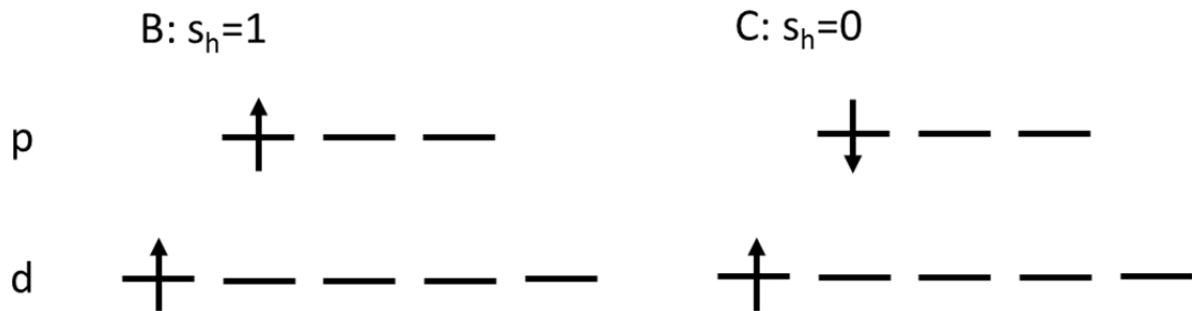


**Figure 5.9: Hole spin configuration of the features B and C of the Ni spectrum. For feature B, the final hole configuration is the XMCD active triplet state (hole spin  $s_h = 1$ ). For feature C, the final hole configuration is the XMCD inactive singlet state ( $s_h = 0$ ).**

Feature D denotes the energy region between the Ni  $L_3$  and  $L_2$  edge. Even when subtracting the step-like background function, the XAS as well as the XMCD signal does not vanish in this energy region. O'Brien and Tonner attributed this feature to a so-called "diffuse magnetism" [136, 137]. They suggest that the XMCD signal in this diffuse region

stems from a contribution of states resulting from an additional hybridization of the actual Ni 3d states with delocalized, and spin polarized 4s electrons.

A comparison of the XAS and XMCD spectra of the triangular and spherical Ni clusters are shown in figure 5.10 and figure 5.11. In order to discuss changes in the 3 eV (B) and the 6 eV (C) satellite, the respective areas have been magnified in the inset of the XMCD (feature B)/XAS (feature C) spectrum.

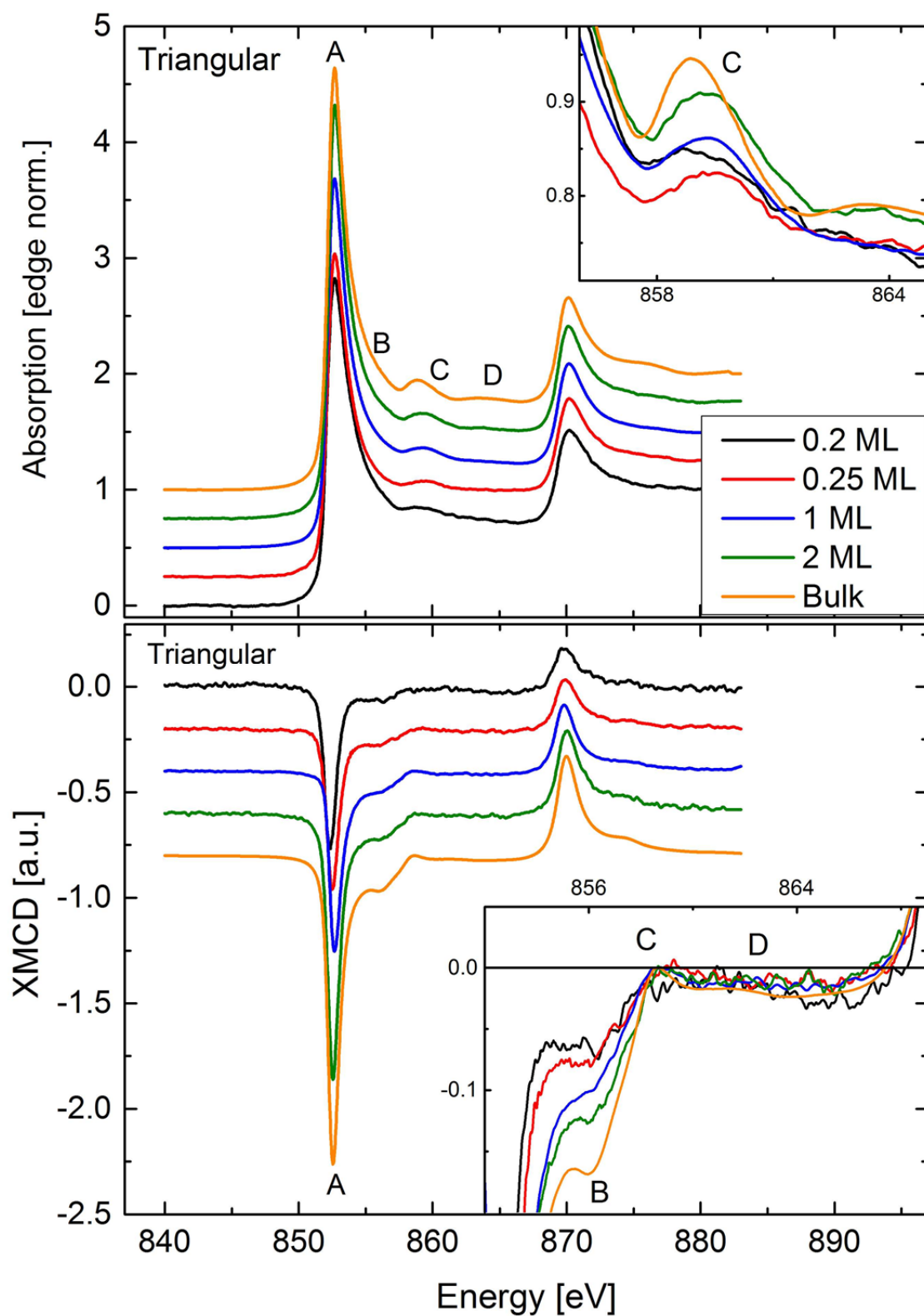


Figure 5.10: Comparison of  $L_{2,3}$ -edge XAS and XMCD spectra of triangularly shaped Ni nanoclusters of different nominal deposition. Additionally, the bulk reference spectrum is plotted. The insets show the magnification of the Ni 6 eV (XAS/XMCD) and the 3 eV (XMCD) satellite peak regions. Spectral features are labeled with letters A-D (see text).

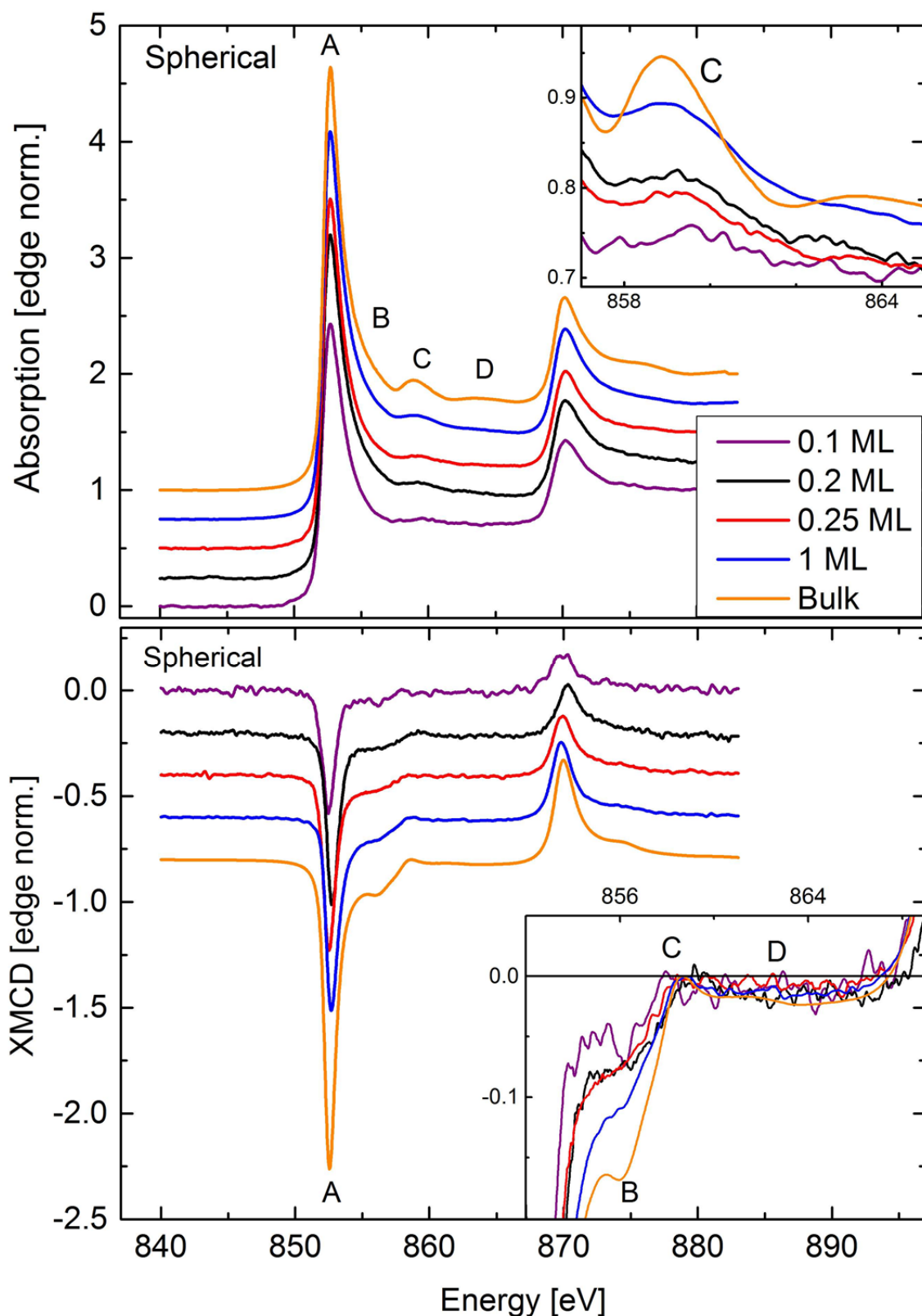


Figure 5.11: Comparison of  $L_{2,3}$ -edge XAS and XMCD spectra of spherically shaped Ni nanoclusters of different nominal deposition. Additionally the bulk reference spectrum is plotted. The insets show the magnification of the Ni 6 eV (XAS/XMCD) and the 3 eV (XMCD) satellite peak regions. Significant spectral features are labeled with letters A-D.



### 5.4.2. Scaling of the main L<sub>3</sub>-peak: Estimating the number of holes $n_h$

As already mentioned in section 3.2.3, it is essential to know the number of holes  $n_h$  in order to apply magnetic sum rules and to estimate the respective magnetic moments accordingly. Usually  $n_h$  is derived from band structure calculations. However, these calculations are based on bulk transition metal properties and the theoretically estimated values scatter considerably for the relevant transition metals Fe, Co, and Ni. For example, for bulk Ni, literature values for  $n_h$  are found ranging from 1.0 ([138]), 1.45 ([139]), 1.66 ([27]), 1.75 ([7]), to 1.8 ([34]). In addition, the electronic structure of nanocluster and thin film systems can deviate strongly from the bulk properties, as highlighted in section 3.3. Therefore it is not automatically justified to simply use (one of) the literature value(s) of  $n_h$  to calculate magnetic moments from magnetic sum rules, especially not in the present case.

Feature A represents the main L<sub>3</sub>-peak, the transition from the initial  $2p^6 3d^9$  to the  $2p^5 3d^{10}$  final states (see equation (5.4)) and is therefore a direct measure of the unoccupied density of 3d states, namely  $n_h$ . Therefore, it is reasonable to start the discussion of the electronic properties with the size dependent scaling of the main L<sub>3</sub>-peak of the respective XAS spectra in figure 5.10 and figure 5.11.

The L<sub>3</sub> white line intensity and therefore  $n_h$  increases with increasing the cluster size. This effect is found for both, triangular and spherical shaped clusters. In order to determine quantitative values for  $n_h$ , the so-called “charge sum rule”, according to equation (3.51), can be applied:  $C \cdot n_h = \langle I_{L_3} + I_{L_2} \rangle = \langle I_{WL} \rangle$ , where  $\langle I_{WL} \rangle$  denotes the integrated white line intensity. In order to avoid influence of the diffuse part D as well as possible near-edge effects, the XAS intensity was integrated up to the L<sub>3</sub> maximum for each spectrum. Prior to the integration, a step-like background was subtracted, assuming an L<sub>3</sub>-L<sub>2</sub> edge intensity ratio of 2:1. The constant value  $C$  can be determined by normalization to the bulk reference value. The bulk reference value for  $n_h$  is set to  $n_h = 1.45$ . This value was selected from Srivastava et. al. [139], who conducted a similar analysis for ultrathin Ni layers on Cu(100). They reported similar findings on the scaling of the Ni electronic structure in dependence of the nominal Ni layer thickness. The integrated XAS intensity and the resulting values for  $n_h$ , in dependence of the cluster size and shape, are displayed in figure 5.12 and listed in table 5.3.

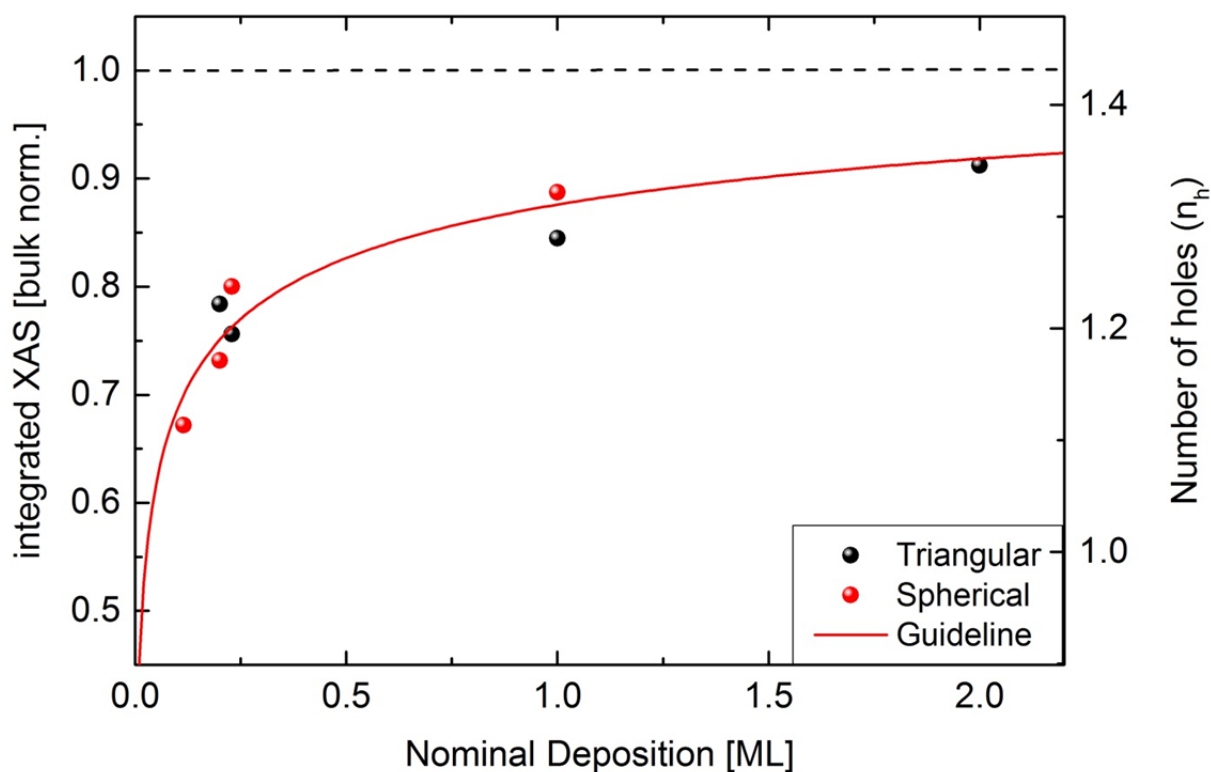


Figure 5.12: Estimating the number of 3d holes ( $n_h$ ) from integrating the XAS intensity up to the  $L_3$ -main peak as a function of the nominal deposition for both, triangular and spherical Ni nanoclusters. The integrated intensity has been normalized to the bulk value ( $n_h = 1.45$ , dashed black line).

**Table 5.3: Integrated white line intensity, given in arbitrary units and the corresponding number of unoccupied 3d states ( $n_h$ ).**

Nominal Deposition [ML]	Spherical Clusters		Triangular Clusters	
	Int. XAS	$n_h$	Int. XAS	$n_h$
0.15	0.67	0.97		
0.2	0.73	1.06	0.78	1.13
0.25	0.8	1.16	0.75	1.09
1	0.88	1.28	0.85	1.23
2			0.91	1.32
Bulk Ni [139]	1	1.45	1	1.45

For the lowest nominal deposition of 0.15 ML Ni, one finds  $n_h = 0.97$  (spherical shape), which is only 66% of the bulk value.  $n_h$  increases quickly when the nominal deposition is increased. The values for spherical and triangular shaped clusters scatter within close distance around the combined trend line. Comparing spherical and triangular nanoclusters, for 0.2 ML nominal deposition  $n_h = 1.06$  (spherical), respectively  $n_h = 1.13$  (triangular) is found. The values increase to  $n_h = 1.16 / n_h = 1.09$  for 0.25 ML, and  $n_h = 1.28 / n_h = 1.32$  for 1 ML nominal deposition. For nominal deposition of 2 ML one finds  $n_h = 1.32$  which is already  $\sim 90\%$  of the bulk value. The trendline of  $n_h$  is similar for triangular and spherical clusters, i.e. no obvious shape dependence can be reported.

In summary the decrease of  $n_h$  which is reflected by the change of feature A, the main  $L_3$  peak, indicates an increased fraction of  $|d^{10}\rangle$  states of the Ni atoms in smaller nanoclusters.

These findings resemble the results of ultrathin films of Ni on Co (111) and Cu (111) substrates. Although grown on different substrates, Dhesi [140] (via high resolution low energy electron diffraction (HRLEED) on Ni/Co) and Boeglin [110] (via STM on Ni/Cu) found, that the sub-ML growth of Ni on Co (111) and Cu (111) results in a similar triangular growth morphology than the RT deposited Ni nanoclusters on a graphene Moiré template.

Srivastava et. al. performed XAS investigations on ultrathin films of Ni on Cu (111), varying the Ni thickness. They report a scaling of  $n_h$  similar to the results found within this

thesis [139, 141]. Furthermore, they report a decrease of  $n_h$  from 1.45 (bulk value which evolved at 14.4 ML film thickness) to 1.02 for 0.6 ML nominal deposition.

A similar study was carried out by Dhesi et. al [140, 142]. on the slightly different Ni/Co(4 ML)/Cu(001) system. They found a similar trend for the scaling of  $n_h$  in dependence of the nominal Ni film thickness: for 0.2 ML Ni/Co/Cu they report  $n_h = 0.84$ , this is a decrease of 42 % with respect to the bulk value.

Nietubyc el. al. [143] thoroughly investigated the properties of the Ni L-edge XAS spectrum Ni thin films on Cu(001), varying the thickness from 0.07 ML to 3.1 ML. Although the respective authors make no statement on the absolute value of  $n_h$ , they also report a decrease in the unoccupied density of states for smaller nominal film thicknesses. However, they report a stabilization of the Ni bulk properties already for a very low coverage of 0.75 ML.

A comparison of the results found for this thesis and the above mentioned literature data is shown in figure 5.13. Note that for the results from reference [143] the relative intensity is given, thus the results are valid for the right hand y-axis only.

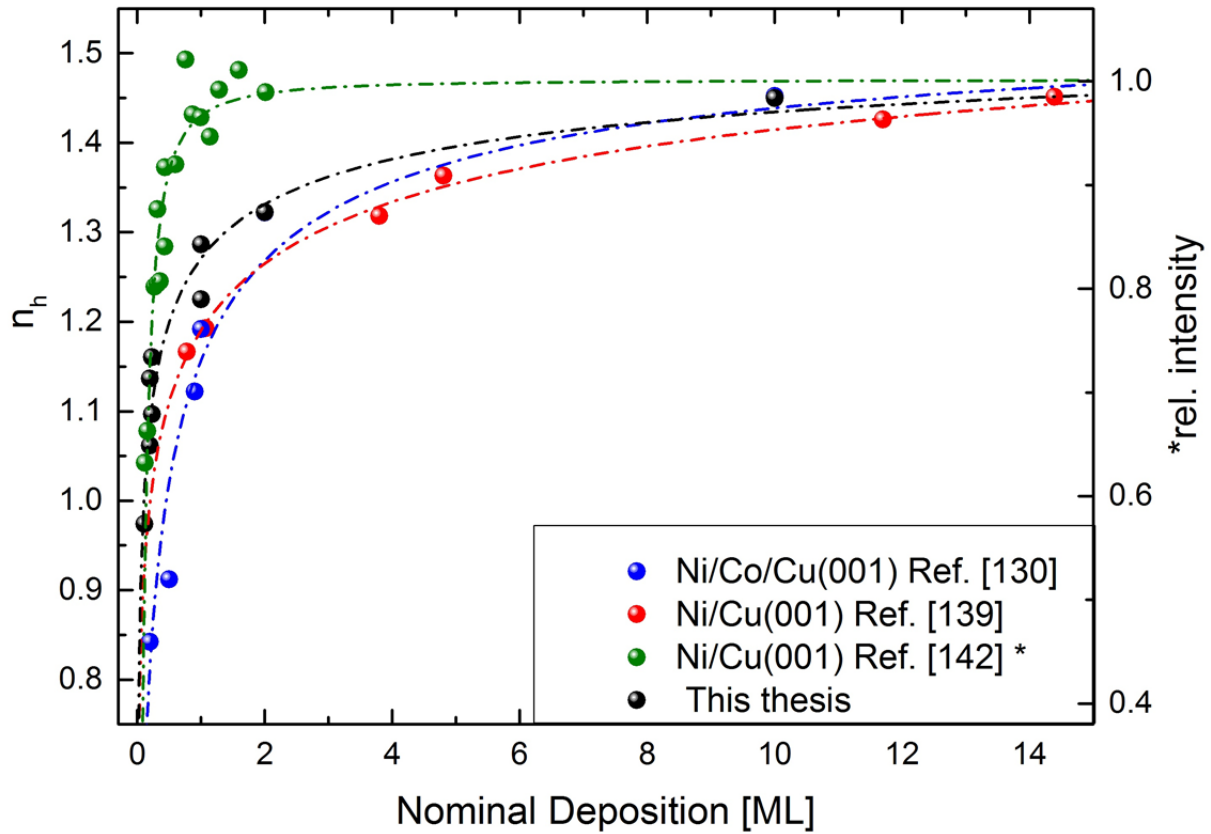


**Figure 5.13: Comparing number of holes  $n_h$  found in this thesis with results reported from other groups for ML and sub-ML Ni on Cu (001) substrates, which exhibit a morphology similar to triangularly shaped nanoclusters on Gr/Ir (111). The trend lines are similar. In all cases, a reduction of  $n_h$  was observed for smaller nominal deposition.**

As a possible explanation of their results, the respective author propose that the reduction of  $n_h$  is caused by hybridization of Ni with Co/Cu d-bands which induces charge transfer from the Cu to the Ni 3 d orbitals. Thus the numbers of electrons in the Ni d-orbitals increase and in reverse the number of unoccupied states  $n_h$  decreases. This behavior is somehow expectable for the Ni/Cu (001) system, as these elements are neighbors in the periodic table and thus possess similar chemical properties.

However, the similarity in the increased occupancy of the Ni d-states for the Ni/graphene system is somewhat more surprising. As a matter of principle, there could also be a stronger hybridization between the Ni d-states (mainly the  $d_{z^2}$ ,  $d_{xz}$ , and  $d_{yz}$  orbitals) and especially the out-of-plane graphene  $p_z$  states. The decrease of unoccupied d-states may stem from either charge transfer from graphene to Ni or a complete electronic reconfiguration of the Ni atoms in smaller clusters where they lacking neighboring Ni atoms

and are unable to establish a bulk like band structure. Information on the electronic configuration may be extracted from the Ni satellite which will be discussed in the next subsection. In order to reveal more details of the interaction of the Ni clusters with the graphene substrate, the C-K edge and thus the graphene states have been probed. These results will be discussed in section 5.4.4.

### 5.4.3. Ni satellite features

Of particular interest is the behavior of the distinct satellite peaks in the Ni spectrum because their modification reveals at least qualitative information on the electronic configuration of the investigated system. Therefore, the 3 eV (B) and 6 eV (C) satellite were magnified in the insets of figure 5.10 and figure 5.11. Owing to the band effect related broadening of the main Ni  $L_3$ -edge, the 3 eV satellite appears as a shoulder at the higher energy flank of the main  $L_3$  peak and is difficult to identify in the XAS spectrum. However, the feature is clearly cognoscible in the XMCD spectrum.

The modification of the Ni 3 eV satellite feature in the XMCD spectrum in dependence of the nominal deposition and for both cluster types is shown in figure 5.14. Figure 5.14 a) shows the absolute XMCD intensity at the 3 eV satellite energy position. For both, triangular and spherical clusters, the satellite intensity reduces with decreasing cluster size. The satellite feature becomes less distinct but can still be identified even at the lowest nominal coverage of 0.1 ML, where the signal exhibits a high noise level.

In figure 5.14 b) the satellite peak values were normalized to the main  $L_3$ -edge XMCD peak. For the bulk reference sample, the intensity ratio  $I_{3\text{eV}} / I_{L_3\text{XMCD}}$  is 0.115 or 11.5 %. For the Ni nanoclusters the intensity ratio decreases with decreasing the cluster size, although the main XMCD peak at the  $L_3$ -edge is decreasing as well. Whereas the size dependence is quite strong (see guide line in the respective figures) there is no obvious shape dependence. The decrease of the 3 eV satellite feature indicates a reduction of the triplet  $3d^8$  ground state and thus a derogated contribution of transitions from this ground state to the overall Ni XMCD signal.

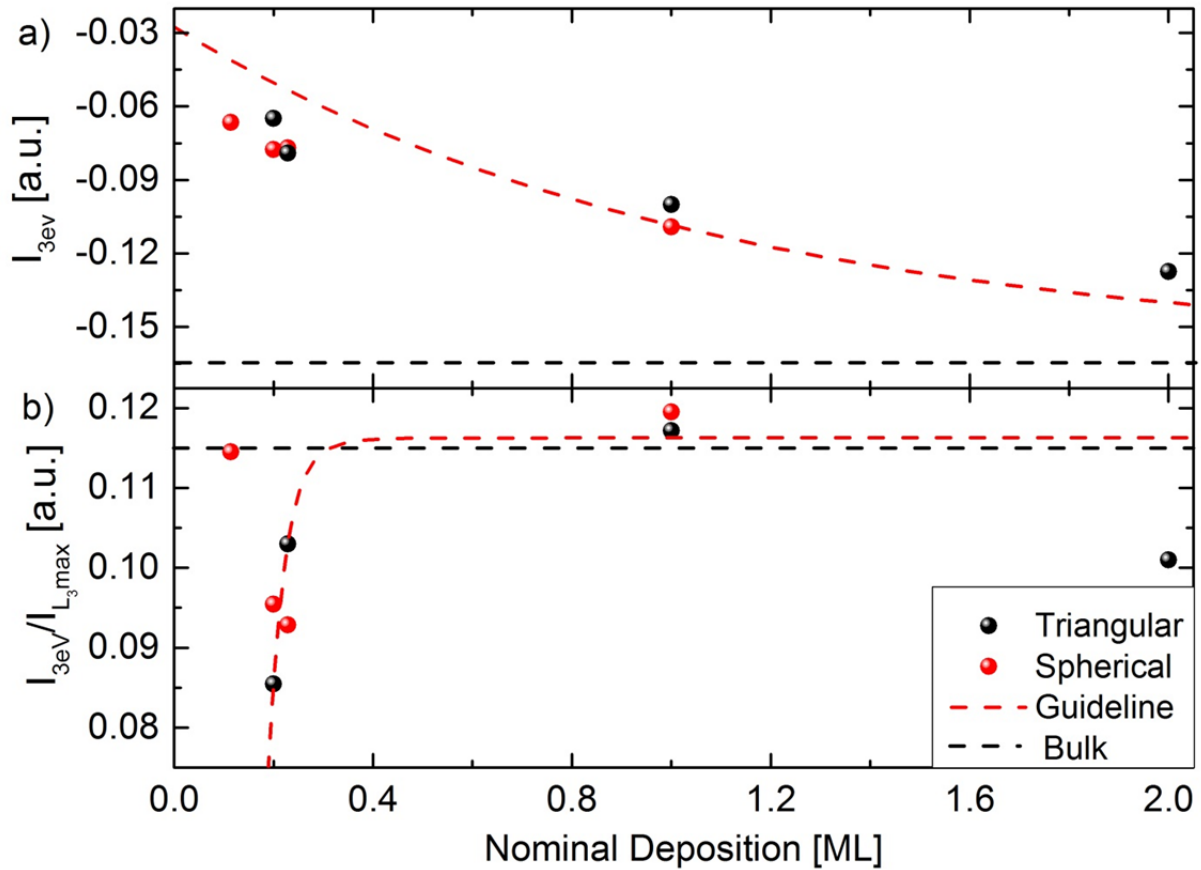


**Figure 5.14 a): Deposition dependent intensity of the satellite feature located 3 eV above the main  $L_3$  XMCD peak. b) 3 eV satellite intensity, normalized to the main  $L_3$  XMCD peak height. Dashed black lines label the respective ratios obtained from the bulk reference sample.**

The XAS intensity at the energy position of the 6 eV satellite (feature C) is shown in figure 5.15 a). For the smallest clusters, the satellite structure is still visible, albeit strongly decreased. Hence, even for the lowest nominal coverage, the XMCD effect vanishes at the 6 eV satellite energy position (see XMCD insets in figure 5.10 and figure 5.11). With increasing cluster size, the satellite feature becomes more pronounced, indicating a stronger admixture of  $3d^8$  states with increasing cluster size. However, the change of the satellite with respect to the white line intensity shows an inverse trend, as shown in figure 5.15 b). This indicates that the feature is not just a simple “feedback” of the main peak intensity. In the XMCD signal the 6 eV satellite energy position is clearly visible as zero of the XMCD effect. This distinct feature is, within the noise level, conserved even for lowest nominal Ni deposition and independent of the cluster shape.

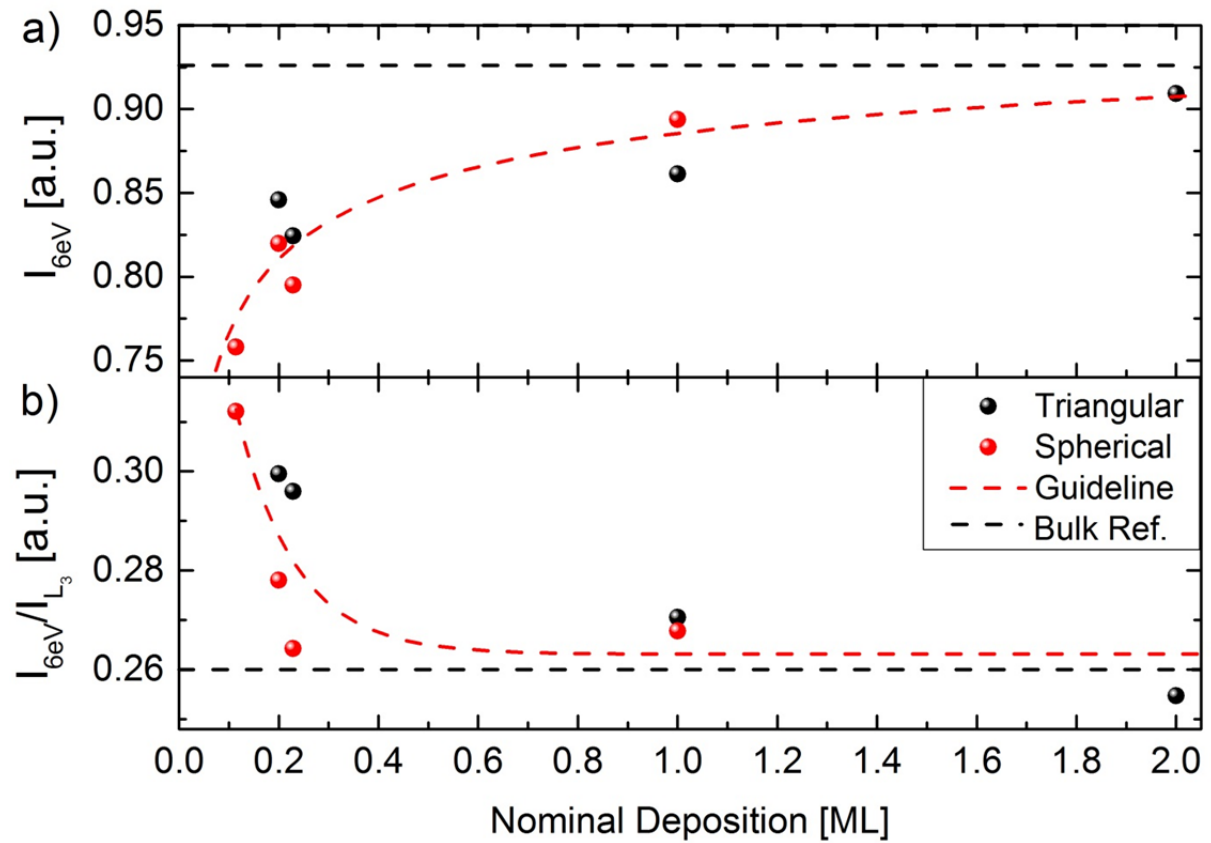


**Figure 5.15 a): Ni 6 eV satellite peak intensity in dependence of the nominal deposition. b): 6 eV satellite peak intensity, normalized to the main  $L_3$  peak intensity. Dashed black lines label the respective ratios obtained from the bulk reference sample.**

The “diffuse” region between the  $L_3$  and the  $L_2$ -edge of the Ni XMCD spectra is displayed in figure 5.16 a) for triangularly and figure 5.16 b) for spherically shaped clusters. The respective spectra have been normalized to the main  $L_3$  XMCD peak in order to probe the relative shift from convenient to “diffuse” contributions to the overall XMCD spectrum. For both cluster types, one finds no obvious change of the “diffuse” region that stands out from the noise level. In terms of the “diffuse” magnetism model, this indicates that the relative contribution of the Ni 4s states to the total XMCD signal remains unaffected.



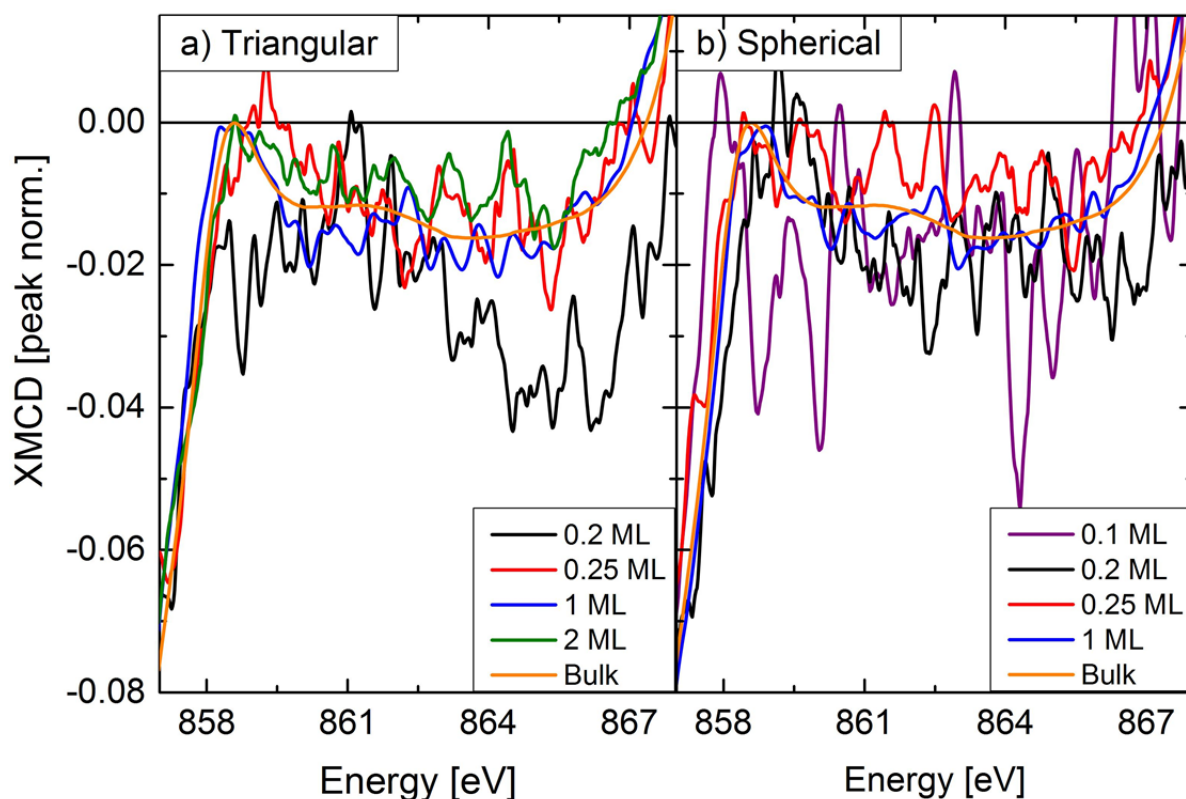


**Figure 5.16: XMCD spectra magnification of the “diffuse magnetism” region between the  $L_3$  and the  $L_2$ -edge for both a) triangularly and b) spherically shaped Ni nanoclusters. All XMCD spectra were normalized to equal  $L_3$ -edge dichroism.**

Due to similar results obtained for the unoccupied density of states, it seems vindicated to compare the results of the post  $L_3$ -edge spectral features to results obtained for Ni/Cu (001) and Ni/Co/Cu (001) systems investigated by Srivastava and Dhesi.

The results reported by Srivastava et. al. [139] for Ni/Cu (001) are limited to the non-dichroic XAS spectra of Ni films on Cu (001) with various thickness. The nominal Ni film thickness in their report ranges from 0.6-14.4 ML Ni/Cu (001). Besides the already mentioned change of  $n_h$ , they report that the 6 eV satellite feature completely disappears for the smallest Ni film thickness of 0.6 ML and 0.8 ML. The intensity of the 6 eV recovers when increasing the Ni film thickness as a consequence of increased fraction of  $3d^8$  in the ground state and a changed hybridization between  $2p^5 3d^9$  and  $2p^5 3d^{10}$  configurations in the final state.

Dhesi et. al. [140] report XMCD and XAS spectra for thin films of Ni/Co/Cu (001). They found that the 6 eV satellite decreases with decreasing the nominal Ni film thickness and finally vanishes for very small film thickness of 0.2 ML. The corresponding distinct “zero” of

the XMCD spectrum at this energy position loses its distinction with decreasing Ni film thickness.

The 3 eV satellite feature in the XMCD spectrum is more distinct for smaller Ni film thickness. With increasing Ni film thickness the distinct 3 eV feature reduces strongly.

In addition, they report increasing dichroism for the “diffuse” region between the  $L_3$  and the  $L_2$ -edge when decreasing the Ni film thickness, which could not be observed for the Ni/graphene system.

Compared to the above mentioned literature reports one finds similarities as well as certain distinctions between Ni thin films on transition metals and Ni nanoclusters on graphene. Besides the alterations of  $n_h$ , a reduction respective disappearance of the 6 eV satellite feature in the XAS signal is reported. On the other hand, the 3 eV and 6 eV satellite features and the “diffuse” region in the respective XMCD spectra deviate from the present results.

Thus a possible explanation is a strong interaction of Ni with the underlying graphene substrate, due to a strong hybridization of the Ni 3d with the graphene  $p_z$  states. The deviating behavior of the satellite features with respect to any Ni/TM system could be given by differences in the d-d and d- $p_z$  hybridization, where Ni on graphene is closer to its “natural”, namely bulk electronic states. However, from present measurements it is difficult to exactly quantify changes in the electronic configurations and propose a detailed mechanism which leads to the observed changes in the satellite intensities. This would require more detailed theoretical study which is beyond the framework of this thesis.

To summarize, following changes of the electronic structure of Ni in the Ni-cluster/graphene/Ir(111) system:

1. Feature A: The main  $L_3$ -peak representing the  $3d^9$  fraction in the Ni ground state as well as the number of holes  $n_h$ , decreases with decreasing cluster size. This trend is found for both, spherical and triangular shaped Ni clusters.
2. Feature B: The absolute and relative 3 eV satellite, representing the triplet (XMCD active)  $3d^8$  ground state, intensity decreases with decreasing cluster size. This effect is also found for both types of clusters. As it represents the triplet  $3d^8$  ground state, this indicates a partial loss of spin polarization of the Ni d-shell.

3. Feature *C*: The absolute 6 eV satellite representing the singlet (XMCD inactive)  $3d^8$  ground state intensity decreases with decreasing cluster size, for both cluster types, triangular and spherical. In relation to the main  $L_3$ -peak, the satellite intensity increases. In the respective XMCD spectra the 6 eV satellite is present as zero of the dichroic signal, even for the lowest nominal deposition of 0.1 ML.
4. Feature *D*: The “diffuse” region between the  $L_3$  and the  $L_2$ -edge exhibits no obvious change in dependence of the cluster size or shape.

#### 5.4.4. Ni cluster/graphene substrate interaction

In the CI picture, a reduction of feature *A* is linked to a reconfiguration of the initial  $3d^9$  to the XAS inactive  $3d^{10}$  states. This is found especially for the smaller clusters, where an elevated number of “interface” atoms is found compared to the overall cluster atoms. Therefore, the reduction of  $n_h$  is supposed to stem from hybridization of the graphene substrate with the Ni valence d-states of the interfacial cluster atoms. The carbon atoms in the graphene honeycomb exhibit a strong in-plane  $\sigma$  bonding. Thus chemical bonding is usually made by the  $p_z$  orbitals, forming  $\pi$ -orbitals oriented perpendicular to the graphene sheet.

In principle, the electronic properties of the graphene  $\sigma$  and  $\pi$  orbitals and their interaction with interfacial Ni atoms can be detected by XAS measurements on the C-K edge. This was demonstrated e.g. by Weser et. al. [144] for the monolayer graphene on a ferromagnetic Ni (111) substrate. As the  $\sigma$  and  $\pi$  orbitals have different energy levels and spatial orientations, they can be identified by angle dependent XAS scans over the C-K edge. As an example, angle dependent XAS spectra of the C-K edge of a monolayer graphene on a ferromagnetic Ni (111) substrate from reference [144] are shown in figure 5.17 (b). Note that these spectra were recorded with linearly polarized light and in the partial electron yield (PEY) mode, which is even more surface sensitive than the TEY mode. Two different spectral features are present in the XAS spectra: One arising from the  $1s \rightarrow \pi^*$  transition in the range of 283-289 eV. This feature increases with decreasing angle  $\alpha$ , the angle between the incoming beam direction and the sample surface, attesting an out-of-plane character for the  $\pi^*$  orbital. The other one is found in the region above 289 eV, corresponding to the  $1s \rightarrow \sigma^*$  transition. As the  $\sigma$  orbitals lay in plane, this feature evolves with increasing angle  $\alpha$ .

Compared to pristine graphite, the  $1s \rightarrow \pi^*$  transition exhibits a side peak which is related to further hybridization of the carbon respectively graphene  $p_z$  states with the underlying Ni substrate.

To probe the hybridization of the graphene  $\pi$  hybrid orbitals with the Ni d-states, similar measurements have been conducted for this thesis. As comparison, angle dependent XAS spectra of the C-K edge of graphene covered with nominally 0.15 ML Ni is shown in figure 5.17 a). For the reasons of clarity, the angle in this graph is given applying the same conversion as the referenced spectra, where  $\alpha$  denotes the angle between the incoming beam and the surface plane and not the surface normal. One can recognize three different features: One peak at 285.1 eV, which represents the C-K “main” peak. A smaller side feature appears at 287 eV. These two peak should address the  $1s \rightarrow \pi^*$  transition. Comparing the  $90^\circ$  to the  $25^\circ$  spectrum, no significant change is observed for the first peak, but a slight increase of the second feature at 289 eV is found. This feature seems to be slightly angle sensitive. A further peak is found at 291.5 eV which should represent the  $1s \rightarrow \sigma^*$  transition. However, in this region, there is no significant change in the XAS spectra measured at different angles.

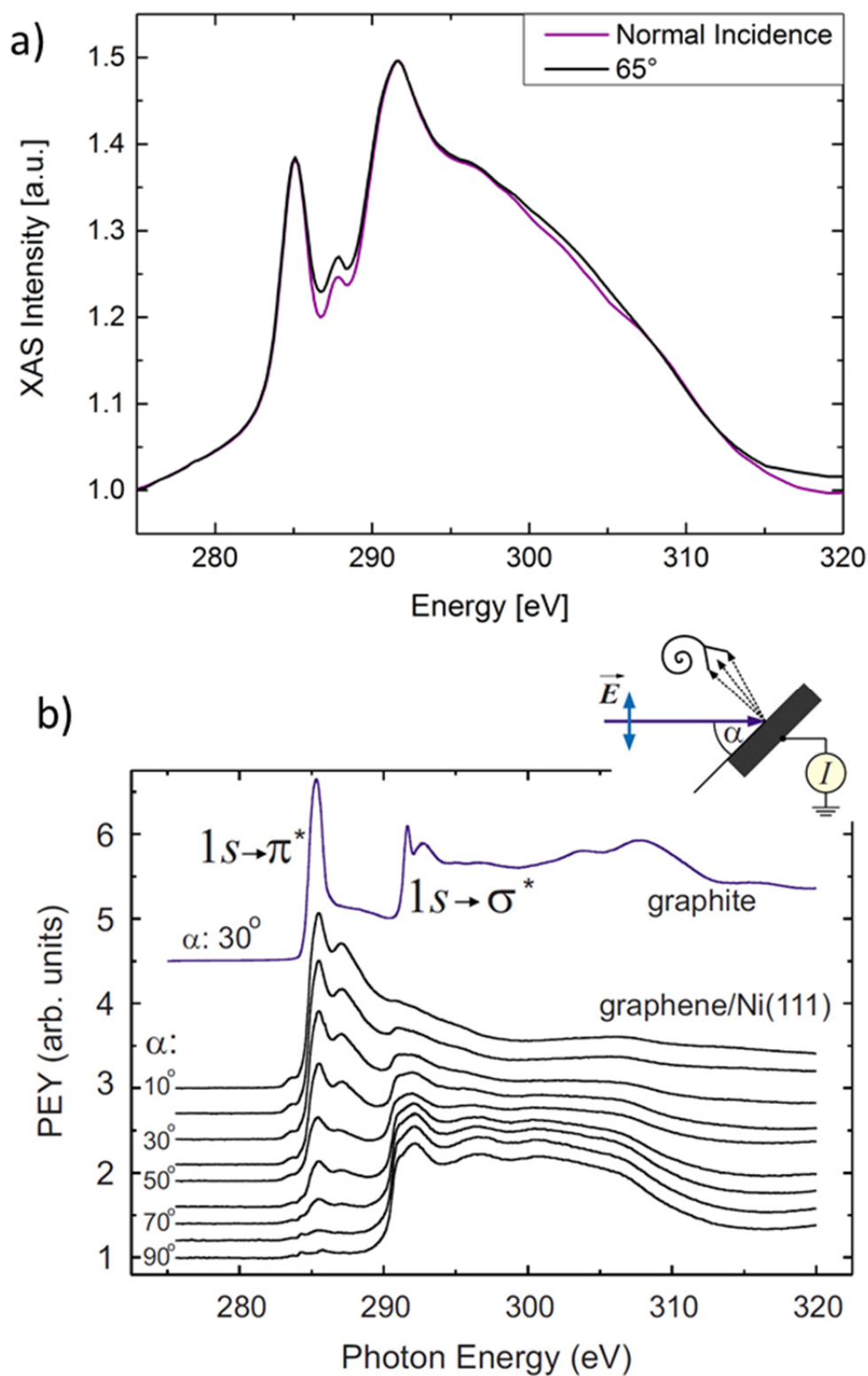


Figure 5.17: Comparison of a TEY XAS spectrum of the C-K edge of Ni/graphene (a) with angle dependent PEY XAS spectra of graphene/Ni (111) (b). The peaks corresponding to the  $1s \rightarrow \sigma$  and  $1s \rightarrow \pi$  could not be resolved with measurements in the TEY mode. (b) with permission from [144]. Copyright 2010, AIP Publishing LLC.

One also notes a certain difference in the overall appearance and the quality of the measured and the referenced spectrum, especially concerning the post-edge region. This difference stems from the following reasons:

1. The Ni cluster height is in the range of 1-2 nm (see section 5.2.1 and 5.3.1). Thus, the TEY signal from graphene areas that are contacted to the clusters is strongly damped compared to uncovered sample regions.
2. Although the underlying SC substrate is cleaned thoroughly, the presence of residual carbon in the Ir(111) matrix cannot be excluded. An (unwanted) contribution of residual carbon atoms to the overall XAS signal is possible. Although trying to remove background similar to the procedure described in section 4.4.4, it was not possible to isolate the single layer graphene XAS signal from background signal properly.
3. Another major problem measuring C-K edge XAS spectra is the contamination of the beamline optics with carbon atoms from residual carbon gases (for details see [145]). By time, carbon is burnt to the optical elements of the beamline setup, which results in a strong loss of incoming beam intensity and a change of the polarization degree in the region of the C-K edge (see e.g. [145-148], also for possible optical element cleaning procedures). The loss of intensity problem is usually solved by normalizing the sample drain current to the  $I_0$  signal. However, in this case this method failed because the  $I_0$  gold mesh was contaminated by residual carbon as well. Cleaning of beamline optics and in-situ refreshment of the  $I_0$  gold mesh to improve the spectra quality was abandoned, owing to the very high efforts for proper sample preparation and the uncertainty in the results to be expected.

Due to the aforementioned physical and technical restrictions, interpretation of the C-K edge measurements is difficult.

However, there is a number of mainly DFT based theoretical and a few experimental works that investigated the electronic properties of the Ni/graphene interface. The principal question concerns the hybridization mechanism and its consequences especially on the Ni band structure.

This can be understood by trying to place a single Ni atom on the graphene sheet. In principle, the adatom can occupy three different sites on the graphene, either the hollow site in the honeycomb center, a bridge site atop the center of one of the C-C bonds or a site atop one of the carbon atoms. Theoretical calculations [149-153] as well as STM investigations [154] report that single Ni atoms adsorb preferentially on the hollow site at the honeycomb center (these findings account also for the other transition metals like Fe and Co). Here, the coordination number for the Ni atom is maximized and the Ni d-states will couple to the graphene. Owing to the coupling between Ni and graphene, an electronic reconfiguration of the Ni s- and d-states takes places and also charge transfer to the graphene support occurs.

Duffy and Blackman investigated properties of 3d transition metal adatoms and dimers on graphene<sup>30</sup> with DFT based theoretical calculations [152]. They found a general tendency that the TM 3d states lower their energy at the expense of the 4s states, the preferred electronic configuration (in an atomic picture) therefore changes from  $3d^n 4s^2$  to  $3d^{n+2} 4s^0$ . In particular, their calculations yield a  $3d^{9.2} 4s^{0.6}$  configuration for a Ni atom adsorbed in the center of the graphene hexagon. The remaining 0.2 electrons are transferred from Ni to graphene. For Dimers, they predict a  $3d^{9.1} 4s^{0.8}$  configuration and a charge transfer of 0.1 electrons from Ni to graphene, indicating that the reconfiguration and charge transfer process becomes less pronounced effect with increasing number of Ni atoms adsorbed on the graphene substrate.

Cao et. al. found similar results performing a DFT study on the TM atoms/dimers on graphene [150]. Starting from a free Ni atom with a  $3d^8 4s^2$  configuration, they report a reconfiguration for the Ni atom adsorbed to graphene. The d-states are populated on the expense of the 4s orbitals resulting in a  $3d^{9.13} 4s^{0.17}$  configuration. The initial Ni 4s electrons are partially transferred into the Ni 3d band and the graphene substrate ( $q = 0.7$ ). For dimers, they estimated a Ni configuration of  $3d^{8.85} 4s^{0.67}$ . Charge transferred from Ni to graphene is  $q = 0.48$  electrons.

In the same context, Johll et. al. found for a Ni adatom an electronic reconfiguration from  $3d^{8.77} 4s^{1.23}$  for the free Ni atom to  $3d^{9.12} 4s^{0.16}$  for the Ni atom adsorbed on a graphene substrate [151]. Consistent with the aforementioned publication, they predict a resulting

---

<sup>30</sup> The results were published in 1998; hence graphene was labeled “monolayer graphite” then.

charge transfer from Ni to graphene of 0.7 q. They also treated the adsorption of Ni dimers on graphene. There are several stable binding geometries, the one with the smallest binding energy is identified the Ni-Ni axis located parallel to the graphene plane and with the respective Ni atoms located atop of the hollow honeycomb center. Here, the charge transfer to the graphene is still high (0.59 q/Ni atom), and both Ni atoms strongly interact with the graphene sheet. Another stable configuration corresponds to one Ni atom occupying the hollow site and the other one piling atop of it. Then, the total charge transfer to the graphene sheet is reduced, resulting only from the interface Ni atom, while the Ni atom placed further away from the graphene sheet almost exhibits “atomic” character.

Johll et. al. extended their DFT investigations also to TM tri- and tetramers [153]. For both systems, one can find more than one possible stable adsorption geometry, thus only the results for the most stable (and thus most probable ones) shall be summarized. In the case of a free Ni trimere they report an electronic configuration  $3d^{9.14}4s^{0.86}$  for each Ni atom (Ni atoms arranged in an equilateral triangle). In case of Ni trimere adsorption on graphene, the geometric configuration with the highest binding energy is where the trimere triangle plane is aligned perpendicular to graphene. The two base Ni atoms are then located between two neighboring C atoms. Electron transfer mainly affects the two base atoms next to the graphene (0.41 and 0.49 q), whereas the top atom remains unaffected. However, the electron transfer stems mainly from the Ni s-electrons, as the base atom configuration changes to  $3d^{8.97}4s^{0.62}$  and the top atom configuration to  $3d^{8.94}4s^{1.17}$ .

For the tetramere, again only the interfacial Ni atoms undergo a significant change in electronic configuration, thus they conclude that these interfacial Ni atoms are shielding the next-next Ni layer atoms from any influence of the graphene substrate. A summary of Ni adatom configurations is given in table 5.4.



**Table 5.4: Electronic configuration of Ni adatoms on graphene as reported in literature. N denotes the number of adatoms. In columns “3d” and “4s”, the respective configuration is given, and  $n_h = 10 - 3d$  describes the number of holes per Ni adatom. In column  $\Delta q$  the electron transfer between Ni adatoms and the graphene substrate are given. Positive sign denotes electron transfer from Ni to graphene.**

Reference	n	3d	4s	$n_h$	$\Delta q$ [e <sup>-</sup> ]
Duffy et. al. [152]	1	9.2	0.6	0.8	0.2
	2	9.1	0.8	0.9	0.1
Cao et. al. [150]	1	9.13	0.17	0.87	0.7
	2	8.89	0.67	1.11	0.48
Johll [151, 153]	1	9.12	0.16	0.88	0.72
	2	8.97	0.50	1.03	0.59

Experimental work on the field of Ni adatom interaction with a graphene substrate has been performed for example by Gyamfi using STM and scanning tunnel spectroscopy (STS) [154] and Eelbo using XAS/XMCD methods [155].

Gyamfi et. al. investigated Ni adatoms and clusters deposited at low temperatures (12 K) on graphene on SiC (0001) [154]. They performed STM measurements and report, in agreement with theory results summarized above, that Ni adatoms sit preferably into the hollow honeycomb site of graphene. The corresponding STS spectrum and theoretically derived LDOS (using DFT methods) are shown in figure 5.18. The STS spectrum (dashed red line in figure 5.18 a)) was measured at the Ni adatom site and shows several well pronounced peaks at -1.3 V, -0.7 V, and +0.45 V. The bare graphene substrate lacks any kind of peaks. In order to reveal the origin of these peaks, they compare their STS results with simulated LDOS obtained from DFT calculation with different initial configurations ( $3d^8$  to  $3d^{10}$ ) of the Ni adatom, as shown in figure 5.18 b). The STS peaks match best with the calculated LDOS of Ni in  $d^{10}$  configuration. The peaks at -1.3 V and -0.7 V correspond to d-state resonances, the peak at +0.45 V is related to Ni s-states. Hence, they conclude that the Ni adatom on graphene is present mainly in the  $3d^{10}$  configuration.

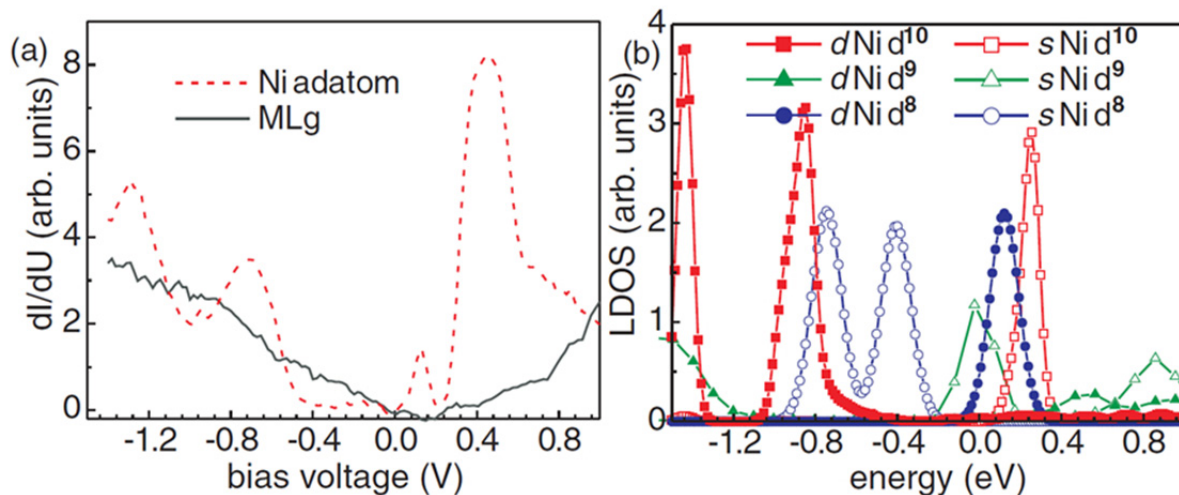


**Figure 5.18: a) Comparison of an STS curve of a Ni monomer on graphene/SiC (0001) (red dashed line) with the STS curve of the bare graphene substrate (black solid line). b) Theoretical calculation of the LDOS of Ni monomer with different electronic configuration. Reprinted with permission from [154]. Copyright (2012) by the American Physical Society.**

Further experimental investigations of Ni mono-/dimers on a graphene substrate have been performed by Eelbo et. al. [155]. They applied XAS/XMCD techniques similar to this thesis, although their nominal Ni deposition (labeled as “mono layer equivalent, (MLE)” in the referenced paper) is much lower, 0.007 MLE and 0.014 MLE of Ni corresponding to mono-/dimers on graphene respectively. The measurements were carried out under similar conditions: sample temperature of 10 K and applied field of 5 Tesla and in two different geometries: Ni ( $0^\circ$ ) and  $70^\circ$  with respect to the incoming beam intensity. Their results are shown in figure 5.19 a) and b).

At first glance one notes that the spectral shape is different from the spectra presented in figure 5.4 and figure 5.7. They report a multiplet like structure with two pronounced peaks (A, B, respectively C, D, not to be confused with the 3 and 6 eV satellites discussed before) in contrary to the single main peak that would be found in a bulk like Ni XAS spectrum. According to their argumentation this multiplet feature is related to a hybridization of Ni  $d_{z^2}$  and s-orbitals (peak A), and Ni  $d_{x^2-y^2}$  and  $d_{xy}$  orbitals with the graphene  $p_z$  states (peak B). Indeed, similar multiplet splitting is reported from highly coordinated Ni in a  $Cs[NiCr(CN)_6] \cdot H_2O$  complex [156]. Furthermore, for the Ni adatom the XMCD signal vanishes completely and they conclude that Ni is present in the nonmagnetic  $d^{10}$  configuration. However, a pure  $d^{10}$  configuration would result in a different, only step-

like XAS spectrum, as observed for example for Cu [7] or Zn [71]. For the Ni dimer they report a similar multiplet XAS spectrum and a small but measurable XMCD signal. They explain the occurrence of a sizeable XMCD signal to stem from a partial depopulation of Ni d-states, while s-states are repopulated. Values for magnetic spin and orbital moments are not provided. However, from reproduced data one obtains  $m_l \sim 0.01 \mu_B/n_h$ ,  $m_s \sim 0.016 \mu_B/n_h$ ,  $m_{\text{tot}} \sim 0.026 \mu_B/n_h$  for the orbital, spin, and total angular momentum respectively. The XMCD signal shows no obvious angle dependency, indicating absent or only very small magnetic anisotropy.

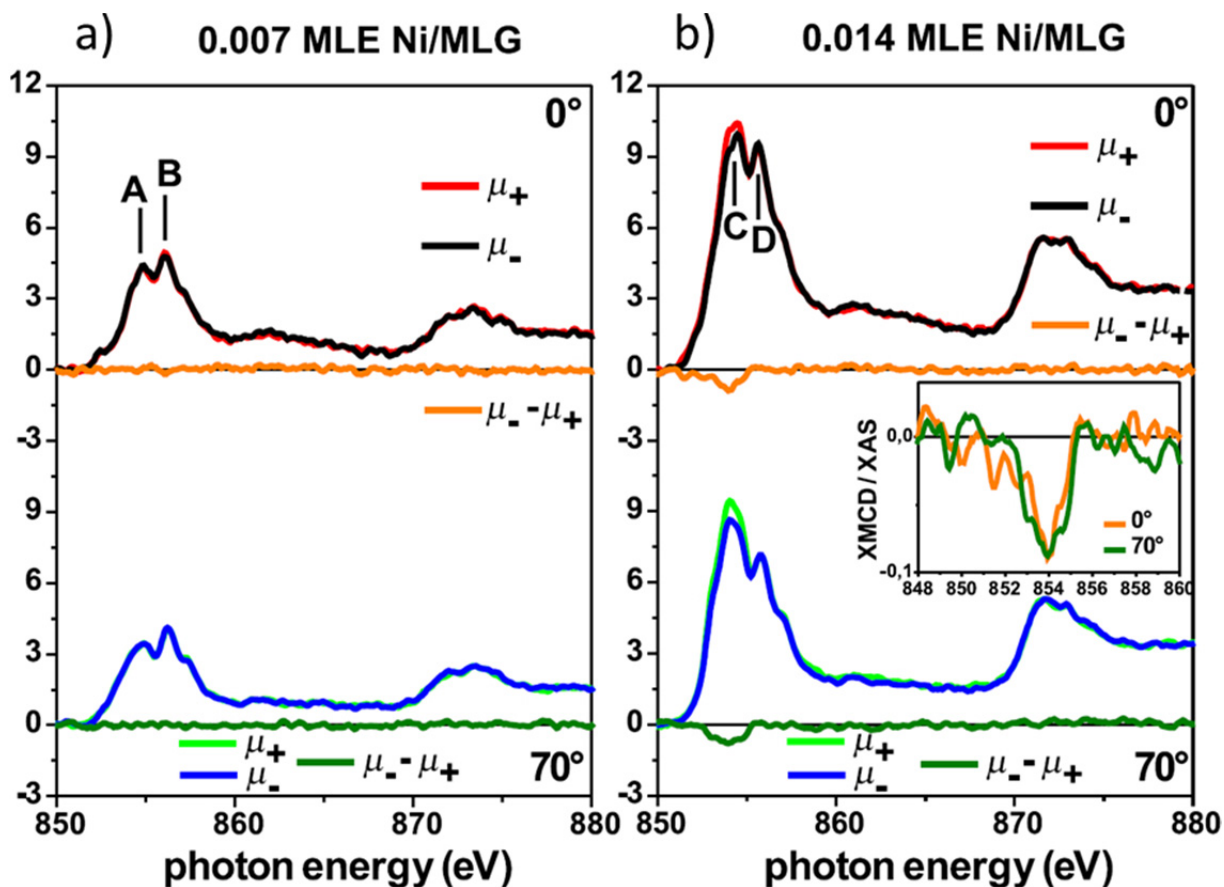


Figure 5.19:  $L_{2,3}$ -edge XAS and corresponding XMCD spectra of a Ni adatom (a), and a Ni dimer (b) on graphene/SiC (0001) in NI (0°, upper panel) and 70° geometry (lower panel). Reprinted with permission from [155]. Copyright (2013) by the American Physical Society.

For a larger Ni/Graphene contact area, interfacial properties are often considered in terms of the work function difference of both materials. For Ni work function values between 5.12 eV [157], 5.3 eV [158], and 5.5 eV [159] are reported. The work function of graphene is 4.6 eV [158]. Due to the higher work function of Ni, electron transfer from

graphene to Ni is expected. For example, Stokbro et. al. [160] and Liu et. al. [161] predict electron transfer from Ni to graphene (p-doping of graphene), using DFT calculations in order to determine charge transport properties at the Ni/graphene interface. Thus electron transfer from graphene would also result in increased d-state occupancy. For the present thesis, the work function approach is certainly simplifying the experimental conditions too much, as graphene has a much larger contact area with the Ir (111) SC than with the Ni nanoclusters. On the other hand, the difference in work functions could also explain the similarity to the electronic behavior of ultrathin films of Ni on Cu (001). The work function of Cu is 4.9 eV [159], which is only 0.3 eV higher than the work function of graphene, indicating electron transfer from Cu to Ni. Indeed, a similar trend of increasing  $n_h$  with increasing film thickness was reported [139, 140, 142] and a strong hybridization of the Ni and Cu dstates was suggested to cause the filling of the Ni d-band.

In summary literature reports agree on a change in the Ni d-band structure when brought in contact with graphene, although the quantitative values may differ partially. The interaction with the graphene substrate leads to a change of the electronic states in the Ni atoms located directly at the cluster/graphene interface. As a consequence, their d-states are populated and the ratio of the different possible ground state configurations of the respective Ni atoms ( $|d^8\rangle, |d^9\rangle, |d^{10}\rangle$ ) is shifted towards the  $|d^{10}\rangle$  ground state. The most extreme case is the pure  $d^{10}$  configuration of a single Ni adatom on graphene reported by Gyamfi [154]. The change of d-band states is attenuated when increasing the cluster size, as atoms located further away from the graphene sheet are “shielded” by their interfacial counterparts. For small cluster size, there are an elevated number of interfacial atoms with respect to the total number of Ni atoms in the clusters. The interfacial atoms interact with the graphene substrate and exhibit mainly a  $|d^{10}\rangle$  configuration which results in a strong damping of the main Ni  $L_3$ -peak line in the XAS spectrum and a reduction of the number of holes  $n_h$ . In contrast to the single atom or dimer case (see figure 5.19), the total number of atoms is sufficient to yield a significant magnetic XMCD signal. While increasing the cluster size, growth occurs not only lateral but also vertical. This results in a disproportionately increase of the ratio between the number of total and interfacial atoms. Thus, the shift towards the  $|d^{10}\rangle$  configuration is still sizeable but with increasing cluster size, properties are shifted strongly towards bulk Ni values. As magnetism in TM is mainly “made” from a

spin imbalance in the d-states (see section 3.1.4), this change of the electronic configuration will also affect the magnetic properties of the clusters. This will be shown in the following subsection.

#### 5.4.5. Ni magnetic moment analysis

The  $n_h$  normalized total magnetic moment for both, triangular and spherical clusters is displayed in figure 5.20, summarizing the values of table 5.1 and table 5.2. For both, spherical and triangular clusters one finds a common trend line and no significant change in dependence of the cluster shape is found. The combined presentation shows a magnetic moment that decreases strongly with decreasing cluster size, for triangular and spherical shapes.

The decline of magnetic moment with decreasing cluster size can be well understood in terms of the electronic properties discussed above. The interfacial Ni atoms shift towards a  $d^{10}$  configuration, which is nonmagnetic as the d-shell is completely filled. The magnetic moment per atom (per  $n_h$ ) is then reduced as well. With increasing cluster size, the influence of the Ni atoms located at the graphene interface and their  $d^{10}$  character reduces on the benefit of magnetic  $d^8$  and  $d^9$  states. The magnetic behavior finally converges towards bulk properties above a nominal deposition of 2 ML.

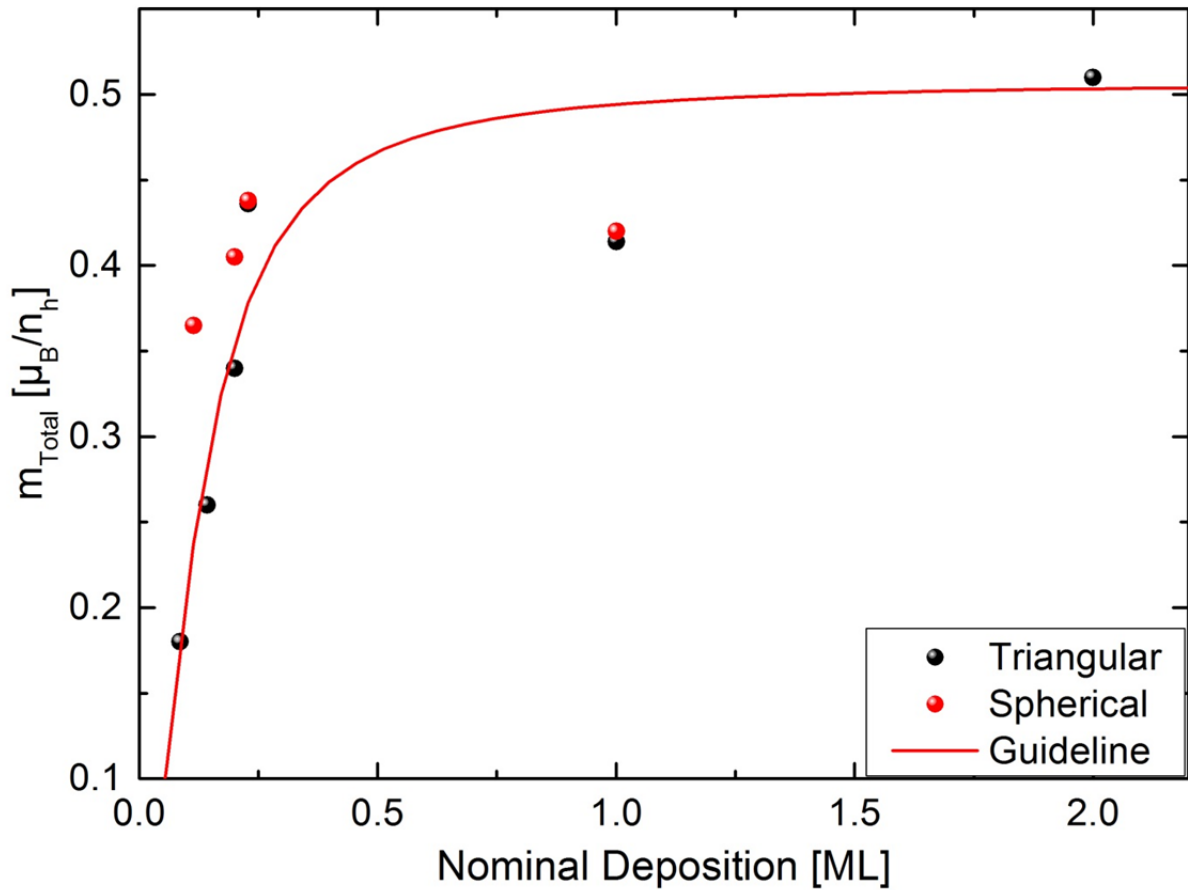


**Figure 5.20: Magnetic moments of Ni clusters/graphene in dependence of nominal Ni deposition and normalized to  $n_h$ . The magnetic moment converges towards the bulk Ni value with increasing cluster size. No obvious shape dependence was observed.**

Owing to the strong change in  $n_h$  for Ni clusters on graphene, it is of prominent importance to regard this change in the unoccupied density of states before applying sum rules. Although many size dependent XMCD studies on TM cluster have been performed, most of them calculate magnetic moments simply using the constant bulk value for  $n_h$ . Here, the results for  $n_h$  summarized in table 5.3/figure 5.13 were applied together with equations (3.54) and (3.55) to estimate the magnetic spin and orbital moments.

The results are shown in figure 5.21 and listed in table 5.5. The total magnetic moment varies from  $0.12 \mu_B$  for 0.1 ML to  $0.65 \mu_B$  for 2 ML nominal deposition of Ni. The size dependence follows a convolution of the trend line of the  $n_h$  normalized magnetic moment in figure 5.20 and the  $n_h$  curves in figure 5.13. For 2 ML nominal deposition, the total magnetic moment is  $0.65 \mu_B$ . At the end, the trend line converges towards the bulk value of

$0.76 \mu_B$  beyond nominal deposition of 2 ML. The origin of this effect has been discussed above for the  $n_h$  normalized magnetic moments and accounts also here.

In principle, the guideline for the magnetic moment could be extended with the results of Eelbo (see figure 5.19) down to the atomic scale (0.007 ML), where the XMCD signal and thus the magnetic moment completely vanishes [155].

The ratio of the orbital to the spin magnetic moment  $m_l/m_s$ , is tabulated on the very right of table 5.5 and plotted in figure 5.22. Usually, smaller cluster exhibit an enhanced orbital magnetic moment, therefore an enhancement of the  $m_l/m_s$  ratio with respect to the bulk properties is expected. The smallest clusters show indeed a slight increase of  $m_l/m_s$ . For nominal deposition lower than 0.25 ML, the  $m_l/m_s$  ratio is larger than 20 %, for triangular and spherical clusters. The trend line then converges progressively towards the bulk ratio of approximately 12 %, which is obtained at a nominal deposition of 0.25 ML for triangular and spherical cluster. The increase of  $m_l/m_s$  with decreasing cluster size seems, at first glance, in accordance with the expected result (see e.g. section 3.3). However, considering the absolute numbers, there is no effective increase of the orbital magnetic moment. The increased ratio  $m_l/m_s$  a result of the loss of spin polarization of the d-states and the resulting decrease of the spin magnetic moment  $m_s$ .

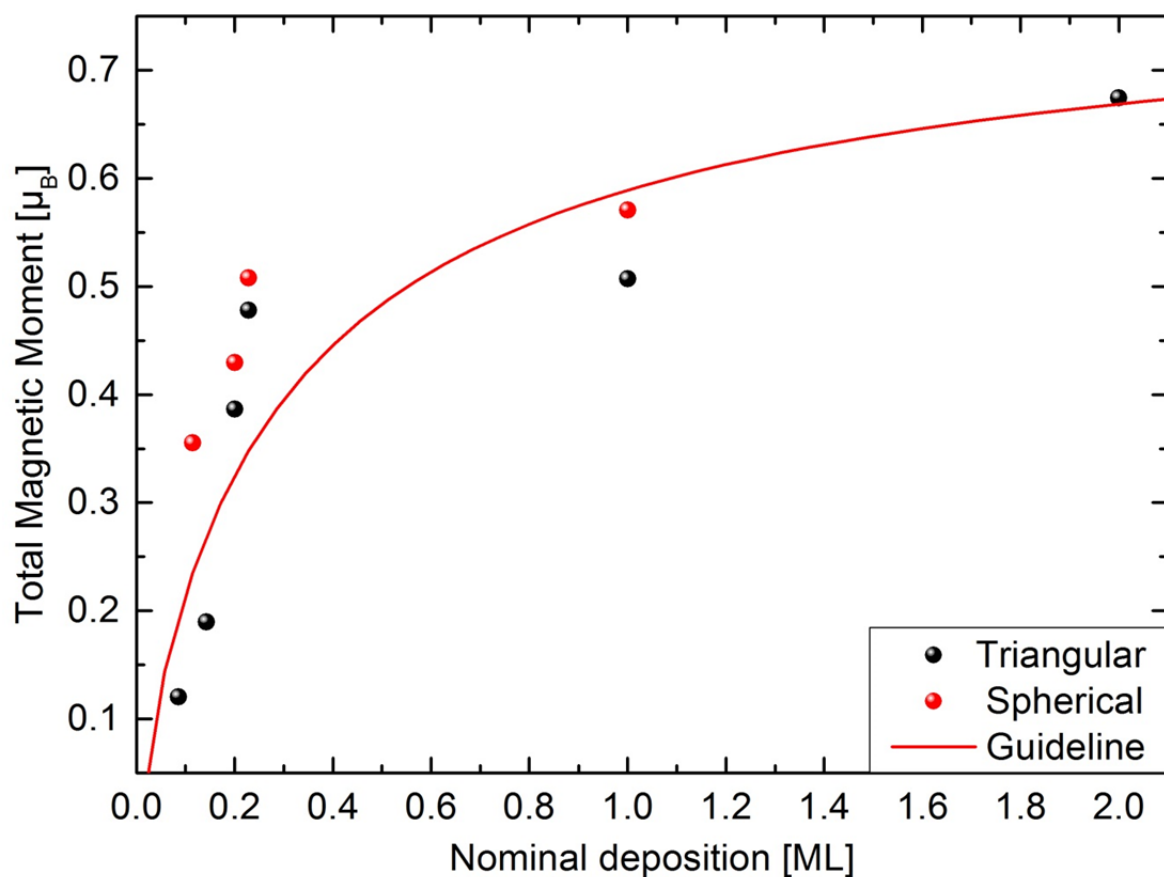


Figure 5.21: Total magnetic moment  $\mu_{\text{tot}}$  in dependence of the nominal Ni deposition after taking the change of electronic configuration of the Ni d-band into account. The overall magnetic moment increases with increasing cluster size, converging towards the bulk value above a nominal deposition of 2 ML.



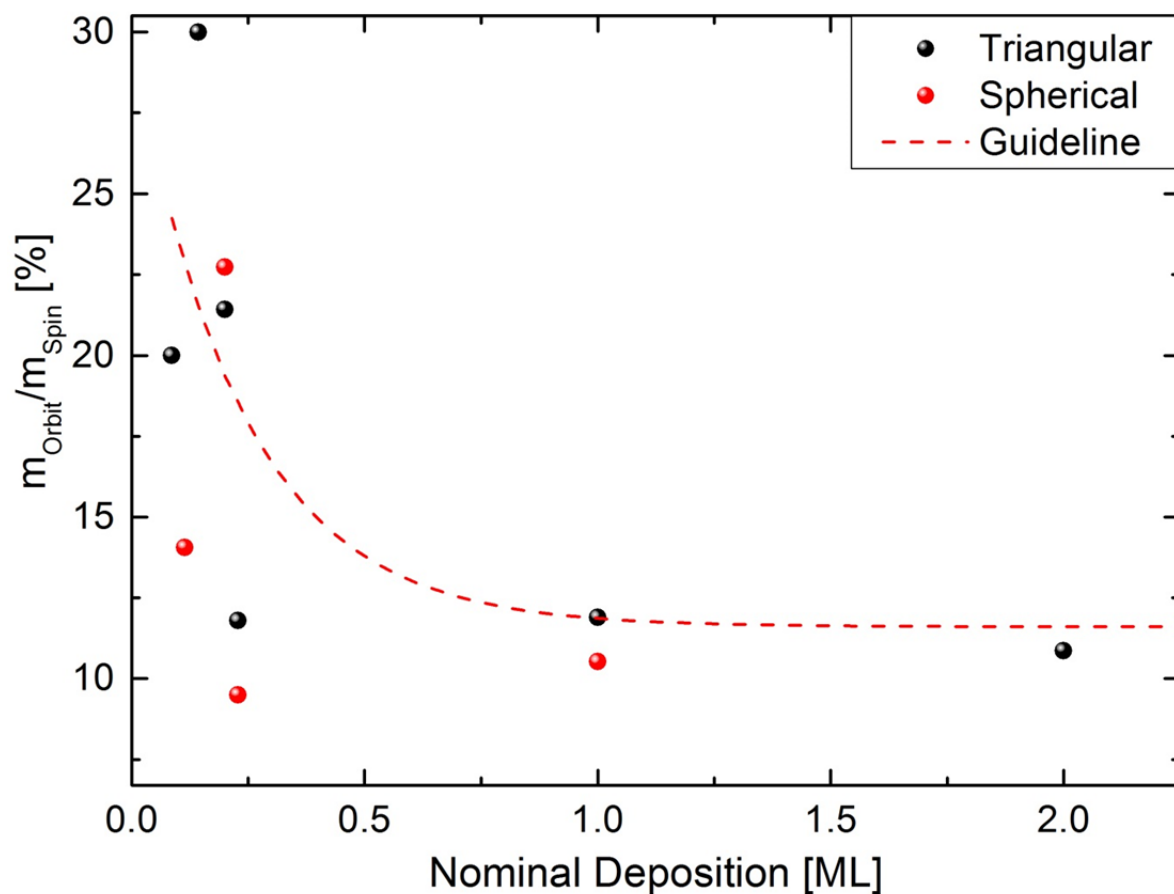


Figure 5.22: Orbital to spin moment ratio,  $m_l/m_s$ , in dependence of the nominal Ni deposition, for both, spherical (red dots) and triangular (black) shaped nanoclusters. For smaller clusters the ratio is enhanced as expected for nanocluster systems, however only due to the reduction of  $m_s$ .

**Table 5.5: Spin ( $m_s$ ), orbital ( $m_l$ ), total ( $m_{tot}$ ) magnetic moment, as well as the orbital to spin magnetic moment ratio in dependence of the nominal deposition.**

Nominal Deposition [ML]	$m_s$ [ $\mu_B$ /atom]	$m_l$ [ $\mu_B$ /atom]	$m_{Total}$ [ $\mu_B$ /atom]	$m_l/m_s$ [%]
<b>Spherical</b>				
0.15	0.23	0.04	0.27	14.1
0.2	0.4	0.065	0.465	22.7
0.25	0.3	0.03	0.33	10
1	0.53	0.06	0.59	10.5
<b>Triangular</b>				
0.1	0.1	0.02	0.12	20.0
0.15	0.15	0.04	0.19	30.0
0.2	0.32	0.07	0.39	21.4
0.25	0.43	0.05	0.48	11.8
1	0.45	0.05	0.50	11.9
2	0.61	0.07	0.68	10.9
<b>Bulk Ref.</b>	0.68	0.08	0.76	12.8

The loss of magnetic moment with decreasing cluster size contradicts the results found for (interaction) free Ni clusters that was been observed by Billas et. al. [36, 37]. They reported magnetic moments of up to  $1.2 \mu_B$  per atom for Ni clusters from a cluster beam (see also section 3.3, in particular figure 3.11 a)).

However, due to the electronic properties (see previous subsection) the present findings can be well explained. The diminished magnetic moment for smaller Ni clusters is a consequence of the d-shell filling of the Ni atoms with additional electrons due to their interaction with the underlying graphene interface.

In order to illustrate this qualitatively the spin polarized density of Ni 3 d-states, calculated by Park et. al. [162] for bulk fcc Ni, is shown in figure 5.23. Most of the majority ( $\uparrow$ ) spin states are located below the Fermi level, whereas states above the Fermi level are almost exclusively of minority ( $\downarrow$ ) spin character. Additional electrons, e.g. transferred from graphene to Ni, will populate the states located directly above the Fermi level. This will

result in a shift of the Fermi level from the solid black to the dashed black line in figure 5.23. As a consequence, the spin polarization of the d-states and thus the magnetization decreases. For example, from the integrated DOS, one can determine the magnetization according to equation (3.30). For bulk Ni one finds  $n_{\uparrow} \sim 4.66$ ,  $n_{\downarrow} \sim 3.98$ ,  $m = 0.68 \mu_B$ <sup>31</sup> and from the reported results  $n_h = 1.45$ . For triangular Ni cluster graphene with 0.2 ML nominal deposition it was found that  $n_h = 1.13$ , meaning that 0.32 electrons had to be transferred to the Ni d-band. Adding these 0.32 electrons to the band structure in figure 5.23 shifts the Fermi level approximately 0.16 eV to the right and the number of spin up and down states changes accordingly:  $n_{\uparrow} \sim 4.68$ ,  $n_{\downarrow} \sim 4.30$ . This results in a net magnetic moment of  $m = 0.38 \mu_B$ , which close to the experimentally determined value for the spin magnetic moment. Besides the reduction in the magnetic moment, one should note that the additional electrons are mainly populating minority spin states. The spin dependent charge transfer is in total  $\Delta n_{\uparrow} \sim +0.02$  and  $\Delta n_{\downarrow} \sim +0.32$ . Note that referring to bulk Ni DOS calculations is not accurate. However, as properties of the Ni clusters approach bulk properties quickly one may state that their electronic states are closer to the bulk than to the isolated atom properties. Furthermore, this approximation suggests that charge transfer from graphene to Ni clusters atop is spin dependent. This is an important feature of the Ni/graphene system as such a spin transfer is desired for graphene based spin tronic devices.

---

<sup>31</sup> Note that values in reference [162] are given with higher accuracy. However, due to a particular uncertainty in the digitization procedure, values are given as approximation.

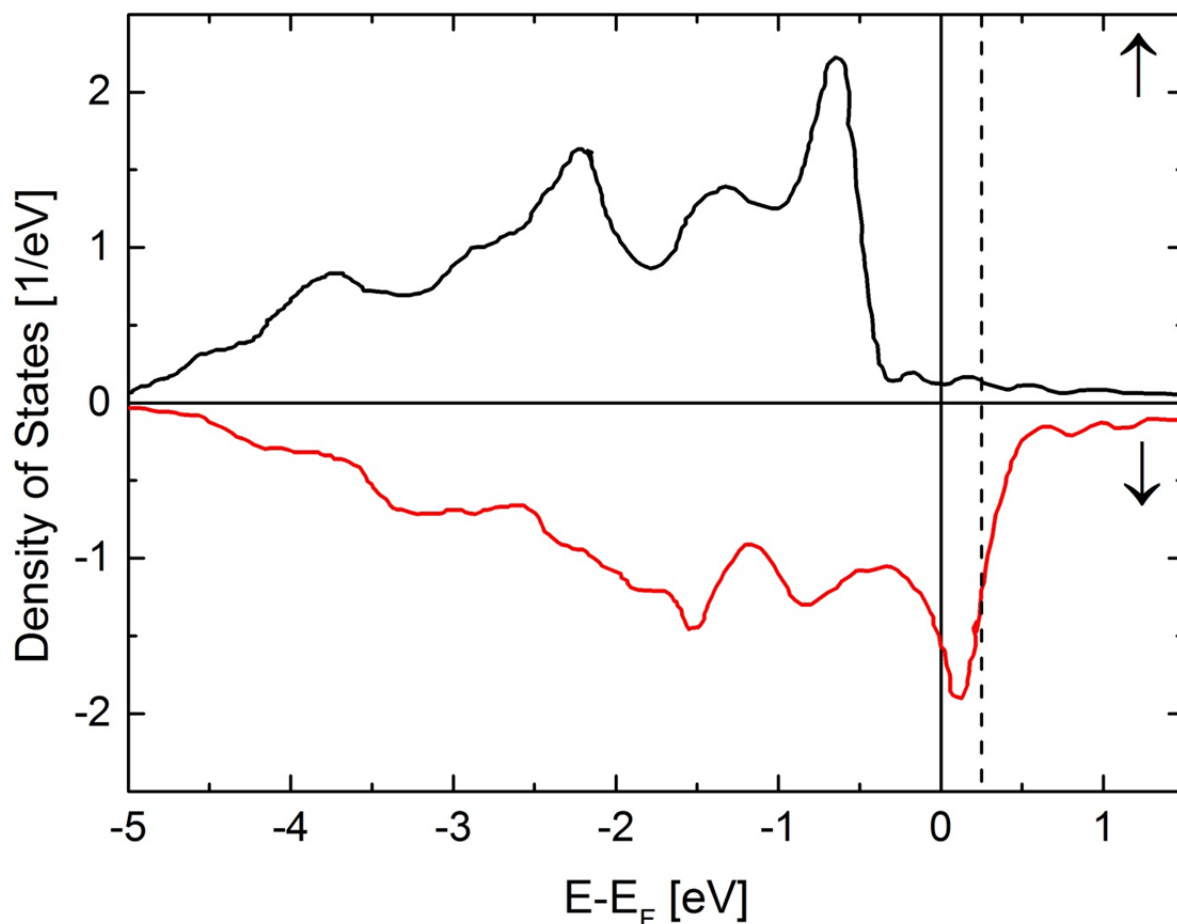


**Figure 5.23: Spin polarized density of Ni d-states in (001) fcc Ni. Due to charge transfer to Ni the d-states occupancy increases and the Fermi level shifts to higher energy (solid to dashed line), resulting in a decreased spin polarization in the Ni d-shell. Data reproduced from reference [162].** The influence of the Ni-graphene interaction becomes less pronounced with increasing number of Ni atoms, especially if the Ni atoms are not in direct contact with the underlying graphene. With increasing cluster size, the fraction of interfacial with respect to volume atoms and their influence on the electronic properties decreases. This has been found for the cluster system investigated within this thesis and is reported as well as in several literature studies.

Theoretical calculations for single atoms on graphene were performed for example by Johll et. al. [151], Duffy and Blackman [152] (on the structurally equal graphite surface), Yagi [163], Wehling et. al. [149], and Cao et. al. [150] (all of them using DFT methods) and consistently yielded a vanishing Ni magnetic moment. These results are experimentally supported by the XMCD results from Eelbo [155] shown in figure 5.19, where the XMCD signal of single Ni adatoms (0.007 MLE) on graphene disappears completely, although measurements were performed at high fields of 5 T and low temperature of 10 K.

For an increasing number of Ni atoms, e.g. for Ni dimers on graphene reported results are ambiguous, as they are strongly depending on the respective location of the dimer and also the calculation method (LDA, PBE).

Duffy and Blackman [152] report vanishing of the magnetic moment also for Ni dimers on graphite (for comparison they report  $1 \mu_B$  for the unsupported case) and that there is no induced magnetic moment on the carbon atom sites at the graphite surface.

Johll et. al. [151] report  $\sim 0.99 \mu_B/\text{atom}$  for the most stable dimer configuration (bond axis perpendicular to graphene sheet and both Ni atoms piled above each other), which equals almost their free Ni dimer moment of  $1 \mu_B/\text{atom}$ . However, they report also of a possible, albeit energetically less favorable, configuration with vanishing magnetic moment of the Ni atoms (bond axis parallel to the graphene sheet). In a further publication [153], they investigated tetra- and dimers with magnetic moments of  $0.68 \mu_B/\text{atom}$  and  $0.5 \mu_B/\text{atom}$  for the most stable configurations, respectively. Generally, they report that the magnetic moment of atoms facing the graphene substrate directly is lower than for atoms with another Ni neighbor in between.

Cao et. al. [150] report similar results, but here the most stable configuration depends on whether LDA or PBE was applied in the DFT calculations. For LDA calculations, the dimer bond axis is parallel to the graphene sheet with a vanishing magnetic moment. For PBE calculations the case is similar to Johll et. al. mentioned above, bonding axis is aligned perpendicular to the graphene sheet and the magnetic moment is  $2.04 \mu_B/\text{dimer}$  ( $1.02 \mu_B/\text{atom}$ ). For comparison, they report  $2 \mu_B/\text{dimer}$  ( $1 \mu_B/\text{atom}$ ) for free Ni dimer.

Eelbo et. al. investigated also higher nominal Ni deposition on graphene (0.014 ML). Here they find a sizeable XMCD signal, but it is only 1 % with respect to the white line intensity. They report no sum rule value of the magnetic moment; from the reproduced data one obtains approximately  $m_l = 0.01 \mu_B/n_h$ ,  $m_s = 0.016 \mu_B/n_h$ ,  $m_{\text{Tot}} = 0.026 \mu_B/n_h$  for the  $n_h$  normalized orbital, spin, and total angular moment respectively. However, using DFT calculations they found a maximum magnetic moment of  $0.85 \mu_B/\text{atom}$  for a monolayer of Ni on graphene. They claim that Ni clusters consisting of less than four Ni atoms remain nonmagnetic on the graphene substrate.

Further studies consider the other extreme case were (multi-) layers of Ni are brought into contact with a layer of graphene. Using spin-polarized first-principle calculations, Bertoni et. al. [164] found a decreasing Ni magnetic moment for the contacting layer of up to

~ 22 % with respect to bulk properties ( $0.514 \mu_B/\text{Ni atom}$ ) for a graphene sheet on multiple Ni layers. The loss of magnetic moment propagates also to the neighboring Ni layer.

Similar findings were reported by Abtew et. al. [165], using first principles electronic structure methods to calculate the magnetic moment of Ni atoms in multiple Ni layers on graphene. They report a decrease of the Ni magnetic moment for the first three Ni layers. They report that the magnetic moment of Ni at the graphene interface is  $0.54 \mu_B/\text{atom}$ . For Ni atoms in the second layer they found  $0.65 \mu_B/\text{atom}$ . For further Ni layers, the magnetic moment increases to  $0.68 \mu_B/\text{Ni atom}$ . Note that they obtain a bulk magnetic moment value for Ni (111) of  $0.72 \mu_B/\text{Ni atom}$ .

Dedkov et. al. [166] analyzed spin-polarized secondary electron emission from the graphene/Ni interface. They found a reduction of the spin polarization for the graphene/Ni system compared to bulk Ni (111) and estimate an interface magnetic moment of about  $0.52 \mu_B/\text{atom}$  which is a reduction of 27.7 % compared to  $0.72 \mu_B/\text{atom}$  which they report for the pure Ni (111) surface. A summary of these literature values is given in table 5.6.

**Table 5.6:** Summary of literature reports of the Ni magnetic moment for mono-, multimers on graphene and at the graphene/Ni (111) interface. Bulk references, as listed in the respective reference, are in brackets.

Reference	Ni <sub>n</sub>	Method	$\mu_{\text{Ni}}$ ( $\mu_{\text{Bulk}}$ ) [ $\mu_{\text{B}}$ /atom]
Johll [151, 153]	1	DFT	0
	2		0.99
	3		0.68
	4		0.5
Duffy [152]	1	DFT	0
	2		0 (1)
Yagi [163]	1	DFT	0
Wehling [149]	1	DFT	0
Cao [150]	1	DFT	0
	2		0
Eelbo [155]	1 (0.007 MLE)	XMCD	0
	“multiple” (0.014 MLE)		$\sim 0.026/n_h$ <sup>32</sup>
Bertoni [164]	Layer	DFT	0.514 (0.716)
Abtew [165]	Layer	DFT	0.54 (0.72)
Dedkov [166]	Layer	SPEES	0.52 (0.72)

Literature reports of magnetic properties of Ni on graphene are mostly of theoretical background and thus limited to either single or few atoms or to interaction between Ni and graphene layers. Investigations on Ni clusters in the nanometer range comparable to the ones investigated for the present thesis have been performed mainly on Cu and/or Co supports. Due to the similarity of the electronic structure of Ni/graphene and e.g. Ni/Cu, the discussion given at the end of the previous subsection shall be picked up here.

<sup>32</sup> Approximated from reproduced data.

To remind, the size and morphology of thin Ni films on TM supports are similar to that of triangular Ni clusters investigated within this thesis (reported by Boeglin using STM [110], and Dhesi using HRLEED on Ni/Cu [140]).

Besides the Ni cluster electronic properties, Dhesi et.al. [140] also systematically investigated the deposition dependent scaling of the magnetic moment of nominally 0.2 ML to 2 ML Ni on Co/Cu (001). They report that the total magnetic moment decreases to  $0.28 \mu_B/\text{Ni}$  for 0.2 ML Ni, which is a decrease of nearly 60 % with respect to the bulk value. For increasing nominal Ni thickness, they find an increasing magnetic moment, e.g. for 2 ML Ni, they report a total magnetic moment of  $0.48 \mu_B$ . They state, that Ni atoms at the interface hybridize with the neighboring Cu atoms. The resulting charge transfer (from Cu to Ni) reduces the d-state occupancy of the Ni and thus the magnetic moment (see figure 5.23).

Boeglin et. al. [110] report magnetic moment values for 0.3 ML and 1.2 ML Ni on Cu (111). They found a maximum Ni magnetic moment of  $0.047 \mu_B/\text{atom}$  and  $0.15 \mu_B/\text{atom}$  respectively.

Srivastava et.al. [167] report Ni magnetic moments for 4 ML and 4.3 ML Ni on Cu (001). They found  $0.275 \mu_B/\text{atom}$  and  $0.29 \mu_B/\text{atom}$ , respectively.

The reduction of the magnetic moment with respect to bulk properties, respectively its recovery can be “delayed” by sandwiching the Ni layer between two Cu films. For example, Hope et. al. [168] investigated the thickness dependence of the magnetic moment of Ni films in the wedged Cu/Ni/Cu/Si (0001) system by XMCD and polarized neutron reflection (PNR). They report a strong delay in recovery of Ni magnetic moment in the presence of a second Cu/Ni interface. For a nominal thickness of 3 nm (corresponding to 8 ML), they find  $\mu_{\text{Tot}} = 0.1 \mu_B$ . Bulk properties evolve above Ni thickness of approximately 15 nm (corresponding to 43 ML). However, they claim that the reduction of the magnetic moment is related to stress. Cu exhibits a larger lattice constant, thus bending the Ni lattice at the interface and reducing the exchange interaction within the interfacial Ni layers. Lee et. al. [169] reports similar results applying XMCD on the same sample system.

Another principal cause for reduced magnetic moment is a spin reorientation transition in thin Ni films. This is reported by Amemiya et. al. [170] who performed thickness dependent XMCD measurements on Ni/Cu. They report, that the spin and thus the magnetization direction turns from in- to out-of-plane if the thickness of the Ni films on Cu is increased. Probing the Ni clusters in e.g. NI geometry will address only the out-of-plane



component, because XMCD determines the projection of magnetic moments along a preferred direction (see section 3.2). If the magnetization direction lays completely in-plane the XMCD signal would vanish.

However, spin reorientation can be excluded as possible explanation of the result of this thesis. The magnetization has been measured in different geometries (NI and  $65^\circ$ ) to probe for both, in- and out-of-plane magnetization. Although the magnetic easy axis lays in-plane, no significant difference in the magnetic moment values were found between in- and out-of-plane measurements when samples were magnetized to saturation.

The general statement of the aforementioned publications is, in agreement with this thesis, a decrease of the Ni total magnetic moment with decreasing nominal deposition. In figure 5.24 a) magnetic moments of thin Ni films on different substrates reported in literature are compared to results found within this thesis. There is a divergence in the qualitative thickness dependence which might be related to the particular sample properties, e.g. different substrates (Cu/Co/graphene) or different sample modifications (sandwiched structure). The reason for the magnetic moment reduction is the interaction of interfacial Ni atoms with the substrate and/or the capping layer. As a consequence, the Ni d-states are additionally populated, shifting the Fermi level and reducing the spin polarization in the Ni d-band. The effect is even stronger, if a second, capping interface is present. The sandwiched Ni layers have to possess a much higher thickness in order to evolve bulk magnetic properties, see figure 5.24 b). However, the magnetic moment reduction is similar for Ni on graphene and on the transition metals Cu and Co.

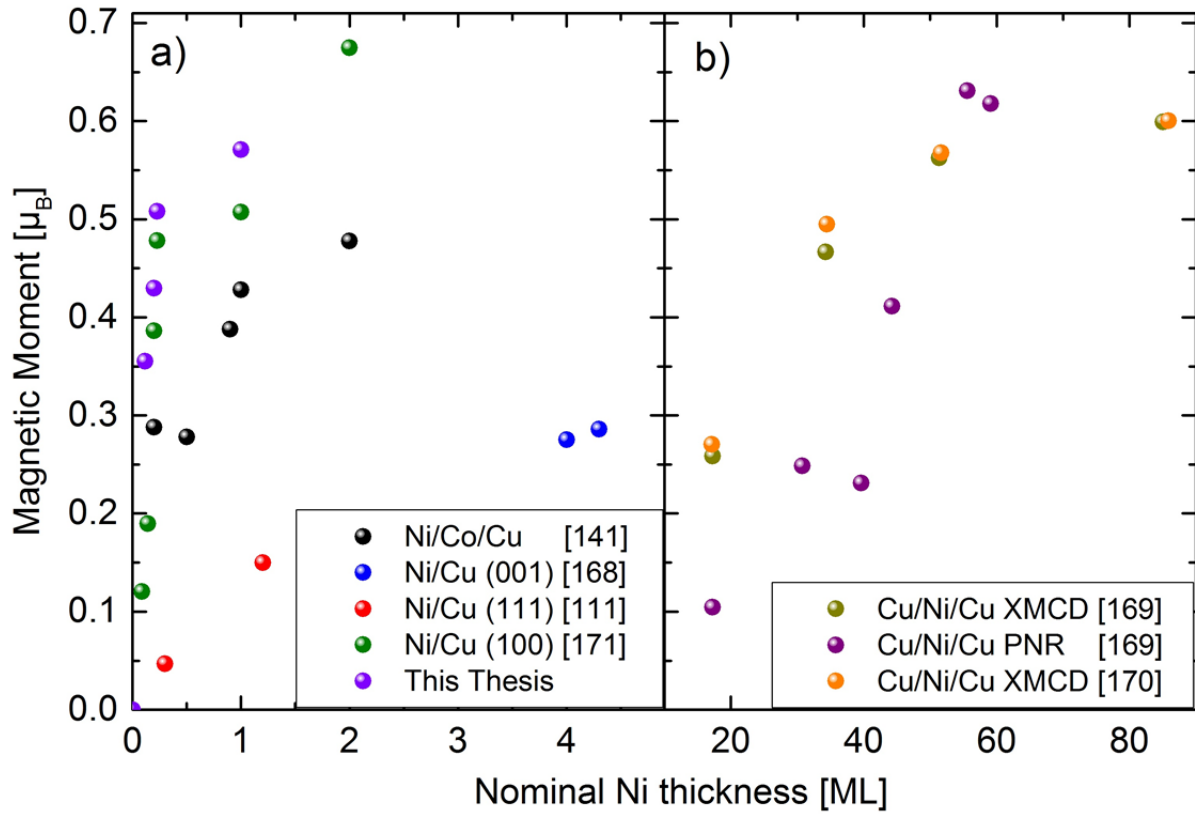


**Figure 5.24 a):** Comparison of Ni magnetic moments  $\mu_{\text{Tot}}$  from selected literature reports and the results of Ni/graphene from this thesis. **b)** Magnetic moments of thin Ni films sandwiched between two Cu films. Recovery of bulk properties for thin Ni films trapped between two Cu contact planes is strongly delayed.

#### 5.4.6. Magnetism at the Ni/graphene interface

In the previous section it was shown that the magnetic properties of Ni/graphene are altered strongly due to their interfacial interaction. Hence, probing the magnetic properties of the underlying graphene substrate for any possible magnetic interaction with the Ni clusters atop is reasonable. If a sizeable magnetic moment is present in the graphene layer, there should be an XMCD signal at the C-K edge although the typical graphene XAS spectrum could not have been isolated properly (see figure 5.17). The XMCD spectrum on the C-K edge of graphene with 0.25 ML Ni atop, measured at 10 K and an applied magnetic field of 2 T, is shown in figure 5.25 a). Although the XMCD signal is magnified by a factor of 1000 no significant magnetic signal can be identified.

For comparison, the field dependent XAS spectra and the corresponding XMCD signal for a single layer of graphene on Ni (111), measured by Weser et. al. [144], are shown in

figure 5.25 b) and c). The  $\pi$ - and  $\sigma$ -states of the graphene are clearly visible in the XAS spectrum (measured in PEY mode), as well as their magnetic polarization in the corresponding XMCD spectrum. Weser et. al. estimate a value of 0.05-0.1  $\mu_B$  for the induced magnetic moment per graphene carbon atom. A similar (theoretically calculated) value of 0.05  $\mu_B$ /C atom is reported by Abtew et. al. [165].

Although induction of a magnetic moment in graphene is principally possible when brought into contact with a ferromagnetic Ni interface, no XMCD signal is found at the C-K edge for Ni clusters on graphene. A possible explanation could be that the reduced magnetic moment of the Ni clusters is insufficient to cause a net magnetic moment in the graphene layer. On the other hand, it would be a bit hasty to generally rule out the scenario of induced magnetic moments in graphene from contacts with Ni (or any other TM) clusters. The absence of an XMCD signal may also stem from experimental restrictions. For example, Weser et. al. investigated graphene on Ni, here the scenario is vice versa. Photo electrons from the Ni/graphene interface have to penetrate 1-2 nm of Ni before leaving the sample and are therefore reduced with respect to other photoelectrons escaping the sample in uncovered regions.

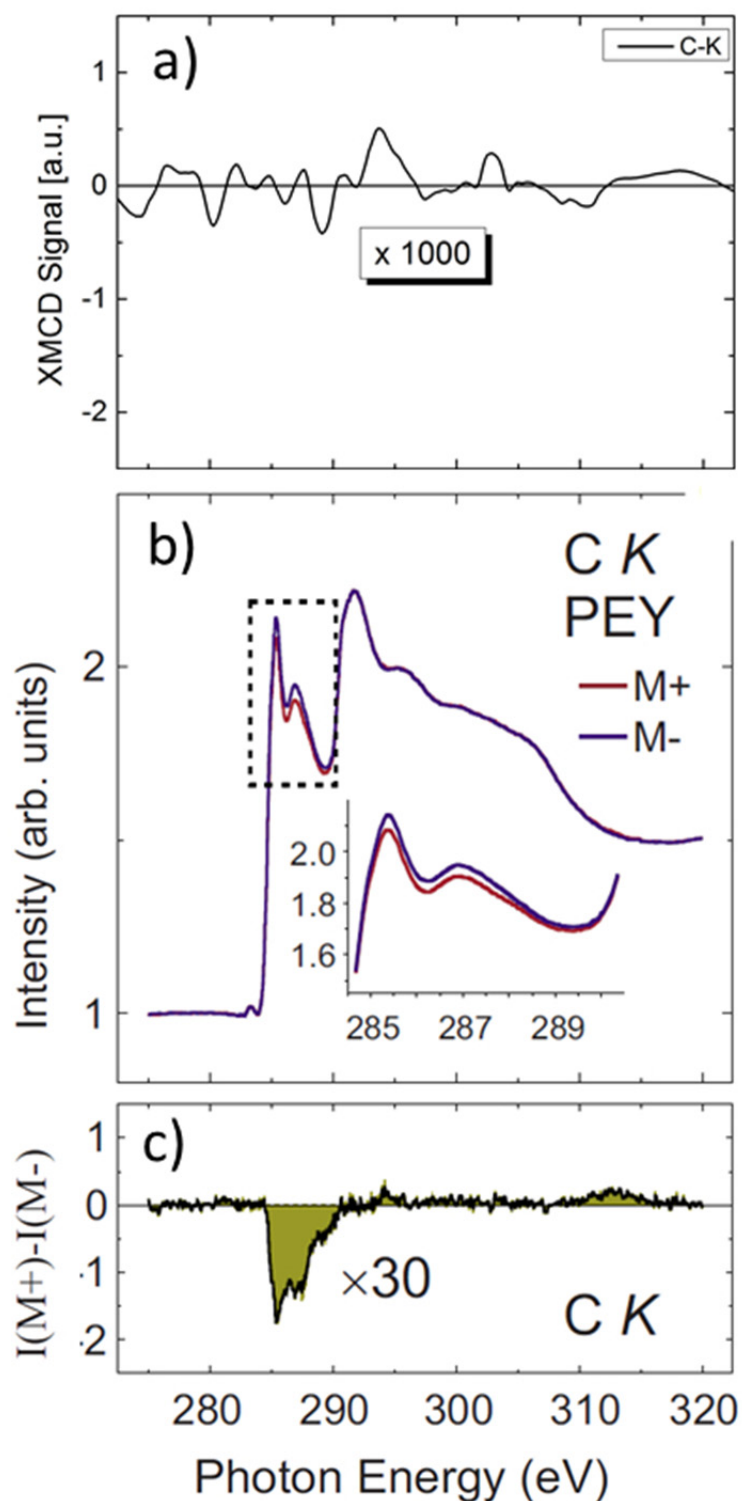


Figure 5.25: Comparison of the XMCD signal of graphene with a significant magnetic polarization at the C-K edge for the graphene/Ni interface as reported by Weser et. al. with the XMCD signal on the C-K edge of graphene with clusters atop. (b, c adopted and with permission from [144]. Copyright 2010, AIP Publishing LLC.)

### 5.4.7. Magnetic Anisotropy

With the magnetic moments given in table 5.5, the hysteresis loops in figure 5.5 and figure 5.8 can now be used to estimate the magnetic anisotropy energy (MAE) of Ni/graphene quantitatively. Therefore, one considers the energy needed to saturate the Ni clusters along the easy and the hard axis respectively. According to equation (3.31) one obtains the effective magnetic anisotropy:

$$\Delta E = E_{out} - E_{in} = K_{eff} V \cdot \sin^2(90^\circ) - \vec{\mu} \cdot \vec{H} - K_{eff} V \sin(0^\circ) + \vec{\mu} \cdot \vec{H} = K_{eff} V \quad (5.6)$$

where  $K_{eff}$  is the effective magnetic anisotropy (energy per unit volume),  $V$  is the cluster volume,  $\vec{\mu}$  and  $\vec{H}$  the saturation magnetization and the applied magnetic field respectively.

On the other hand, the energy which is necessary to magnetize a sample in a specific direction is given by the area below its magnetization curve. Therefore, the energy difference in equation (5.6) equals the area between the in- ( $M_{in}$ ) and out-of-plane ( $M_{out}$ ) magnetization curves (see [2]):

$$\Delta E = \int_0^M \mu_0 H dM_{out} - \int_0^M \mu_0 H dM_{in} \quad (5.7)$$

As an example, the magnetization loops of triangular shaped, 2 ML nominal deposited Ni clusters are shown in figure 5.26. The highlighted area (shaded grey) between 65° (blue line) and NI geometry (black line) magnetization curves is estimated by integration, similar to equation (5.7), and equals the energy per unit volume (here per atom) which is necessary to fully magnetize the clusters in the respective direction. Using the relations  $1 \mu B = 9.247 \text{ J/T}$  and  $1 \text{ J} = 6.241 \cdot 10^{18} \text{ eV}$  (from [3]), the y-axis was converted to a  $\mu\text{eV/atom}$  scale.

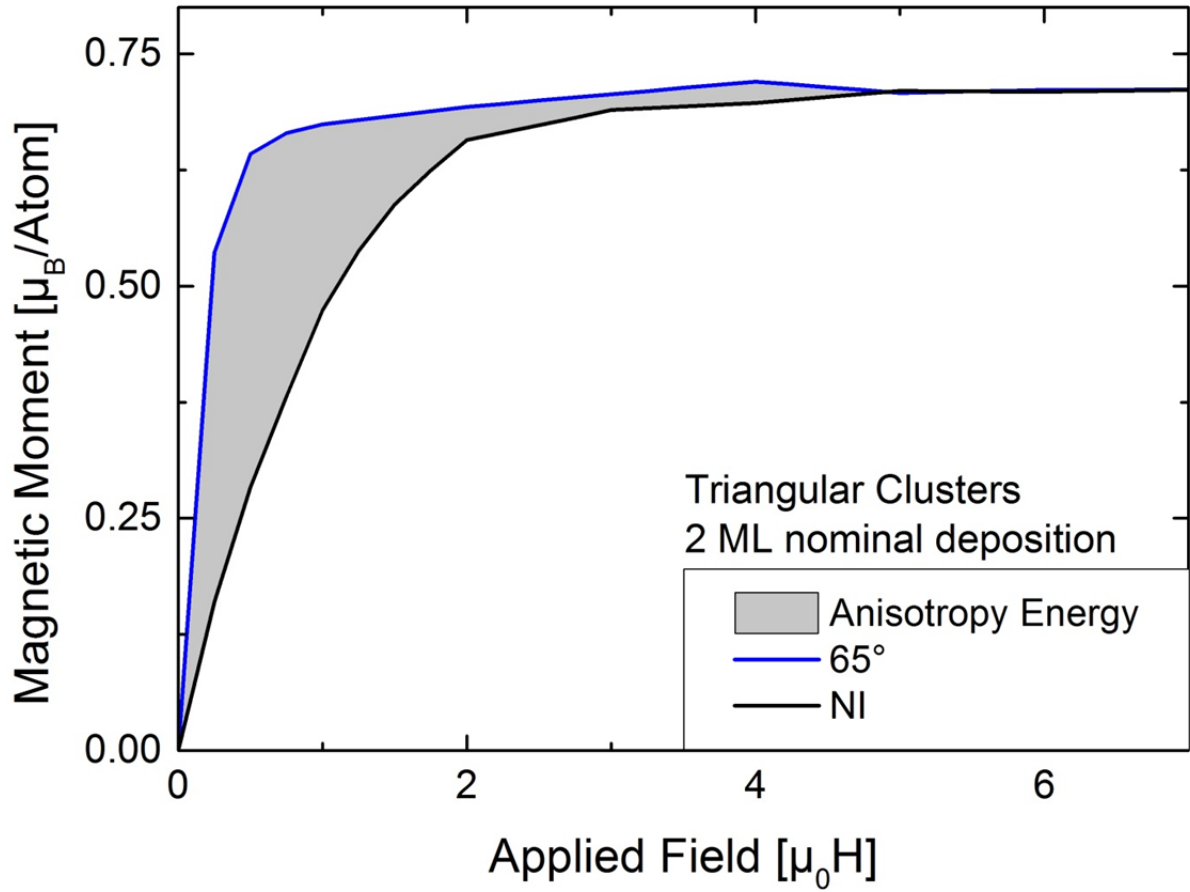


**Figure 5.26:** Illustration of the method used to extract the MAE from XMCD magnetization curves. The MAE can be extracted estimating the area between NI and 65° magnetization loops. See text for details.

In order to determine the anisotropy between in- and out-of-plane, the measurement geometry and the respective angles have to be considered properly. The sample alignment for XMCD measurements is displayed in figure 5.27.  $\theta$  denotes, as defined earlier in figure 3.5, the angle between the magnetic easy axis and the magnetization direction,  $a$  labels the out-of-plane, and  $c$  the in-plane easy axis direction. Hence  $\theta = 90^\circ$  for NI and  $\theta = 25^\circ$  for measurements in 65° geometry in equation (5.6) and the grey shaded area in figure 5.26 reflects 82% of the total MAE. The respective values have been calculated accordingly. Mind also that in this notation in-plane magnetization is obtained with positive  $K_{eff}$ .

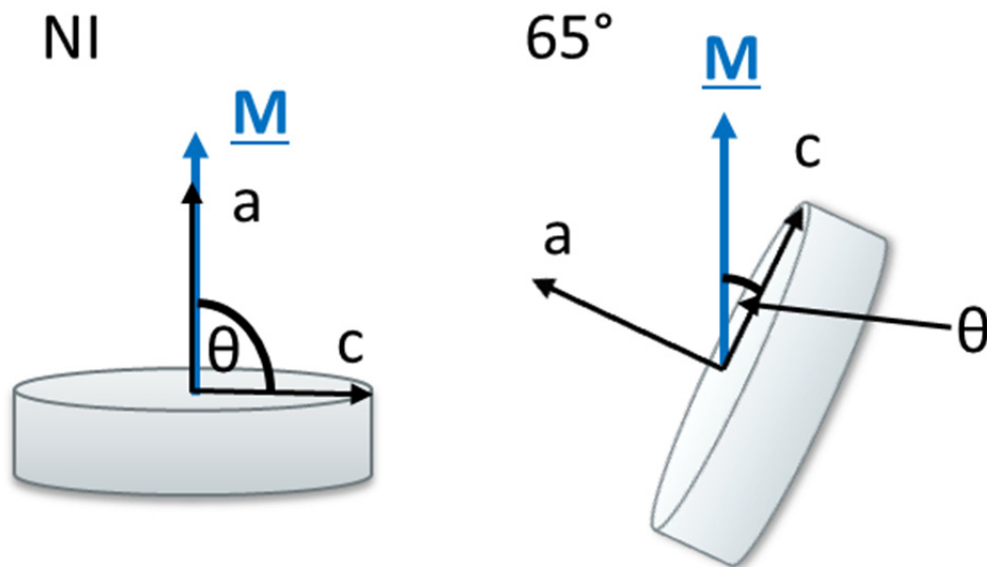


**Figure 5.27: Standard sample alignment that was used in order to record XCMD magnetization loops for NI (left) and 65° (right) geometry. Note that  $\theta$  denotes the angle between magnetization direction and easy axis here.**

The effective anisotropy in dependence of the nominal deposition is shown in figure 5.28. In general, the trend line is similar to the one obtained for magnetic moments. For larger cluster, the anisotropy is also large and it decreases with decreasing cluster size in a strongly nonlinear way. It is remarkable that the spherical clusters exhibit a higher anisotropy at smaller cluster size than the triangular ones.

For the largest triangular clusters with 2 ML nominal deposition, one obtains a magnetic anisotropy of 29.51  $\mu\text{eV}/\text{atom}$ . For the triangular 1 ML one finds 16.83  $\mu\text{eV}/\text{atom}$ . For triangular clusters with 0.25 ML nominal deposition, the anisotropy drops to 12.73  $\mu\text{eV}/\text{atom}$ . The relative decrease of the magnetic anisotropy is nearly 57 %.

For the spherical clusters, one finds 28.24  $\mu\text{eV}/\text{atom}$  for 1 ML nominal deposition (almost the same anisotropy value as triangular clusters with 2 ML), 25.22  $\mu\text{eV}/\text{atom}$  for 0.25 ML, 20.29  $\mu\text{eV}/\text{atom}$  for 0.2 ML and 16.05  $\mu\text{eV}/\text{atom}$  for 0.1 ML nominal deposition. Here, the relative decrease of the anisotropy is 43 %. These results are summarized in table 5.7.

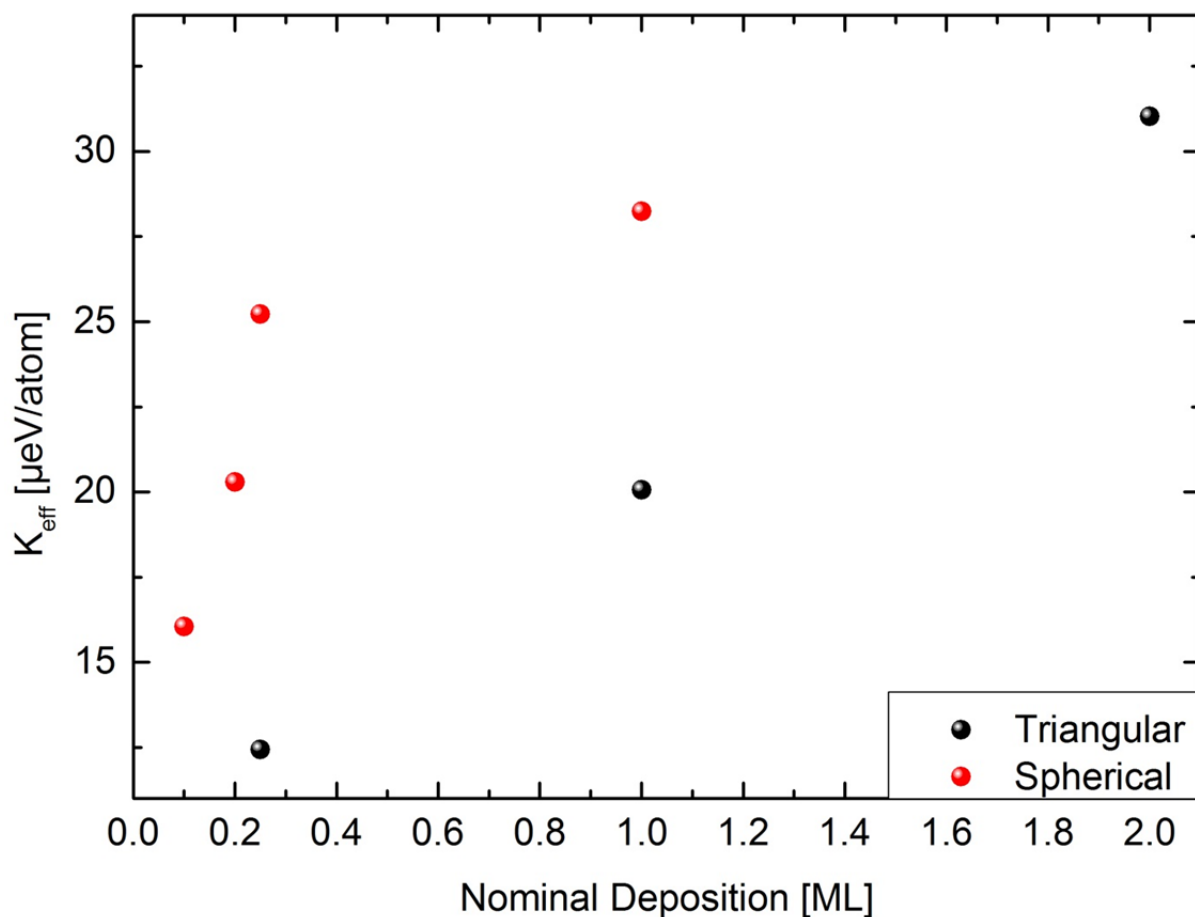


Figure 5.28: Effective, uniaxial magnetic anisotropy  $K_{\text{eff}}$  in dependence of nominal Ni deposition and cluster type. The magnetic anisotropy mainly follows the trend line of the corresponding magnetic moments, but is larger for spherically shaped clusters.



**Table 5.7: Effective (uniaxial) and shape anisotropy of triangular and spherical Ni clusters on graphene in dependence of the nominal deposition.**

Nominal deposition [ML]	$K_{eff}$ [ $\mu\text{eV}/\text{atom}$ ]	$K_{shape}$ [ $\mu\text{eV}/\text{atom}$ ]
<b>Triangular</b>		
2	29.51	11.90
1	16.83	6.72
0.25	12.73	5.98
<b>Spherical</b>		
1	28.24	8.52
0.25	25.22	6.75
0.2	20.29	4.83
0.1	16.05	3.30

In a phenomenological model (see e.g. the pioneering work of Jungblut or Johnson [171, 172]), the effective magnetic anisotropy energy  $K_{eff}$  can be considered as the sum of several different magnetic anisotropy contributions. Owing to the reduced geometries in clusters and thin films one usually separates  $K_{eff}$  into a constant volume part  $K_V$  and a size dependent surface/interface contribution  $K_{i,s}$  (after [171]):

$$K_{eff} = K_V + \frac{K_{i,s}}{d} + K_{shape} \quad (5.8)$$

The size independent  $K_V$  usually contains all size independent anisotropies such as the magnetocrystalline anisotropy  $K_{MCA}$  and magnetoelastic anisotropy contributions  $K_{ME}$  due to e.g. substrate related strain. Although  $K_V$  contains a magnetocrystalline contribution, it should not be mixed up with the magnetic anisotropy energy of bulk Ni. In some publications  $K_V$  also contains the shape anisotropy:

$$K_{shape} = \frac{1}{2} \mu_0 \mu_{sat}^2 \quad (5.9)$$

Here it is listed separately due to the strong size dependency of the saturation magnetization  $\mu_{sat}$  of the investigated Ni clusters.  $K_{i,s}$  consists of anisotropy contributions that become negligible when the sample size is significantly increased. These contributions

contain e.g. anisotropy caused by broken symmetry on the surface and/or interfacial anisotropy by strain and interaction with the substrate. A detailed quantification of the magnetoelastic contributions to  $K_V$  and  $K_{i,s}$  is difficult in the present case because it requires knowledge of e.g. the lattice and the magnetostriction constant. These constants are known for the bulk material but not for the Ni/graphene system investigated within this thesis. One should note that this approximation was shown to be valid for monolayers of thin transition metal films [173], not necessarily for the sub-monolayer range. However, as the effective cluster thickness in the nm range, which equals several MLs of Ni, the use of equation (5.8) seems to be justified at least as a close approximation. Furthermore, the model spares out any microscopic description, however it was able to describe the transition from in-plane to perpendicular magnetization in Ni thin films properly [172].

In order to estimate  $K_V$  and  $K_{i,s}$ ,  $(K_{eff} - K_{Shape}) \cdot t$  is plotted over the nominal Ni deposition in figure 5.29.  $K_{Shape}$  values listed in table 5.7 have been subtracted here in order to remove the influence of  $K_{Shape}$ , which is also strongly deposition dependent in this case.

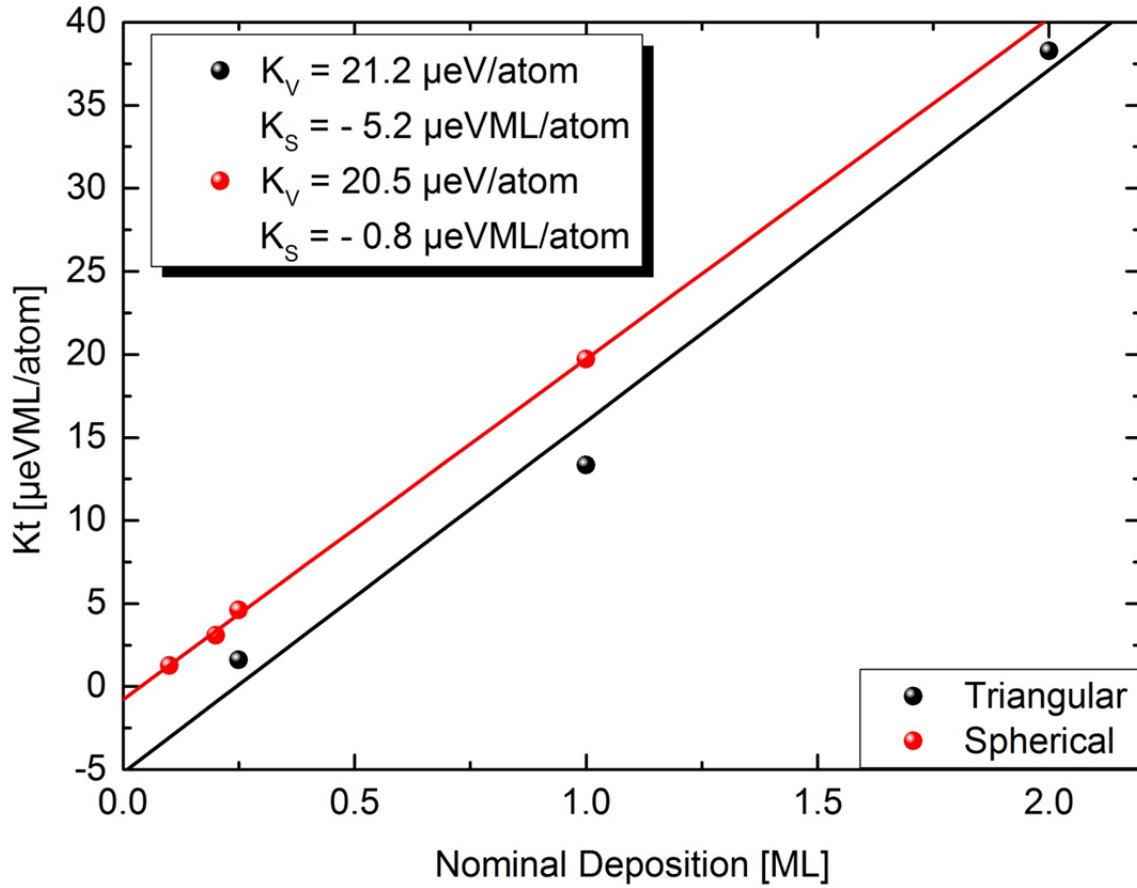


**Figure 5.29:**  $K_{\text{eff}} \cdot t$  in dependence of the nominal Ni deposition in order to estimate the respective surface/interface and volume fractions of the effective magnetic anisotropy. The strongly deposition dependent shape anisotropy  $K_{\text{shape}}$  was subtracted beforehand.

$K_V$  and  $K_{i,s}$  can be estimated from the slope and the intercept respectively of the linear fits in figure 5.29. For triangular clusters, one obtains  $K_V = 21.2 \mu\text{eV}/\text{atom}$  for the volume and  $K_{i,s} = -5.2 \mu\text{eV}\cdot\text{ML}/\text{atom}$  for the surface/interface anisotropy. For spherical clusters, one obtains  $K_V = 20.5 \mu\text{eV}/\text{atom}$  and  $K_{i,s} = -0.8 \mu\text{eV}\cdot\text{ML}/\text{atom}$ . Note that  $K_V$  is not identical with the magnetocrystalline anisotropy energy of bulk Ni, which is approximately  $4 \mu\text{eV}/\text{atom}$ .

First of all one can see that  $K_V$  is nearly identical for spherical and triangular clusters. In addition to  $K_{\text{shape}}$  the volume part of the anisotropy also benefits an in-plane easy axis. The surface/interface  $K_{i,s}$  contribution to the magnetic anisotropy is negative and thus benefits a perpendicular easy axis. It is noteworthy that for spherical clusters, the surface/interface anisotropy is much smaller than for triangular clusters.

The transition to perpendicular magnetic anisotropy, which is preferred for technical implications, is given by the intercept of the fitted lines with the x-axis, when the negative surface/interface anisotropy starts dominating the positive contribution of the volume term.

From figure 5.29, one can approximate, that transition to perpendicular easy axis occurs (mathematically) below 0.2 ML nominal deposition for triangular clusters. For spherical clusters, the transition occurs below 0.03 ML nominal deposition.

Note that good care must be taken interpreting the quantitative value here, because only the nominal deposition is well known and growth of Ni on graphene is not layer by layer.

Furthermore, the linear trend lines in figure 5.29 indicate that the clusters are single domain particles. Domain formation would result in a power law behavior as reported by Hug et. al. ( $K_{\text{eff}} \sim t^{-0.7}$  see [174, 175]) and Hameed et. al. ( $K_{\text{eff}} \sim t^{-0.64}$  see [176]) due to further, more complex domain wall related contributions to the magnetic anisotropy energy in equation (5.8).

One can also try to separate  $K_{i,s}$  into the respective surface and interface contributions  $K_s$  and  $K_i$ . Gradmann [177] et. al. estimated the anisotropy energy of the Ni (111)/UHV interface, with  $K_{\text{UHV/Ni}} = -160 \mu\text{eV}$  per surface Ni atom, meaning the surface contribution favors an out-of-plane easy axis. Assuming  $K_{i,s} \sim K_s + K_i$  and using the aforementioned value as surface contribution, the interface anisotropy contribution is  $K_i = 154.8 \mu\text{eV}$  per surface Ni atom for triangular and  $K_s = 159.2 \mu\text{eV}$  per surface Ni atom for spherical clusters. Therefore, the interface term is strongly favoring an in-plane magnetic easy axis.

Like for the magnetic and electronic structure, studies to estimate the magnetic anisotropy energy of Ni nanostructures and thin films have been performed, mainly for the Ni/Cu system. Boeglin et. al. [110] estimated the anisotropy energy of triangular shaped Ni nanocluster on Cu (111) and found an effective magnetic anisotropy of  $75 \mu\text{eV/atom}$ . They determined the magnetic anisotropy in a different way, according to the method introduced by Bruno [41]. With this method the magnetic anisotropy energy is calculated from the difference of orbital momentum along easy and hard magnetic axis. However they did not determine volume and surface/interface contributions to the magnetic anisotropy energy separately. Further studies mostly investigated the spin reorientation transition from in- to out- and back to in-plane preferred magnetization direction of Ni thin films on Cu. As the Ni clusters on graphene exhibit a preferred in-plane easy axis, one should compare the present values of  $K_s$  and  $K_v$  to those reported for Ni thin films with in-plane easy axis as well. Jungblut et. al. [171] report  $K_v = 10.85 \mu\text{eV/atom}$  and  $K_s/1 \text{ ML} = -301 \mu\text{eV/atom}$  for Ni (111) film on

Cu. The respective values were converted to units of  $\mu\text{eV}/\text{atom}$  using factors given by Farle et. al [178].

Other literature values are available for Ni films with out-of-plane easy axis. Kuch et. al. [179] investigated a doubly wedged Ni/Co thin film using XMCD and Brunos model [41] to determine the magnetic anisotropy energy. They report an anisotropy energy of  $K_{\text{eff}} = -60 \mu\text{eV}/\text{atom}$  for an out-of-plane magnetized Ni thin film.

It should be pointed out that comparison to literature values have to be treated with caution because they mainly treat (assumed) completed layers of Ni with perpendicular anisotropy and not nanostructures with in-plane easy axis, except for the case of Boeglin et. al [110]. On the other hand, the obtained anisotropy energies are in the same order of magnitude as most literature results, namely several  $10 \mu\text{eV}/\text{atom}$ , which should be the case for system with nearly equal electronic and magnetic properties.

### 5.5. Summary: Magnetism of Ni nanoclusters on graphene

Within this thesis, the size and shape dependent electronic and magnetic properties of Ni clusters on a graphene Moiré template have been investigated by means of combined XAS and XMCD spectroscopy. Two different types of nanoclusters have been prepared *in-situ*: spherical and triangular shaped. The size of the respective cluster systems has been varied by variation of the nominal Ni deposition. Furthermore, a bulk Ni sample was prepared *in-situ* in order to obtain a reference sample system.

#### Electronic Properties: Changes in Ni d-state occupancy and configuration

The electronic properties of Ni nanoclusters on graphene have been determined performing XAS on the Ni  $L_{2,3}$  edge, which is sensitive to the unoccupied density of Ni d-states  $n_h$ . It was found that  $n_h$  changes strongly as a function of the nominal deposition/cluster size. The intensity of the main L3 peak, attributed to Ni in a  $3d^9$  ground state, and thus the value of  $n_h$  is, strongly reduced with respect to the bulk reference sample ( $n_h = 1.45$ ) when the nominal deposition is decreased. Over the complete range of cluster size,  $n_h$  decreases from  $n_h = 1.32$  for 2 ML to  $n_h = 0.97$  for 0.1 ML nominal Ni deposition.

This means vice versa an increased occupancy of the Ni d-states due to filling with additional electrons. For small clusters, the ratio of interfacial to the total number of atoms is significantly large, thus it is proposed that the change in the Ni d-states stems from a strong interaction with the underlying graphene substrate. With increasing cluster size,  $n_h$  converges towards bulk properties. Here, the contributions of interfacial atoms have little effect on the overall electronic properties. Although  $n_h$  changes strongly nonlinear with increasing cluster size, no significant shape dependence has been observed.

Furthermore changes of the distinct satellite features in the Ni XAS spectrum have been observed. The satellite feature 3 eV above the main Ni  $L_3$ -peak, attributed to Ni in a magnetic  $3d^8$  ground state, is reduced with decreasing cluster size, indicating a reduced admixture of this state for smaller clusters.

The characteristic of the satellite feature 6 eV above the main Ni  $L_3$ -peak, attributed to Ni in a nonmagnetic  $3d^8$  ground state, is reduced with decreasing cluster size as well.

In terms of a configuration interaction model, the strong size dependent changes in distinct features the Ni XAS spectrum can be explained by a reshuffle of the Ni d-states. The loss of both, the  $3d^9$  characteristic represented by the main  $L_3$ -peak, and the  $3d^8$

characteristics represented by satellite features, indicates an increased occupation of (spectroscopic inaccessible)  $3d^{10}$  ground states of Ni atoms in the respective clusters. The results found within this thesis in principle agree with results found for thin films of Ni on transition metal supports, although differences in the satellite features indicate a different hybridization mechanism between Ni and graphene in comparison to e.g. Ni and Cu or Co.

Due to large background from the underlying Ir (111) SC substrate, details of the electronic structure of graphene could not have been revealed within this thesis.

### **Magnetic Properties: Reduction of Ni magnetic moment**

Using XMCD, the size and shape dependent total angular momentum  $m_{\text{Tot}}$  of Ni nanoclusters on graphene has been determined. It was found that  $m_{\text{Tot}}$  decreases strongly with decreasing cluster size, from  $0.68 \mu_B$  for 2 ML nominal Ni deposition to  $0.35 \mu_B$  for 0.1 ML nominal Ni deposition. No obvious shape dependence could have been detected. For smaller clusters, the orbital magnetic moment is enhanced with respect to the spin magnetic moment. However, this feature is related to the strong decrease of the spin magnetic moment rather than to an actual enhancement that was found for other magnetic nanocluster.

In order to determine the magnetic anisotropy energy, magnetic hysteresis loops have been measured in normal incidence and under an angle of  $65^\circ$  with respect to the incoming beam intensity. An in-plane magnetic easy axis was found. The magnetic anisotropy energy was determined in dependence of the cluster size and shape. In a phenomenological model, the magnetic anisotropy was partitioned into a constant, size independent volume and a size dependent surface/interface part. The volume anisotropy is  $K_V = 21.2 \mu\text{eV/atom}$  for triangularly and  $K_V = 20.5 \mu\text{eV/atom}$  for spherically shaped nanoclusters. The surface/interface anisotropy  $K_{i,s}$  is rather small and negative, opposing the volume anisotropy. It is the only sample property exhibiting a distinct shape dependence. For triangular clusters  $K_{i,s} = -5.2 \mu\text{eV/atom}$  (and deposited ML), for spherical clusters  $K_{i,s} = -5.2 \mu\text{eV/atom}$  (and deposited ML). Transition to perpendicular magnetic easy axis is predicted to occur below 0.2 ML and 0.03 ML nominal deposition for triangular and spherical clusters respectively. However, especially at 0.03 ML the magnetic moment of triangular cluster is expected to be disappeared completely.

Furthermore, the graphene substrate has been probed for potential, induced magnetic moment, as apparent in e.g. graphene on a Ni substrate. Even for 2 ML nominal deposited Ni/graphene, where the Ni magnetic moment reached nearly 90 % of the bulk value, applying a magnetic field of 7 Tesla and cooling the sample down to 10 K, no significant XMCD signal at the C-K edge could be detected.



## 6. Magnetism in nanograined, undoped ZnO Systems

As introduced in section 3.5 the origin of magnetism in doped and especially undoped ZnO is still a controversial topic within the scientific community. FM in this system is mainly proofed using macroscopic methods although its source is supposed to be of microscopic origin, e.g. vacancies and/or grain boundaries. With a more detailed knowledge on the microscopic mechanism of FM one could alter sample properties accordingly so that e.g. nanograined or crystalline/amorphous multilayers of ZnO can be implemented as future spin tronic devices.

Thus, this section is dedicated to the analysis of the origin of FM in nanograined ZnO.

### 6.1. Sample Preparation and Structural Properties

In order to probe the influence of nanograining on the magnetic properties of nanograined ZnO, it is necessary to prepare samples with a defined grain size distribution. One dedicated method is the so-called liquid ceramics method [74, 81, 180]. Here, the nanograined ZnO films are produced by thermal pyrolysis of a Zn containing organic solution. ZnO(II)-butanoate ( $\text{Zn(II)-C}_3\text{H}_7\text{CO}_2$ ) with a concentration of  $4 \text{ kg/m}^3$  was drop-coated onto a (102) sapphire ( $\text{Al}_2\text{O}_3$ ) substrate, and dried at  $100^\circ \text{C}$ . Prior to the coating, the substrate has been cleaned with acetone and ethanol. Subsequently, the substrate has been annealed in order to remove possible solvent remains. The working principle of the liquid ceramics method is displayed in figure 6.1.

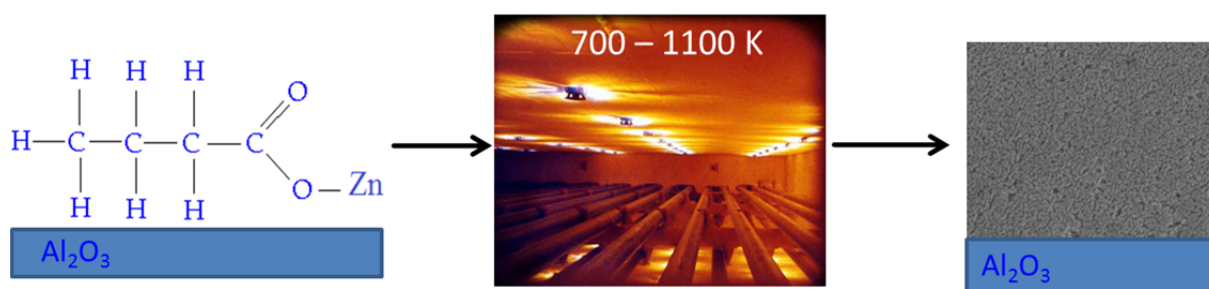


**Figure 6.1: Working principle of the liquid ceramics method. Zn-(II)-butanoate is dropped onto a sapphire substrate (left). Subsequent annealing (center) oxidizes the ZnO and forms a nanograined ZnO “foam” (right) on the substrate.**

In order to find a conclusive result for the grain size dependent effect of FM in ZnO, two different ZnO thin films have been produced: one sample with small grains and a large

specific grain boundary area  $s_{GBA}$ , annealed at 700 K for 1 h hour followed by a slow cool down. This sample will be labeled  $ZnO_{700K}$  in the following. A sample consisting of coarse grains and a smaller  $s_{GBA}$ , annealed at 1100 K for 24 h. In analogy, this sample will be labeled as  $ZnO_{1100K}$ . The  $ZnO_{700K}$  sample will be linked with a red, the  $ZnO_{1100K}$  with a blue color code in the following sections. A commercial ZnO (0001) single crystal from Mateck Company (Jülich, Germany) has been used as a non-magnetic reference sample for SQUID and  $\mu$ SR measurements (labeled black in the following).

The film thickness and the grain size distribution were estimated by focused ion beam (FIB) and transmission electron microscopy (TEM). The TEM measurements were performed using a Jeol JEM-4000FX microscope from the Stuttgart Center of Electron Microscopy (StEM). The acceleration voltage was set to 400 kV. In the same step energy dispersive x-ray spectroscopy (EDX) was used to probe the presence of Fe, Ni, Co or other magnetic ions contaminations. Their concentration was below the resolution limit of 0.1 at. %.

A TEM picture comparison of lateral cuts through the thin film samples is shown in figure 6.2. For the  $ZnO_{700K}$  sample, the film thickness is approximately 200 nm. For the  $ZnO_{1100K}$  sample, the film thickness is 470 nm. The films are located between the sapphire substrate and a Pt covering required for FIB preparation of TEM measurements. Apparently, grains in the  $ZnO_{700K}$  sample are much smaller than grains in the  $ZnO_{1100K}$  sample.

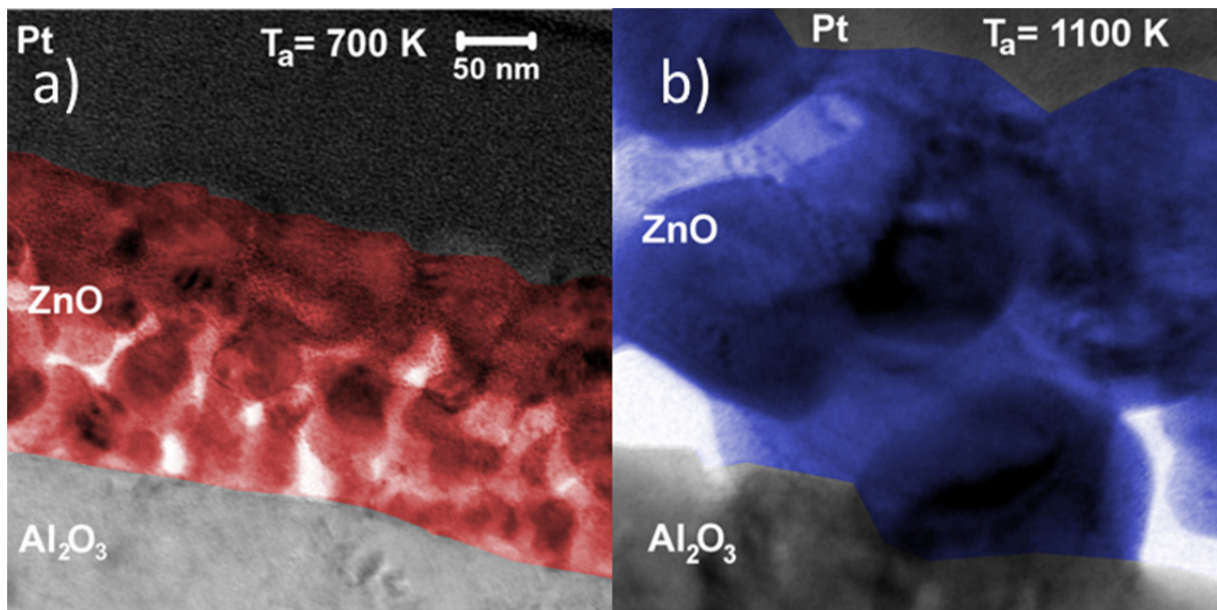


**Figure 6.2 a):** Lateral cut of the  $ZnO_{700K}$  sample. ZnO nanograins are highlighted red. The sapphire substrate is located at the bottom part, topped with Pt for FIB. **b)** Same scheme picture of the  $ZnO_{1100K}$  sample, with ZnO grains highlighted blue.

In order to estimate the grain size, respectively the  $s_{GBA}$  distribution and the resulting mean grain size, a detailed analysis of a multitude of higher magnified TEM pictures of both samples has been performed. The  $s_{GBA}$  has been estimated using the definition given by equation (3.57):  $s_{GBA} = \frac{1.65 \cdot a}{D}$ , where,  $D$  denotes the mean grain width and  $a < 1$  is the grain aspect ratio. The respective  $s_{GBA}$  distribution functions for  $ZnO_{700K}$  and  $ZnO_{1100K}$  are plotted in figure 6.3. A second scale converting the  $s_{GBA}$  axis to the corresponding grain size was added to the plot.

For  $ZnO_{700K}$ , the average grain boundary area is  $s_{GBA} = 5.32 \cdot 10^7 \text{ m}^{-1}$ , corresponding to an average grain size of 31 nm. For  $ZnO_{1100K}$ , an average  $s_{GBA} = 2.65 \cdot 10^7 \text{ m}^{-1}$  was found, corresponding to an average grain size of 65 nm. According to results reported by Straumal et. al. [74], the threshold condition for ferromagnetism is located in the vicinity of  $s_{GBA} > 5.0 \cdot 10^7 \text{ m}^{-1}$ , corresponding to a grain size smaller than 40 nm. This threshold value is marked by the dashed black line in figure 6.3, virtually separating nonmagnetic (NM) and ferromagnetic (FM) grains from each other. Grains fulfilling the FM condition shall thus be labeled “magnetic grains” in the following.

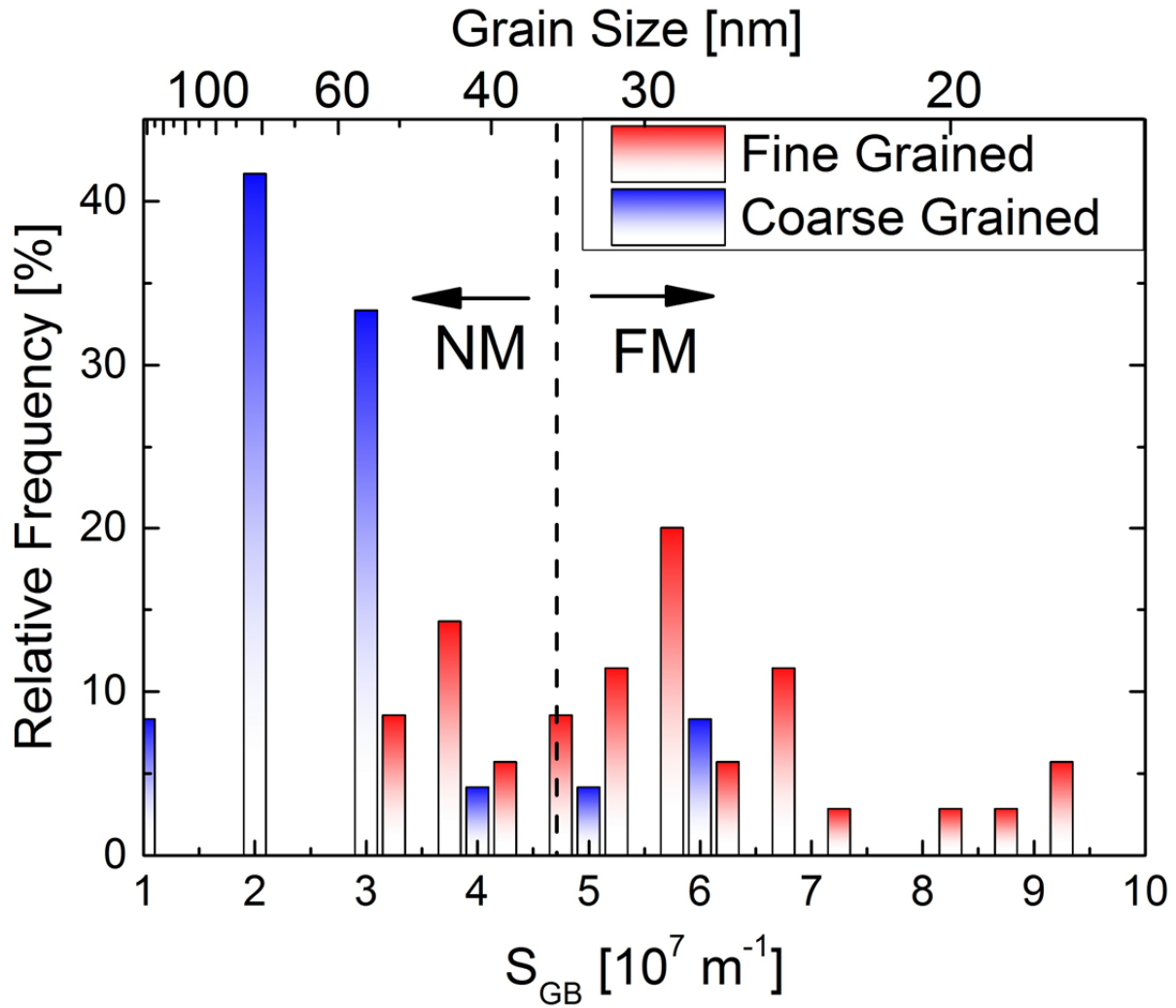


Figure 6.3: Distribution of the specific grain boundary area  $s_{GBA}$  obtained from multiple TEM pictures. Plotted is the relative frequency of grains with a certain  $s_{GBA}$ . Results are highlighted red and blue, for the ZnO<sub>700K</sub> and the ZnO<sub>1100K</sub> sample respectively. The dashed line marks the critical  $s_{GB}$  threshold for the occurrence of ferromagnetism, as reported in [74].

It is apparent from figure 6.1 that ZnO grains are not uniformly shaped in both samples. Thus, particular attention has to be paid to the grain size distribution rather than to the average grain size itself.

In general, the grain size follows a Gaussian distribution in both samples. It is noteworthy, that although the average  $s_{GBA}$  of the ZnO<sub>1100K</sub> sample is smaller than the FM threshold, a small fraction of 10 % of its grains still lays above the FM border line. Therefore, even though the average  $s_{GBA}$  is smaller than the required threshold value, one may expect a small but sizeable magnetization even in the ZnO<sub>1100K</sub> sample. For the ZnO<sub>700K</sub> sample, the

distribution function starts also below the threshold value but is stretching far beyond it. The fraction of “magnetic grains” is  $\sim 55\%$ , suggesting a sample with a higher magnetization compared to  $\text{ZnO}_{1100\text{K}}$ . On the other hand, a number of grains are supposed to be NM grains. Thus NM regions are supposedly present in this sample. Table 6.1 summarizes the respective grain size,  $s_{\text{GBA}}$  and the fraction of magnetic grains.

**Table 6.1: Summary of structural properties analyzed by TEM of  $\text{ZnO}_{700\text{K}}$  and  $\text{ZnO}_{1100\text{K}}$ . Values for the single crystal reference were taken from [74].**

Sample	Average grain size [nm]	$s_{\text{GBA}} [10^7 \text{ m}^{-1}]$	“Magnetic grains” [%]
$\text{ZnO}_{700 \text{ K}}$	30	5.32	$\sim 55$
$\text{ZnO}_{1100 \text{ K}}$	65	2.65	$\sim 15$
Single Crystal	$\infty$	$4 \cdot 10^{-5}$	0

## 6.2. Magnetic Properties

In order to probe the magnetic properties of the samples, two different techniques have been applied: SQUID and XMCD. The first was applied to proof ferromagnetism and to determine the sample magnetization. The latter was applied in order to detect any possible induced O K- or Zn  $L_{2,3}$ -edge and in addition to EDX exclude any contamination with other magnetic ions<sup>33</sup>.

### 6.2.1. SQUID Measurements

The magnetic characterization was performed using a MPMS-XL superconducting quantum interference device (SQUID) from the Quantum Design Company (San Diego, USA). SQUID measurements have been performed at RT and at 50 K, applying magnetic fields of up to 6 Tesla. In order to divulge thickness dependent effects, SQUID magnetization curves have been normalized to the volume of the films, using the film thickness estimated by TEM pictures. The single crystal magnetization curve has been normalized to its volume

<sup>33</sup> With the present XMCD setup, magnetic moments of less than  $10^{-4} \mu_{\text{B}}$  can be detected, even if they originate from strongly diluted, non-interacting magnetic ions.

(5x5x0.5 mm<sup>3</sup>). All SQUID magnetization curves were corrected for substrate diamagnetism. The magnetic field was applied perpendicular to the sample surface.

The resulting SQUID magnetization curves at RT (closed triangles) and at 50 K (open triangles) are shown in figure 6.4. At RT ZnO<sub>700K</sub> (closed red triangles) exhibits a maximum saturation magnetization of 8.3 emu/cm<sup>3</sup>. The RT saturation magnetization of ZnO<sub>1100K</sub> sample (closed blue triangles) is almost 6 times lower: 1.25 emu/cm<sup>3</sup>. These values correspond to a magnetic moment of  $4 \cdot 10^{-2} \mu_B$  and  $6 \cdot 10^{-3} \mu_B$  per ZnO unit cell respectively, assuming a homogeneous distribution of magnetic moments within ZnO films. Furthermore, both samples exhibit small but sizeable remnance and coercivity, shown in the inset of figure 6.4. In comparison, the saturation magnetization of the single crystal reference is quite small, only  $2 \cdot 10^{-4}$  emu/cm<sup>3</sup>.

This result is in agreement with the expectation from the grain size distribution analysis. ZnO<sub>700K</sub> contains 55 % of magnetic grains; thus this sample should exhibit the highest saturation magnetization, which is the sum of all microscopic magnetic moments within the sample. The magnetization of ZnO<sub>1100K</sub> should be a smaller in comparison to ZnO<sub>700K</sub>, as it contains only 10 % of magnetic grains. Indeed, the saturation magnetization is, like the fraction of critical grains, 6 times smaller.

Great care must be taken when claiming FM of actual nonmagnetic materials. Especially contaminations with TMs, e.g. due to sample manipulation with metallic tweezers, is a well-known problem [181, 182]. In this case, one obtains superparamagnetic magnetization curves which are similar to those in figure 6.4 (see also section 3.1.5). In order to distinguish FM from SPM magnetization curves, one utilizes temperature dependent measurements. Whereas for SPMs the magnetization scales with  $1/T$ , magnetization curves of ZnO are nearly temperature independent and show a so-called “anhysteretic” behavior [183]. Thus, in addition to RT measurements, SQUID magnetization curves were also recorded at 50 K for ZnO<sub>1100K</sub> and ZnO<sub>700K</sub>. The respective magnetization curves are plotted as open triangles in figure 6.4. The respective 50 K and RT magnetization curves are nearly identical, in both saturation magnetization and shape of the respective curves. Furthermore, small but sizeable remnance and coercivity were found for ZnO<sub>700K</sub> and ZnO<sub>1100K</sub>, as shown in the inset of figure 6.4.

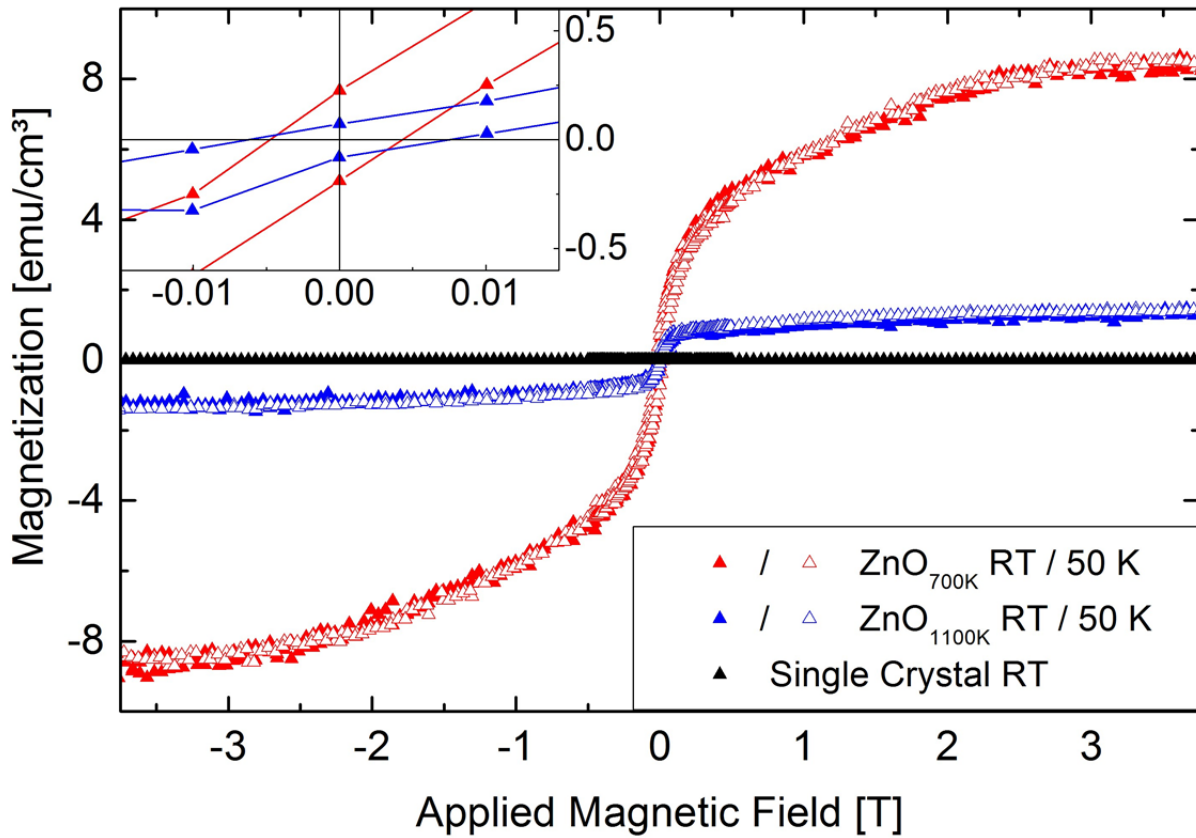


Figure 6.4: Comparison of SQUID magnetization curves for  $\text{ZnO}_{700\text{K}}$ ,  $\text{ZnO}_{1100\text{K}}$  and the nonmagnetic SC reference sample, measured at RT and at 50 K. The magnetization was normalized to the thin film respectively the single crystal volume.

Table 6.2: Saturation magnetization, remnance and coercivity for the FM ZnO films and the NM SC reference estimated by SQUID.

Sample	$M_S$ [emu/cm <sup>3</sup> ]	$H_R$ [emu/cm <sup>3</sup> ]	$H_C$ [mT]
$\text{ZnO}_{700\text{K}}$	8.3	0.23	5
$\text{ZnO}_{1100\text{K}}$	1.2	0.07	8
Single Crystal	$2.4 \cdot 10^{-4}$	0	0

### 6.2.2. XMCD Measurements

In order to exclude possible magnetic “contaminations” and especially possible magnetic effects caused by magnetic polarization of the OK or Zn- $L_{2,3}$  edge, additional XAS and XMCD measurements were performed at the WERA beamline at ANKA using the XMCD setup described in section 4.3. All measurements have been performed at low temperatures

( $\sim 15$  K) using the fast-continuous measurement mode described in section 4.4.2. In order to obtain maximum XMCD contrast, e.g. to detect possible paramagnetic contaminations, a maximum magnetic field of 7 Tesla has been applied. Large scale non-dichroic  $I_0$ -normalized overview scans (0.5 eV/s monochromator speed) have been performed to probe for magnetic impurities. The result is shown in figure 6.5. As guidelines, the locations of the important magnetic transition metals and the O K-edge are marked with black lines at the respective TM  $L_3$ -edge energy position.

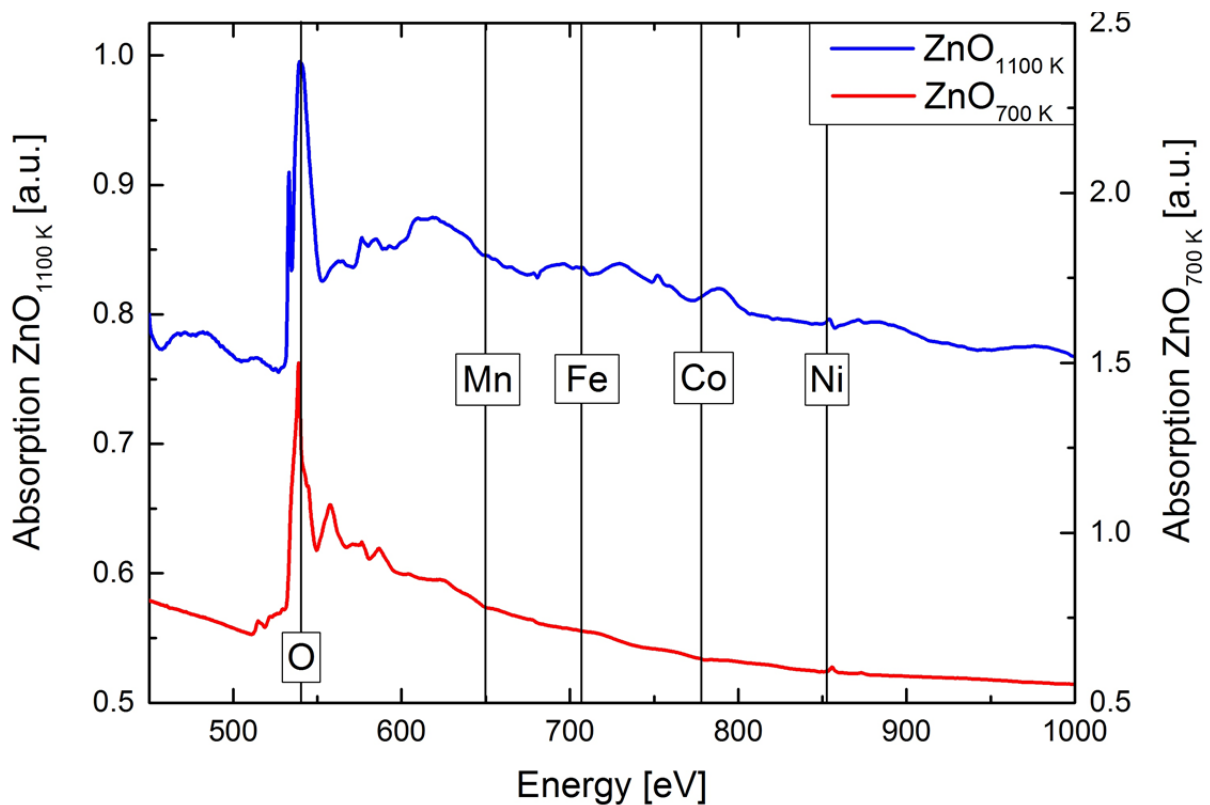


**Figure 6.5:** XAS overview scans of  $\text{ZnO}_{1100\text{K}}$  (blue) and  $\text{ZnO}_{700\text{K}}$  (red). In addition, the  $L_3$  absorption lines of the important magnetic transition metals are given.

Despite the slightly different fine structure of the OK edge, no significant absorption signal was found on the respective transition metal absorption lines. The XMCD setup detection limit is  $\sim 10^{-5} \mu_B$  for bulk and  $\sim 10^{-4} \mu_B$  for diluted magnetic systems. Typically, magnetic ions in a ZnO matrix exhibit a larger magnetic moment, for example in  $\text{Co}(5\%):\text{ZnO}$ , the magnetic moment is  $0.1 \mu_B$  per Co atom [71, 73, 184] (in an applied field of 2 Tesla) and clearly detectable with TEY technique. However it should be noted that a segregation of contaminations at e.g. the sample substrate surface (see e.g. [185]) cannot be completely



ruled out. As the samples were carefully kept away from metallic pincers during preparation procedure, this case is very unlikely.

The other possible source of magnetism in ZnO samples is oxygen, which shows an XMCD signal in CrO<sub>2</sub> for instance [99, 186]. From SQUID measurements, one can appraise the magnetization per O atom, assuming a hexagonal wurzite ZnO lattice and all oxygen atoms contributing equally to the sample magnetization. For ZnO<sub>1100K</sub>, one obtains  $2 \cdot 10^{-2} \mu_B/\text{O atom}$ , for ZnO<sub>700K</sub> sample, the magnetic moment per O atom should be  $3.2 \cdot 10^{-3} \mu_B/\text{O atom}$ . These magnetic moment values should be easily identified, if magnetism in the investigated samples really originates from oxygen.

The result of combined XAS/XMCD spectra of the OK edge for ZnO<sub>1100K</sub> and ZnO<sub>700K</sub> are shown in figure 6.6. The spectra have been obtained at a temperature of 15 K and an applied magnetic field of 7 Tesla. In order to enhance the accuracy of the measurements, a set of 5 spectra at both helicities was averaged. For both samples, no significant XMCD signal above the noise level could be detected at the OK edge, thus ruling out oxygen as a source of ferromagnetism in the FM ZnO samples.

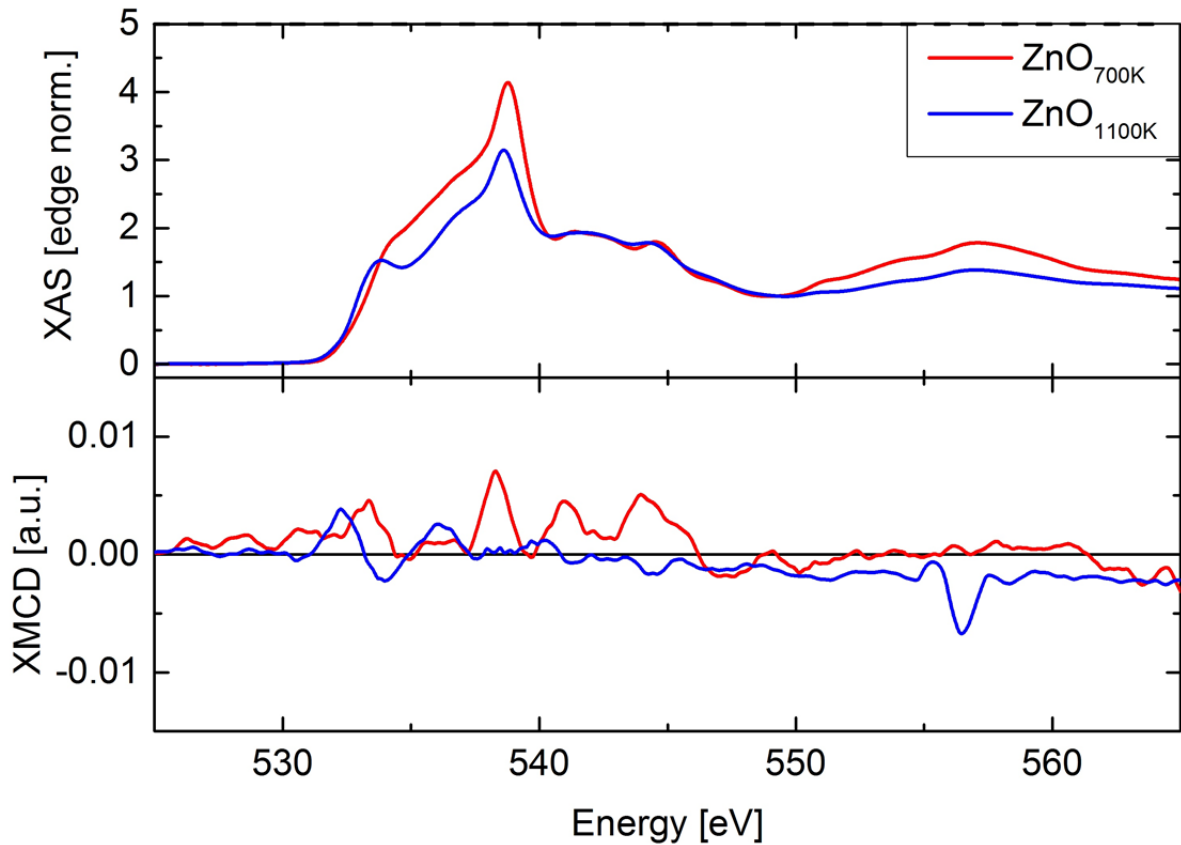


**Figure 6.6: XAS (top) and XMCD (bottom) signal comparison of ZnO<sub>1100K</sub> (black) and ZnO<sub>700K</sub> (red), measured at 15 K and an applied magnetic field of 7 Tesla.**

### 6.3. $\mu$ SR Measurements

The third method that has been applied to the nanograined samples and the single crystal reference is zero field low energy muon spin rotation/relaxation (LE-ZF  $\mu$ SR). All measurements have been performed at the LEMU beamline of the SpS at the PSI in Villigen, Switzerland. The beamline setup has been already introduced in section 4.2 and the  $\mu$ SR technique is described in details in section 3.6.

One key parameter that can be changed in the experiment is the penetration depth of muons into the sample, so that thickness dependent measurements can be performed. In order to tune the implantation depth, the sample surface is set to positive high voltage. The muon penetration into the sample also depends on the samples material. The calculated ZnO implantation depth in dependence of the applied sample voltage is shown in figure 6.7. In the following, the implantation depth will be given in the experimental parameter, sample voltage, instead of the length scale value. The mean depth values in dependence of the sample voltage are additionally listed in table 6.3.

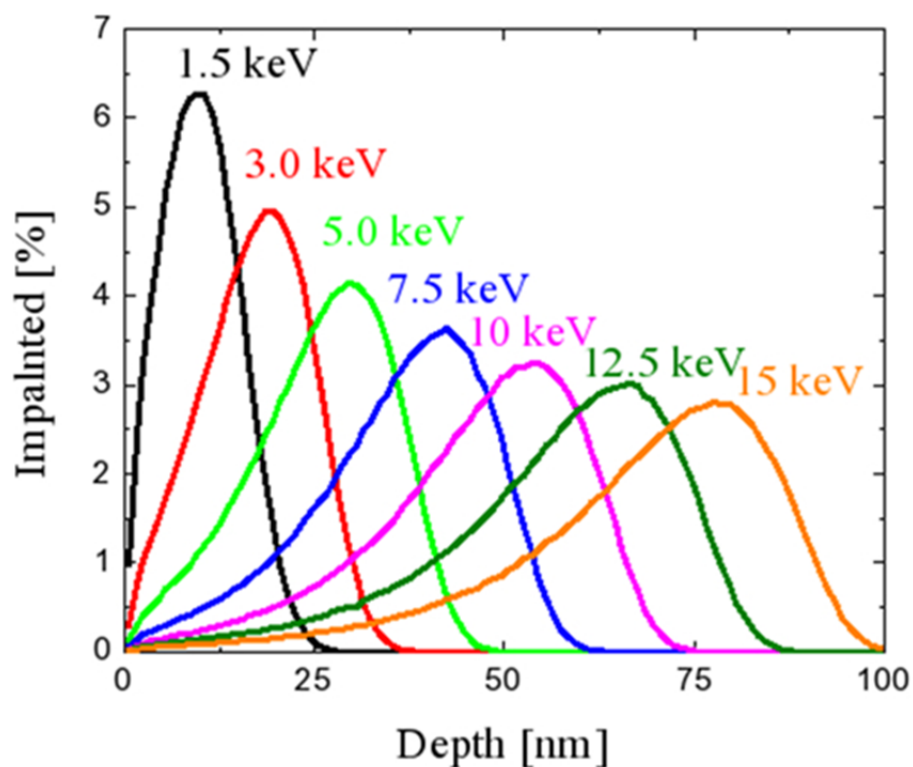


Figure 6.7: Muon implantation depth, given in nm, in dependence of the respective muon energy [187].

Table 6.3: Mean implantation depth given in nm in dependence of the sample voltage.

Voltage [keV]	Mean Implantation Depth [nm]
1.5	~10
3.0	~20
5.0	~30
7.5	~45
10	~55
12.5	~70
15	~80

For  $\text{ZnO}_{700\text{K}}$  and  $\text{ZnO}_{1100\text{K}}$ ,  $\mu$ SR experiments have been performed at zero field (ZF) and various sample voltages, ranging from 3.0 keV to 14.0 keV in order to probe the films for thickness related effects. The sample temperature was varied in three steps, 50 K, 100 K, and 250 K. For the single crystal reference, only low temperature measurements at 50 K with ZF

were performed, as a possible magnetic signal would be quite small due to the nearly vanishing SQUID magnetization curve at RT.

A of ZF- $\mu$ SR results for the three samples is shown in figure 6.8, where the detector asymmetry, normalized to its initial value at  $t = 0 \mu\text{s}$ , is plotted over time (see section 3.6). The respective spectra have been obtained by averaging spectra measured at different sample voltages (equivalent to an integration over the sample thickness) in order to obtain comparability to the SQUID measurements. Like for SQUID measurements, one observes clearly distinguishable signals for the respective samples.

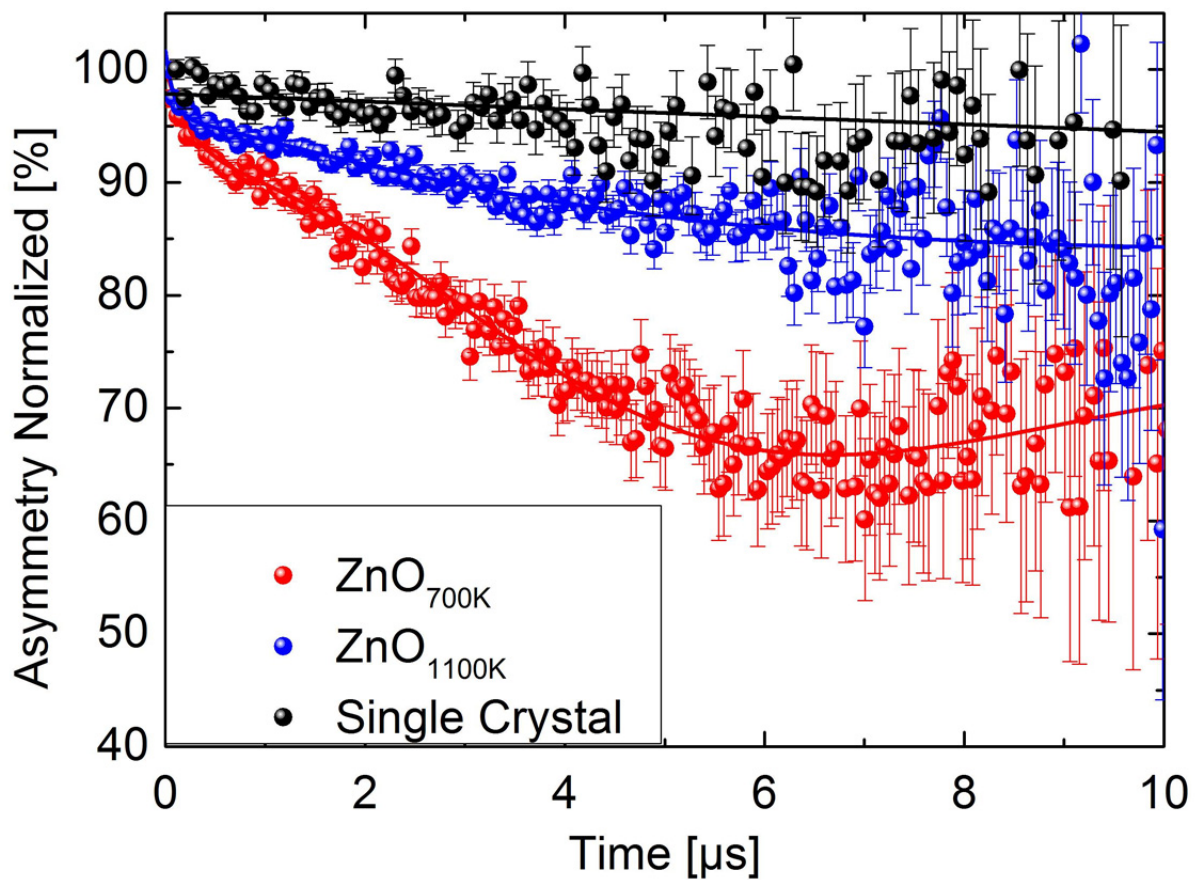


**Figure 6.8:** Comparison of ZF- $\mu$ SR spectra of the three different samples measured at 250 K (50 K for SC). Whereas the single crystal signal (black dots) is almost constant, the  $\text{ZnO}_{1100\text{K}}$  (blue dots) and  $\text{ZnO}_{700\text{K}}$  (red dots) sample curves show a clear loss asymmetry. Solid lines represent the respective fitted curves.

First of all, the single crystal signal (black dots) does not show any significant loss of asymmetry, in contrary to the magnetic ZnO samples. This result confirms the corresponding SQUID measurements were nearly no magnetic signal could be tracked.

For  $\text{ZnO}_{1100\text{K}}$  (blue dots) and  $\text{ZnO}_{700\text{K}}$  (red dots), there is a notable loss of asymmetry. This loss of asymmetry is an indicator for the magnetic volume fraction; one can thus conclude that  $\text{ZnO}_{700\text{K}}$  has a larger magnetic volume fraction than  $\text{ZnO}_{1100\text{K}}$ . The loss of asymmetry correlates with the fraction of magnetic grains and the SQUID related magnetization curves. A larger fraction of magnetic grains ( $\text{ZnO}_{700\text{K}}$ ) leads to a larger saturation magnetization (sum of all internal magnetic moments) and results in a stronger loss of  $\mu$ SR asymmetry. In the following sections, the  $\mu$ SR results for the respective magnetic ZnO samples will be discussed quantitatively.

### 6.3.1. $\text{ZnO}_{1100\text{K}}$ Sample

In order to obtain detailed information on the magnetic volume fraction and the distribution of internal magnetic fields, all ZF- $\mu$ SR asymmetry scans have been analyzed using fitting functions provided by the program MUSRFit [85]. The ZF- $\mu$ SR asymmetry scan for  $\text{ZnO}_{1100\text{K}}$  and its corresponding fit function is plotted in figure 6.9.

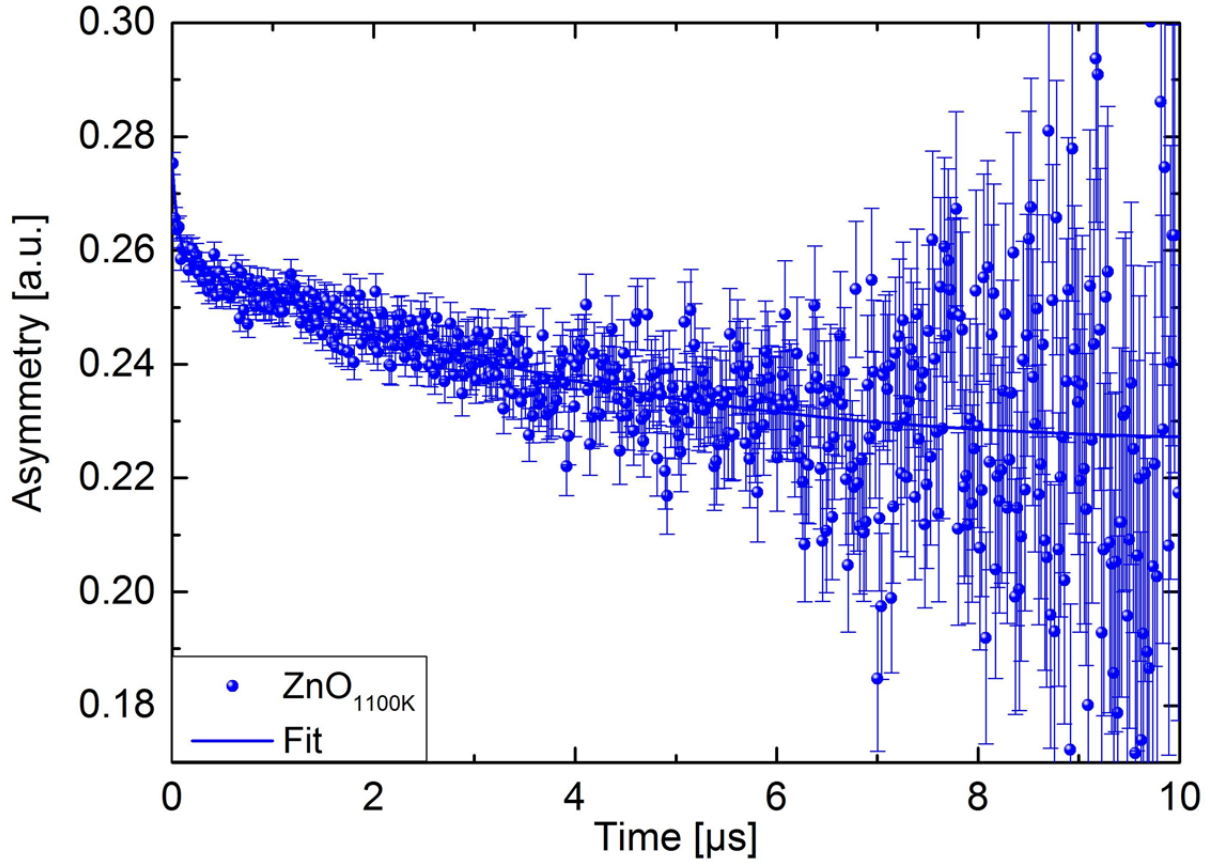


Figure 6.9: Averaged ZF LE- $\mu$ SR spectrum of the  $\text{ZnO}_{1100\text{K}}$  sample and corresponding fitting curve. As the fit parameters show no obvious dependence of implantation depth and measurement temperature, single histograms have been averaged to obtain a dataset of improved quality.

The experimental asymmetry functions of  $\text{ZnO}_{1100\text{K}}$  were best fitted using a combination of three different decay functions:

$$A_0 \cdot P_{\text{ZF}}(t) = \underbrace{A_{\text{Fast}} \cdot \exp(-\lambda_f t)}_{\text{high field}} + \underbrace{A_{\text{Slow}} \left[ \frac{1}{3} + \frac{2}{3} (-\lambda_s t)^{-\alpha} \cdot \exp\left(-\frac{\lambda_s t}{\alpha}\right) \right]}_{\text{low field}} + A_{\text{Non}} \quad (6.1)$$

- $A_{\text{Fast}}$  represents the fast and strong exponential loss of asymmetry in the  $\mu$ SR spectrum on the small time scale (0-1  $\mu$ s). This kind of decay is caused by quick dephasing of the muons due to a broad distribution of internal magnetic fields (see also section 3.6.4). The parameter  $\lambda_f$  corresponds to the field distribution width.

- $A_{Slow}$  represents the additional loss of asymmetry on intermediate to high time scale (5-10  $\mu$ s). The corresponding decay function is a Voigtian-Kubo-Toyabe (VKT) function [89]. It is a mixture between the Gaussian-Kubo-Toyabe (GKT) and the Lorentz-Kubo-Toyabe (LKT) (see equation (3.82)).  $\lambda_s$  is the width of the magnetic field distribution and  $\alpha$  a weighting coefficient. If  $\alpha = 1$  one obtains a pure LKT function, if  $\alpha = 2$  one obtain a pure GKT function.
- $A_{Non}$  represents the non-magnetic fraction of the  $\mu$ SR spectrum, simply represented by a constant term.

The magnetic properties can be extracted from the decay parameters, namely the field distribution width of local magnetic fields, which are assumed to be generated by magnetic moments located within the sample. Using the muon gyromagnetic ratio,  $\gamma_\mu = 2\pi \cdot 135 \text{ MHz/T}$  one can convert the decay parameters directly into magnetic field values:

$$B_{F,S} = \frac{2\pi \cdot \lambda_{F,S}}{\gamma_\mu} \quad (6.2)$$

However, fitting the fast and slow components at the same time is rather difficult, considering the fact that on a time scale larger than the muon lifetime data points scatter drastically and error bars are quite large. This may lead to an underestimation or negligence of the fast component when trying to “feed” the fit curve through the scattered data points on larger time scale. Thus the fast component was determined from the fast Fourier transform (FFT) of the experimental asymmetry spectrum. The half width at half maximum (HWMW) of the corresponding Lorentz curve<sup>34</sup> equals the decay parameter  $\lambda_f$ . Note that only the parameter  $\lambda_f$  was determined applying FFT. Applying the same approach to determine  $\lambda_s$  is inappropriate here. The main implication is the contribution of the constant nonmagnetic signal to the FFT, which is delta peak function. However, because the integration boundaries are on finite scale, the delta peak is broadened and dominating the narrow FFT peak of the VKT (a Voigtian line profile).

---

<sup>34</sup> The exponential decay function  $e^{-at}$  is the characteristic function of a Lorentzian line profile with HWHM  $a$ .

The averaged magnetic field distribution width of the fast decay part is  $9.3 \pm 0.2$  mT. Due to its rather broad field distribution, this part, respectively sample region will be labeled as “high field” region in the following. The averaged magnetic field width of the slow decay part is  $0.14 \pm 0.04$  mT. Due to its narrow field distribution width, this sample region will be called “low field” region in the following. The depth and temperature dependent field width values for the high and low magnetic field parts are shown in the upper respectively lower panel of figure 6.10. No obvious dependence of the implantation depth or measurement temperature was observed, which is in agreement with the temperature independent SQUID measurements.

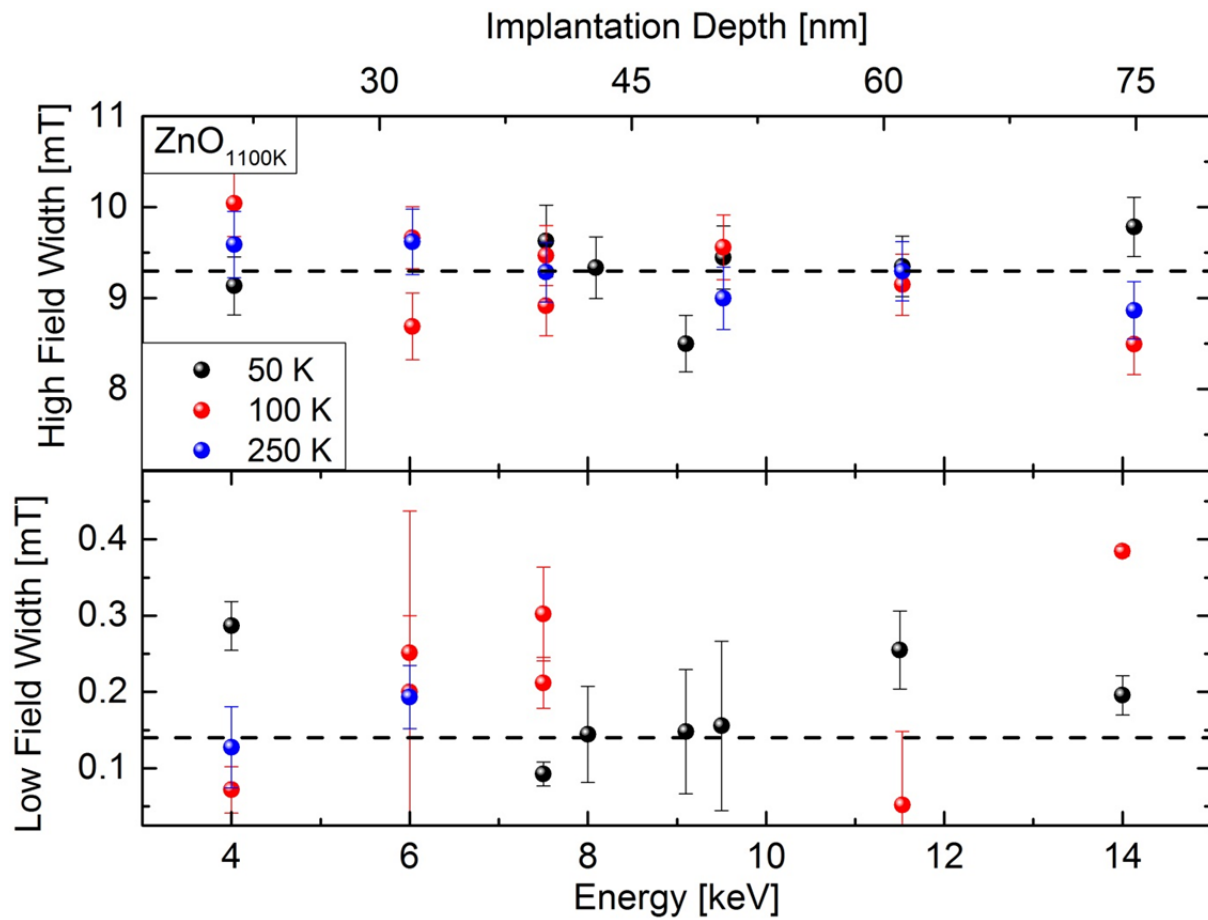


Figure 6.10: Upper part: Magnetic field width of the high magnetic field sample region in dependence of the muon implantation depth and the temperature (color coded dots). The average high field width is 9.3 mT (dashed line). Lower part: The same plot for the low magnetic field region. The average low field width is 0.14 mT (dashed line).



Of further particular interest is the relative loss in asymmetry which is directly related to the magnetic volume fraction (MFV). It can be calculated relating the respective asymmetry coefficient  $A_i$  to the total asymmetry  $A_{tot} = \sum A_i$ :

$$MFV_i = \frac{A_i}{A_{Fast} + A_{Slow} + A_{non}} \quad (6.3)$$

ZnO<sub>1100K</sub> sample, the high field magnetic volume fraction is 5.8 %, the low field magnetic volume fraction is 13.4 %, and congruously 80.8 % of the sample is non-magnetic. The magnetic field distribution width and the magnetic volume fraction of the high, the low, and the nonmagnetic sample region are summarized in table 6.4.

**Table 6.4: Magnetic field distribution width and magnetic volume fraction of the three differently magnetic regions that have been identified in ZnO<sub>1100K</sub>.**

Region	Field Dist. Width [mT]	Fitparameter $A_i$	MFV
High field	9.3±0.2	0.0157±0.0022	5.8 %
Low field	0.14±0.04	0.0366±0.0072	13.4 %
Nonmagnetic	0	0.2203±0.0058	80.8 %

### 6.3.2. ZnO<sub>700K</sub> Sample

The ZF- $\mu$ SR asymmetry scans of ZnO<sub>700K</sub> have been analyzed in the same way as the spectra of ZnO<sub>1100K</sub>. A set of ZF- $\mu$ SR spectra has been measured for different muon implantation depths and for the same temperatures: 50 K, 100 K and 250 K respectively. The averaged  $\mu$ SR asymmetry spectrum and the corresponding fit function are shown in figure 6.11.

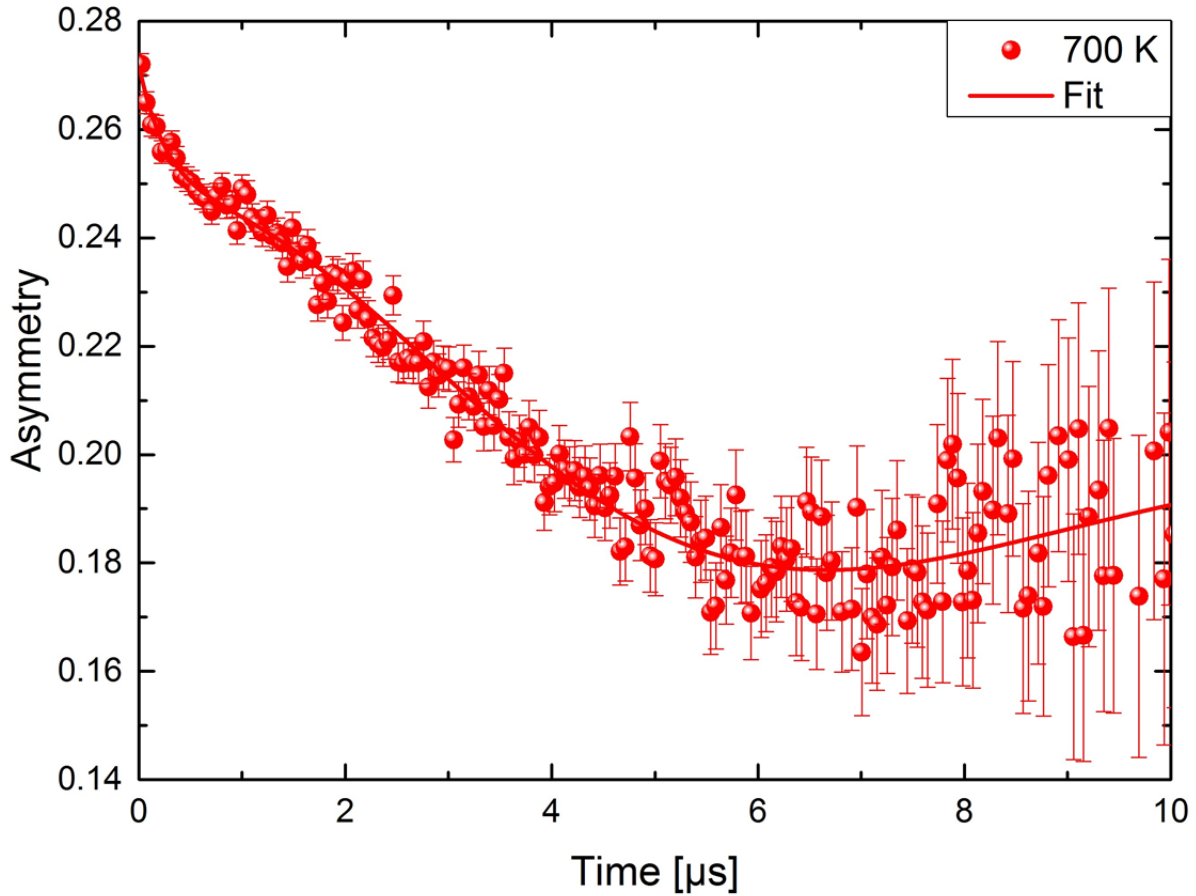


**Figure 6.11:** ZF LE- $\mu$ SR spectrum and corresponding fit function of  $\text{ZnO}_{700\text{ K}}$ . As the fit parameters show no obvious dependence of implantation depth and measurement temperature, single histograms have been averaged to obtain a dataset of improved quality.

Similar to the procedure for  $\text{ZnO}_{1100\text{ K}}$ , the experimental  $\mu$ SR asymmetry scans were fitted using the program MUSRFIT [85].  $\mu$ SR asymmetry spectra were best fitted using three different contributions:

$$A_0 \cdot P(t) = \underbrace{A_{\text{Fast}} \cdot \exp(-\lambda_F t)}_{\text{high field}} + \underbrace{A_{\text{Slow}} \cdot \left[ \frac{1}{3} + \frac{2}{3} \left[ 1 - \sigma_{\text{Slow}}^2 t^2 \right] \exp\left(-\frac{1}{2} \sigma_{\text{Slow}}^2 t^2\right) \right]}_{\text{low field}} + A_{\text{Non}} \quad (6.4)$$

- $A_{\text{Fast}}$  is, similar to the result  $\text{ZnO}_{1100\text{ K}}$ , representing the fast and strong exponential loss of asymmetry in the  $\mu$ SR spectrum on the small time scale (0-1  $\mu$ s). It is caused by quick dephasing of the muons due to the rather broad distribution of stronger internal magnetic fields (see section 3.6.4). Following

the nomenclature of the previous section, the fast decay part of the sample shall be labeled high field region.

- $A_{slow}$  is representing the additional loss of asymmetry on intermediate time scale (1-6  $\mu$ s) and its recovery on large time scale (6-10  $\mu$ s). The corresponding decay function is a Gaussian-Kubo-Toyabe (GKT) function, described by equation(3.79) [87]. The GKT decay stems from randomly oriented weak but in the respective area densely distributed internal magnetic fields. This region shall be labeled as low field region in the following.
- $A_{Non}$  is a constant term and representing the non-magnetic fraction of the  $\mu$ SR spectrum.

The magnetic field distribution width for the high and low field regions were determined similar to the procedure applied to the  $ZnO_{1100K}$  sample, determining  $\lambda_F$  from FFT and  $\sigma_{slow}$  from the respective fitting parameters. The averaged high field distribution width is  $8.7 \pm 1.4$  mT, the low field distribution width is  $0.18 \pm 0.02$  mT. The result is plotted in the upper respectively lower panel of figure 6.12 and additionally listed in table 6.5.

The respective magnetic volume fractions can be determined using equation (6.3). For the  $ZnO_{700K}$  sample, the volume fraction of the strong field leading to the fast decay  $A_{Fast}$  is  $\sim 8.4$  %, the volume fraction  $A_{GKT}$  were low magnetic fields are found is  $\sim 26.6$  %, congruously a volume fraction of 65 % of the sample is non-magnetic.

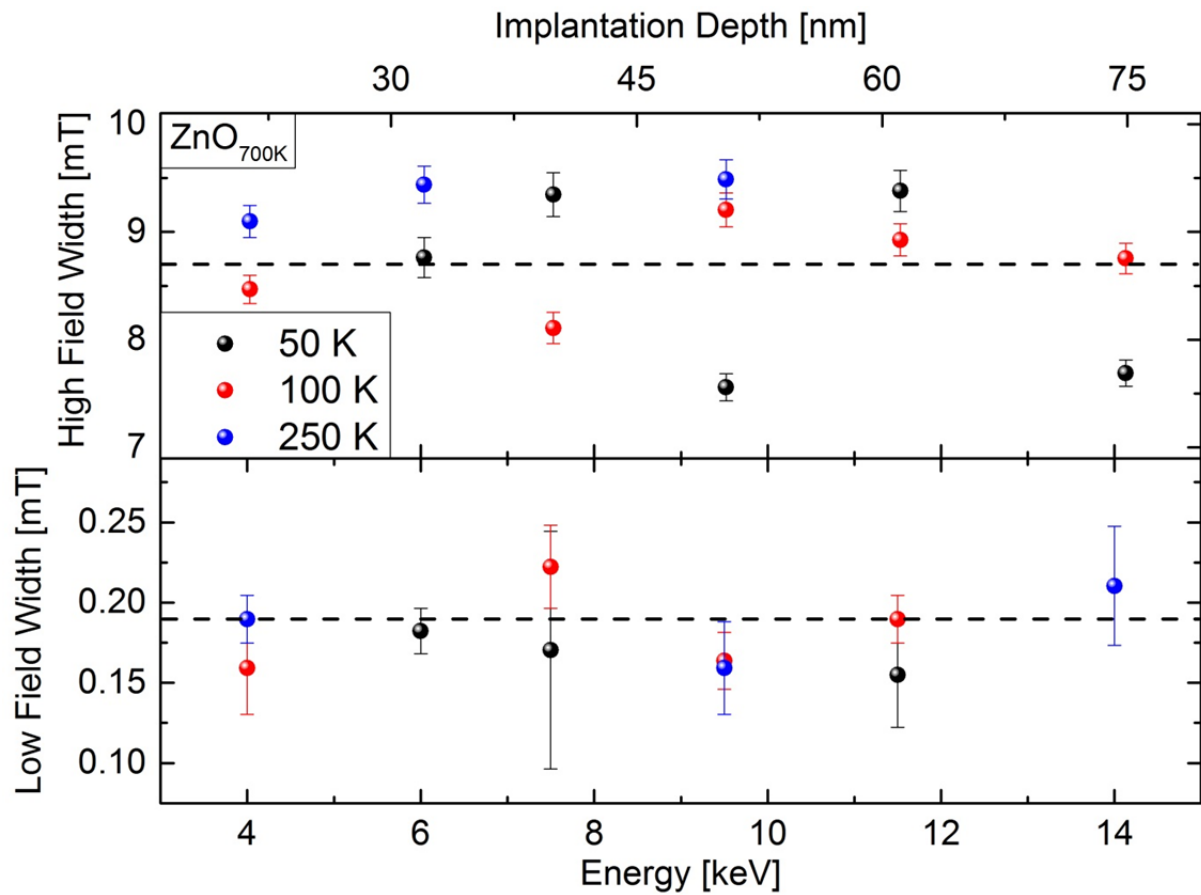


Figure 6.12: Upper part: High magnetic field distribution width of  $\text{ZnO}_{700\text{K}}$  in dependence of the measurement temperature and the muon implantation depth. The average high magnetic field width is 8.7 mT. Lower Part: The same plot for the low magnetic field distribution width. The average low magnetic field width is 0.18 mT. No obvious tendencies were found tuning the temperature and the muon implantation depth.

Table 6.5: Magnetic field distribution width and magnetic volume fraction of the three differently magnetic regions that have been identified in  $\text{ZnO}_{700\text{K}}$ .

Region	Field Dist. Width [mT]	Fitparameter $A_i$	MVF
High field	$8.7 \pm 1.4$	$0.0256 \pm 0.005$	9 %
Low field	$0.18 \pm 0.02$	$0.084 \pm 0.023$	26.5 %
Nonmagnetic	0	$0.0177 \pm 0.024$	64.5 %

## 6.4. Discussion

### 6.4.1. Formation of Muonium

An important issue in  $\mu$ SR studies of e.g. semiconductors is the formation of so-called muonium (see e.g. [188]). LE- $\mu$ SR is performed actually using “anti-muons”, positively charged muons that can in principle “catch” an electron from the delocalized electrons of the Zn 3d or O 4s bands and form a hydrogen like muonium state:  $Mu = [\mu^+ e^-]$ . In the case of ZnO this state is known as “shallow donor” and has been observed previously [189-191]. The muonium state in ZnO can be identified performing  $\mu$ SR asymmetry scans in an applied magnetic field.

The muonium state can be probed by measuring the  $\mu$ SR asymmetry at temperatures below 40 K, and small applied magnetic fields. Cox et. al. [189] performed LE- $\mu$ SR measurements on ZnO powder, at 5 K and an applied field of 20 mT in order to proof the existence of the muonium shallow donor state in ZnO. Their results are shown in figure 6.13 a) and b).

The asymmetry scan (figure 6.13 a)) shows a distinct beating. The corresponding Fourier transform (figure 6.13 b)) shows, in addition to a center Larmor peak, two additional symmetrically placed side peaks. The convolution of these additional components finally leads to the beating in figure 6.13 a). Cox et. al. address these side peaks to a hyperfine interaction of a single electron that is “caught” by the positively charged muon.

In comparison, results from similar measurements on ZnO<sub>700K</sub> are shown in figure 6.13 c) and d). The actual conditions were slightly different compared to Cox et. al.. The temperature was 50 K and the applied magnetic field was set to 10 mT. The asymmetry scan in figure 6.13 c) shows, in contrary to figure 6.13 a), no distinct beating. A detailed look at the corresponding Fourier transform in figure 6.13 d) shows no sign of additional “side peaks”, except the main “Larmor” peak. Similar results were found for the ZnO<sub>1100K</sub> sample and the ZnO single crystal reference.

Thus, the formation of muonium can be ruled out as a cause of the magnetic signals in the corresponding ZF- $\mu$ SR measurements of ZnO<sub>1100K</sub> and ZnO<sub>700K</sub>.

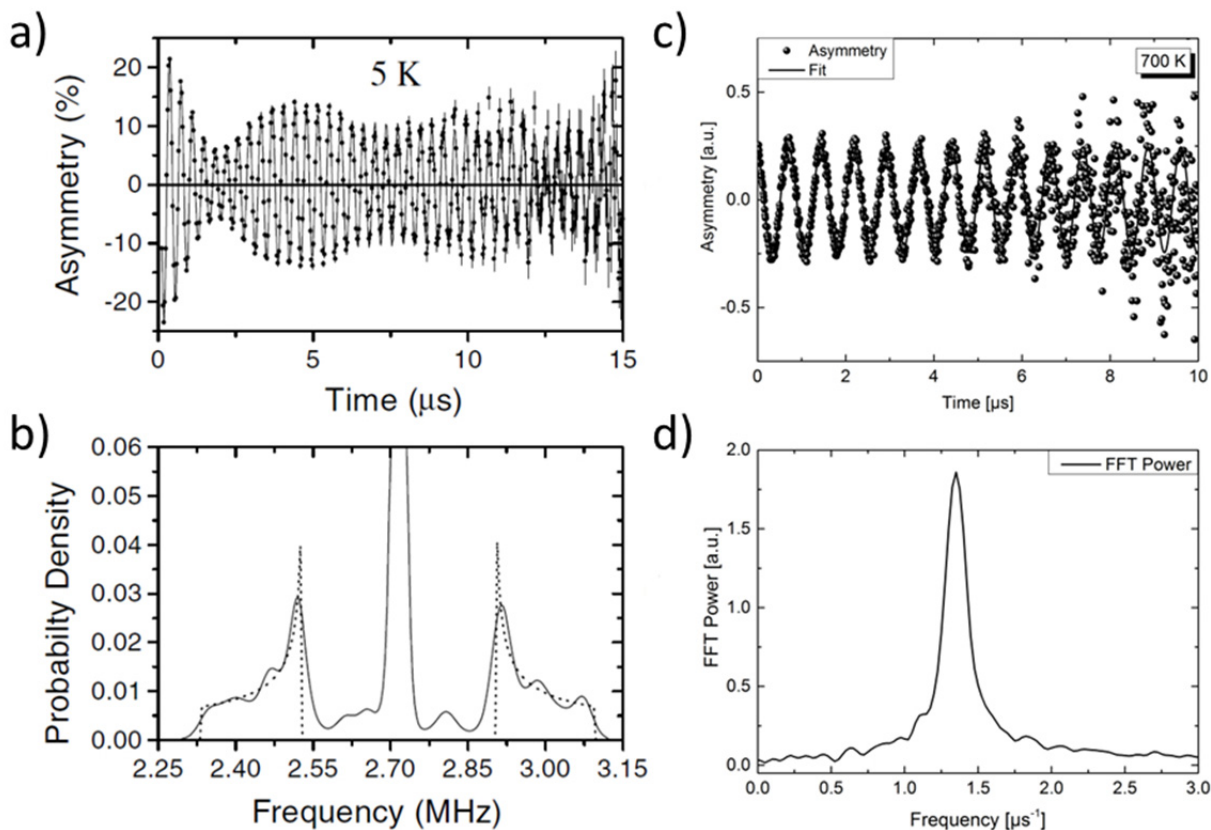


**Figure 6.13 a):** Asymmetry scan of a ZnO single crystal, measured at 50 K and an applied magnetic field of 20 mT, showing a beat frequency pattern. **b)** The corresponding Fourier transform. **c)** Shows asymmetry scan of ZnO<sub>700K</sub> at 50 K and 10 mT. **d)** Shows the corresponding Fourier transform. **a)** and **b)** reprinted with permission from [189]. Copyright (2001) by the American Physical Society.

#### 6.4.2. Magnetic Grain Boundary Area

In the previous section, it was demonstrated that ZnO<sub>1100K</sub> and ZnO<sub>700K</sub> contain regions with broader (high field region) and narrower (low field region) magnetic field distributions. Their respective average field distribution widths are almost equal. The average high field distribution widths are  $9.3 \pm 0.2$  mT and  $8.7 \pm 1.4$  mT for ZnO<sub>1100K</sub> and ZnO<sub>700K</sub> respectively. The average low field distribution widths are  $0.14 \pm 0.04$  mT and  $0.18 \pm 0.02$  mT for ZnO<sub>1100K</sub> and ZnO<sub>700K</sub> respectively. This indicates that the actual offspring of the magnetic fields is the same in both samples and the difference in saturation magnetization between ZnO<sub>700K</sub> and ZnO<sub>1100K</sub> is a congruous consequence of different magnetic volume fractions.

Using the results from ZF-μSR measurements, one can now probe the relation between the magnetic volume fraction estimated by μSR asymmetry scans and the volume

fraction occupied by grain boundaries determined from TEM pictures. Figure 6.14 a) shows a TEM picture of multiple grains in  $\text{ZnO}_{1100\text{K}}$ . The amorphous grain boundary area (highlighted yellow) is located between the single crystalline grains, exhibiting a thickness of typically 1-2 nm.

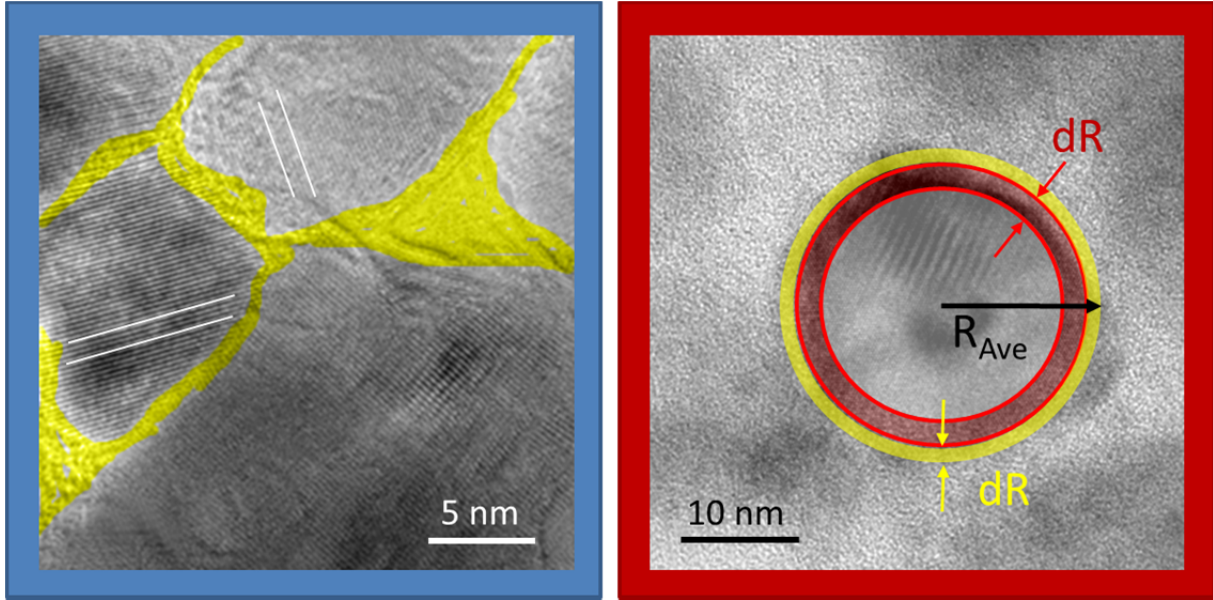


**Figure 6.14:** Sketching the idea of magnetism in ZnO stemming from magnetic grain boundaries. In a simple approach, one can assume that all magnetic moments causing the loss of  $\mu\text{SR}$  asymmetry are located within the grain boundaries, highlighted yellow in a). In b), the definition of the grain boundary thickness and the mean radius of a single grain in order to calculate the grain boundary volume fraction are sketched.

One now can approximate the respective portion of this grain boundary volume with respect to the total grain volume and compare it to the MFV estimated from  $\mu\text{SR}$  measurements. Figure 6.14 b) shows a ZnO grain of the  $\text{ZnO}_{700\text{K}}$  sample and its surrounding grain boundary. The grain is assumed to be a nonmagnetic sphere with radius  $R_{\text{Ave}}$  and volume  $V_{\text{Grain}}$ :

$$V_{\text{Grain}} = \frac{4}{3}\pi \cdot R_{\text{Ave}}^3 \quad (6.5)$$

In this model,  $V_{\text{Grain}}$  corresponds to the nonmagnetic part of the  $\mu\text{SR}$  measurements.

The grain boundary is approximated as spherical shell, highlighted yellow, and supposed to be the high magnetic field region. The reddish shell at the inner close vicinity of

the grain boundary is supposed to be the low magnetic field region. The effective thickness of each shell shall be  $dR$ , their respective shell volume:

$$V_m = 4\pi \cdot R_{Ave}^2 \cdot dR \quad (6.6)$$

The volume fraction of the supposedly magnetic grain boundary sphere shell with respect to the nonmagnetic grain volume is then given by:

$$\frac{V_m}{V_{Grain}} = \frac{4\pi \cdot R_{Ave}^2 \cdot dR}{\frac{4}{3}\pi \cdot R_{Ave}^3} = \frac{3 \cdot dR}{R_{Ave}} \quad (6.7)$$

Equating expression (6.7) with the  $\mu$ SR related MFV in table 6.4 and table 6.5 one obtains the effective thickness of the high and low shield sphere:

$$dR = \frac{MFV \cdot R_{Ave}}{3} \quad (6.8)$$

$R_{Ave}$  was set according to the average grain size determined in section 6.1,  $R_{Ave} = 31 \text{ nm}$  for  $\text{ZnO}_{700\text{K}}$  and  $R_{Ave} = 65 \text{ nm}$  for  $\text{ZnO}_{1100\text{K}}$ .

For the thickness of the high magnetic field shell, one obtains  $dR = 0.95 \text{ nm}$  and  $dR = 1.3 \text{ nm}$  for  $\text{ZnO}_{700\text{K}}$  and  $\text{ZnO}_{1100\text{K}}$ , calculated using  $\mu$ SR related MFV of 9 % and 5.8 % respectively. The respective values are exactly in the range of the typical grain boundary thickness of 1-2 nm. The thickness of the low magnetic field shell is  $dR = 3.1 \text{ nm}$  and  $dR = 2.8 \text{ nm}$  for  $\text{ZnO}_{700\text{K}}$  and  $\text{ZnO}_{1100\text{K}}$ , calculated using  $\mu$ SR related MFV of 26.5 % and 13.4 % respectively. This value is typical for dipolar like fields decaying beyond the  $\mu$ SR detection limit [10], thus possibly corresponding to  $\mu$ ons sensing the stray field from the actual magnetic grain boundary rather than magnetic moments from this “intermediate” shell. The results are summarized in table 6.6.



**Table 6.6: Volume fraction and respective sphere shell thickness of the magnetic regions in  $\text{ZnO}_{1100\text{K}}$  and  $\text{ZnO}_{700\text{K}}$ .**

	$\text{ZnO}_{700\text{K}}$	$\text{ZnO}_{1100\text{K}}$
$R_{\text{Ave}}$	31 nm	65 nm
$\text{MFV}_{\text{HF}}$	9 %	5.6 %
$dR_{\text{HF}}$ (yellow)	0.95 nm	1.3 nm
$\text{MFV}_{\text{LF}}$	26.5 %	13.4 %
$dR_{\text{LF}}$ (reddish)	3.1 nm	2.8 nm

These quantitative calculations provide consistent results between the magnetic volume fractions estimated by ZF- $\mu\text{SR}$  and the respective volume fraction occupied by grain boundaries. The idea of magnetic grain boundaries was also confirmed by density functional theory (DFT) calculations on grain boundaries in ZnO [192, 193]. It was found that there are a significant number of free electrons in the grain boundaries. These electrons can couple with other electrons in two different ways: the nonmagnetic singlet (electron spin anti-parallel) and the magnetic triplet state (electron spin parallel) resulting in a sizable magnetic moment. The energy barrier between the two states is rather large in the ZnO SC (4.3 eV) but within typical band widths for the grain boundary systems (0.2 eV). If the grain size is small enough to fulfill the percolation condition, even undoped ZnO can become FM.

### 6.5. Summary: Magnetism in nanograined ZnO

In order to investigate the origin of FM in nanograined ZnO systems, differently grained samples were investigated within this thesis. Three samples were studied in details in order to probe the relation between the specific grain boundary area/the average grain size and the magnetic properties. A relation between the volume occupied by grains and the magnetic volume fraction was found suggesting that magnetic moments are located in the grain boundary, causing FM if a certain threshold limit is exceeded. This threshold limit is located at  $\sim 40$  nm grain size corresponding to a  $s_{GB}$  of  $\sim 5 \cdot 10^7 \text{ m}^{-1}$ .

Using the hydrothermal method, two differently nanograined ZnO thin film samples were grown on a sapphire substrate, tuning the annealing temperature: one sample with average grain size of 30 nm (annealing temperature: 700 K), one sample with average grain size of 65 nm (annealing temperature: 1100 K). The samples are labeled according to their annealing temperature: ZnO<sub>700K</sub> and ZnO<sub>1100K</sub>. A commercial single crystal served as mainly grain boundary free nonmagnetic reference system. SQUID, XMCD, TEM, and LE- $\mu$ SR techniques were applied in order to probe the magnetic and structural sample properties.

TEM pictures were analyzed in order to determine the grain size distribution of the respective samples more detailed. For both samples, a Gaussian distribution of the grain size was found. For both samples, a certain fraction grains were small enough to fulfill the magnetic threshold condition, namely 10 % of grains in ZnO<sub>1100K</sub> and 55 % of grains in ZnO<sub>700K</sub>.

SQUID measurements of the nanograined samples showed magnetic hysteresis loops with significant saturation magnetization, remnance, and coercivity at RT, whereas the grain boundary free SC was nonmagnetic. The saturation magnetization increases when the sample contains a larger number of smaller grains, namely  $8 \text{ emu/cm}^3$  for ZnO<sub>700K</sub> and  $1.25 \text{ emu/cm}^3$  for ZnO<sub>1100K</sub>. In addition, SQUID hysteresis loops were recorded at 50 K as well, to proof FM and distinguish from SPM, e.g. due to contamination with magnetic impurities. No significant difference between the RT and the 50 K magnetization curves were found. Thus one can indeed claim FM of the respective samples.

Contributions from magnetic impurities were also excluded by low temperature XAS and XMCD measurements. Furthermore, no significant magnetic polarization of the O-K or the Zn L<sub>2,3</sub>-edges could be detected.

ZF LE- $\mu$ SR measurements were performed on the magnetic samples and the SC reference in order to determine magnetic volume fractions and the general distribution of internal magnetic fields. Two different magnetic regions were identified in both samples, one with a broad field distribution, indicating high internal magnetic fields, one with a narrower field distribution, indicating low internal magnetic fields. The  $\mu$ SR-related magnetic volume fractions are in agreement with predictions from TEM analysis. In ZnO<sub>700K</sub> a total magnetic volume fraction of 35.5 % was found, 9 % related to the high and 26.5 % related to the low magnetic field region. The field distribution widths were  $8.7 \pm 1.4$  mT and  $0.18 \pm 0.02$  mT for the high and low field region respectively. In ZnO<sub>1100K</sub> the total magnetic volume fraction was 19.2 %, 5.8 % related to the high, and 13.4 % related to the low magnetic field region. The field distribution widths were  $9.3 \pm 0.2$  mT and  $0.14 \pm 0.04$  mT for the high and low field distribution respectively. There is no general difference in field distribution and distribution widths, indicating similar offspring of magnetic fields and thus magnetic moments within the samples. The difference in SQUID related saturation magnetization values can be explained by different magnetic volume fractions.

A quantitative model was proposed, showing the relation between the  $\mu$ SR related magnetic volume fraction and the volume occupied by grain boundaries. It proves the possibility that the magnetic fields were caused by magnetic moments trapped within the grain boundaries. Assuming the high and low field magnetic regions as spherical magnetic shells around the nonmagnetic, single crystalline ZnO grain, and calculating their respective thickness from  $\mu$ SR related magnetic volume fractions identify the high field region as grain boundary ( $\sim 1$  nm shell thickness). The low field region is identified as region where  $\mu$ ons still sense magnetic stray fields from the grain boundary before they fall below the detection limit ( $\sim 3$  nm shell thickness). Recent MD and DFT based theoretical calculations predict a possible magnetic coupling of electrons in grain boundaries.

Using the combination of integrating (SQUID), element specific (XAS, XMCD), and local probe magnetic characterization techniques, proof for FM in undoped ZnO samples and their microscopic origin, magnetic moments in grain boundaries, were found and predictions based on previous experimental observations were confirmed. These results strongly support that FM in undoped ZnO, and principally in other oxide semiconductors, is an intrinsic property and not related to e.g. contamination or characterization issues.

The findings of this thesis could clear the path for a new type of unconventional electronic devices. Instead of nanograins, one could try to produce ferromagnetic semiconductor devices consisting of alternating layers of crystalline and amorphous ZnO.

## 7. Thesis Summary

The aim of this thesis was to investigate the influence of the nanostructure on the magnetic properties of certain materials, using the sophisticated, accelerator based x-ray magnetic circular dichroism and muon spin rotation/relaxation techniques. Two different, nanoscaled sample systems were investigated: Nickel nanoclusters on a graphene Moiré template and ferromagnetic, nanograined ZnO.

### **Results: Nickel clusters on graphene**

Electronic and magnetic properties of Ni nanoclusters on graphene were investigated using XMCD and XAS techniques. Two differently shaped nanocluster types were produced: with triangular and spherical/elliptical shape. Furthermore, the cluster size was altered. From XAS measurements it was found, that the number of unoccupied Ni d-states changes with the cluster size but not with cluster shape.

- For smaller cluster size, the occupancy of the Ni d-states increases strongly with respect to bulk Ni properties.
- The Ni 4s states remain unaffected, indicating that filling of d-states is related to charge transfer from graphene to Ni.

This result supposedly is a consequence of strong hybridization between graphene  $p_z$  and Ni d-states. With increasing cluster size, interfacial effects become less pronounced and electronic properties of the nanoclusters converge towards bulk properties.

As a direct consequence, the magnetic properties of the nanoclusters are altered as well; as a function of cluster size but independent of cluster shape.

- With decreasing cluster size, the total magnetic moment is decreasing with respect to bulk Ni properties.
- The ratio between spin and orbital magnetic moment is increased for smaller cluster sizes.

This result is a consequence of distinct features in the Ni d-band structure, where unoccupied states are mainly of minority spin character. Adding additional electrons shifts the Fermi level and reduces the spin polarization of the Ni d-band. Thus the total magnetic

moment is reduced and the enhancement of the orbital with respect to spin magnetic moment is a consequence of the reduction of the latter.

- Therefore, charge transferred from graphene to Ni is supposedly of minority spin character.

To reveal more details of the graphene/Ni interaction, XAS and XMCD measurements were also performed on the carbon K-edge.

- The signal from interfacial graphene could not be isolated properly.
- No significant XMCD effect could be detected.

Isolating a sober graphene signal turned out to be impossible with the present experimental setup. The signal on the carbon edge was convoluted with a large background and the interfacial signal was strongly damped by Ni clusters atop. Thus a conclusive statement for affections of graphene is difficult.

Using XMCD, angle dependent magnetization curves were measured and the magnetic anisotropy energy was determined. The nanoclusters are superparamagnetic, with an in-plane magnetic easy axis.

- The magnetic anisotropy energy consists of a size dependent surface/interface a size independent volume contribution and contributions from the shape anisotropy.
- The volume contribution to the anisotropy energy is similar for triangular and spherical nanoclusters.
- The surface contribution to the anisotropy energy is deviating for triangular and spherical nanoclusters.
- Transition to perpendicular magnetic easy axis is predicted to occur below 0.2 ML and 0.03 ML for triangular and spherical nanoclusters respectively.

The transition from in-plane to perpendicular magnetization, as it is desired for high density data storage devices, can be (principally) achieved for very low nominal deposition.

---

**Results: Ferromagnetic, undoped ZnO**

Undoped and differently nanograined ZnO samples were investigated by the combination of TEM, SQUID, XAS and XMCD and the local magnetic probe method of  $\mu$ SR. Correlating the sample volume occupied by grain boundaries and the  $\mu$ SR related magnetic volume fraction, the microscopic origin of RT-FM in ZnO has been identified. Furthermore, magnetic properties of nanograined ZnO samples deviate strongly compared to a single crystal reference sample.

- The nanograined ZnO samples show ferromagnetic behavior, confirmed by temperature independence of their respective SQUID magnetization curves.

The respective saturation magnetization and  $\mu$ SR determined magnetic volume fraction increase with increasing fraction of grains that are smaller than the required threshold grain size. Furthermore, two different types of magnetic field distributions could be identified within the ferromagnetic ZnO samples: a small volume fraction containing high and larger volume fraction containing low magnetic fields.

- The average field strength of the internal magnetic field is nearly equal for each ferromagnetic ZnO sample, indicating that their source is identical.
- The  $\mu$ SR related magnetic volume fraction of the high field component is similar to the volume fraction occupied by grain boundaries in each sample, identifying grain boundaries as high magnetic field volume.
- The  $\mu$ SR related magnetic volume fraction of the low field component is similar to the typical decay length of dipolar like fields. It is suggested that within these regions  $\mu$ ons sense magnetic stray fields from the actual magnetic grain boundaries.

In contrary to the ferromagnetic ZnO samples, grain boundary free single crystal reference sample shows neither significant SQUID nor  $\mu$ SR related magnetic response.

---

## Experimental Achievements

In order to perform the investigations presented within this thesis, several upgrades on the existing XMCD setup as well as on data acquisition and data analysis procedures were performed.

- A new, fast switching, superconducting, and cryo-free magnet system with maximum magnetic field of 7 T was implemented into the existing XMCD-setup. The 7 T magnet system is described in details in section 4.3.
- A new preparation chamber was designed, built, and further developed in order to match the requirements for in-situ graphene and nanocluster preparation. Details on the preparation section of the XMCD setup can be found in section 4.3.

Besides the above mentioned technical achievements, further major improvements concerning data acquisition and analysis were realized:

- The so-called “fast continuous” measurement mode was introduced for the existing XMCD setup. It reduces the measurement time for a pair of absorption spectra for XMCD by one order of magnitude compared to the previously used measurement mode, where the magnetic field was flipped at each data point. A detailed description of the fast-continuous mode can be found in section 4.4.2.
- In order to remove the dominating substrate background signal, a new background subtraction procedure was developed, using background reference signals. The background was modeled accordingly and removed from raw data, resulting in high quality Ni spectra. Even at the lowest nominal Nickel deposition satellite peaks with lower intensity can be resolved. A detailed description on the background removal procedure using reference spectra is given in sections 4.4.4 and 4.4.5

Both, technical and methodical progresses were vital for the progress and success of the topics presented within this thesis. Furthermore, this thesis set standards in data acquisition and analysis, clearly improving the pre-existing experimental setup.



---

## Outlook

This thesis shall be closed with an outlook concerning the research areas of magnetic nanoclusters on graphene templates and magnetic, undoped ZnO.

First of all, investigations on the electronic and magnetic properties of nanoclusters on graphene can be extended to other magnetic materials, especially the close by transition metals iron and cobalt. Another task would be detailed measurements on the carbon K-edge in order to probe the interaction of the deposited material and the graphene substrate. This is a challenging task, from technical and analytical point of view. Thorough cleaning of beamline optics and high quality reference spectra would be required to isolate the graphene signal from raw data. Measurements at a steep grazing incident could yield the necessary surface sensitivity while photo electrons could still escape the sample surface even through the transition metal clusters.

For ferromagnetic, undoped ZnO upcoming projects could involve stacked layers of crystalline ZnO with an amorphous phase in-between. A possible thickness/stacking dependency could also assist more detailed theoretical studies on this topic and clear the path towards ZnO based ferromagnetic semiconductors.



## Literature

- [1] S.J. Blundell, Magnetism in Condensed Matter, Oxford Master Series in Condensed Matter Physics, Oxford University Press, (2010).
- [2] B.D. Cullity, C.D. Graham, Introduction to Magnetic Materials, IEEE Press Wiley, New Jersey, 2009.
- [3] H. Haken, H.C. Wolf, Atom- und Quantenphysik (7. Auflage), Springer Verlag Berlin, (2001).
- [4] Bergmann, Schaefer, K. (Ed.), Lehrbuch der Experimentalphysik: Gase, Nanosysteme, Flüssigkeiten, Walter de Gruyter, (2006).
- [5] C. Kittel, Einführung in die Festkörperphysik (12. Auflage), R. Oldenburg Verlag (München, Wien), (1999).
- [6] K. Kopitzki, P. Herzog, Einführung in die Festkörperphysik (5. Auflage), B. G. Teubner (Stuttgart, München, Wiesbaden), (2004).
- [7] J. Stöhr, H.C. Siegmann, Magnetism - From Fundamentals to Nano Scale Dynamics, Springer Verlag, (2006).
- [8] G. Schütz, E. Goering, H. Stoll, Synchrotron Radiation Techniques Based on X-ray Magnetic Circular Dichroism, in: Handbook of Magnetism and Advanced Magnetic Materials, John Wiley & Sons, Ltd, 2007.
- [9] P. Bakule, E. Morenzoni, Generation and applications of slow polarized muons, Contemporary Physics, 45 (2004) 203-225.
- [10] S.J. Blundell, Spin-polarized muons in condensed matter physics, Contemporary Physics, 40 (1999) 175-192.
- [11] S.F.J. Cox, Implanted muon studies in condensed matter science, Journal of Physics C: Solid State Physics, 20 (1987) 3187.
- [12] P.D.d. Réotier, A. Yaouanc, Muon spin rotation and relaxation in magnetic materials, Journal of Physics: Condensed Matter, 9 (1997) 9113.
- [13] E. Morenzoni, Introduction to  $\mu$ SR Muon Spin Rotation/Relaxation, Lecture Script of ETH Zürich, (2010).
- [14] J.E. Sonier, MuSR brochure, [www.muon.neutron-eu.net/muon/files/musrbrochure.pdf](http://www.muon.neutron-eu.net/muon/files/musrbrochure.pdf), (downloaded December 2013).
- [15] J.C. Maxwell, A Dynamical Theory of the Electromagnetic Field, Philosophical Transactions of the Royal Society of London, 155 (1865) 459-512.
- [16] P. Reineker, M. Schulz, B.M. Schulz, Theoretische Physik II - Elektrodynamik, Wiley-VCH, Weinheim, (2006).
- [17] E.C. Stoner, Collective Electron Ferromagnetism. II. Energy and Specific Heat, Proceedings of the Royal Society of London. Series A. Mathematical and Physical Sciences, 169 (1939) 339-371.

- 
- [18] C.P. Bean, J.D. Livingston, Superparamagnetism, *J Appl Phys*, 30 (1959) S120-S129.
- [19] M. Knobel, W.C. Nunes, L.M. Socolovsky, E. De Biasi, J.M. Vargas, J.C. Denardin, Superparamagnetism and Other Magnetic Features in Granular Materials: A Review on Ideal and Real Systems, *J Nanosci Nanotechnol*, 8 (2008) 2836-2857.
- [20] G. Schütz, W. Wagner, W. Wilhelm, P. Kienle, R. Zeller, R. Frahm, G. Materlik, Absorption of circularly polarized x rays in iron, *Phys Rev Lett*, 58 (1987) 737.
- [21] E. Goering, Habilitationsschrift, Max-Planck-Institut für Metallforschung, (2006).
- [22] J. Mathon, A. Umerski, in *Physics of Low Dimensional Systems*, p363, in *Physics of Low Dimensional Systems*, p363, Kluwer/Plenum, New York, (2001).
- [23] J. Stöhr, Y. Wu, *New Directions in Research with Third-Generation Soft XRay Synchrotron Radiation Sources*, *New Directions in Research with Third-Generation Soft XRay Synchrotron Radiation Sources*, ed. by A.S. Schlachter, F.J. Wuilleumier (Kluwer, Netherlands), p. 221, (1994).
- [24] B.T. Thole, P. Carra, F. Sette, G. van der Laan, X-ray circular dichroism as a probe of orbital magnetization, *Phys Rev Lett*, 68 (1992) 1943-1946.
- [25] P. Carra, B.T. Thole, M. Altarelli, X. Wang, X-ray circular dichroism and local magnetic fields, *Phys Rev Lett*, 70 (1993) 694-697.
- [26] R. Wu, D. Wang, A.J. Freeman, First principles investigation of the validity and range of applicability of the x-ray magnetic circular dichroism sum rule, *Phys Rev Lett*, 71 (1993) 3581-3584.
- [27] R. Wu, A.J. Freeman, Limitation of the Magnetic-Circular-Dichroism Spin Sum Rule for Transition Metals and Importance of the Magnetic Dipole Term, *Phys Rev Lett*, 73 (1994) 1994-1997.
- [28] C.T. Chen, Y.U. Idzerda, H.J. Lin, N.V. Smith, G. Meigs, E. Chaban, G.H. Ho, E. Pellegrin, F. Sette, Experimental Confirmation of the X-Ray Magnetic Circular Dichroism Sum Rules for Iron and Cobalt, *Phys Rev Lett*, 75 (1995) 152-155.
- [29] E. Goering, S. Gold, A. Bayer, Ground-State-Moment-Analysis: A quantitative tool for X-ray magnetic circular dichroism analysis for 3d transition metals, *Appl Phys a-Mater*, 78 (2004) 855-865.
- [30] E. Goering, X-ray magnetic circular dichroism sum rule correction for the light transition metals, *Philos Mag*, 85 (2005) 2895-2911.
- [31] M. Weser, Y. Rehder, K. Horn, M. Sicot, M. Fonin, A.B. Preobrajenski, E.N. Voloshina, E. Goering, Y.S. Dedkov, Induced magnetism of carbon atoms at the graphene/Ni(111) interface, *Appl Phys Lett*, 96 (2010) -.
- [32] J.D. Aiken Iii, R.G. Finke, A review of modern transition-metal nanoclusters: their synthesis, characterization, and applications in catalysis, *Journal of Molecular Catalysis A: Chemical*, 145 (1999) 1-44.

- 
- [33] L. Fritsche, J. Noffke, H. Eckardt, A relativistic treatment of interacting spin-aligned electron systems: application to ferromagnetic iron, nickel and palladium metal, *Journal of Physics F: Metal Physics*, 17 (1987) 943.
- [34] O. Eriksson, A.M. Boring, R.C. Albers, G.W. Fernando, B.R. Cooper, Spin and orbital contributions to surface magnetism in 3d elements, *Phys Rev B*, 45 (1992) 2868-2875.
- [35] S.R. Liu, H.J. Zhai, L.S. Wang, s-d hybridization and evolution of the electronic and magnetic properties in small Co and Ni clusters, *Phys Rev B*, 65 (2002).
- [36] I.M.L. Billas, A. Châtelain, W.A. de Heer, Magnetism of Fe, Co and Ni clusters in molecular beams, *Journal of Magnetism and Magnetic Materials*, 168 (1997) 64-84.
- [37] I.M.L. Billas, A. Châtelain, W.A. de Heer, Magnetism from the Atom to the Bulk in Iron, Cobalt, and Nickel Clusters, *Science*, 265 (1994) 1682-1684.
- [38] X.S. Xu, S.Y. Yin, R. Moro, W.A. de Heer, Magnetic moments and adiabatic magnetization of free cobalt clusters, *Phys Rev Lett*, 95 (2005).
- [39] F.W. Payne, W. Jiang, J.W. Emmert, J. Deng, L.A. Bloomfield, Magnetic structure of free cobalt clusters studied with Stern-Gerlach deflection experiments, *Phys Rev B*, 75 (2007).
- [40] R.A. Guirado-López, J. Dorantes-Dávila, G.M. Pastor, Orbital Magnetism in Transition-Metal Clusters: From Hund's Rules to Bulk Quenching, *Phys Rev Lett*, 90 (2003) 226402.
- [41] P. Bruno, Tight-binding approach to the orbital magnetic moment and magnetocrystalline anisotropy of transition-metal monolayers, *Phys Rev B*, 39 (1989) 865.
- [42] L. Gerrit van der, Microscopic origin of magnetocrystalline anisotropy in transition metal thin films, *Journal of Physics: Condensed Matter*, 10 (1998) 3239.
- [43] P. Gambardella, S. Rusponi, M. Veronese, S.S. Dhesi, C. Grazioli, A. Dallmeyer, I. Cabria, R. Zeller, P.H. Dederichs, K. Kern, C. Carbone, H. Brune, Giant Magnetic Anisotropy of Single Cobalt Atoms and Nanoparticles, *Science*, 300 (2003) 1130-1133.
- [44] K.S. Novoselov, A.K. Geim, S.V. Morozov, D. Jiang, Y. Zhang, S.V. Dubonos, I.V. Grigorieva, A.A. Firsov, Electric field effect in atomically thin carbon films, *Science*, 306 (2004) 666-669.
- [45] K.S. Novoselov, A.K. Geim, S.V. Morozov, D. Jiang, M.I. Katsnelson, I.V. Grigorieva, S.V. Dubonos, A.A. Firsov, Two-dimensional gas of massless Dirac fermions in graphene, *Nature*, 438 (2005) 197-200.
- [46] D.A. Abanin, K.S. Novoselov, U. Zeitler, P.A. Lee, A.K. Geim, L.S. Levitov, Dissipative quantum Hall effect in graphene near the Dirac point, *Phys Rev Lett*, 98 (2007) -.
- [47] E.W. Hill, A.K. Geim, K. Novoselov, F. Schedin, P. Blake, Graphene spin valve devices, *Ieee T Magn*, 42 (2006) 2694-2696.
- [48] A.K. Geim, A.H. MacDonald, Graphene: Exploring carbon flatland, *Phys Today*, 60 (2007) 35-41.
- [49] A.K. Geim, K.S. Novoselov, The rise of graphene, *Nat Mater*, 6 (2007) 183-191.

- [50] K. Novoselov, A. Geim, Graphene detects single molecule of toxic gas, *Mater Technol*, 22 (2007) 178-179.
- [51] A.H. Castro Neto, F. Guinea, N.M.R. Peres, K.S. Novoselov, A.K. Geim, The electronic properties of graphene, *Rev Mod Phys*, 81 (2009) 109-162.
- [52] A.T. N'Diaye, J. Coraux, T.N. Plasa, C. Busse, T. Michely, Structure of epitaxial graphene on Ir(111), *New J Phys*, 10 (2008).
- [53] Y. Gamo, A. Nagashima, M. Wakabayashi, M. Terai, C. Oshima, Atomic structure of monolayer graphite formed on Ni(111), *Surf Sci*, 374 (1997) 61-64.
- [54] D. Martoccia, P.R. Willmott, T. Brugger, M. Bjorck, S. Gunther, C.M. Schleputz, A. Cervellino, S.A. Pauli, B.D. Patterson, S. Marchini, J. Wintterlin, W. Moritz, T. Greber, Graphene on Ru(0001): A 25x25 supercell, *Phys Rev Lett*, 101 (2008) -.
- [55] P. Sutter, J.T. Sadowski, E. Sutter, Graphene on Pt(111): Growth and substrate interaction, *Phys Rev B*, 80 (2009) -.
- [56] S. Marchini, S. Gunther, J. Wintterlin, Scanning tunneling microscopy of graphene on Ru(0001), *Phys Rev B*, 76 (2007) -.
- [57] J. Coraux, A.T. N'Diaye, M. Engler, C. Busse, D. Wall, N. Buckanie, F. Heringdorf, R. van Gastel, B. Poelsema, T. Michely, Growth of graphene on Ir(111), *New J Phys*, 11 (2009).
- [58] L. Gao, J.R. Guest, N.P. Guisinger, Epitaxial Graphene on Cu(111), *Nano Lett*, 10 (2010) 3512-3516.
- [59] J. Wintterlin, M.L. Bocquet, Graphene on metal surfaces, *Surf Sci*, 603 (2009) 1841-1852.
- [60] A.T. N'Diaye, S. Bleikamp, P.J. Feibelman, T. Michely, Two-dimensional Ir cluster lattice on a graphene moire on Ir(111), *Phys Rev Lett*, 97 (2006) -.
- [61] Q. Liao, H.J. Zhang, K. Wu, H.Y. Li, S.N. Bao, P. He, Nucleation and growth of monodispersed cobalt nanoclusters on graphene moire on Ru(0001), *Nanotechnology*, (2011) 125303 (125306 pp.).
- [62] Z.H. Zhou, F. Gao, D.W. Goodman, Deposition of metal clusters on single-layer graphene/Ru(0001): Factors that govern cluster growth, *Surf Sci*, 604 (2010) 1071-L1038.
- [63] M. Sicot, S. Bouvron, O. Zander, U. Rudiger, Y.S. Dedkov, M. Fonin, Nucleation and growth of nickel nanoclusters on graphene Moireacute on Rh(111), *Appl Phys Lett*, 96 (2010) -.
- [64] P. Yi, G. Min, H. Li, L. Feng, H.J. Gao, Directed self-assembly of monodispersed platinum nanoclusters on graphene Moire template, *Appl Phys Lett*, (2009) 093106 (093103 pp.).
- [65] Y.S. Dedkov, M. Fonin, U. Rudiger, C. Laubschat, Graphene-protected iron layer on Ni(111), *Appl Phys Lett*, 93 (2008) -.
- [66] M. Sicot, P. Leicht, A. Zusan, S. Bouvron, O. Zander, M. Weser, Y.S. Dedkov, K. Horn, M. Fonin, Size-Selected Epitaxial Nanoislands Underneath Graphene Moiré on Rh(111), *Acs Nano*, 6 (2012) 151-158.

- 
- [67] T. Dietl, H. Ohno, F. Matsukura, J. Cibert, D. Ferrand, Zener model description of ferromagnetism in zinc-blende magnetic semiconductors, *Science*, 287 (2000) 1019-1022.
- [68] J.M.D. Coey, M. Venkatesan, C.B. Fitzgerald, Donor impurity band exchange in dilute ferromagnetic oxides, *Nat Mater*, 4 (2005) 173-179.
- [69] M. Venkatesan, C.B. Fitzgerald, J.G. Lunney, J.M.D. Coey, Anisotropic ferromagnetism in substituted zinc oxide, *Phys Rev Lett*, 93 (2004).
- [70] T. Dietl, A ten-year perspective on dilute magnetic semiconductors and oxides, *Nat Mater*, 9 (2010) 965-974.
- [71] M. Gacic, G. Jakob, C. Herbort, H. Adrian, T. Tietze, S. Bruck, E. Goering, Magnetism of Co-doped ZnO thin films, *Phys Rev B*, 75 (2007) -.
- [72] E. Goering, S. Bruck, T. Tietze, G. Jakob, M. Gacic, H. Adrian, Absence of element specific ferromagnetism in Co doped ZnO investigated by soft X-ray resonant reflectivity, *J Phys Conf Ser*, 200 (2010).
- [73] T. Tietze, M. Gacic, G. Schutz, G. Jakob, S. Bruck, E. Goering, XMCD studies on Co and Li doped ZnO magnetic semiconductors, *New J Phys*, 10 (2008) -.
- [74] B.B. Straumal, A.A. Mazilkin, S.G. Protasova, A.A. Myatiev, P.B. Straumal, G. Schütz, P.A. van Aken, E. Goering, B. Baretzky, Magnetization study of nanograined pure and Mn-doped ZnO films: Formation of a ferromagnetic grain-boundary foam, *Phys Rev B*, 79 (2009) 205206.
- [75] B.B. Straumal, S.G. Protasova, A.A. Mazilkin, A.A. Myatiev, P.B. Straumal, G. Schutz, E. Goering, B. Baretzky, Ferromagnetic properties of the Mn-doped nanograined ZnO films, *J Appl Phys*, 108 (2010).
- [76] B.B. Straumal, A.A. Mazilkin, S.G. Protasova, P.B. Straumal, A.A. Myatiev, G. Schütz, E.J. Goering, T. Tietze, B. Baretzky, Grain boundaries as the controlling factor for the ferromagnetic behaviour of Co-doped ZnO, *Philos Mag*, 93 (2012) 1371-1383.
- [77] B.B. Straumal, S.G. Protasova, A.A. Mazilkin, T. Tietze, E. Goering, G. Schütz, P.B. Straumal, B. Baretzky, Ferromagnetic behaviour of Fe-doped ZnO nanograined films, *Beilstein Journal of Nanotechnology*, (2013).
- [78] Y.-C. Chen, E. Goering, L. Jeurgens, Z. Wang, F. Phillipp, J. Baier, T. Tietze, G. Schütz, Unexpected room-temperature ferromagnetism in bulk ZnO, *Appl Phys Lett*, 103 (2013) -.
- [79] B.B. Straumal, S.G. Protasova, A.A. Mazilkin, B. Baretzky, A.A. Myatiev, P.B. Straumal, T. Tietze, G. Schütz, E. Goering, Amorphous interlayers between crystalline grains in ferromagnetic ZnO films, *Mater Lett*, 71 (2012) 21-24.
- [80] B.B. Straumal, A.A. Myatiev, P.B. Straumal, A.A. Mazilkin, S.G. Protasova, E. Goering, B. Baretzky, Grain boundary layers in nanocrystalline ferromagnetic zinc oxide, *Jetp Lett*, 92 (2010) 396-400.
- [81] B. Straumal, B. Baretzky, A. Mazilkin, S. Protasova, A. Myatiev, P. Straumal, Increase of Mn solubility with decreasing grain size in ZnO, *J Eur Ceram Soc*, 29 (2009) 1963-1970.

- [82] B.B. Straumal, A.A. Mazilkin, S.G. Protasova, A.A. Myatiev, P.B. Straumal, B. Baretzky, Increase of Co solubility with decreasing grain size in ZnO, *Acta Mater*, 56 (2008) 6246-6256.
- [83] J.C. Street, E.C. Stevenson, New Evidence for the Existence of a Particle of Mass Intermediate Between the Proton and Electron, *Physical Review*, 52 (1937) 1003-1004.
- [84] A. Suter, musrfit: a free platform-independent framework for  $\mu$ SR data analysis, arXiv:1111.1569v1 [physics.data-an], (2011).
- [85] A. Suter, B.M. Wojek, Musrfit: A Free Platform-Independent Framework for  $\mu$ SR Data Analysis, *Physics Procedia*, 30 (2012) 69-73.
- [86] D.H. Ryan, J.v. Lierop, J.M. Cadogan, Zero-field muon spin relaxation studies of frustrated magnets: physics and analysis issues, *Journal of Physics: Condensed Matter*, 16 (2004) S4619.
- [87] R. Kubo, T. Toyabe, *Magnetic Resonance and Relaxation* In: Blinc, R. (Ed.), *Magnetic Resonance and Relaxation*, (1967).
- [88] Y.J. Uemura, T. Yamazaki, D.R. Harshman, M. Senba, E.J. Ansaldo, Muon Spin Relaxation in Aufe and Cumn Spin-Glasses, *Phys Rev B*, 31 (1985) 546-563.
- [89] M.R. Crook, R. Cywinski, Voigtian Kubo - Toyabe muon spin relaxation, *Journal of Physics: Condensed Matter*, 9 (1997) 1149.
- [90] [http://www.helmholtz-berlin.de/media/media/angebote/arbeiten\\_lernen/lehrmaterialien/beschleunigerphysik/der\\_speicherring/10bessy.pdf](http://www.helmholtz-berlin.de/media/media/angebote/arbeiten_lernen/lehrmaterialien/beschleunigerphysik/der_speicherring/10bessy.pdf), (downloaded October 2012).
- [91] [http://www.spring8.or.jp/en/news\\_publications/publications/sp8\\_brochure/sr.html](http://www.spring8.or.jp/en/news_publications/publications/sp8_brochure/sr.html), (downloaded October 2012).
- [92] W.B. Peatman, *Gratings, Mirrors and Slits: Beamline Design for Soft X-Ray Synchrotron Radiation Sources*, Crc. Pr. Inc., 1997.
- [93] [http://ankaweb.fzk.de/file/htmlarea/Image/instrumentation/Beamlines/Layouts/Bitmap%20in%20E\\_WERA\\_fuer%20BMPS\\_72dpi.jpg](http://ankaweb.fzk.de/file/htmlarea/Image/instrumentation/Beamlines/Layouts/Bitmap%20in%20E_WERA_fuer%20BMPS_72dpi.jpg), (downloaded October 2012).
- [94] S. Schuppler, Personal Communication, (October 2012).
- [95] [http://www.bessy.de/users\\_info/02.beamlines/linespdf/D\\_11\\_1A.pdf](http://www.bessy.de/users_info/02.beamlines/linespdf/D_11_1A.pdf), (downloaded May 2007).
- [96] <http://www.psi.ch/media/protonenbeschleunigeranlage-des-psi>, (January 2014).
- [97] T. Prokscha, E. Morenzoni, K. Deiters, F. Foroughi, D. George, R. Kobler, A. Suter, V. Vrankovic, The new beam at PSI: A hybrid-type large acceptance channel for the generation of a high intensity surface-muon beam, *Nuclear Instruments and Methods in Physics Research Section A: Accelerators, Spectrometers, Detectors and Associated Equipment*, 595 (2008) 317-331.
- [98] <http://lmu.web.psi.ch/lem/moderator.html>, (January 2014).



- 
- [99] E. Goering, S. Gold, J. Will, Surface magnetization reversal of sputtered CrO<sub>2</sub>, *Z Metallkd*, 93 (2002) 372-376.
- [100] E. Goering, M. Justen, J. Geissler, U. Rudiger, M. Rabe, G. Guntherodt, G. Schutz, Magnetic anisotropy of textured CrO<sub>2</sub> thin films investigated by X-ray magnetic circular dichroism, *Appl Phys a-Mater*, 74 (2002) 747-753.
- [101] E. Goering, T. Tietze, M. Gacic, G. Schutz, G. Jakob, S. Bruck, XMCD studies on Co and Li doped ZnO magnetic semiconductors, *New J Phys*, 10 (2008).
- [102] E.J. Goering, M. Lafkioti, S. Gold, G. Schuetz, Absorption spectroscopy and XMCD at the Verwey transition of Fe<sub>3</sub>O<sub>4</sub>, *Journal of Magnetism and Magnetic Materials*, 310 (2007) E249-E251.
- [103] E. Goering, M. Lafkioti, S. Gold, Comment on "Spin and orbital magnetic moments of Fe<sub>3</sub>O<sub>4</sub>", *Phys Rev Lett*, 96 (2006).
- [104] S.H. Baker, C. Binns, K.W. Edmonds, M.J. Maher, S.C. Thornton, S. Louch, S.S. Dhesi, Enhancements in magnetic moments of exposed and Co-coated Fe nanoclusters as a function of cluster size, *Journal of Magnetism and Magnetic Materials*, 247 (2002) 19-25.
- [105] J. Bansmann, A. Kleibert, Magnetism of mass-filtered nanoparticles on ferromagnetic supports, *Applied Physics A: Materials Science & Processing*, 80 (2005) 957-964.
- [106] J. Bansmann, A. Kleibert, M. Getzlaff, A.F. Rodriguez, F. Nolting, C. Boeglin, K.H. Meiwes-Broer, Magnetism of 3d transition metal nanoparticles on surfaces probed with synchrotron radiation - from ensembles towards individual objects, *Phys Status Solidi B*, 247 (2010) 1152-1160.
- [107] A. Kleibert, K.H. Meiwes-Broer, J. Bansmann, Size-dependent magnetic spin and orbital moments of Fe nanoparticles deposited onto Co/W(110), *Phys Rev B*, 79 (2009) 125423.
- [108] P. Ohresser, N.B. Brookes, S. Padovani, F. Scheurer, H. Bulou, Magnetism of small Fe clusters on Au(111) studied by x-ray magnetic circular dichroism, *Phys Rev B*, 64 (2001) 104429.
- [109] P. Blonski, A. Lehnert, S. Dennler, S. Rusponi, M. Etzkorn, G. Moulas, P. Bencok, P. Gambardella, H. Brune, J. Hafner, Magnetocrystalline anisotropy energy of Co and Fe adatoms on the (111) surfaces of Pd and Rh, *Phys Rev B*, 81 (2010).
- [110] C. Boeglin, S. Stanescu, S. Cherifi, J.P. Deville, P. Ohresser, A. Barbier, N.B. Brookes, High dipolar magnetic moment observed on Ni/Cu(100/100) nanostructures by magnetic circular X-ray dichroism, *Surf Sci*, 507-510 (2002) 522-529.
- [111] K. Fauth, G.E. Ballentine, C. Praetorius, A. Kleibert, N. Wilken, A. Voitekans, K.H. Meiwes-Broer, Magnetic properties of Fe nanoclusters on Cu(111) studied with X-ray magnetic circular dichroism, *Phys Status Solidi B*, 247 (2010) 1170-1179.
- [112] K. Fauth, S. Gold, M. Heßler, N. Schneider, G. Schütz, Cluster surface interactions: small Fe clusters driven nonmagnetic on graphite, *Chem Phys Lett*, 392 (2004) 498-502.

- [113] A. Kleibert, F. Bulut, R.K. Gebhardt, W. Rosellen, D. Sudfeld, J. Passig, J. Bansmann, K.H. Meiwes-Broer, M. Getzlaff, Correlation of shape and magnetic anisotropy of supported mass-filtered Fe and FeCo alloy nanoparticles on W(110), *J Phys-Condens Mat*, 20 (2008).
- [114] T. Koide, H. Miyauchi, J. Okamoto, T. Shidara, A. Fujimori, H. Fukutani, K. Amemiya, H. Takeshita, S. Yuasa, T. Katayama, Y. Suzuki, Angle-, field-, temperature-, and size-dependent magnetic circular X-ray dichroism in Au/Co nanoclusters/Au(1 $\times$ 1 $\times$ 1), *J Electron Spectrosc*, 136 (2004) 107-115.
- [115] A. Lehnert, S. Drenner, P. Blonski, S. Rusponi, M. Etzkorn, G. Moulas, P. Bencok, P. Gambardella, H. Brune, J. Hafner, Magnetic anisotropy of Fe and Co ultrathin films deposited on Rh(111) and Pt(111) substrates: An experimental and first-principles investigation, *Phys Rev B*, 82 (2010).
- [116] G. Moulas, A. Lehnert, S. Rusponi, J. Zabloudil, C. Etz, S. Ouazi, M. Etzkorn, P. Bencok, P. Gambardella, P. Weinberger, H. Brune, High magnetic moments and anisotropies for Fe(x)Co(1-x) monolayers on Pt(111), *Phys Rev B*, 78 (2008).
- [117] P. Ohresser, G. Ghiringhelli, O. Tjernberg, N.B. Brookes, M. Finazzi, Magnetism of nanostructures studied by x-ray magnetic circular dichroism: Fe on Cu(111), *Phys Rev B*, 62 (2000) 5803-5809.
- [118] S. Rohart, V. Repain, A. Tejada, P. Ohresser, F. Scheurer, P. Bencok, J. Ferre, S. Rousset, Distribution of the magnetic anisotropy energy of an array of self-ordered Co nanodots deposited on vicinal Au(111): X-ray magnetic circular dichroism measurements and theory, *Phys Rev B*, 73 (2006).
- [119] V. Sessi, K. Kuhnke, J. Zhang, J. Honolka, K. Kern, A. Enders, P. Bencok, S. Bornemann, J. Minar, H. Ebert, Cobalt nanoclusters on metal-supported Xe monolayers: Influence of the substrate on cluster formation kinetics and magnetism, *Phys Rev B*, 81 (2010).
- [120] C. Vo-Van, Magnetism of cobalt nanoclusters on graphene on iridium, *Appl. Phys. Lett.*, 99 (2011) 142504.
- [121] N. Weiss, T. Cren, M. Eppe, S. Rusponi, G. Baudot, S. Rohart, A. Tejada, V. Repain, S. Rousset, P. Ohresser, F. Scheurer, P. Bencok, H. Brune, Uniform magnetic properties for an ultrahigh-density lattice of noninteracting Co nanostructures, *Phys Rev Lett*, 95 (2005).
- [122] T. Tietze, Röntgenzirkulardichroische Untersuchungen an ferromagnetischen verdünnten Halbleitersystemen, in: Max-Planck-Institute for Metals Research, University Stuttgart (DE), Stuttgart, 2007.
- [123] M.R. Howells, Some fundamentals of cooled mirrors for synchrotron radiation beam lines, *Optical Engineering*, 35 (1996) 1187-1197.
- [124] P. Nagel, Personal Communication, in.
- [125] C. Johann, T.N.D. Alpha, E. Martin, B. Carsten, W. Dirk, B. Niemma, J.M.z.H. Frank, G. Raoul van, P. Bene, M. Thomas, Growth of graphene on Ir(111), *New J Phys*, 11 (2009) 023006.

- [126] D.G. Castner, B.A. Sexton, G.A. Somorjai, Leed and Thermal Desorption Studies of Small Molecules ( $H_2$ ,  $O_2$ ,  $Co$ ,  $Co_2$ ,  $No$ ,  $C_2H_4$ ,  $C_2H_2$  and  $C$ ) Chemisorbed on Rhodium (111) and (100) Surfaces, *Surf Sci*, 71 (1978) 519-540.
- [127] B.E. Nieuwenhuys, G.A. Somorjai, Adsorption of carbon monoxide, oxygen, hydrogen, nitrogen, ethylene and benzene on an iridium (110) surface; Correlation with other iridium crystal faces, *Surf Sci*, 72 (1978) 8-32.
- [128] H. Hattab, A.T. N'Diaye, D. Wall, G. Jnawali, J. Coraux, C. Busse, R. van Gastel, B. Poelsema, T. Michely, F.J.M.z. Heringdorf, M.H.-v. Hoegen, Growth temperature dependent graphene alignment on Ir(111), *Appl Phys Lett*, 98 (2011) 141903-141903.
- [129] E. Loginova, S. Nie, K. Thürmer, N.C. Bartelt, K.F. McCarty, Defects of graphene on Ir(111): Rotational domains and ridges, *Phys Rev B*, 80 (2009) 085430.
- [130] P. Leicht, Personal Communication, (November 2012).
- [131] R. Nakajima, J. Stöhr, Y.U. Idzerda, Electron-yield saturation effects in L-edge x-ray magnetic circular dichroism spectra of Fe, Co, and Ni, *Phys Rev B*, 59 (1999) 6421-6429.
- [132] C.T. Chen, F. Sette, Y. Ma, S. Modesti, Soft-x-ray magnetic circular dichroism at the  $L_{2,3}$  edges of nickel, *Phys Rev B*, 42 (1990) 7262-7265.
- [133] N.V. Smith, C.T. Chen, F. Sette, L.F. Mattheiss, Relativistic tight-binding calculations of x-ray absorption and magnetic circular dichroism at the  $L_{2,3}$  edges of nickel and iron, *Phys Rev B*, 46 (1992) 1023-1032.
- [134] T. Jo, G.A. Sawatzky, Ground state of ferromagnetic nickel and magnetic circular dichroism in Ni 2p core x-ray-absorption spectroscopy, *Phys Rev B*, 43 (1991) 8771-8774.
- [135] G.v.d. Laan, B.T. Thole, Electronic correlations in Ni 2p and 3p magnetic X-ray dichroism and X-ray photoemission of ferromagnetic nickel, *Journal of Physics: Condensed Matter*, 4 (1992) 4181.
- [136] W.L. O'Brien, B.P. Tonner, Orbital and spin sum rules in x-ray magnetic circular dichroism, *Phys Rev B*, 50 (1994) 12672-12681.
- [137] W.L. O'Brien, B.P. Tonner, G.R. Harp, S.S.P. Parkin, Experimental investigation of dichroism sum rules for V, Cr, Mn, Fe, Co, and Ni: Influence of diffuse magnetism, *J Appl Phys*, 76 (1994) 6462-6464.
- [138] D.A. Papaconstantopoulos, Handbook of the band structure of elemental solids, Plenum Publ., New York [u.a.], 1986.
- [139] P. Srivastava, N. Haack, H. Wende, R. Chauvistré, K. Baberschke, Modifications of the electronic structure of Ni/Cu(001) as a function of the film thickness, *Phys Rev B*, 56 (1997) R4398-R4401.
- [140] S.S. Dhesi, H.A. Dürr, G. van der Laan, E. Dudzik, N.B. Brookes, Electronic and magnetic structure of thin Ni films on Co/Cu(001), *Phys Rev B*, 60 (1999) 12852-12860.
- [141] P. Srivastava, F. Wilhelm, A. Ney, N. Haack, H. Wende, K. Baberschke, Modifications in the electronic structure of 3d single-, bi- and tri-layers on Cu(001), *Surf Sci*, 402-404 (1998) 818-821.

- [142] S.S. Dhesi, H.A. Dürr, E. Dudzik, G.v.d. Laan, N.B. Brookes, Magnetism and electron redistribution effects at Ni/Co interfaces, *Phys Rev B*, 61 (2000) 6866-6870.
- [143] R. Nietubýć, A. Föhlich, L. Glaser, J.T. Lau, M. Martins, M. Reif, W. Wurth, L-edge x-ray absorption fine structure study of growth and morphology of ultrathin nickel films deposited on copper, *Phys Rev B*, 70 (2004) 235414.
- [144] M. Weser, Y. Rehder, K. Horn, M. Sicot, M. Fonin, A.B. Preobrajenski, E.N. Voloshina, E. Goering, Y.S. Dedkov, Induced magnetism of carbon atoms at the graphene/Ni(111) interface, *Appl Phys Lett*, 96 (2010) 012504-012503.
- [145] F. Eggenstein, F. Senf, T. Zeschke, W. Gudat, Cleaning of contaminated XUV-optics at BESSY II, *Nuclear Instruments and Methods in Physics Research Section A: Accelerators, Spectrometers, Detectors and Associated Equipment*, 467–468, Part 1 (2001) 325-328.
- [146] T. Koide, T. Shidara, M. Yanagihara, S. Sato, Resuscitation of carbon-contaminated mirrors and gratings by oxygen-discharge cleaning. 2: Efficiency recovery in the 100–1000-eV range, *Appl. Opt.*, 27 (1988) 4305-4313.
- [147] E.D. Johnson, S.L. Hulbert, R.F. Garrett, G.P. Williams, M.L. Knotek, In situ reactive glow discharge cleaning of x-ray optical surfaces, *Rev Sci Instrum*, 58 (1987) 1042-1045.
- [148] R.A. Rosenberg, J.A. Smith, D.J. Wallace, Plasma cleaning of beamline optical components: Contamination and gas composition effects, *Rev Sci Instrum*, 63 (1992) 1486-1489.
- [149] T.O. Wehling, A.I. Lichtenstein, M.I. Katsnelson, Transition-metal adatoms on graphene: Influence of local Coulomb interactions on chemical bonding and magnetic moments, *Phys Rev B*, 84 (2011) 235110.
- [150] C. Cao, M. Wu, J. Jiang, H.-P. Cheng, Transition metal adatom and dimer adsorbed on graphene: Induced magnetization and electronic structures, *Phys Rev B*, 81 (2010) 205424.
- [151] H. Johll, H.C. Kang, E.S. Tok, Density functional theory study of Fe, Co, and Ni adatoms and dimers adsorbed on graphene, *Phys Rev B*, 79 (2009) 245416.
- [152] D.M. Duffy, J.A. Blackman, Magnetism of 3d transition-metal adatoms and dimers on graphite, *Phys Rev B*, 58 (1998) 7443-7449.
- [153] H. Johll, J. Wu, S.W. Ong, H.C. Kang, E.S. Tok, Graphene-adsorbed Fe, Co, and Ni trimers and tetramers: Structure, stability, and magnetic moment, *Phys Rev B*, 83 (2011) 205408.
- [154] M. Gyamfi, T. Eelbo, M. Waśniowska, T.O. Wehling, S. Forti, U. Starke, A.I. Lichtenstein, M.I. Katsnelson, R. Wiesendanger, Orbital selective coupling between Ni adatoms and graphene Dirac electrons, *Phys Rev B*, 85 (2012) 161406.
- [155] T. Eelbo, M. Waśniowska, P. Thakur, M. Gyamfi, B. Sachs, T.O. Wehling, S. Forti, U. Starke, C. Tieg, A.I. Lichtenstein, R. Wiesendanger, Adatoms and Clusters of 3d Transition Metals on Graphene: Electronic and Magnetic Configurations, *Phys Rev Lett*, 110 (2013) 136804.

- 
- [156] F.M.F. de Groot, M.A. Arrio, P. Saintavit, C. Cartier, C.T. Chen, Fluorescence yield detection: Why it does not measure the X-ray absorption cross section, *Solid State Commun*, 92 (1994) 991-995.
- [157] B.E. Nieuwenhuys, O.G. Van Aardenne, W.M.H. Sachtler, Adsorption of xenon on group VIII and Ib metals studied by photoelectric work function measurements, *Chem Phys*, 5 (1974) 418-428.
- [158] O. Chuhei, N. Ayato, Ultra-thin epitaxial films of graphite and hexagonal boron nitride on solid surfaces, *Journal of Physics: Condensed Matter*, 9 (1997) 1.
- [159] W. Ekardt, Work function of small metal particles: Self-consistent spherical jellium-background model, *Phys Rev B*, 29 (1984) 1558-1564.
- [160] K. Stokbro, M. Engelund, A. Blom, Atomic-scale model for the contact resistance of the nickel-graphene interface, *Phys Rev B*, 85 (2012) 165442.
- [161] H. Liu, H. Kondo, T. Ohno, Contact effects of nickel and copper on electron transport through graphene, *Phys Rev B*, 86 (2012) 155434.
- [162] C.H. Park, B.C. Lee, J.I. Lee, Spin-Asymmetry of the Density of States for Bulk and Surface Fe, Co, and Ni, *Journal of the Korean Physical Society*, 47 (2005) 10.
- [163] Y. Yagi, T.M. Briere, M.H.F. Sluiter, V. Kumar, A.A. Farajian, Y. Kawazoe, Stable geometries and magnetic properties of single-walled carbon nanotubes doped with 3d transition metals: A first-principles study, *Phys Rev B*, 69 (2004) 075414.
- [164] G. Bertoni, L. Calmels, A. Altibelli, V. Serin, First-principles calculation of the electronic structure and EELS spectra at the graphene/Ni(111) interface, *Phys Rev B*, 71 (2005) 075402.
- [165] T. Abtew, B.-C. Shih, S. Banerjee, P. Zhang, Graphene-ferromagnet interfaces: hybridization, magnetization and charge transfer, *Nanoscale*, 5 (2013) 1902-1909.
- [166] Y.S. Dedkov, M. Fonin, C. Laubschat, A possible source of spin-polarized electrons: The inert graphene/Ni(111) system, *Appl Phys Lett*, 92 (2008) -.
- [167] P. Srivastava, F. Wilhelm, A. Ney, M. Farle, H. Wende, N. Haack, G. Ceballos, K. Baberschke, Magnetic moments and Curie temperatures of Ni and Co thin films and coupled trilayers, *Phys Rev B*, 58 (1998) 5701-5706.
- [168] S. Hope, J. Lee, P. Rosenbusch, G. Lauhoff, J.A.C. Bland, A. Ercole, D. Bucknall, J. Penfold, H.J. Lauter, V. Lauter, R. Cubitt, Thickness dependence of the total magnetic moment per atom in the Cu/Ni/Cu/Si(001) system, *Phys Rev B*, 55 (1997) 11422-11431.
- [169] J. Lee, G. Lauhoff, M. Tselepi, S. Hope, P. Rosenbusch, J.A.C. Bland, H.A. Dürr, G. van der Laan, J.P. Schill  and, J.A.D. Matthew, Evidence for a strain-induced variation of the magnetic moment in epitaxial Cu/Ni/Cu/Si(100) structures, *Phys Rev B*, 55 (1997) 15103-15107.
- [170] K. Amemiya, E. Sakai, D. Matsumura, H. Abe, T. Ohta, T. Yokoyama, Spin-reorientation transition of Ni / Cu(100) and Co / Ni / Cu(100): Separation of the surface and bulk components of the x-ray magnetic circular dichroism spectrum, *Phys Rev B*, 71 (2005) 214420.

- [171] R. Jungblut, M.T. Johnson, J. aan de Stegge, A. Reinders, F.J.A. den Broeder, Orientational and structural dependence of magnetic anisotropy of Cu/Ni/Cu sandwiches: Misfit interface anisotropy, *J Appl Phys*, 75 (1994) 6424.
- [172] M.T. Johnson, P.J.H. Bloemen, F.J.A.d. Broeder, J.J.d. Vries, Magnetic anisotropy in metallic multilayers, *Reports on Progress in Physics*, 59 (1996) 1409.
- [173] H. Abe, K. Amemiya, D. Matsumura, S. Kitagawa, H. Watanabe, T. Yokoyama, T. Ohta, Spin reorientation transitions of studied by using the depth-resolved X-ray magnetic circular dichroism technique, *Journal of Magnetism and Magnetic Materials*, 302 (2006) 86-95.
- [174] H.J. Hug, B. Stiefel, A. Moser, I. Parashikov, A. Klicznik, D. Lipp, H.J. Güntherodt, G. Bochi, D.I. Paul, R.C. O'Handley, Magnetic domain structure in ultrathin Cu/Ni/Cu/Si(001) films (invited), *J Appl Phys*, 79 (1996) 5609-5614.
- [175] G. Bochi, C.A. Ballentine, H.E. Inglefield, C.V. Thompson, R.C. O'Handley, H.J. Hug, B. Stiefel, A. Moser, H.J. Güntherodt, Perpendicular magnetic anisotropy, domains, and misfit strain in epitaxial Ni/Cu<sub>{1-x}</sub>Ni<sub>{x}</sub>/Cu/Si (001) thin films, *Phys Rev B*, 52 (1995) 7311-7321.
- [176] S. Hameed, P. Talagala, R. Naik, L.E. Wenger, V.M. Naik, R. Proksch, Analysis of disordered stripe magnetic domains in strained epitaxial Ni(001) films, *Phys Rev B*, 64 (2001) 184406.
- [177] U. Gradmann, R. Bergholz, E. Bergter, Magnetic surface anisotropies of clean Ni, *Magnetics, IEEE Transactions on*, 20 (1984) 1840-1845.
- [178] M. Farle, B. Mirwald-Schulz, A.N. Anisimov, W. Platow, K. Baberschke, Higher-order magnetic anisotropies and the nature of the spin-reorientation transition in face-centered-tetragonal Ni(001)/Cu(001), *Phys Rev B*, 55 (1997) 3708-3715.
- [179] W. Kuch, J. Gilles, S.S. Kang, S. Imada, S. Suga, J. Kirschner, Magnetic-circular-dichroism microspectroscopy at the spin reorientation transition in Ni(001) films, *Phys Rev B*, 62 (2000) 3824-3833.
- [180] B. Straumal, A. Mazilkin, P. Straumal, A. Myatiev, Distribution of impurities and minor components in nanostructured conducting oxides, *Int. J. of Nanomanufacturing*, 2 (2008) 253-270.
- [181] A. Ney, et al., Structural, chemical and magnetic properties of secondary phases in Co-doped ZnO, *New J Phys*, 13 (2011) 103001.
- [182] V. Ney, S. Ye, K. Ollefs, T. Kammermeier, F. Wilhelm, A. Rogalev, A. Ney, Co-Doped ZnO Epitaxial Films: From a Brillouin-Like Paramagnet to a Phase-Separated Superparamagnetic Ensemble, *J Nanosci Nanotechno*, 10 (2010) 5958-5963.
- [183] J.M.D. Coey, P. Stamenov, R.D. Gunning, M. Venkatesan, K. Paul, Ferromagnetism in defect-ridden oxides and related materials, *New J Phys*, 12 (2010).

- 
- [184] A. Barla, G. Schmerber, E. Beaurepaire, A. Dinia, H. Bieber, S. Colis, F. Scheurer, J.P. Kappler, P. Imperia, F. Nolting, F. Wilhelm, A. Rogalev, D. Muller, J.J. Grob, Paramagnetism of the Co sublattice in ferromagnetic  $\text{Zn}_{1-x}\text{Co}_x\text{O}$  films, *Phys Rev B*, 76 (2007).
- [185] A. Ney, M. Opel, T.C. Kaspar, V. Ney, S. Ye, K. Ollefs, T. Kammermeier, S. Bauer, K.W. Nielsen, S.T.B. Goennenwein, M.H. Engelhard, S. Zhou, K. Potzger, J. Simon, W. Mader, S.M. Heald, J.C. Cezar, F. Wilhelm, A. Rogalev, R. Gross, S.A. Chambers, Advanced spectroscopic synchrotron techniques to unravel the intrinsic properties of dilute magnetic oxides: the case of  $\text{Co:ZnO}$ , *New J Phys*, 12 (2010).
- [186] E. Goering, A. Bayer, S. Gold, G. Schutz, M. Rabe, U. Rudiger, G. Guntherodt, Strong anisotropy of projected 3d moments in epitaxial  $\text{CrO}_2$  films, *Phys Rev Lett*, 88 (2002).
- [187] Z. Salman, Personal Communication, (2009).
- [188] B.D. Patterson, Muonium states in semiconductors, *Rev Mod Phys*, 60 (1988) 69-159.
- [189] S.F.J. Cox, E.A. Davis, S.P. Cottrell, P.J.C. King, J.S. Lord, J.M. Gil, H.V. Alberto, R.C. Vilão, J. Piroto Duarte, N. Ayres de Campos, A. Weidinger, R.L. Lichti, S.J.C. Irvine, Experimental Confirmation of the Predicted Shallow Donor Hydrogen State in Zinc Oxide, *Phys Rev Lett*, 86 (2001) 2601.
- [190] J.M. Gil, H.V. Alberto, R.C. Vilão, J. Piroto Duarte, N. Ayres de Campos, A. Weidinger, J. Krauser, E.A. Davis, S.P. Cottrell, S.F.J. Cox, Shallow donor muonium states in II-VI semiconductor compounds, *Phys Rev B*, 64 (2001) 075205.
- [191] K. Shimomura, K. Nishiyama, R. Kadono, Electronic Structure of the Muonium Center as a Shallow Donor in  $\text{ZnO}$ , *Phys Rev Lett*, 89 (2002) 255505.
- [192] T. Tietze, P. Audehm, Y.C. Chen, G. Schütz, E. Goering, B.B. Straumal, S. Protasova, A. Mazilkin, P.B. Straumal, T. Prokscha, H. Luetkens, Z. Salman, A. Suter, B. Baretzky, K. Fink, W. Wenzel, D. Danilov, Interfacial dominated ferromagnetism in nanograined  $\text{ZnO}$ : a  $\mu\text{SR}$  and DFT study, to be published, (2014).
- [193] D. Danilov, K. Fink, W. Wenzel, B. Baretzky, Personal Communication, (2014).

## Danksagung

Zum Schluss möchte ich mich bei all jenen bedanken, ohne deren tatkräftige Unterstützung und Mithilfe es diese Arbeit nicht geben würde.

Meinem Betreuer PD Dr. Eberhard Goering möchte ich für eine spannende und abwechslungsreiche Arbeit und für eine tolle, lehr- und ereignisreiche Zeit in seiner Arbeitsgruppe danken. Er stand stets mit Rat und Tat zur Seite, sei es bei physikalischen, technischen oder auch „weltlichen“ Fragen und Problemen.

Frau Prof. Dr. Gisela Schütz für Aufnahme bzw. Übernahme in ihre Abteilung und die Möglichkeit, diese Arbeit durchzuführen.

Prof. Dr. Martin Dressel danke ich für die freundliche Übernahme des Mitberichts und Prof Dr. Günter Wunner für Übernahme des Vorsitzes des Prüfungsausschusses.

Meinen Kooperationspartnern von der Universität Konstanz, Mikhail Fonin und seinen Mitarbeitern Muriel Sicot, Andreas Zusan, Samuel Bouvron, Eugen Zimmermann, Hendrik Flammersperger, Ole Zander und ganz besonders Philipp Leicht danke ich herzlich für die *in-situ* Graphen- und Clusterpräparation bei zahlreichen, wochenlangen Strahlzeiten und die Bereitstellung von (technischem) Know-How zur Probenpräparation und Design der Präparationseinheit.

Meinen ZnO Kooperationspartnern Boris Straumal, Peter Straumal, Svetlana Protasova, Andrey Mazilikin, Brigitte Baretzky, Karin Fink, Denis Danilov und Wolfgang Wenzel danke ich herzlich für die Präparation der ZnO Proben sowie theoretischen Berechnungen und fruchtbare Diskussionen über das Thema „grain boundary magnetism“ allgemein.

Ein herzlicher Dank geht auch an die Betreuer der WERA-Beamline, Michael Merz, Peter Nagel und Stefan Schuppler, ohne deren Unterstützung, die weit über das Normalmaß der Nutzerbetreuung hinaus ging, so manche Strahlzeit erfolglos geblieben wäre. Ebenfalls danken möchte ich dem ganzen ANKA-Team für freundliche Unterstützung aller Art sowie das ein oder andere Extraphoton.

Den Beamlinebetreuern der LEMU beamline an der SpS möchte ich ebenfalls herzlich danken, für die Unterstützung bei den  $\mu$ SR-Messungen, der anschließenden Datenauswertung und ertragreiche Diskussion der Ergebnisse.

Torsten Kachel, für die Unterstützung unserer Messzeiten an der PM 3 Beamline bei BESSY in Berlin.



Meinen Kollegen der (erweiterten) Arbeitsgruppe Goering, Sapana Tripathi, Patrick Audehm, Yu-Chun Chen, Joachim Gräfe, Markus Weigand und Mathias Schmidt möchte ich mich für das tolle Arbeitsumfeld, zahlreiche Diskussion und die Mithilfe und Unterstützung bei der einen oder anderen Strahlzeit danken. Hier sollen auch meine ehemaligen Kollegen Daniela Nolle, Sebastian Brück und Khalid Zafar nicht unerwähnt bleiben.

Ein besonderer Dank gilt Bernd Ludescher für die Hilfe beim Einbau des neuen Magneten in das bestehende System sowie die Hilfe beim Entwurf und Bau der Präparationseinheit.

Dem technischen Personal, Ulrike Eigenthaler für die FIB-Schnitte der TEM-Proben, Peter Kopold für die Aufnahme der TEM-Bilder und EDX, Theresa Dragon und Ingrid Sorger für Schnitte und Hilfe bei chemischer Behandlung von Proben/Substraten, Michael Bechtel für seine Unterstützung bei meinen BESSY-Strahlzeiten und Siegfried Hansel für die Bereitstellung optimaler Rechner neusten Stands.

Monika Kotz für alle organisatorische Unterstützung während der letzten Jahre.

Der Feinmechanikwerkstatt und der Werkstatt des MPI Stuttgarts für das zügige, teilweise kurzfristige Fertigen verschiedenster anspruchsvoller Bauteile.

Meinen Kollegen vom „Lauftreff“, Matthias Kammerer, Mathias Schmidt und Sergej Subkow, für den einen oder anderen Muskelkater.

Bei meiner Freundin Julia für ihre tolle Unterstützung, ihr Verständnis vor allem während der langen Strahlzeiten und für einfach alles was Du für mich getan hast.

Schließlich bei meinen Eltern und meiner Familie, die mir mein Studium ermöglicht haben und mich mit allen möglichen Mitteln unterstützt haben.



## Publikationsliste

M. Gacic, G. Jakob, C. Herbort, H. Adrian, **T. Tietze**, S. Brück, E. Goering, Magnetism of Co-doped ZnO thin films, *Phys Rev B*, 75. 205206, (2007).

**T. Tietze**, M. Gacic, G. Schutz, G. Jakob, S. Brück, E. Goering, XMCD studies on Co and Li doped ZnO magnetic semiconductors, *New J Phys* 10, 055009, (2008).

D. Nolle, E. Goering, **T. Tietze**, G. Schutz, A. Figuerola, L. Manna, Structural and magnetic deconvolution of FePt/FeO(x)-nanoparticles using x-ray magnetic circular dichroism, *New J Phys*, 11, 033034, (2009).

E. Goering, S. Brück, **T. Tietze**, G. Jakob, M. Gacic, H. Adrian, Absence of element specific ferromagnetism in Co doped ZnO investigated by soft X-ray resonant reflectivity, *J Phys Conf Ser*, 200 (2010).

D.K. Satapathy, M.A. Uribe-Laverde, I. Marozau, V.K. Malik, S. Das, T. Wagner, C. Marcelot, J. Stahn, S. Brück, A. Rühm, S. Macke, **T. Tietze**, E. Goering, A. Frañó, J.H. Kim, M. Wu, E. Benckiser, B. Keimer, A. Devishvili, B.P. Toperverg, M. Merz, P. Nagel, S. Schuppler, C. Bernhard, Magnetic Proximity Effect in  $\text{YBa}_2\text{Cu}_3\text{O}_7/\text{La}_{2/3}\text{Ca}_{1/3}\text{MnO}_3$  and  $\text{YBa}_2\text{Cu}_3\text{O}_7/\text{LaMnO}_{3+\delta}$  Superlattices, *Phys Rev Lett*, 108, 197201, (2012).

B.B. Straumal, A.A. Mazilkin, S.G. Protasova, P.B. Straumal, A.A. Myatiev, G. Schütz, E.J. Goering, **T. Tietze**, B. Baretzky, Grain boundaries as the controlling factor for the ferromagnetic behaviour of Co-doped ZnO, *Philos Mag*, 93 (2012), 1371-1383.

B.B. Straumal, S.G. Protasova, A.A. Mazilkin, B. Baretzky, A.A. Myatiev, P.B. Straumal, **T. Tietze**, G. Schütz, E. Goering, Amorphous interlayers between crystalline grains in ferromagnetic ZnO films, *Mater Lett*, 71 (2012), 21-24.

Y.-C. Chen, E. Goering, L. Jeurgens, Z. Wang, F. Phillipp, J. Baier, **T. Tietze**, G. Schütz, Unexpected room-temperature ferromagnetism in bulk ZnO, *Appl Phys Lett*, 103 (2013) -.

B.B. Straumal, S.G. Protasova, A.A. Mazilkin, **T. Tietze**, E. Goering, G. Schütz, P.B. Straumal, B. Baretzky, Ferromagnetic behaviour of Fe-doped ZnO nanograined films, *Beilstein Journal of Nanotechnology*, 4 (2013), 361-369.

U. Heinzmann, A. Helmstedt, N. Dohmeier, N. Müller, A. Gryzia, A. Brechling, V. Hoeke, E. Krickemeyer, T. Glaser, M. Fonin, S. Bouvron, P. Leicht, **T. Tietze**, E. Goering, K. Kuepper, The local magnetic properties of  $[\text{Mn III } 6 \text{ Cr III } ]^{3+}$  and  $[\text{Fe III } 6 \text{ Cr III } ]^{3+}$  single-molecule magnets deposited on surfaces studied by spin-polarized photoemission and XMCD with circularly polarized synchrotron radiation, *Journal of Physics: Conference Series*, 488 (2014), 132001.

## **Selbständigkeitserklärung**

Hiermit erkläre ich, dass ich die Dissertation eigenständig verfasst habe und nur die genannten Hilfsmittel und Quellen verwendet habe.

---

(Ort, Datum, Unterschrift)